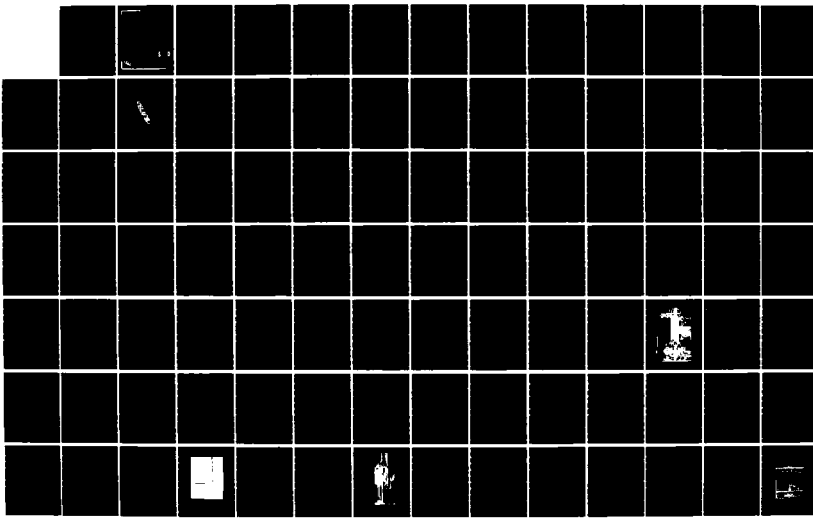
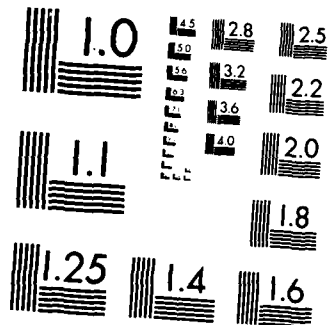


AD-A173 245 INVESTIGATION OF MATERIAL PROBLEMS FOR HIGH TEMPERATURE 1/5  
HIGH POWER SPACE. (U) ARIZONA STATE UNIV TEMPE COLL OF  
ENGINEERING AND APPLIED SCIE. D L JACOBSON ET AL.  
UNCLASSIFIED JUL 86 AFOSR-TR-86-0019 AFOSR-83-0067 F/G 11/6 NL





MICROCOPY RESOLUTION TEST CHART  
NATIONAL BUREAU OF STANDARDS-1963-A

DTIC FILE COPY

AD-A173 245

AFOSR-TR- 86-0819 (2)

## mechanical and aerospace engineering

mechanical engineering, aerospace engineering, energy systems engineering, engineering science, materials science

### INVESTIGATION OF MATERIAL PROBLEMS FOR HIGH TEMPERATURE, HIGH POWER SPACE ENERGY-CONVERSION SYSTEMS

#### Final Report

GRANT AFOSR-83-0067C

For the period

5/01/83 to 4/30/86

Approved for public release;  
distribution unlimited.

1. DRAFTED BY: R. L. JACOBSON  
2. APPROVED BY: R. L. JACOBSON  
3. RELEASED BY: R. L. JACOBSON  
4. DATE: APR 1986  
5. APPROVAL NUMBER: AFOSR-86-0819-12  
6. DISTRIBUTION: UNLIMITED  
7. TECHNICAL INFORMATION DIVISION

Produced for the

AIR FORCE OFFICE OF SCIENTIFIC RESEARCH

AFOSR/NE Bld. 410

Bolling Air Force Base

Washington, D.C., 20332

#### Contributors:

Dean L. Jacobson, James F. Morris, Mysore Ramalingam,  
Shlomo Snir, Charles Bice, Derek Tang, Peter Lee, Bang-Hung Tsao,  
Rick Stout, Nelson Moraga

#### ATTENTION:

Major Joseph W. Hager  
Program Manager  
Electronic and Material Sciences

DTIC  
ELECTE  
OCT 21 1986  
S D  
D



College of Engineering & Applied Sciences  
Arizona State University  
Tempe, Arizona 85287



CR-R

**UNCLASSIFIED**

SECURITY CLASSIFICATION OF THIS PAGE

**REPORT DOCUMENTATION PAGE**

1a. REPORT SECURITY CLASSIFICATION UNCLASSIFIED	1b. RESTRICTIVE MARKINGS D		
2a. SECURITY CLASSIFICATION AUTHORITY	3. DISTRIBUTION/AVAILABILITY OF REPORT Approved for public release; distribution unlimited.		
2b. DECLASSIFICATION/DOWNGRADING SCHEDULE			
4. PERFORMING ORGANIZATION REPORT NUMBER(S)	5. MONITORING ORGANIZATION REPORT NUMBER(S) <b>AFOSR-TR-86-U 819</b>		
6a. NAME OF PERFORMING ORGANIZATION Arizona State University	6b. OFFICE SYMBOL (If applicable)	7a. NAME OF MONITORING ORGANIZATION Air Force Office of Scientific Research	
6c. ADDRESS (City, State and ZIP Code) Tempe, Arizona 85287		7b. ADDRESS (City, State and ZIP Code) Bolling AFB, DC 20332-6448	
8a. NAME OF FUNDING/SPONSORING ORGANIZATION AFOSR	8b. OFFICE SYMBOL (If applicable) NE	9. PROCUREMENT INSTRUMENT IDENTIFICATION NUMBER AFOSR-83-0067	
8c. ADDRESS (City, State and ZIP Code) Bolling AFB, DC 20332-6448		10. SOURCE OF FUNDING NOS.  <b>6102F</b>	
		PROGRAM ELEMENT NO.      PROJECT NO.      TASK NO.      WORK UNIT NO. 2308      K1	
11. TITLE (Include Security Classification) INVESTIGATION OF MATERIAL PROBLEMS FOR HIGH TEMPERATURE, HIGH			
12. PERSONAL AUTHOR(S) Dr. Dean L. Jacobson			
13a. TYPE OF REPORT Final	13b. TIME COVERED FROM 01 May 83 TO 30 Apr 86	14. DATE OF REPORT (Yr., Mo., Day) 1986, July	15. PAGE COUNT 325
16. SUPPLEMENTARY NOTATION			
17. COSATI CODES	18. SUBJECT TERMS (Continue on reverse if necessary and identify by block number)		
FIELD	GROUP	SUB. GR.	
19. ABSTRACT (Continue on reverse if necessary and identify by block number) The final report has been divided in six sections. The first one is an introduction. In the second section, the theory of dilute-solutions ultralloys from tungsten sintering with special eutectic applications is presented, together with a comprehensive literature survey including 95 references. In the third one, the results for the work function evaluation of tungsten-rhenium sintered alloys, obtained by using thermionic emission microscopy, are presented. The influence of rhenium content in the range 3 percent to 20 percent, and temperature, between 1946 to 2339K in the work function are reported. The fourth section includes the determination of effective work function, normal spectral emissivity, recrystallization temperature and microhardness of tungsten-rhenium and tungsten-rhenium-thoriated alloys, in the temperature range between 1400 to 2500K. Section No. 5 summarizes the research on the influence of heating time, temperature and alloying content of rhenium in the work function of tungsten alloys as determined in the Vacuum Emissionehicle. Finally, in the last section, the mechanical properties of tungsten-30 percent rhenium were investigated by using an Instron tensile testing equipment with a high temperature, ultrahigh			
20. DISTRIBUTION/AVAILABILITY OF ABSTRACT UNCLASSIFIED/UNLIMITED <input checked="" type="checkbox"/> SAME AS RPT. <input type="checkbox"/> DTIC USERS <input type="checkbox"/>		21. ABSTRACT SECURITY CLASSIFICATION UNCLASSIFIED	
22a. NAME OF RESPONSIBLE INDIVIDUAL Major Joseph W. Hager		22b. TELEPHONE NUMBER (Include Area Code) (202) 767-4933	22c. OFFICE SYMBOL NE

UNCLASSIFIED

SECURITY CLASSIFICATION OF THIS PAGE

#19. ✓vacum system. The relationship between the normalized Young's modulus, ultimate tensile strength, yield strength, elongation and test temperature was examined.

UNCLASSIFIED

SECURITY CLASSIFICATION OF THIS PAGE

TABLE OF CONTENTS :

<u>SECTION</u>	<u>PAGE</u>
1. INTRODUCTION . . . . .	1.1
2. DILUTE-SOLUTION ULTRALLOYS FROM TUNGSTEN SINTERING WITH SPECIAL EUTECTIC ACTIVATORS	
2.1 ABSTRACT . . . . .	2.1
2.2 SPACE-POWER AIMS DEFINE ULTRALLOY TARGETS . . . . .	2.2
2.3 SINTERING . . . . .	2.9
2.4 ENHANCED SINTERING . . . . .	2.10
2.5 SOME SUPERFICIAL SINTERING THEORY . . . . .	2.11
2.6 PHASE DIAGRAM CONSIDERATIONS FOR ACTIVATED SINTERING OF TUNGSTEN . . . . .	2.14
2.7 SINTERING AND STRENGTHENING W WITH AN IR, TH, HF ACTIVATOR, GETTER EUTECTIC . . . . .	2.21
2.8 REFERENCES . . . . .	2.22
2.9 APPENDIX . . . . .	2.26
3. THERMIONIC EMISSION MICROSCOPY OF SINTERED TUNGSTEN RHENIUM ALLOYS	
3.1 ABSTRACT . . . . .	3.iii
3.2 INTRODUCTION . . . . .	3.1
3.3 THERMIONIC ELECTRON EMISSION . . . . .	3.5
3.4 EXPERIMENTAL APPARATUS . . . . .	3.14
3.5 EXPERIMENTAL PROCEDURE . . . . .	3.28
3.6 RESULTS . . . . .	3.50
3.7 CONCLUSIONS AND RECOMMENDATIONS . . . . .	3.60
3.8 REFERENCES . . . . .	3.73



Availability Codes	Avt. & U or Special	A-1

TABLE OF CONTENTS (Continued)

4.	INVESTIGATION OF SINTERED TUNGSTEN, RHENIUM ADDITIVE ALLOYS FOR HIGH TEMPERATURE SPACE APPLICATIONS	
4.1	ABSTRACT	. . . . . 4.iii
4.2	INTRODUCTION	. . . . . 4.1
4.3	THERMIONIC EMISSION CHARACTERISTICS OF W,RE, AND THORIATED W,RE ALLOYS	. . . . . 4.11
4.4	EFFECT OF TEMPERATURE ON THE EMISSIVITY OF W,RE AND THORIATED W,RE ALLOYS	. . . . . 4.63
4.5	RECRYSTALLIZATION AND GRAIN GROWTH CHARACTERISTICS OF SINTERED W,RE AND THORIATED W,RE ALLOYS	. . . . . 4.91
4.6	HIGH TEMPERATURE, HIGH VACUUM MECHANICAL TESTING OF W,RE AND W,RE, ThO <sub>2</sub> ALLOYS	. . . . . 4.117
4.7	FACILITY DEVELOPMENT	. . . . . 4.150
4.8	GENERAL CONCLUSIONS	. . . . . 4.154
4.9	RECOMMENDATIONS FOR FUTURE RESEARCH ACTIVITY	. . . . . 4.157
4.10	REFERENCES	. . . . . 4.160
5.	DETERMINATION OF WORK FUNCTION OF TUNGSTEN-RHENIUM ALLOYS USING VACUUM EMISSION VEHICLE	
5.1	ABSTRACT	. . . . . 5.1
5.2	INTRODUCTION	. . . . . 5.2
5.3	THERMIONIC EMISSION THEORY	. . . . . 5.4
5.4	DESIGN AND FABRICATION OF 3.556 MM DIAMETER COLLECTOR ASSEMBLY	. . . . . 5.9
5.5	EXPERIMENTAL APPARATUS	. . . . . 5.21
5.5	EXPERIMENTAL PROCEDURE	. . . . . 5.28
5.6	EXPERIMENTAL RESULTS AND DISCUSSION	. . . . . 5.38
5.7	CONCLUSIONS	. . . . . 5.50
5.8	REFERENCES	. . . . . 5.52

TABLE OF CONTENTS (Continued)

6.	HIGH TEMPERATURE, HIGH VACUUM MECHANICAL TESTING OF TUNGSTEN-30 PERCENT RHENIUM ALLOY	
6.1	ABSTRACT	.6.1
6.2	INTRODUCTION	.6.2
6.3	EXPERIMENTAL PROCEDURE	.6.6
6.4	EXPERIMENTAL RESULTS	.6.10
6.5	SUMMARY	.6.12
6.6	REFERENCES	.6.13

**SECTION 1**  
**INTRODUCTION**

## 1. INTRODUCTION

This is the final report for grant AFOSR 83-0067. The period covered is May 1, 1983 to April 30, 1986. Partial results of the research have been reported previously in two annual reports entitled, Material Problems for High-Temperature, High-Power Space Energy-Conversion Systems, and Investigation of Material Problems for High Temperature, High Power Space Energy-Conversion Systems, in May of 1984 and May of 1985, respectively.

The final report has been divided in six sections. The first one is an introduction. In the second section, the theory of dilute-solutions ultralloys from tungsten sintering with special eutectic applications is presented, together with a comprehensive literature survey including 95 references. In the third one, the results for the work function evaluation of tungsten-rhenium sintered alloys, obtained by using thermionic emission microscopy, are presented. The influence of rhenium content in the range 3 percent to 30 percent, and temperature, between 1946 to 2339K in the work function are reported. The fourth section includes the determination of effective work function, normal spectral emissivity, recrystallization temperature and microhardness of tungsten-rhenium and tungsten-rhenium-thoriated alloys, in the temperature range between 1400 to 2500K. Section No. 5 summarizes the research on the influence of heating time, temperature and alloying content of rhenium in the work function of tungsten alloys as determined in the Vacuum Emission Vehicle. Finally, in the last section, the mechanical properties of tungsten-30 percent rhenium were investigated by using an Instron tensile testing equipment with a high temperature, ultrahigh vacuum system. The relationship between the normalized Young's modulus, ultimate tensile strength, yield strength, elongation and test temperature was examined.

Contributors to the reported work include: Dean Jacobson, James Morris, Charles Bice, Derek Tang, Kurt von Braum, Joe Vittengel, Mysore Ramalingam, Peter Lee, Rick Stout, Bang-Hung Tsao and Nelson Moraga.

The advanced degrees awarded, including dates, recipients, types of degrees, and thesis titles are:

Date	Recipient	Degree	Thesis title
1. May 85	Charles Bice	M.S.	Emissivity Data for Metals at High Temperature.
2. Dec 85	Shlomo Snir	M.S.	Thermionic Emission Microscopy of Sintered Tungsten Rhenium Alloys.
3. May 86	Mysore Ramalingam	Ph.D.	Investigation of Sintered Tungsten, Rhenium Additive Alloys for High Temperature Space Applications.
4. Aug 86	Peter Lee	M.S.	Determination of Work Function of Tungsten-Rhenium Alloys using Vacuum Emission Vehicle.

The names of papers presented orally at conferences are listed below:

1. J. Morris, Ultralloys for Nuclear Thermionic Conversion. 18th Annual Intersociety Energy Conversion Eng. Conference Orlando, Florida August 1983 (Paper requested by session organizer, author served as session chairman).
2. J. Morris, Space-Nuclear-Reactor Questions. 18th Annual Intersociety Energy Conversion Eng. Conference Orlando, Florida August 1983 (Paper requested by session organizer).
3. J. Morris, Better, Cheaper In-Core Thermionic Energy Conversion (ICTEC) with Pre-1973 Ultralloys. 19th Annual Intersociety Energy Conversion Eng. Conference San Francisco, California August 1984.
4. D. Jacobson and J. Morris, Thermionic Energy Conversion for Space-Power and Terrestrial-Topping Applications. International Telecommunications Energy Conference (INTELEC 84), November 1984.

5. D. Jacobson and J. Morris, TEC and Ultralloys for High-Power Space Systems. 1985 Intersociety Energy Conversion Eng. Conference Miami Beach, Florida August 1985.
6. V. C. Bice and D. Jacobson, Emissivity Data for Metals at High Temperature. AIAA 20th Thermophysics Conference Williamsburg, Virginia, June 1985.
7. M. L. Ramalingam and D. L. Jacobson, An Accurate Method for the Determination of Normal Spectral Emissivities of Refractory Alloys, sent to AIAA 25th Aerospace Sciences Meeting Reno, Nevada, January 1987.

The list of articles about the research that have been published and accepted for publication is:

1. J. Morris, Decreased Creep for Increased Space Power, Engineering Fracture Mechanics, Vol. 24, No. 1, pp. 77-95, 1986.
2. M. L. Ramalingam, S. Snir and D. L. Jacobson, Thermionic Emission Characteristics of Sintered Tungsten, Rhenium Alloys, accepted to be published at Journal of Materials for Energy Systems.
3. M. L. Ramalingam and D. L. Jacobson, Elevated Temperature Softening of Progressively Annealed and Sintered Tungsten, Rhenium Alloys, accepted to be published at Journal of Less Common Metals.

**SECTION 2**

**DILUTE-SOLUTION ULTRALLOYS FROM TUNGSTEN SINTERING  
WITH SPECIAL EUTECTIC ACTIVATORS**

## ABSTRACT

Rapidly accelerating space-power requirements intensify demands for ultimate alloys based on the most refractory metal -- tungsten. These ultralloys must maintain the high-temperature advantages of W increase its resistance to creep, recrystallization and embrittlement enable its quality control and simplify its processing if possible. Such an alloy system appears to be achievable. This W modification involves the order-of-1% addition of the probable ternary eutectic comprising ~60a/o Ir approximately completed with the ~2-to-1 Th-to-Hf eutectic (Th, ~32a/o Hf ~1450 C) and probably melting near 1500 or 1600 C. The binary Ir, 43a/o Th eutectic (or perhaps Ir, 10a/o Th both melting at ~1540 C) and to a lesser extent Ir, 37.7a/o Hf (~2080 C) qualify similarly: Ir with 5d<sup>7</sup> electrons and good solubility of W but poor solubility in W is a promising candidate for activated sintering of W -- a metal it renders considerably more ductile as well. Furthermore appropriate inclusions of Th and Hf substantially reduce the Ir melting point (~2450 C) and maximize gettering of O,C and N segregated as W oxide, carbide and nitride encrustations at granule surfaces. Such reactions provide Ir access to W and disperse extremely stable ThO<sub>2</sub>, HfC and HfN intergranularly to oppose grain growth, creep, cavitation and embrittlement. These chemical reactions also remove metallic Th and Hf finally which with W solution in and of Ir raise the ultralloy fusion temperature to approach that of W itself. Thus proper W, Ir, Th, Hf combinations (with slight O and/or C additions if indicated) offer excellent potentialities for improvement of W processing and properties. This liquid-phase activated sintering of W offers ultralloys--upgraded in contrast with degraded characteristics produced by usual approaches utilizing Ni or Pd with their comparatively low melting points, high vapor pressures and poor gettering capabilities. Although Th, ~15a/o Ir (~1340 C) Hf, ~17a/o Ir (~1430 C) and probable Th, ~28a/o Hf, ~16a/o Ir (~1400 C) hold some W-activated-sintering interest they appear to reduce the Ir effect too much. Another bonus is the dilute-solution simplification of basic research contributing to prototypic space ultralloys.

## TABLE OF CONTENTS

SECTION	PAGE
ABSTRACT . . . . .	1
SPACE-POWER AIMS DEFINE ULTRALLOY TARGETS . . . . .	2
SINTERING . . . . .	9
ENHANCED SINTERING . . . . .	10
SOME SUPERFICIAL SINTERING THEORY . . . . .	11
PHASE-DIAGRAM CONSIDERATIONS FOR ACTIVATED SINTERING OF TUNGSTEN . . . . .	14
SINTERING AND STRENGTHENING W WITH AN IR, TH, HF ACTIVATOR, GETTER EUTECTIC . . . . .	21
REFERENCES . . . . .	22
APPENDIX . . . . .	26

## SPACE-POWER AIMS DEFINE ULTRALLOY TARGETS

Space-mission goals of minute pulses tenths of a gigawatt above steady states up to several megawatts pose problems that challenge even optimistic material projections. Such great temporal power integration in space demands ultimate thermophysicochemical capabilities. And one categorical requirement is excellent tensile creep strength at extremely high temperatures in hard vacuum. This requisite essentially specifies dilute-addition alloys of the maximal metal tungsten [1]. W offers the greatest elemental self-diffusion (creep) activation energy (-0.6MJ/mole), the highest tensile strength above 1-1900K, the lowest vapor pressure ( $-4 \times 10^{-7}$  torr at 2000K) and the maximum metallic melting point (~3680K, higher than Ta by >400K and Mo by ~800K). These and other high-temperature advantages of W must also characterize its ultralloys. But there low concentrations of specifically active additives must reduce creep, recrystallization and embrittlement as well as facilitate processing and quality control if possible.

Improvement of W properties in dilute-addition ultralloys receives considerable attention in references 1 to 6. In fact reference 1 discusses the alloy efficacy of several percent Re, the order of one percent Os or a few tenths percent Ir dissolved in W. Enhancement of such dilute-solution effects is possible with small added quantities of the excellent "getters" Th and Hf (Figures 1 to 3, Table 1): Th exhibits an extreme affinity for O forming  $\text{ThO}_2$  "which thermodynamically is the most stable oxide" [7] with "a melting point of 3300°C...the highest of all oxides" [8]. And Hf evidences great chemical attraction for C as well as N producing  $\text{HfC}$  "the most refractory binary composition known" (~4120K) and  $\text{HfN}$  "the most refractory of all known nitrides" (~3580K) [8]. Therefore slight Th and Hf additions convert deleterious W-particle encrustations of oxides, carbides and nitrides to propitious intergranular dispersions of exceedingly stable interstitial-impurity reaction products [1-6].

This strategically located conversion of embrittling weakening grain-surface films to ductilizing strengthening interparticulate dispersoids attains specific importance in both completely fused and sintered W because of its inherently limited solubilities for problematic elements [9]:

The extent to which the plasticity of refractory metals is affected by the interstitials varies depending on the kind of impurity. On the basis of studies of the interactions of impurities with VIA-group metals the following "embrittlement sequence" (in the order of decreasing effect) has been established: carbon, oxygen, nitrogen, hydrogen [10-12]. As far as metals of the VA group are concerned the sequence may be written as follows: hydrogen, nitrogen, oxygen, carbon [13]. Oxygen is the most harmful impurity for rhenium [14]. Hard and brittle nonmetallic compounds in the form of films or sheets precipitated along the subgrains are particularly harmful. The bond between the subgrains is sharply decreased in this case resulting in brittle fracture. For example 0.006% oxygen is enough for all grains in the molybdenum crystal to be surrounded by its oxides. When the content of interstitial impurities does not exceed the solubility limit the VA and VIA group metals are plastic at low temperatures [10].

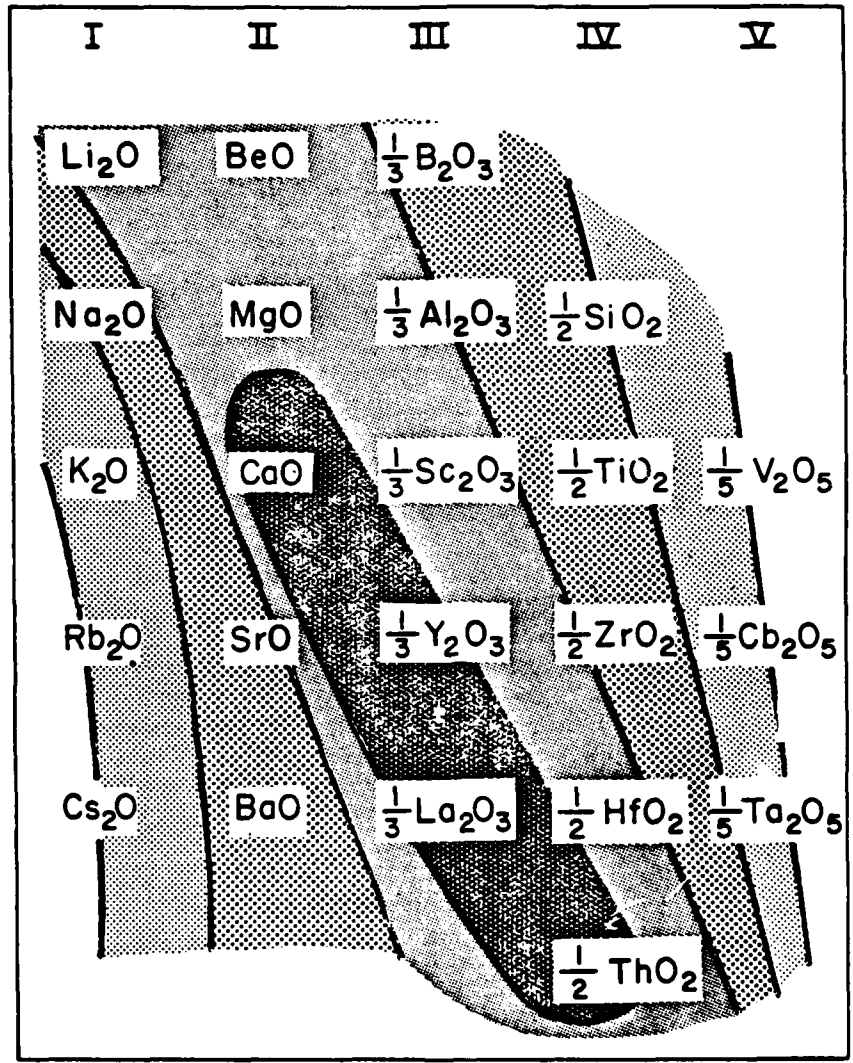
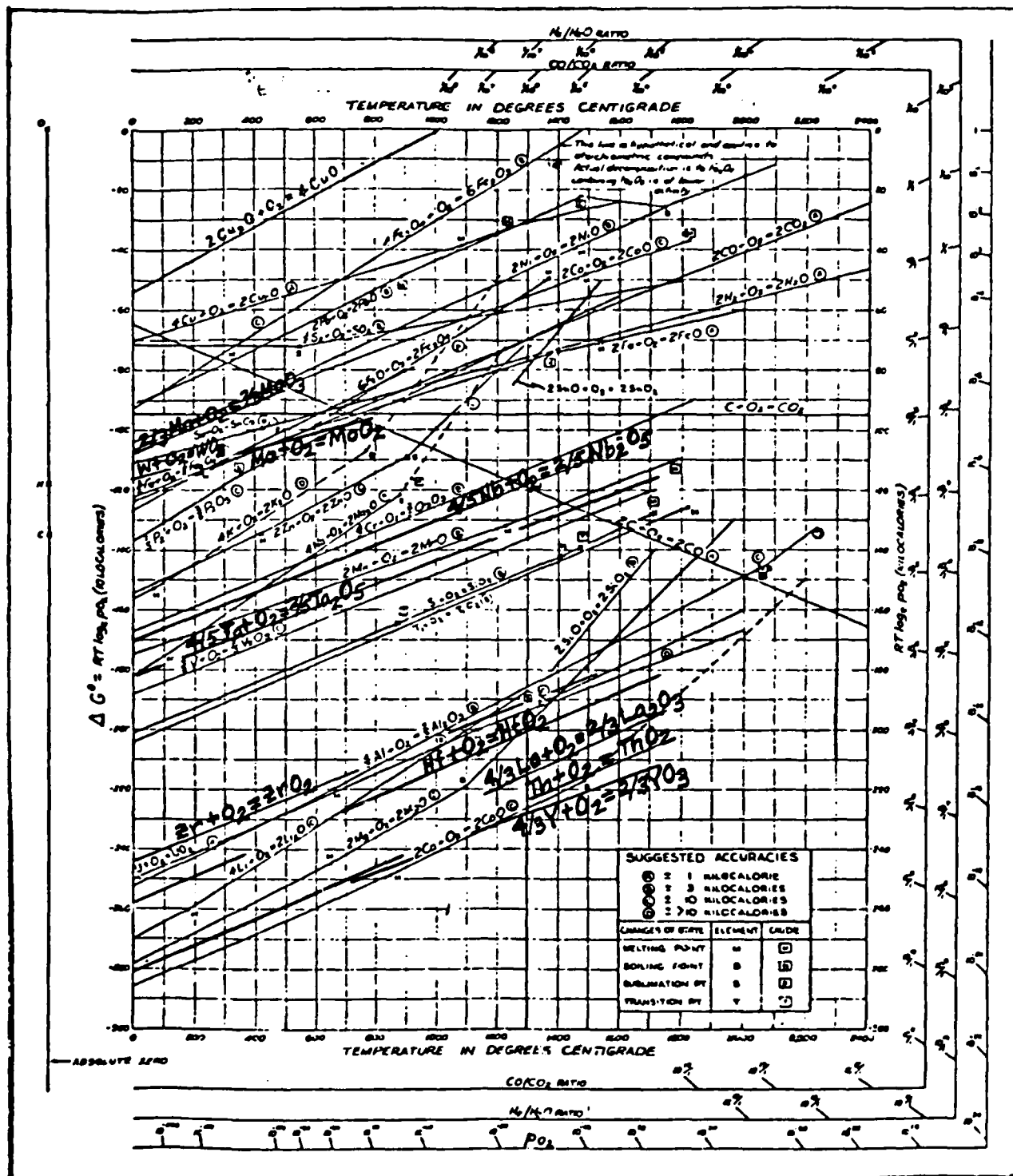


FIGURE 1. STABILITY RELATIONSHIPS OF REFRACTORY OXIDES

Solid lines are lines of constant standard free energy of formation from the elements. The darkly shadowed area is the region of greatest stability.



**Fig. 2.** Free-energy data for oxide formation (after Richardson and Jeffes, 1948).

$$1 \text{ kcal} = 4.1868 \text{ kJ}, 2.303 R = 19.1546 \text{ J/mol degC};$$

$$1 \text{ atm} = 101.325 \text{ kN/m}^2, 1 \text{ V equiv.} = 96.406 \text{ kJ.}$$

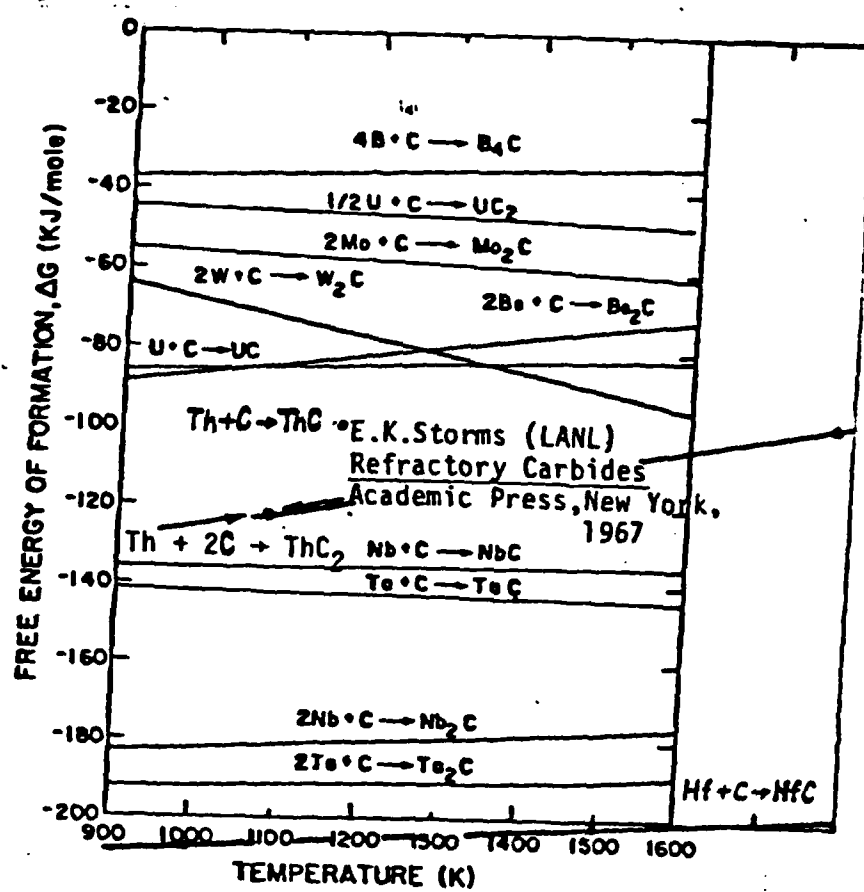


Fig. 3 Comparison of free energy of formation.  
(LA-7858)

TABLE 1  
BOND ENERGIES FOR SOME OXIDES AND CARBIDES (KJ/MOL.)

	Sc	Y	La	Ti	Zr	Hf	Th	V	Nb	Ta	Cr	Mo	W
H-O <sup>a</sup>	672	713	796	661	757	766	828	617	753	812	423	485	649
H-C <sub>2</sub>	560	634	662	569	661	-	702	570	-	-	445	-	-
O-H-O <sup>a</sup>	1450 <sup>b</sup>	1464 <sup>b</sup>	1570 <sup>b</sup>	1310	1443	1506	1623	1213	1427	1435	925	1130	1238
C <sub>2</sub> -H-C <sub>2</sub>	1207	1271	1310	1214	-	-	-	1193	-	-	-	-	-

<sup>a</sup>Oxide values taken from J. Drowart and P. Goldfinger, Angew. Chem. Int. Ed. 6, 581, 1967.

<sup>b</sup>Predicted values.

A film of a second phase is not always revealed when intergranular embrittlement takes place. Nucleation and propagation of the crack in this case occur due to the intergranular segregation of impurities from the solid solution [15]. The impurities are clustered in the surface layers of the crystal to the depth of 2-3 atomic diameters. Auger-electron spectrometry may be used to reveal these impurities [16,17].

The interstitial impurities of the solid solution also considerably deteriorate the plasticity of refractory metal mainly due to the locking of dislocations and to the decrease of the resistance to crack propagation [18]. However the impurities in solution exert a smaller effect on the brittleness of refractory metals than as if they were present in the form of a second phase [19]. For example a large number of coarse carbide and oxide inclusions are present in poly- and single-crystalline tungsten of commercial purity (carbon  $> 10^{-3}$  and oxygen  $> 10^{-3}$  wt-%). When reducing the carbon and oxygen content down to  $10^{-6}$  and  $10^{-5}$  wt-% respectively W<sub>2</sub>C and WC are rarely formed. Using transmission electron microscopy (1000kV) the inclusions were revealed in the tungsten single crystals with given carbon and oxygen content containing in addition silicon, phosphorous, boron and sulfur. The elements listed above are present in the original material. They then pass to tungsten during the chemico-technological processing and the growth of the single crystal. They amount to  $10^{-3}$  -  $10^{-4}$  wt-% each. This considerably exceeds the solubility limit of these elements in tungsten at room temperature [20-24] thus resulting in the formation of the second-phase inclusions....

This discussion by Savitsky emphasizes the need for utilization of gettering metals such as Th and Hf. In fact Savitsky strongly advocates the use of Hf to form HfC because of "its high thermodynamic stability in tungsten" as it "raises the temperature of the onset of structural changes on recovery and recrystallization by 300-600°C,...increases the overall resistance of the material to brittle failure and improves the mechanical properties" [25].

Furthermore elements such as Hf and in particular Th that differ considerably from W in crystal-ionic radii exhibit nearly nil solubility in W and therefore alter its characteristics substantially as minute inclusions. In support of this observation reference 26 asserts, "The recrystallization temperature of tungsten is strongly affected by small additions of zirconium, hafnium and boron with an atomic radius differing greatly from that of tungsten and with very slight solubility in tungsten." The crystal-ionic radii of Zr(0.79A,+4), Hf(0.78A,+4) and B(0.23A,+3) deviate considerably from 0.62A for W (+6). This difference is particularly great for B which raises the W recrystallization temperature 400°C at only 0.005 w/o [26]. But B has notorious interstitial-diffusion tendencies and a 2000K vapor pressure two orders of magnitude higher than that of Zr or Hf. In contrast Th vaporizes comparably with Zr and Hf at 2000K and stands in size opposition to B with a 1.02A crystal-ionic radius (+4). This radial mismatch with W should assure more impressive results at lower concentrations than for Zr or Hf. And again Th segregates intergranularly: There its excellent gettering capabilities contribute to freeing W from embrittling encrustations of compounds with

interstitial impurities and distribute resulting stable intergranular refractory dispersoids to further benefit ultralloys [1,3]. But if such dispersions are necessary in greater quantities to optimize resistance to creep, recrystallization and embrittlement appropriate adjustments are possible.

Accordingly low-concentration additives enable desired W-alloy-property improvements. However effective, efficient, quality-controlled processing remains a problem: Melting in vacuum or high-purity cover gas is expensive and time-consuming as is chemical vapor deposition. So physically compacting then sintering prevails although this process provides neither the best nor the most precise product. Of course homogeneity is unapproachable except in extremely pure single-crystal W which is prohibitively costly. But sintering invites segregation difficulties beginning with production and control of the powder characterized by purity, size, shape, porosity, microstructure, defects, specific surface, size distribution, density, flowability and compressibility.

These somewhat simplistic divisions subdivide further as exemplified by the preceding discussion of purity effects depending at least on chemical types, amounts, locations, processing, interacting impurities, specific additives.... The unintended inclusions initiate of course in the ores, scheelite (predominantly CaWO<sub>4</sub>) and wolframite (primarily FeWO<sub>4</sub> and MnO<sub>4</sub>), which contain many difficultly removed impurities. The resulting W oxides generally undergo hydrogen reduction yielding W powders with the following extraneous-elements analyses [27].

#### TYPICAL ANALYSES OF HYDROGEN-REDUCED TUNGSTEN POWDERS (PPM)

Element	Low Grade	Commercial Grade	Very High Purity
O*	1000-3000	500-1500	150
C	100-300	80	30
N	50	50	30
H	50	20	10
Mo	50-300	100	30
Ni	200	30	20
Fe	100-200	50	20
Mn	100	<10	<<10
Si	100	10	10
Al	50-100	10	10

\*Oxygen content depends on particle-size distribution (next table).

### TYPICAL FISHER SUBSIEVE SIZE OF HYDROGEN-REDUCED TUNGSTEN POWDERS

Type	Average Size, $\mu\text{m}$	Range from 10w/o Smaller to 10w/o Larger, $\mu\text{m}$
C-3	0.7-0.8	---
C-5	1.05-1.20	0.8-4.0
C-6	1.80	---
C-8	2.60-3.50	1.8-5.2
C-10	4.50-5.50	2.8-6.8
C-20	6.50-7.02	3.4-8.2
C-40	8.00-8.50	---

These tables merely imply composition and size distributions typifying W powders entering the simplest, cheapest consolidation process -- sintering.

In view of these and other previously discussed complications some special adaptations are necessary to reduce creep, recrystallization and embrittlement; to maintain high melting points and low vapor pressures; to facilitate processing and quality control; and yet to continue to produce consolidated W alloys by sintering. In any event the preceding enumerations of objectives and impediments indicate how space-power aims define ultralloy targets.

### SINTERING

Powder metallurgy leans heavily on consolidation by physical compaction then thermal contraction. The latter actually comprises thermophysicochemical processes "to weld together partially and without melting" the compressed products of the former operation. While that particular dictionary definition is simplistic it conveys a rudimentary feeling for "sintering." But efforts to define this subject in detail began long ago. For example Adamson in his 1960 text [28] recalls the 1942 contributions of "Huttig [29] in an extensive study of the sintering process" and continues the elaboration:

Although sintering by definition occurs while the particles are still apparently solid the temperature must not be too far from the melting point, and the first marked effects usually occur from 0.75 of the melting point on. At such temperatures bulk flow in response to the pressure gradient of the curved surfaces of the pores may be important. Mackenzie and Shuttleworth [30] concluded that this effect was the one mainly responsible for the density increase on sintering and that it represented a cooperative phenomenon in that although it could not occur for an isolated pore it could in the case of a porous mass.... Herring on the other hand felt that surface diffusion and other transport processes rather than plastic flow are usually dominant [31]. More recently Kuczynski [32] in reviewing the matter concluded that densification during sintering was mainly due to volume diffusion with grain boundaries acting as sinks.

Sintering-mechanism debates persisted through the interim until today fragmentation of this technology might be expected.

However the contemporary technological status is one of agglomeration [33]: "Various types of material transport including viscous flow, plastic flow, evaporation-condensation, surface diffusion, grain boundary diffusion, and volume diffusion may occur during sintering. Models and sintering equations with a circular neck shape assumption have been proposed [34-40] to describe these mechanisms." There is a lesson in socioscientific sintering to be learned here: Incorporate the complete distribution of reasonable mechanistic fragments and consolidate them within the lowest-free-energy (and simplest) model geometry. But even with such simplification sintering and its products are complex, heterogeneous, difficult to define and therefore incapable of complete control -- especially for highly refractory materials.

#### ENHANCED SINTERING

"The densification rate in sintering tungsten powder can be significantly increased by small additions (1-4%) of group VIII transition metals as activators (Hayden and Brophy, 1963) [41]. Among them palladium and nickel appear to have the greatest effect. With 0.25% palladium densities of 93.5 and 99.5% of the theoretical are obtained after sintering 30 minutes and 16 hours respectively at 1100°C (2012°F) in hydrogen. Tungsten powder at this temperature and without such added elements can only be presintered. Metallic activation however results in a brittle product although some improvement is possible by a postsintering treatment (Toth, 1965) [42]. The mechanism for this increased densification rate has been proposed (Brophy et alii, 1961) [43]. The activating element appears on the tungsten surface forming 'carrier phase' layer. Tungsten dissolves preferentially into the layer at points of particle contacts and diffuses outward in the interface between the carrier phase layer and the particle itself. The result is a decrease in distance between adjacent particle centers and an overall shrinkage of the powder compact. This activation process may prove to be associated with the fact that group VIII transition elements dissolve 10-20% tungsten but are soluble in tungsten only to a very limited extent at the sintering temperatures employed" [27].

So group VIII "metallic activation" initiated enhanced sintering formally over a quarter of a century ago. But similar to simple sintering [33] this advanced technology also generalizes readily [44]: "Enhanced sintering refers to any special process aimed at improving the sintering rate of a powder compact...to effectively lower...temperature, shorten...time or improve...properties [45]. Enhanced sintering has had its greatest advancement in the refractory metals. The problems associated with understanding conventional sintering studies are compounded in enhanced sintering studies by the presence of a second phase or supplemental treatment [46-48]....Enhancement of the sintering process is generally relegated to one or more changes in the fundamental material properties resulting from special treatment [49]. The strongest effects are those associated with changes in the interfacial properties....As can be imagined any change in material under study which induces an enhanced defect concentration, higher atomic mobility or promotes the operation of new mass transport processes is an example of enhanced sintering....There are two common nonpressure based approaches to sintering enhancement of metal powders, activated sintering and liquid phase sintering....The fundamental difference is that liquid sintering uses a

wetting liquid which flows between particles while activated sintering relies on a high diffusivity solid phase segregated to grain boundaries."

What processes and properties characterize activated and liquid-phase sintering? Utilizing a "wetting liquid" subtends cavities and extends contacts between particles: Such bridging and broadening short-circuit previously circuitous diffusion paths accelerating interparticulate mass transport which increases sintering rates and densities. But substantial volume fractions of intergranular materials with relatively low melting points and probably comparatively high vapor pressures often obtrude other processing and property problems on the sintered product.

In contrast to the preceding simplistic modelling of liquid-phase sintering, postulates for the activated version initiate in the electronic subshells of the transition-metal additives: The most effective sintering activators for W and Mo according to an electron-concentration theory advanced by Samsonov et alii are far-right group-VIII elements [50-52]. These are the transition metals with high d-shell numbers such as Ni ( $3d^8$ ), Rh( $4d^8$ ), Pt( $5d^8$ ) and Pd( $4d^{10}$ ).

"The addition of group VIII transition metals greatly enhances densification by increasing diffusion of base material through the activator-rich area....It is believed that activated and liquid-phase sintering are kinetically activated processes where the second phase alters the energy barrier for transport....Several criteria are recognized for a segregated phase to act as a sintering activator. First and foremost the additive must reduce the activation energy for diffusion below that for the corresponding self-diffusion case....Second the additive must have a high solubility for the base metal....In many cases of activated sintering it is observed that the reverse solubility (the solubility of the additive in the base metal) is low....In order for the additive to provide a short-circuit diffusion path it must remain segregated at the grain boundaries. This requires that the liquidus and solidus temperatures decrease with increasing additive [53]. Also a segregated phase is preferred which does not lower the grain boundary cohesive energy. Thus we require a small atom size, large sublimation energy, inherently ductile additive [54-56]." These criteria from reference 57 also include a considerably lower melting point for the activator than for the base metal.

Thus although activator, base-metal interactions simplify sintering they complicate modelling and interpretation of transport mechanisms compared with those for simple thermally enhanced diffusion and contraction.

#### SOME SUPERFICIAL SINTERING THEORY

The titular double-entendre refers to "densification assumed to occur by volume diffusion and grain growth assumed to occur by pore drag controlled by surface diffusion..., and the density change is calculated according to the intermediate stage sintering model [58] proposed by Coble" [59]. Not surprisingly the densification-rate equation from this study of "the application of Herring's scaling law to the sintering of powders" essentially duplicates that for activated sintering [60]: "The densification rate of the compact is proportional to the vacancy flux, diffusion area, vacancy volume and pore density. After evaluating each term (sic) and assuming a bulk diffusion process the densification rate is given by

$$\frac{\partial p}{\partial t} = \frac{DB}{G^3 kT} \dots = \frac{DB}{MtkT} \quad (1)$$

where D is the diffusion coefficient, B is a collection of material and geometric constants, k is Boltzmann's constant, G is the grain size ( $G^3 = G_0^3 + Mt - Mt$  = (grain-boundary mobility)x(time) for a porous compact [58,61]) and T is temperature. This form is applicable to activated sintering where grain boundaries rich in activator provide a rapid heterodiffusion path [62]."

"The rate of sintering is viewed as dependent on several factors. For simplicity a model of pore elimination is given as [63]

$$\frac{d\varepsilon}{dt} = - \frac{g \exp[-Q/RT]}{\varepsilon^{1/2} G^3} [\gamma/r + P] \quad (2)$$

where  $\varepsilon$  = porosity, t = time, g = a collection of geometric and material constants, Q = activation energy, R = gas constant, T = absolute temperature, G = grain size,  $\gamma$  = surface energy (sic, force/length or pressure x length), r = pore size and P = effective pressure. In hot pressing the effective pressure is large and dominates the rate of pore elimination. In liquid phase sintering the surface energy of the wetting liquid dominates sintering. However in solid-state sintering the activation energy and small grain size both promote sintering densification" [64].

In view of the predominance of intermediate-temperature grain-boundary diffusion in sintering, similarities are not surprising between equations (1), (2) and the expression for Coble creep [3,65]:

$$\dot{\varepsilon} = \frac{C_c b^{\alpha}}{kT d^3} D_{bo} \exp[-Q_b/RT] = \frac{D_b B_b}{G_b^3 kT} [P_b] \quad (3)$$

Here  $\dot{\varepsilon}$  is the steady-state strain rate;  $C_c$ , a morphochemophysical constant;  $\alpha$ , applied stress; d, grain size;  $D_{bo}$ , a frequency factor; and  $Q_b$ , the diffusion-activation energy. In fact Coble was studying sintering mechanisms in alumina when he recognized that at relatively low temperatures creep depends primarily on rapid grain-boundary diffusion -- rather than on much slower lattice diffusion through much greater cross-sections. These aspects of diffusion as well as continual references to grain sizes, surfaces and growth problems in sintering also stress its similitude to the "formation and migration of large-angle grain boundaries" ["Recrystallization" from 5:Appendix].

Thus although particle extension and segregation ideally characterize liquid-phase and activated sintering the uncontrolled or improperly directed interactions of these phenomena produce some undesirable properties [3,5,9,25-27,54,56,66-76]. As the preceding referential citations indicate much information exists on grain-boundary-migration effects in general and on their sintering implications in particular. Of course these mechanisms also heighten segregation of interparticulate impurities through "dragging" forces, interfacial surface reduction and accelerated diffusional approaches to chemical equilibria. Perhaps this last category provides the best beginning for some simplified segregation theory.

Segregating elements encounter greater heterogeneity intergranularly than intragranularly. But even within the crystalline grains homogeneity suffers--particularly in the several atomic layers forming the surface and immediate substrata [9,25,27,55,56,60,71,74].

Thus simplification is essential in initiation of a theoretical description of  $n_c$  and  $n_b$  solute atom with energies  $E_c$  and  $E_b$  when randomly distributed among  $P_c$  and  $P_b$  crystallite and boundary sites ( $n_c + n_b = \text{constant}$ ). Then the total solute-atom free energy  $G$  comprises the sum of  $n_c E_c$  and  $n_b E_b$  minus  $kT$  times the natural logarithm of the entropy for the solute-atom configuration:

$$G = n_c E_c + n_b E_b - kT \ln \frac{P_c! P_b!}{n_c! n_b! (P_c - n_c)! (P_b - n_b)!} \quad (4)$$

Subsequent differentiation with respect to  $n_b$  yields a minimum where the grain-boundary equivalent of the Langmuir free-surface adsorption equation obtains [28,74-86]:

$$\frac{x_b}{x_b^s - x_b} = \frac{x_c}{1-x_c} \exp\left(\frac{-\Delta G}{RT}\right) \text{ or } \frac{x_b}{x_b^s} = \frac{x_c \exp(-\Delta G/RT)}{1+x_c [\exp(-\Delta G/RT)-1]} \quad (5)$$

where  $x$ 's are atomic fractions and  $s$  denotes saturation. For dilute solutions  $x_c \rightarrow 0$  and

$$\frac{x_b}{x_b^s - x_b} \rightarrow x_c \exp\left(\frac{-\Delta G}{RT}\right) \text{ or } \frac{x_b}{x_b^s} \rightarrow \frac{x_c \exp(-\Delta G/RT)}{1+x_c \exp(-\Delta G/RT)} \quad (6)$$

$$\frac{x_b}{x_b^s} \rightarrow [1 + \{x_c \exp(-\Delta G/RT)\}^{-1}]^{-1}$$

This expression equals the dilute-solution equation for the solid-state version [81] of the BET gas-adsorption theory with segregation-site-number simplification [87,88] as well as a general mass-action equation [79].

As an equality ( $x_b = x_b^s [1 + \{x_c \exp(-\Delta G/RT)\}^{-1}]$ ) equation 6 stands on a substantial base of empirical support [85]. Of course more complex segregation theories exist [81-89]. But considerable theoretic simplification appears possible for dilute-solution W alloys advocated here and in [1].

#### PHASE-DIAGRAM CONSIDERATIONS FOR ACTIVATED SINTERING OF TUNGSTEN

Boundary-layer segregation stressed in the preceding section is one of several important interactions and properties in the "enhanced sintering" of W: Activator d-electron numbers, solubility relationships and melting points require attention also.

Comparisons of such integrated effects resulted fifteen years ago from studies of "the influence of additions of transition metals on the sintering behavior of tungsten" directed by the famous Soviet materials expert Samsonov [51]:

The influence of additions of transition metals (Ti, Hf, Nb, Ta, Cr, Re, Fe, Co, Ni, Ru, Rh, Pd, Os, Ir, Pt) in concentrations of 0.05 to 1.0 wt.% on the sintering behavior of tungsten in the temperature range between 1000 and 2000°C and on its properties was studied. It was found that titanium, hafnium, niobium and tantalum retard the sintering process; chromium and the metals of the eighth group promote sintering with the exception of osmium which does not exert any influence in either direction. The influence of transition metal additions on the sintering behaviour of tungsten may be explained with an electron exchange between the alloy components. With an increase of the stable d-bonds in the system the free energy is lowered. The sintering process is activated. The sintering is accelerated by alloying additions for which tungsten acts as an electron donor.

Many subsequent publications discuss these aspects of activated sintering in greater theoretical detail with more specific experimental support [44, 45, 57, 59-62, 66-76, 90].

These considerations pertain not only to processing ease and effectiveness but also to "the alloy efficacy of several percent Re, the order of one percent Os or a few tenths percent of Ir dissolved in W" mentioned in the introductory section [1]. Ir appears to qualify for both activated sintering and improved alloying of W. Superimposing activation requirements on the Ir, W phase diagram supports this observation:

(F. SHUNK: CONSTITUTION OF BINARY ALLOYS, McGRAW-HILL, 1969)

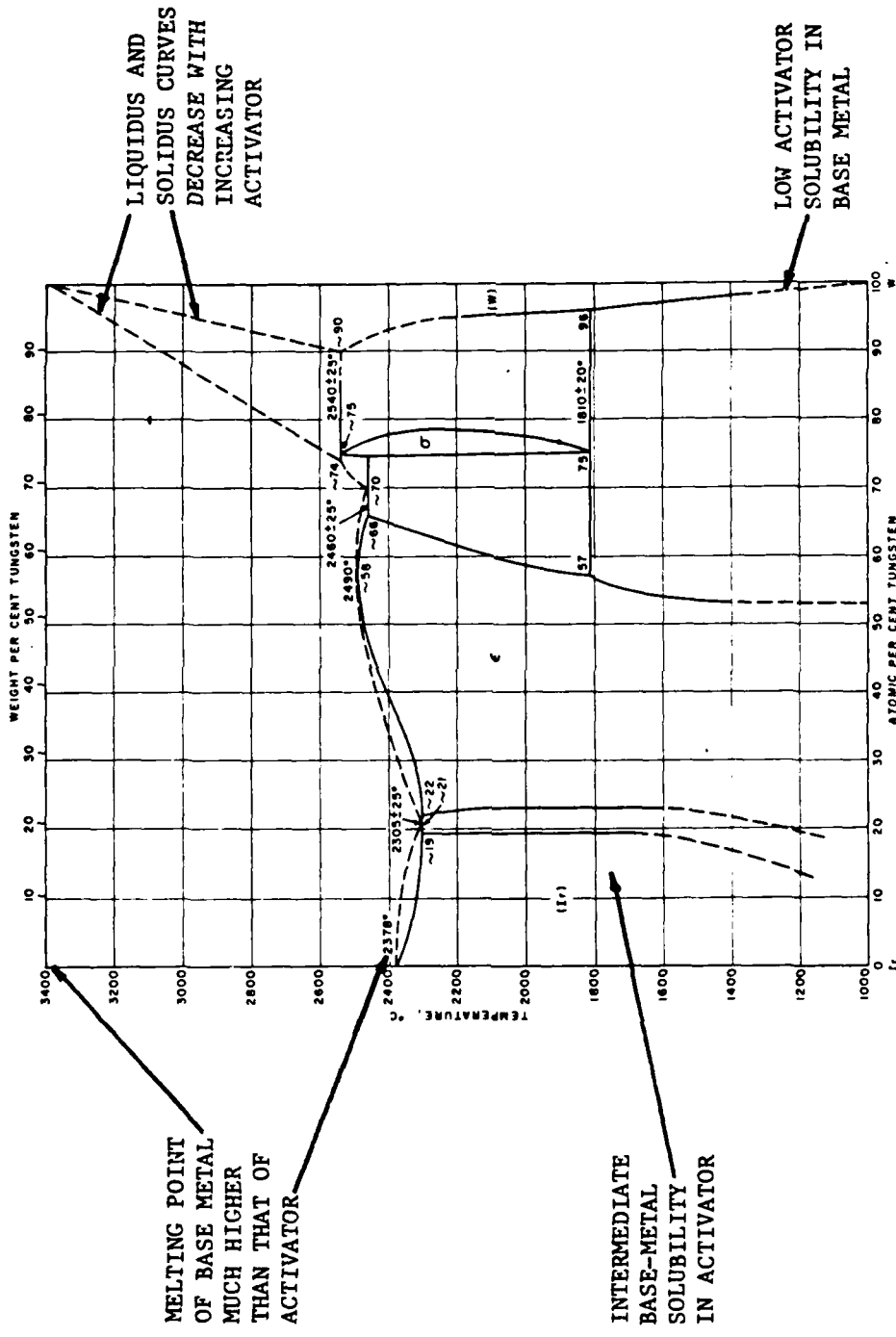


FIGURE 4: IRIDIUM, TUNGSTEN PHASE DIAGRAM

So the basic Ir, W alloy phase diagram presents a promising picture: Ir with its 5d<sup>7</sup> electrons, slight solubility in W, intermediate solubility for W and -1000°C lower melting point than W is a good prospect for sintering activation [51]. Furthermore Ir even increases the ultralloy capabilities of W.

As previously stated W is the ultimate refractory metal for space applications: It offers the highest metallic melting point, the highest recrystallization temperature, the highest self-diffusion activation energies, partially covalent bonding, the lowest vapor pressure...and great high-temperature strength. Some point to the high W density as a detriment. But its great strengths enable W to meet stress requirements at high temperatures with much less weight than its competitors. Over and above all of this a few tenths percent of Ir raises the recrystallization temperature of W, reduces its grain size, increases its creep strength and improves its ductility considerably.

In addition to Ir solution effects HfC precipitation strengthening and ThO<sub>2</sub>, dispersion strengthening separately are well known. They too increase W and W-alloy recrystallization temperatures and ductility as well as strength. And their synergistic effects warrant intensive investigation. But the use of pure Th and/or Hf to convert deleterious segregated O and C in W alloys into productive separate phases "preferentially nucleated at dislocations, grain boundaries or interphase interfaces" requires immediate attention [1-6].

In powdered metallurgical methods very small quantities of comparatively low-melting (1960K) Th and/or Hf (2400K) might also serve to reactively initiate Ir-activated sintering of W powders at greatly reduced temperatures. During the presintering process the Th and/or Hf films would spread over the W particle surfaces encrusted with compounds of segregated O and C because of their great affinities for these interstitials figures 1 to 3, Table 1 and [1-6]. And for the same reason of course the distributed Th and/or Hf would getter these embrittling superficial impurities and deposit them as very-refractory separate-phase particles "preferentially nucleated at dislocations, grain boundaries or interphase interfaces." Simultaneously, "gettering" grain-boundary-segregated and reacted O and C from the W particles would liberate W metal from superficial oxide and carbide compounds, increase its availability to the Ir activator, hence accelerate intergranular transport and thereby enhance its propensities to sinter. But the resulting very refractory Th and/or Hf oxide and carbide particles should also strongly inhibit undesirable grain-growth and creep tendencies.

These mechanisms are of course not those proposed for conventional chemically activated sintering postulated for the simple model of a pure activator (Ni, Pd, Pt...) interacting predominantly intergranularly with pure-refractory-metal particles [45,64,73-76]. Based on this practically unattainable idealization "the electron concentration concept predicts the transition metals with nearly complete d electron subshells (i.e., Ni, Pd and Pt (8, 10 and 9 electrons out of 10 maximally)) to be better sintering activators" [52,64,91]. Mechanistically "activated sintering of refractory metals with certain transition metal additives occurs because the additive lowers the energy barrier for refractory atom transport. The lower activation energy results in increased diffusion of the refractory metal through the additive. The additive remains segregated at the particle-particle contact points because of the unipolar solubility relationship. That is the refractory metal is soluble in the additive, but the additive is relatively insoluble in the refractory metal. The segregated lower melting additive

provides a rapid short-circuit mass transport path throughout the sintering process" [60].

This isolated idealized refractory-metal, activator-metal relationship certainly simplifies theoretic considerations and provides heuristic value. But W powder used in supporting experiments contained 73 ppm C, 180 ppm N and 2090 ppm O [91]; a later Mo powder contained 18 ppm C and 1258 ppm O. For such impurities extreme grain-boundary segregation is probable as discussed in reference 3. Also there the "strong influences of fractions of an atomic percent" of additives, impurities and reaction products on thermophysicochemical properties of refractory alloys received brief but emphatic attention [1-6, 56, 76, 83, 85].

Apparently segregated impurities and microalloying agents deserve if not demand at least as much attention as pure refractory-metal, activator-metal combinations. In fact P, S, Cu and even Ni "segregation to interphase boundaries in liquid-phase sintered tungsten alloys" not only affect the sintering process impressively but also weaken the resulting W, Ni, Cu and W, Ni, Fe compactions [76]. So although Th and/or Hf fail to meet the idealized pure-metal requirements of "nearly complete d electron subshells" (two d electrons each) and "of the unipolar solubility relationship," they offer solutions to some very practical problems: They getter the boundary segregated reacted O, C and other impurities that separate the nearly pure refractory metal from any activator metal. And they provide interfacially dispersed stable refractory-compound precipitates.

Amounts of segregated O and C to react with appropriately adjusted quantities of Th and/or Hf might be varied in original melt compositions [25] or by chemisorption on particles prior to sintering [92, 93]. Suitable levels for truly efficient dispersion improvements are usually fractions of an atomic percent. Th and/or Hf reaction with O and C at very low concentrations in W-alloy melts with subsequent precipitation is also a possibility. But of course the much higher vaporization tendencies of the microalloying agents compared with those of W present a problem. Finally if these localized reaction techniques fall short of optimum  $\text{ThO}_2$  and  $\text{HfC}$  requirements for W ultralloys, conventional addition methods can make up the differences. However such adjustments add to improvements already effected by gettering deleterious impurities and strategically dispersing them through microalloying with Th and/or Hf.

Thus compared with relatively inefficient random dispersion methods the preceding highly specific approach to removing a problem and replacing it with an asset -- at the desired location -- deserves further investigation. This is particularly true when the solution promises not only decreased creep but also greater ductility and recrystallization resistance as well as improved powder-metallurgy processing.

But additional advantages for W sintered by Ir activation with Th and/or Hf getters accrue upon further phase-diagram examination:

(F. SHUNK: CONSTITUTION OF BINARY ALLOYS, McGRAW-HILL, 1969)

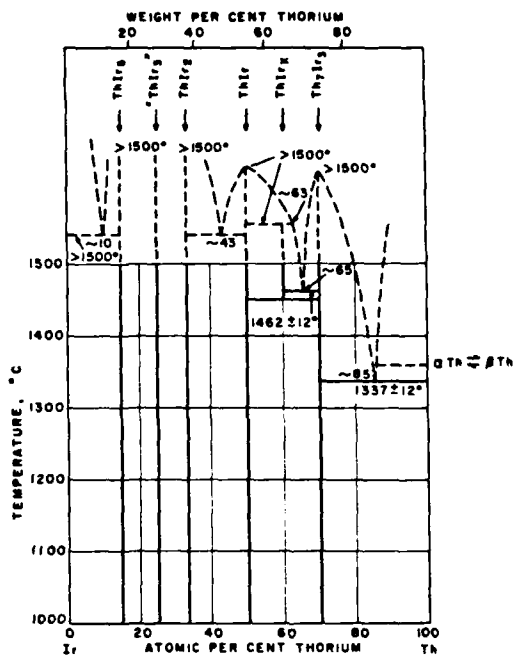


FIGURE 5: IRIDIUM, THORIUM PHASE DIAGRAM

For example ~10 and ~43a/o additions of Th to Ir produce eutectics (Ir, ThIr<sub>2</sub>, and ThIr<sub>2</sub>, ThIr respectively) melting at ~1540°C compared with 2378°C for Ir alone (Figure 4). Probably of less interest are the predominantly Th eutectics at ~35a/o Ir (~1460°C) and ~15a/o Ir (~1340°C). But the low melting points are attractive: Recall that processing with a "liquid phase" is one form of "enhanced sintering." So very low (eutectic) melting points are interesting particularly when they characterize mixtures of sintering activators with smaller fractions of strong interstitial-impurity getters.

(F. SHUNK: CONSTITUTION OF BINARY ALLOYS, McGRAW-HILL, 1969)

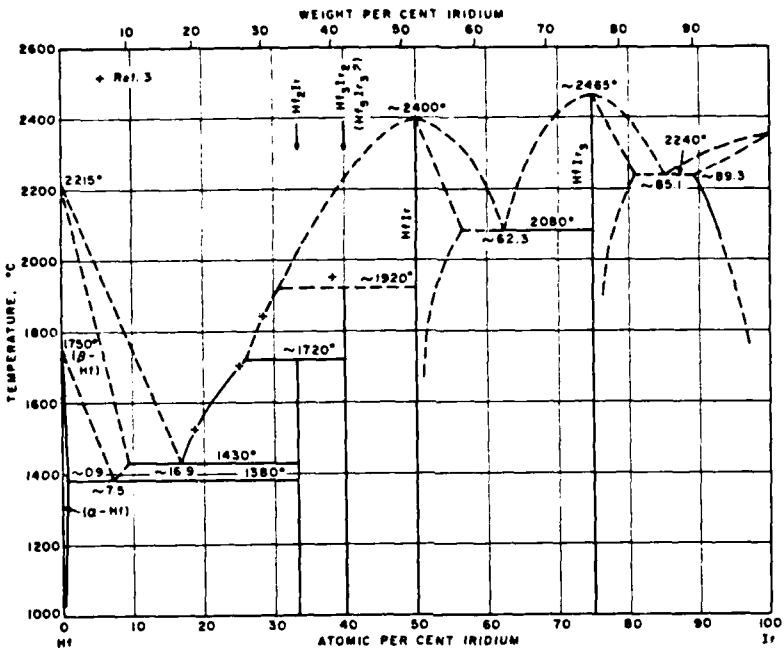


FIGURE 6: IRIDIUM, HAFNIUM PHASE DIAGRAM

Adding -38a/o Hf to Ir results in eutectic (HfIr<sub>3</sub>, HfIr) melting at -2080°C-- considerably higher than -1540°C for -43a/o Th in Ir. Similar to the Th, -15a/o Ir(-1340°C) eutectic however Hf, -17a/o Ir(-1430°C) offers a considerable melting-point reduction at the expense of Ir concentration diminution.

Perhaps the Ir, Hf, Th combination offers predominantly Ir alloys with very low melting points. As Figures 5 and 6 reveal the Ir, Hf and Ir, Th systems exhibit an important mutual characteristic: Both phase diagrams display eutectics at somewhat higher Ir concentrations than those for their equiatomic intermetallic compounds (IrHf and IrTh). In fact these two eutectics occur close to 60a/o Ir (Ir, -38a/o Hf and Ir, ~43a/o Th) as previously noted. Thus, interpolative Ir,Hf,Th predictions should include these eutectic tendencies just to the low Hf,Th side of 50a/o Ir -- at about 60a/o Ir. Unfortunately the Ir, Hf, Th phase diagram appears to be unavailable to verify this estimate. Only the two binary Ir-mixture limits, the Ir, Hf and Ir, Th phase diagrams, are available -- as well as the third boundary manifested as the Th, Hf phase diagram:

(R. ELLIOTT: CONSTITUTION OF BINARY ALLOYS, McGRAW-HILL, 1965)

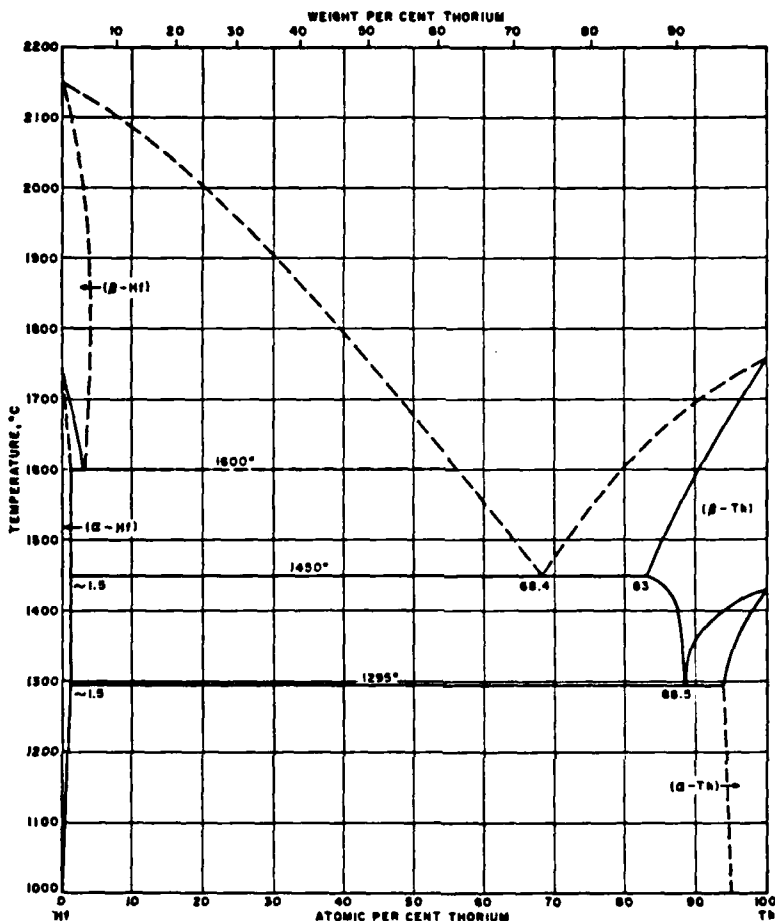


FIGURE 7: THORIUM, HAFNIUM PHASE DIAGRAM

However ~32a/o Hf in Th yields a eutectic with the impressive melting point of ~1450°C. At this temperature the vapor pressure of the Th, Hf mixture should be of the order of 10<sup>-8</sup> torr. And additions to Ir of Th, Hf compositions near their eutectic should yield eutectics between those for Ir, Th and Ir, Hf -- for example Ir, ~27a/o Th, ~13a/o Hf (melting near 1500 or 1600°C) or the possibly interesting Th, ~28a/o Hf, ~16a/o Ir (melting near 1400°C).

In any event the Th, Hf gettering combination greatly reduces the effective melting temperature of the Ir activator while it considerably improves activation access to the W base metal. These are certainly very interesting inferences from the phase-diagram considerations for activated sintering of W.

## SINTERING AND STRENGTHENING W WITH AN IR, TH, HF ACTIVATOR, GETTER EUTECTIC

W sintered and strengthened through gettering and activating mechanisms of Th, Hf, Ir eutectics, as indicated in the preceding section, offers a spectrum of prototypic dilute-solution ultralloys.

The postulated processes involve utilization of the order-of-1% probable ternary eutectic melting near 1500 or 1600°C and comprising ~60a/o Ir with ~40a/o of the -2-to-1 Th-to-Hf binary eutectic added to W powder to produce an extremely interesting sintered alloy: The segregated Ir, ~27a/o Th, 13a/o Hf eutectic should initiate liquid-phase sintering about 500°C above conventional W presintering temperatures (1000 to 1200°C). Then the activator, getter fluid should spread over the W-powder surfaces readily because of the strong affinities of Th and Hf for the interstitial impurities in compound segregation at and near the boundaries of the W grains. Gettering of those interstitial impurities in particle surfaces and substrates by Th and Hf should liberate combined W making it available to Ir-activated diffusion and sintering.

This process will remove elemental Th and Hf from the activator, getter eutectic as highly stable-refractory interstitial-impurity compounds strategically distributed intergranularly. Such ceramic dispersoids between W powder particles and crystallites inhibit grain growth and suppress cavity nucleation as discussed previously [here and 1-3]. During the coefficient intergranular particulate formation and superficial W liberation through interstitial-impurity gettering the reaction-removal of Th and Hf metals from the activator, getter eutectic will drive the Ir, Th, Hf liquid melting point upward abruptly. Raising the sintering temperature accordingly will compensate this effect. And with these processes the Ir activation of W sintering will become more and more effective. But concomitantly a W ultralloy containing small amounts of Ir and ThO<sub>2</sub> (as well as HfC...) will evolve -- similar to "the most ductile alloys" found in the "Development of a Ductile Tungsten Sheet Alloy" [1,94,95]. "Furthermore these ternary additions were found to increase the recrystallization temperature and decrease recrystallized grain size."

Thus sintering W with low concentrations of an Ir, Th, Hf activator, getter eutectic should improve not only processing and quality control but also ductility and recrystallization resistance. The strengthening aspect of the resulting W, Ir, ThO<sub>2</sub>, HfC... alloys comprises preceding discussions [here and 1-3]. And all this improvement potential is subject to the simplified guidance, observation and interpretation of dilute-solution refractory-alloy research which will ultimately lead to space-ultralloy prototypes.

## REFERENCES

1. J. Morris: Dilute-Solution Ultralloys, interim report for the Air Force Office of Scientific Research, AFOSR Grant 83-0067 (Material Problems for High-Temperature High-Power Space Energy-Conversion Systems), Arizona State University report ASU CR-R-85035, October 1985.
2. J. Morris and D. Jacobson: TEC and Ultralloys for High-Power Space Systems, 20th Intersociety Energy Conversion Engineering Conference (IECEC), Miami Beach, Florida, August 1985.
3. J. Morris: Decreased Creep for Increased Space Power, AFOSR-83-0067 interim report, December 1984 (to be published in Engineering Fracture Mechanics).
4. J. Morris: Better, Cheaper In-Core Thermionic Energy Conversion with Pre-1973 Ultralloys, 19th IECEC, San Francisco, California, August 1984.
5. J. Morris: An Introduction to Space Refractory-Materials Problems, AFOSR-83-0067 First Annual Report, May 1984 (ASU CR-R-84032, November 1983).
6. J. Morris: Ultralloys for Nuclear Thermionic Conversion, 18th IECEC, Orlando, Florida, August 1983.
7. R. Jaffee and G. Hahn: Structural Considerations in Developing Refractory Alloys, DMIC Report 82 (BMI), January 1963.
8. C. Lynch (NPAFB, Editor): Handbook of Materials Science, CRC Press, 1974.
9. E. Savitsky, G. Burkhanov and V. Kirillova: Single Crystals of Refractory and Rare Metals, Alloys and Compounds, Crystals Growth, Properties and Applications, Springer-Verlag, Berlin, 1982.
10. E. Savitsky and G. Burkhanov: Single Crystals for Refractory and Rare Metals and Alloys, Moscow: Nauka, 1972.
11. E. Savitsky: The Influence of Temperature on the Mechanical Properties of Metals and Alloys, (O. Sherby Editor), Stanford University Press, USA; Oxford University Press, England; 1961, 1962.
12. E. Savitsky and G. Tsarev: Izv. Acad. Sci. Byelorussian SSR, Section: Physico-Technical Science 2, 84, 1965.
13. R. Jaffee: J. Met. 16, 410, 1964.
14. E. Savitsky and G. Chuprikov: Effect of Oxygen Upon Fine Structure, Strain Mechanism and Physico-Mechanical Properties of Rhenium, Rhenium (E. Savitsky editor), Moscow: Nauka, 1964.
15. J. Low: Trans. AIME 245, 2481, 1969.
16. A. Joshi and D. Stein: Metallurg. Trans. 1, 2543, 1970.
17. H. Marons and P. Palmberg: Trans. TMS AIME 245, 2481, 1969.
18. E. Cottrell: Dislocations and Plastic Flow in Crystals, Moscow: Metallugiedat, 1958 (in Russian).
19. E. Savitsky, G. Burkhanov and M. Ageev: Effect of High-Temperature Quenching on Plasticity and Fine Structure of Tungsten Single Crystals, Single Crystals of Refractory and Rare Metals (E. Savitsky editor), Moscow: Nauka, 1971.
20. P. Marion and C. Choain-Maurin: Chim. Ind. 88, 5, 483, 1962.
21. H. Keiffer, F. Benessovsky and E. Gallisti: Z. Metallk. 4, 8, 285, 1952.
22. R. Elliott: Structure of Binary Alloys, Vol. 1 and 2, Moscow: Metallurgiya, 1962.
23. K. Portnoy et alii: Powder Metallurgy 5, 75, 1967.
24. M. Hansen and K. Andergo: Structure of Binary Alloys, Vol. 1 and 2, Moscow: Metallurgizdat, 1962.

25. Ye. Savitsky, K. Povorova, P. Makarov and Ye. Zavazina: Phase Composition, Structure and Properties of Vacuum-Melted W-C(Zr, Hf, Nb, Ta, Re) Alloys, Planseeberichte fur Pulvermetallurgie 25, 168, 1977 (9th Plansee Seminar).
26. S. Golovanenko, A. Natapoya, B. Llypin and T. Kesaev: Recrystallization of Tungsten Alloys, translated from Metallovedenie Termicheskaya Obrabotka Metallov. No. 9, 59, September 1976 (UDC 669.27:620.186.6).
27. S. Yi and C. Wang: Tungsten Sources, Metallurgy, Properties and Applications, Plenum Press, New York, 1981.
28. A. Adamson: Physical Chemistry of Surfaces, Interscience Publishers, New York, 1960.
29. G. Huttig: Kolloid Z. 98, 263, 1942.
30. J. Mackenzie and R. Shuttleworth: Proc. Phys. Soc. (London) 62B, 833, 1949.
31. C. Herring: Structure and Properties of Solid Surfaces (R. Gomer and C. Smith Editors), 1, University of Chicago Press, 1953.
32. G. Kuczynski, Acta Metallurgica 4, 58, 1956.
33. K. Hwang and R. German: Analysis of Initial Stage Sintering by Computer Simulation, Sintering and Heterogeneous Catalysis, (G. Kuczynski, A. Miller and G. Sargent Editors), Plenum Press, New York, 1984.
34. A. Evans: J. Am. Ceram. Soc. 65(10), 497, 1982.
35. F. Lange and M. Metcalf: Processing Related Fracture Origins, J. Am. Ceram Soc. ("in press").
36. R. Coble: J. Am. Ceram. Soc. 41 (2), 55, 1958.
37. C. Greskovich: Physics of Sintering 4 (1), 33, 1972.
38. J. Woolfrey: J. Am. Ceram. Soc. 55 (8), 383, 1972.
39. R. Dettoff, R. Rummel, H. LaBuff and F. Rhines: Modern Developments in Powder Metallurgy, Vol. I(H. Hausner Editor), Plenum Press, New York, 1968.
40. F. Rhines, R. DeHoff and R. Rummel: Agglomeration, Interscience Publishers, New York, 1962.
41. H. Hayden and J. Brophy: J. Electrochem. Soc. 110, 805, 1963.
42. I. Toth: Activation Sintering of Tungsten and Its Effect on Some Mechanical Properties, Battersea College of Technology, London, 1965.
43. J. Brophy, L. Shephard and J. Wulff: Powder Metallurgy (W. Leseynski editor), Interscience Publishers, New York, 1961.
44. R. German: an Overview of Enhanced Sintering Treatments for Iron, Sintering and Heterogeneous Catalysis (G. Kuczynski, A. Miller and G. Sargent editors), Plenum Press, New York, 1984.
45. R. German and Z. Munir: Activated Sintering of Refractory Metals by Transition Metal Additions, Review Powder Met. Physical Ceram. 2, 9, 1982.
46. A. Reshamwala and G. Tendolkar: Activated Sintering Part 1, Powder Met. Inter. 1, 58, 1969.
47. A Reshamwala and G. Tendolkar: Activated Sintering Part 2, Powder Met. Inter. 2, 15, 1970.
48. J. Barta: Activated Sintering, Powder Met. Inter. 2, 52, 1970.
49. A. Shaler: Activated Sintering -- A Review, Sintering and Related Phenomena, (G. Kuczynski, N. Hooton and C. Gibbon Editors), Gordon and Breach, New York, 1967.
50. G. Samsonov and V. Yakovlev: Activated Sintering of Tungsten with Palladium Additions, Sov. Powder Met. Metal Ceram. 6, 548, 1967.

51. G. Samsonov and V. Yakovlev: Der Einflub von Übergangsmetallzusätzen auf das Sinterverhalten von Wolfram, Z. Metallk, 62, 621, 1971.
52. G. Samsonov, I. Pryadko and L. Pryadko: A Configuration Model of Matter, Consultants Bureau, New York, 1973.
53. J. Burton and E. Machlin: Prediction of Segregation to Alloy Surfaces from Bulk Phase Diagrams, Phys. Rev. Letters 37, 1433, 1976.
54. M. Seah: Adsorption Induced Interface Cohesion, Acta Met. 28, 955, 1980.
55. J. Stark and H. Marcus: The Influence of Segregation on Grain Boundary Cohesion, Met. Trans. 8A, 1423, 1977.
56. E. Hondros and M. Seah: Segregation to Interfaces, Inter. Metals Rev. 22, 262, 1977.
57. P. Zovas, R. German, K. Hwang and C. Li: Activated and Liquid-Phase Sintering-Progress and Problems, J. Metals, 28, January 1983.
58. R. Coble: Sintering Crystalline Solids I. Intermediate and Final State Diffusion Models, J. Appl. Phys. 32, 787, 1961.
59. H. Song and R. Coble: The Applicability of Herring's Scaling law to the Sintering of Powders, Sintering and Heterogenous Catalysis (G. Kuczynski, A. Miller and G. Sargent Editors), Plenum Press, New York, 1984.
60. P. Zovas and R. German: Retarded Grain Boundary Mobility in Activated Sintered Molybdenum, Metall. Trans. 15A, 1103, 1984.
61. T. Ikegami, M. Tsutsumi, S. Matsuda, S. Shirasaki and H. Suzuki: J. Appl. Phys. 48, 4238, 1978.
62. R. German: Science of Sintering 15, 27, 1983.
63. A. Markworth: Scripta Met. 6, 957, 1972.
64. R. German: Diffusional Activated Sintering-Densification, Microstructure and Mechanical Properties, Inter. J. Powder Met. Powder Tech. 19, 277, 1983.
65. R. Coble: A Model for Boundary Diffusion Controlled Creep in Polycrystalline Materials, J. Appl. Phys. 34, 1679, 1963.
66. W. Kaysser and G. Petzow: Grain Boundary Migration During Sintering, Modern Developments in Powder Metallurgy, Volumes 12, 13 and 14 (H. Hausner, H. Antes and G. Smith editors), 397, Metal Powder Industries Federation and American Powder Metallurgy Institute, Princeton, NJ.
67. W. Kaysser and S. Pejobjnik: Grain Boundary Migration During Sintering of Mo with Ni Additions, Sonderdruck aus Zeitschrift fur Metallkunde Band 71, H. 10, S. 649-653, 1980.
68. F. Puckert, W. Kaysser and G. Petzow: Directional Grain Growth During Solid State and Liquid Phase Sintering of W-Ni, Contemporary Inorganic Materials 1981, Proceedings of the Fifth German, Yugoslav Meeting on Materials Science and Development (P. Reynen, P. Schulz, C. Zografou and A. Naumidis editors), Simmerrath-Rurberg, April 6-9, 1981.
69. M. Hofman-Amtenbring, W. Kaysser and G. Petzow: Grain Boundary Migration in Recrystallized Mo Foils in the Presence of Ni, Z. Metallkde Bd. 73, H. 5, 305, 1982.
70. P. Ossi, R. Roberti and G. Silva: On the Rearrangement Mechanisms During Liquid Phase Sintering of a Model System, Scripta Met. 19, 569, 1985.
71. Ekbom: Microstructural Study of the Deformation and Fracture Behavior of a Sintered Tungsten-Base Composite, Modern Developments in Powder Metallurgy, Volumes 12, 13 and 14, (H. Hausner, H. Antes and G. Smith Editors), 177, Metal Powder Industries Federation and American Powder Metallurgy Institute, Princeton, NJ.

72. L. Ekbom: Deformation Behavior of High-Density Tungsten Alloys, Second Charlottesville Conference on High Density KE Penetrator Materials, Army Materials and Mechanics Research Center (Sponsor), Army Foreign Science and Technology Center (Host), Charlottesville, Virginia, October 1980.
73. H. Danner, G. Jangg, B. Lux and E. Lassner: Einflub von Fremdelementen auf das Sinterverhalten und die Eigenschaften von Wolfram-Schwermetallen, High Temp.-High Press 13, 541, 1981.
74. A. Drachinskiy, A. Kraynikov and V. Trefilov: Some Features of Equilibrium Segregation in Refractory Metals of Group VIA, Phys. Met. Metall. 54, 84, 1982.
75. Yu. Kolobov, Yu. Pochivalov and A. Korotzyev: Structural Features of Boundary Regions and Their Influence on the Development of Microplastic Deformation in Molybdenum with Grain-Boundary Segregations of Nickel, Phys. Met. Metall. 54, 180, 1982.
76. C. Lea, B. Muddle and D. Edmonds: Segregation to Interphase Boundaries in Liquid-Phase Sintered Tungsten Alloys, Metallurg. Trans. 14A, 667, 1983.
77. N. Adam: The Physics and Chemistry of Surfaces, Oxford University Press, London, 1941.
78. R. Gomer and C. Smith (Editors): Structure and Properties of Solid Surfaces, Chicago University Press, 1952.
79. D. Graham: Characterization of Physical Adsorption Systems.I, The Equilibrium Function and Standard Free Energy of Adsorption, J. Phys. Chem. 57, 665, 1953.
80. D. McLean: Grain Boundaries in Metals, Oxford University Press, London, 1957.
81. E. Hondros and M. Seah: The Theory of Grain Boundary Segregation in Terms of Surface Adsorption Analogues, Metallurg. Trans. 8A, 1363, 1977.
82. M. Glicksman and R. Masumura: Grain Boundary Structure and Energetics, Metallurg. Trans. 8A, 1373, 1977.
83. M. Guttmann: Grain Boundary Segregation, Two Dimensional Compound Formation and Precipitation, Metallurg. Trans. 8A, 1383, 1977.
84. C. White and W. Coglan: The Spectrum of Binding Energies Approach to Grain Boundary Segregation, Metallurg. Trans. 8A, 1403, 1977.
85. M. Seah: Grain Boundary Segregation (Critical Assessment Article), J. Phys. F: Metal Phys. 10, 1043, 1980.
86. D. Harries and A. Marwick: Nonequilibrium Segregation in Metals and Alloys, Phil. Trans. R. Soc. Land. A295, 197, 1980.
87. S. Brunauer, P. Emmett and E. Teller (BET): Adsorption of Gases in Multimolecular Layers, J. Am. Chem. Soc. 60, 309, 1938.
88. S. Brunauer, L. Deming, W. Deming and E. Teller: On a Theory of the van der Waals Adsorption of Gases, J. Am. Chem. Soc. 62, 1723, 1940.
89. R. Fowler and E. Guggenheim: Statistical Thermodynamics, Cambridge University Press, 1939.
90. V. Skorokhod, L. Chernyshev, L. Kolomiets, L. Shnaiderman and S. Solonin: Activating Effect of Small Additions of Group VIII Metals on Alloy Formation During the Sintering of Tungsten and Molybdenum Powders Mixed with Other Refractory Metals, Soviet Powder Metallurgy and Metal Ceramics 5, 435, 1976.
91. R. German and Z. Munir: Enhanced Low-Temperature Sintering of Tungsten, Metallurg. Trans. A. 7A, 1873, 1976.
92. T. Noda, T. Kainume and M. Okada: Effect of Oxygen on Intergranular Brittleness of Molybdenum, J. Jap. Inst. Metals 43, 25, 1984.

93. T. Noda, T. Kainuma and M. Okada: Oxygen Desorption from Grain Boundaries of Molybdenum During Vacuum Heating, J. Jap. Inst. Metals 48, 30, 1984.
94. J. Ratliff, W. Gibeaut and H. Ogden: Tungsten Research and Development Review 1960-1962, DMIC Report 193, Battelle, Columbus, OH, October 1963.
95. H. Ogden: Development of a Ductile Tungsten Sheet Alloy, Navy BuWeps Contract, Battelle, Columbus, OH, 1960 to 1962.

## APPENDIX

## 1.4 RECRYSTALLIZATION

Because recrystallization implications pervade material problems for high-temperature, high-power space energy-conversion systems, further amplification of its signals seems apropos: The technological jargon for recrystallization has evolved through several levels of understanding to the point where misinterpretation is not only possible but also probable. Primary recrystallization includes nucleation and primary growth which smears into normal grain growth which can occur with discontinuous or secondary recrystallization which sometimes continues as tertiary recrystallization when mean size attains bulk dimensions. Thus "formation and migration of large-angle boundaries" seems a more appropriate definition because "some recrystallization processes occur without nucleation" (ref. 43). However convenience and consensus push steadily toward the use of "recrystallization" to cover the gamut. For greater specificity the numbered descriptions of Table 9 offer reasonable alternatives for differentiating levels of recrystallization.

In any event crystalline equilibrium obtains practically at the center of a huge pure flawless single crystal. In contrast common thermodynamically unstable lattice states derive from chemical impurities and physical imperfections such as point defects, dislocations, grain

TABLE 9  
RECRYSTALLIZATION

REARRANGEMENT AND REDUCTION OF LATTICE IMPERFECTIONS

BELOW THE MATERIAL MELTING POINT LOWERS FREE ENERGY:

1. AGGLOMERATION, REACTION, ULTIMATELY ANNIHILATION OF POINT DEFECTS;
2. SHRINKAGE OF DISLOCATION LOOPS AND DISLOCATION ANNIHILATION;
3. DISLOCATION REARRANGEMENT IN LOW-FREE-ENERGY CONFIGURATIONS;
4. IMPERFECTION REACTIONS PRODUCING LATTICE REGIONS CAPABLE OF GROWTH;
5. GRAIN-BOUNDARY ABSORPTION OF POINT DEFECTS AND DISLOCATIONS;
6. DIMINUTION OF THE TOTAL INTERGRANULAR SURFACE.

1 AND 2 ARE "RECOVERY." 3 CAN BE EITHER "POLYGONIZATION" YIELDING SUBGRAINS WITH LOW-ANGLE BOUNDARIES OR "NUCLEATION." 4 IS "NUCLEATION," ALSO TERMED "PRIMARY RECRYSTALLIZATION." 5 AND 6 ARE "GRAIN GROWTH."

boundaries and external surfaces. Diminishing, ultimately eliminating these instabilities reduces total free energy -- driving recrystallization and its "zone-refining" proclivities toward the huge pure flawless single crystal.

Grain-growth velocity equals the product of the boundary mobility and the resultant driving force. In the usual example cold work produces a driving force equivalent to the free-energy-density difference across the intergranular region which is proportional to the imperfection-density difference across the migrating boundary. A variety of driving forces appears in Table 10 (A and B).

As Table 6 implies dragging forces, which oppose grain-boundary migration, arise from solute atoms, precipitants, dispersed particles, surface grooves.... Concentration of such drag configurations often produces grain-boundary pinning. An inverse drag coefficient can be considered a specific mobility which characterizes boundary migration for each driving force. Mobilities are simple in concept but complicated in evaluation -- often occurring as complex functions grain-boundary velocity. In actuality appropriate mobility summations correspond to resultants for driving and dragging forces.

Reference 47 describes grain-boundary migration as an evolution of the reaction-rate theory, presented for a rather pertinent model in Table 11. On this theoretic basis references 43, 47 and many others contributed to the development of exemplary boundary-migration expressions given in Tables 12 through 15 and illustrated by Figure 1. These equations differ only in the initial factor which oversimplifies the definition and separability of grain-boundary-migration mechanisms. But their heuristic value is undebatable.

DRIVING FORCES FOR GRAIN-BOUNDARY MIGRATION  
RECRYSTALLIZATION

ORIGIN	EQUATION	ESTIMATED MAGNITUDE (N/m <sup>2</sup> )
STORED ENERGY	$\Delta\rho r$	$10^7$
REVERSED-CAPILLARY	$2\gamma f/r$	$10^6$
ELECTRIC	$\lambda E$	$10^5$
CAPILLARY	$2\gamma/r$	$10^4$
SURFACE ENERGY	$2\Delta\gamma/d$	$10^4$
MAGNETIC	$(\frac{1}{2})\Delta\mu H^2$	$10^3$
MECHANICAL	$\theta\sigma$	$10^3$
TEMPERATURE GRADIENT	$\delta S \nabla T$	$10^2$
ELASTIC ENERGY	$(\frac{1}{2})\Delta\sigma^2$	$10^2$
ELECTROMIGRATION	$2\eta q_p Z^* J$	$10^2$

MASTELLER AND BAUER: RECRYSTALLIZATION OF METALLIC MATERIALS

TABLE 1.0B  
RECRYSTALLIZATION.

DRIVING-FORCE SYMBOLS

$\Delta\rho$  = DIFFERENCE BETWEEN DISLOCATION DENSITY ( $\text{m}^{-2}$ ) IN TWO ADJACENT GRAINS DEFINING THE BOUNDARY,  $\Gamma$  = DISLOCATION LINE ENERGY ( $\text{J/m}$ ),  $\gamma$  = INTERFACIAL (GRAIN BOUNDARY) ENERGY ( $\text{J/m}^2$ ),  $f$  = GENERALIZED AMPLIFICATION FACTOR (DIMENSIONLESS),  $r$  = RADIUS OF CURVATURE OF BOUNDARY ( $\text{m}$ ),  $\lambda$  = NET ELECTRIC CHARGE PER UNIT BOUNDARY AREA ( $\text{C/m}^2$ ),  $E$  = ELECTRIC FIELD ( $\text{V/m}$ ),  $\Delta\gamma$  = DIFFERENCE BETWEEN SURFACE ENERGY OF TWO ADJACENT GRAINS DEFINING THE BOUNDARY ( $\text{J/m}^2$ ),  $d$  = SPECIMEN THICKNESS ( $\text{m}$ ),  $\Delta\mu$  = DIFFERENCE BETWEEN MAGNETIC PERMEABILITY IN TWO ADJACENT GRAINS DEFINING THE BOUNDARY ( $\text{H/m}$ ),  $H$  = MAGNETIC FIELD ( $\text{A/m}$ ),  $\theta$  = MISORIENTATION BETWEEN GRAINS DEFINING A (LOW-ANGLE) BOUNDARY (RADIAN),  $\sigma$  = STRESS FIELD ( $\text{Pa}$ ),  $n$  = NUMBER OF ATOMS PER GRAIN BOUNDARY AREA ( $\text{m}^{-2}$ ),  $S$  = ENTROPY ( $\text{J}^{0.0}\text{cm}^3$ ),  $\nabla T$  = TEMPERATURE GRADIENT ( $^{\circ}\text{C}/\text{m}$ ),  $\Delta S$  = DIFFERENCE BETWEEN ELASTIC COMPLIANCE CONSTANTS IN TWO ADJACENT GRAINS DEFINING THE BOUNDARY ( $\text{m}^2/\text{N}$ ),  $q$  = ELECTRIC CHARGES ( $\text{C}$ ),  $\rho$  = ELECTRICAL RESISTIVITY ( $\Omega\text{m}$ ),  $Z^*$  = (NORMALIZED) DIFFERENCE BETWEEN (ELECTRON) SCATTERING CROSS SECTIONS IN THE ACTIVATED AND GROUND STATES (DIMENSIONLESS),  $J$  = CURRENT DENSITY ( $\text{A/m}^2$ ), and  $\delta$  = GRAIN BOUNDARY THICKNESS.

TABLE II  
SIMPLIFIED REACTION-RATE THEORY

FOR PURE-METAL OXIDATION CONTROLLED BY IDEAL-SOLUTION MIGRATION (AFTER EVANS FROM HURLEN) THE ABSOLUTE REACTION-RATE THEORY (EYRING, LAIDLIER AND GLASSSTONE) YIELDS AN EXPRESSION FOR ONE-DIMENSIONAL NET TRANSPORT OF A SPECIES:

$$v = (\lambda kT/h) \exp\left(-\Delta G_0^\ddagger/RT\right) [c \exp(-\alpha zF\phi/RTdx) - (c + \lambda dc/dx) \exp((1 - \alpha)\lambda zF\phi/RTdx)]$$

THE PRE-BRACKET FACTOR, SPECIFIC RATE FOR A UNIT CONCENTRATION WITHOUT FIELDS, INVOLVES NO NET TRANSPORT. THE FIRST TERM IN THE BRACKETED FACTOR REPRESENTS ACCELERATION BY THE FIELD. THE SECOND TERM IN THE BRACKETS COVERS RETARDATION. THEN  $v$  IS THE NET TRANSPORT RATE;  $\lambda$ , THE EQUILIBRIUM DISTANCE BETWEEN MIGRATING CHARGED PARTICLES;  $k$ , BOLTZMANN CONSTANT;  $T$ , DEGREES KELVIN;  $h$ , PLANCK CONSTANT;  $\Delta G_0^\ddagger$ , STANDARD CHEMICAL ACTIVATION ENERGY;  $R$ , GAS CONSTANT;  $c$ , CONCENTRATION OF MIGRATING SPECIES;  $\alpha$ , SYMMETRY FACTOR;  $z$ , MIGRATING-PARTICLE CHARGE;  $F$ , FARADAY EQUIVALENT;  $\phi$ , INNER POTENTIAL; AND  $x$ , DISTANCE IN THE TRANSPORT DIRECTION.

FIGURE 1  
RECRYSTALLIZATION

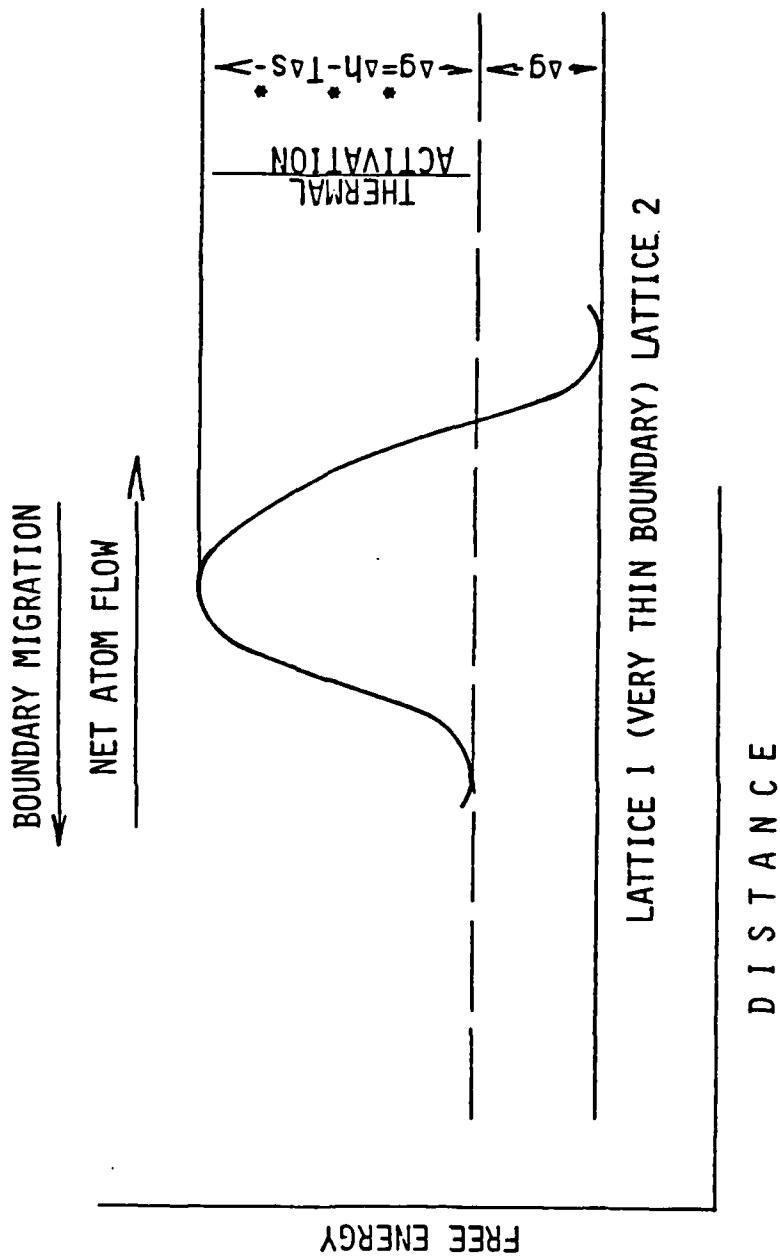


TABLE 12  
RECRYSTALLIZATION

1-T0-2 ATOM FLOW

$$v_1 \exp (-\Delta g^*/kT)$$

2-T0-1 ATOM FLOW

$$v_2 \exp [-(\Delta g^* + \Delta g)/kT]$$

$v_1 = v_2 = v$  = LATTICE-ATOM OSCILLATORY FREQUENCY

NET BOUNDARY -

$$\text{MIGRATION RATE} = v = v \lambda [1 - \exp (-\frac{\Delta g}{kT})] \exp (-\frac{\Delta g^*}{kT})$$

$\lambda$  = EFFECTIVE ATOM DISPLACEMENT THROUGH THE BOUNDARY

$\Delta g/kT \ll 1$  FOR PURE-METAL RECRYSTALLIZATION

$$\text{BOUNDARY-MIGRATION RATE} = v = v \lambda (\frac{\Delta g}{kT}) \exp (-\frac{\Delta g^*}{kT})$$

TABLE 13  
RECRYSTALLIZATION  
CRYSTAL-STEP MODEL FOR GRAIN BOUNDARY MIGRATION

ASSUMPTIONS: CLOSELY PACKED (FCC) PLANES END AT BOUNDARIES IN PERIODIC STEPS HAVING KINKS WHICH CAN RELEASE OR RECEIVE ATOMS THAT DIFFUSE THROUGH INTERGRANULAR REGIONS.  $\Delta g^*$  IS THE SUM OF FREE ENERGIES FOR TRANSITIONS OF SUCH ATOMS;  $\delta$  IS THE GRAIN-BOUNDARY WIDTH, GREATER THAN SINGLE-JUMP  $\lambda$ ;  $f_1$  AND  $f_2$  ARE POSITIVE FUNCTIONS OF STEP DENSITIES ON OPPOSING BOUNDARY SURFACES AND OF VACANCY EFFECTS. THEN -

$$\psi = \frac{\lambda}{\delta} [1 + \frac{\lambda}{\delta} (\frac{1}{f_1} + \frac{1}{f_2})]^{-1} < 1$$

AND -

$$\begin{aligned} \text{GRAIN-BOUNDARY} \\ \text{MIGRATION RATE} &= v = \psi v \lambda (\frac{\Delta g}{kT}) \exp (-\frac{\Delta g^*}{kT}) \end{aligned}$$

GLEITER: ACTA MET. 17, 853, 1969

TABLE 14  
RECRYSTALLIZATION

VACANCY MODELS FOR GRAIN-BOUNDARY MIGRATION

ASSUMPTIONS: MIGRATION VELOCITY INCREASES WITH RISING BOUNDARY VACANCY FRACTION  $C_m$  - AS INDICATED BY NUMEROUS EXPERIMENTS: DIFFUSION JUMPS ACROSS BOUNDARIES OCCUR THROUGH VACANCY-SITE CHANGING PROCESSES. BECAUSE INSTANTANEOUS  $C_m$ 's DEPEND ON VACANCY INJECTION, COLLECTION AND EJECTION MECHANISMS, THEY ARE COMPLEX FUNCTIONS OF BOUNDARY VELOCITIES AND TEMPERATURES AS WELL AS VACANCY SOURCE AND SINK EFFECTS. THEN -

$$\text{GRAIN-BOUNDARY MIGRATION RATE} = v = C_m \nu \lambda \left( \frac{\Delta g}{kT} \right) \exp \left( -\frac{\Delta g^*}{kT} \right)$$

TABLE 15  
RECRYSTALLIZATION  
SATURATION MODEL FOR GRAIN-BOUNDARY MIGRATION

ASSUMPTIONS: DISLOCATION PROCESSES PROPOSED BY LI (1961) AND MODIFIED BY GRABSKI (1969) RESULT IN ALLOWED MATERIAL TRANSPORT ONLY ACROSS AN "ACTIVE CROSS SECTION" FRACTION  $\sigma$  OF THE GRAIN-BOUNDARY SURFACE. THUS SATURATION LIMITS THE MIGRATION VELOCITY:

$$\text{GRAIN-BOUNDARY MIGRATION RATE} = v = \sigma v \lambda \left( \frac{\Delta g}{kT} \right) \exp \left( -\frac{\Delta g^*}{kT} \right)$$

Still further simplifications for grain growth in much more complex two-phase systems appear as radius, time relationships with effective coefficients for various diffusion types in Tables 16 and 17. Effects of dispersed particles on grain-growth control through pinning manifest quite simply in the equation of Table 17.

Many of the recrystallization mechanisms touched only as tops of the complex scientific topography of this important technology submit to description by thermal rules of thumb. Such a mechanistic listing comprises the temperature resolution given in Table 18. Most of these approximate thermal boundaries have been encountered by those who work with high-temperature alloys. Recognition of these transitions emphasizes that direct and side effects of recrystallization exert abstruse influences on strength, creep, compatibility...and ductility of refractory alloys. And those properties are major considerations in ultrathermal alloy applications.

But ductility and recrystallization are often critical parameters in the capability of ultralloys to adapt themselves and ceramics to fabrication and service requirements. Thus a better understanding of refractory-alloy recrystallization is a crucially essential part of overcoming the material problems for high-temperature, high-power space energy-conversion systems.

TABLE 16  
RECRYSTALLIZATION

GRAIN GROWTH OF TWO-PHASE ALLOYS  
(HORNBOGEN: METALL 29, 247, 1975)

ELEVATED TEMPERATURES ACCENTUATE RECRYSTALLIZATION OF TWO-PHASE MICROSTRUCTURES DRIVEN BY INTERFACIAL ENERGY DENSITIES WHICH ARE FUNCTIONS OF GRAIN SIZE  $r_{\alpha\alpha}$ . THEN FOR BOUNDARY

$(D_{\alpha\alpha}$  OR  $D_{\alpha\beta}$ ), DISLOCATION-CORE PIPE ( $D_p$ ) OR VOLUME ( $D_V$ ) DIFFUSION SIMPLE GROWTH, TIME LAWS OBTAIN:

$$r_{\alpha\alpha} \propto (D_{\alpha\alpha} t)^{1/2} \text{ PRIMARY OR SECONDARY RECRYSTALLIZATION}$$

$$r_{\alpha\alpha} \propto (D_{\alpha\alpha} t)^{1/3} \text{ GRAIN GROWTH (RARILY OBSERVED)}$$

$$r_p \propto (D_V t)^{1/3} \text{ DISPERSED-PARTICLE GROWTH (OFTEN SEEN)}$$

$$r_{\alpha\beta} \propto (D_{\alpha\beta} t)^{1/2} \text{ DUPLEX-STRUCTURE GROWTH (GRAIN-SIZE DIFFUSION)}$$

DISTANCES FOR DUPLEX MICROSTRUCTURES RESULT IN RELATIVELY STABLE FINE-GRAINED ALLOYS.)

TABLE 17  
RECRYSTALLIZATION

THERMAL STABILITY OF DUPLEX ALLOYS  
(HORNBOGEN: METALL 29, 247, 1975)

NORMAL-GRAIN AND DUPLEX-STRUCTURE GROWTHS  
SUCCUMB TO DISPERSED-PARTICLE CONTROL WHEN  
DRIVING AND PINNING FORCES ARE EQUAL. THEN -

$$r_{\text{crit.}}(t) = A \frac{r_p(t)}{f} = A^* \frac{(D_v t)^{1/3}}{f}$$

WHERE A\*'S ARE GEOMETRIC FACTORS DEPENDENT ON  
LOCAL-PARTICLE SHAPE AND SIZE DISTRIBUTIONS.  
THE DISPERSED-PARTICLE VOLUME FRACTION f THAT  
STABILIZES GROWTH DECREASES CONSIDERABLY WITH  
PREDOMINANT GRAIN-BOUNDARY PARTICULATE LOCATION.

TABLE 18  
RECRYSTALLIZATION

APPROXIMATE THERMAL BOUNDARIES FOR ALLOYS

HALF THE ABSOLUTE MELTING POINT ( $0.5T_m$ ) OFTEN INDICATES IMPORTANT INCIPIENCE OF THERMALLY ACTIVATED PROCESSES.

BETWEEN  $0.3T_m$  TO  $0.4T_m$  SHORT-RANGE (ELECTRONIC, STACKING-FAULT, LOCAL-ORDER) INTERACTIONS GENERALLY DOMINATE.

LONGER-RANGE SOLUTE, DISLOCATION INTERACTIONS CONTINUE THEIR INFLUENCES TO  $0.5T_m$  OR HIGHER.

ABOVE  $0.75T_m$  TO  $0.8T_m$  INCREASED MOBILITY OF SOLUTE ATOMS GREATLY REDUCES THEIR HINDRANCE OF DISLOCATION MOVEMENT.

ARRHENIUS RELATIONS FOR GRAIN-BOUNDARY MIGRATION VELOCITIES OFTEN BREAK AT  $\sim 0.8T_m$  AND EXHIBIT MUCH LOWER ACTIVATION ENERGIES IN THE HIGHER-TEMPERATURE RANGE.

REFRACTORY-DISPERSION STRENGTHENING GENERALLY EXCELS FOR APPLICATIONS OF ALLOYS NEAR THEIR MELTING POINTS.

## APPENDIX REFERENCES

(Not Cited in Tables)

43. F. Haessner: Recrystallization of Metallic Materials, Dr. Riederer Verlag GmbH, Stuttgart, 1978.
47. J. Christian: The Theory of Transformations in Metals and Alloys, Pergamon Press, Oxford, 1975.

**SECTION 3**

**THERMIONIC EMISSION MICROSCOPY OF SINTERED TUNGSTEN-  
RHENIUM ALLOYS**

## ABSTRACT

In this work, sintered tungsten rhenium alloys were studied and their effective work function has been determined. A thermionic emission microscope was used to perform the above task. The alloys were tungsten base with 3%Re, 10%Re, 25%Re, and 30%Re.

The study was done at high sample temperatures on the order of 2000K and at a high vacuum in the  $10^{-9}$  torr range. The experimental error was calculated to be  $\pm 0.04\text{eV}$  based on the accuracy of the electrometer and the optical pyrometer.

It was observed that the alloying element, rhenium, increased the effective work function of tungsten at low and high concentrations, exhibiting a minimum at 10% Re. The effective work function of the sintered samples increased with increasing temperatures.

Determining the effect of the alloying elements on the base metal with respect to its emission properties can contribute largely to the fabrication of superior electrode materials used in thermionic energy converters.

## TABLE OF CONTENTS

	Page
LIST OF FIGURES .....	viii
LIST OF TABLES .....	x
LIST OF NOMENCLATURE .....	xi
CHAPTER	
1. INTRODUCTION .....	1
2. THERMIONIC ELECTRON EMISSION .....	5
2.1 Introduction .....	5
2.2 Work Function .....	8
2.3 Thermionic Energy Converter .....	9
2.4 Effective Work Function Calculation .....	13
3. EXPERIMENTAL APPARATUS .....	14
3.1 Introduction .....	14
3.2 Emitter Sample (Cathode) .....	17
3.3 Lens and Screen Assembly .....	19
3.4 Faraday Cage Assembly .....	21
4. EXPERIMENTAL PROCEDURE .....	28
4.1 Introduction .....	28
4.2 Sample Preparation .....	33
4.3 Vacuum Generation .....	35
4.4 Instrumentation and Technique .....	38
4.5 Temperature Measurements .....	44
4.6 Safety Precautions .....	49
5. RESULTS .....	50
5.1 Introduction .....	50
5.2 Tabulated Results .....	53
5.3 Discussion .....	66

TABLE OF CONTENTS (continued)

	Page
6. CONCLUSIONS AND RECOMMENDATIONS .....	70
6.1 Conclusions .....	70
6.2 Recommendations .....	71
REFERENCES .....	73

## LIST OF FIGURES

Figure	Page
1.1 - Thermionic Emission Microscope .....	4
2.1 - Schematic of Electron Motive at a Metal-Vapor Interface .....	7
2.2 - Thermionic Energy Converter .....	11
2.3 - Interelectrode Motive Diagram .....	12
3.1 - Thermionic Emission Microscope Assembly and Components .....	16
3.2 - Emitter Assembly .....	18
3.3 - Lens and Screen Assembly With the Various Potentials Along the Column .....	20
3.4 - Decelerating Grid .....	22
3.5 - Guard Ring .....	23
3.6 - Collector .....	23
3.7 - Faraday Cage Assembly .....	24
3.8 - Adjustable Welded Bellows .....	25
3.9 - Electrical Feedthrough .....	26
3.10 - Full Faraday Cage Assembly .....	27
4.1 - Ceramic Insert .....	31
4.2 - Rhenium Sample Used for Calibration .....	32
4.3 - Typical Sample .....	34
4.4 - Electrical Schematic .....	41
4.5 - Emission Current vs. Sample Voltage .....	42
4.6 - Emission Current vs. Decelerating Voltage .....	43

LIST OF FIGURES (continued)

Figure	Page
4.7 - NBS Lamp Circuit .....	47
4.8 - Pyrometer Circuit .....	47
4.9 - Pyrometer Calibration Curve .....	48
5.1 - Emission Micrograph of W,3%Re (T=1951 K) .....	56
5.2 - Emission Micrograph of W,10%Re (T=1946 K) .....	58
5.3 - Emission Micrograph of W,25%Re (T=1951 K) .....	60
5.4 - Emission Micrograph of W,30%Re (T=1946 K) .....	62
5.5 - Temperature Dependence of $\phi_e$ .....	64
5.6 - Variation of $\phi_e$ With Alloy Composition .....	65

## LIST OF TABLES

Table	Page
5.1 - Spectrographic Analysis .....	51
5.2 - Electron Microprobe Analysis Results .....	52
5.3 - Emission Results for Sample I - W,3%Re .....	55
5.4 - Emission Results for Sample II - W,10%Re .....	57
5.5 - Emission Results for Sample III - W,25%Re .....	59
5.6 - Emission Results for Sample IV - W,30%Re .....	61
5.7 - Summary of $\phi_e$ Measurements .....	63

## LIST OF NOMENCLATURE

F( $e$ ) - Fermi Factor  
 $e$  - Electron Total Energy  
 $e_f$  - Fermi Energy  
k - Boltzmann's Constant  
T - Temperature  
V - Potential  
 $\phi$  - Work Function  
 $\phi_e$  - Effective Work Function  
A - Emission Constant  
 $J_s$  - Saturation Current Density  
 $I_i$  - Radiant Flux of Illuminance From the Image  
 $I_s$  - Radiant Flux of Illuminance From the Source  
l - Distance Between the Source and the Image  
I - Saturation Emission Current  
Aa - Area of Screen Aperture

## Chapter 1

### INTRODUCTION

Thermionic emission microscopy is a unique technique that can be employed for a wide array of applications. Some research areas that are suited to this technique are thermionic energy conversion, phase transformations, grain growth and recrystallization, to mention just a few. In this work, the thermionic emission microscope (Figure 1.1) was used to measure the electron emission from cathode surfaces for work function determination.

This technique preceded other forms of electron microscopy with the first microscope built in 1932. It has several characteristics which are somewhat unusual when compared with similar electron microscopy techniques. Thermionic emission microscopy uses the specimen as the source of electrons rather than an electron gun. Its magnification bridges between optical microscopy and conventional types of electron microscopy, and it is applicable for high temperature analysis. Finally, a bulk specimen is used in this case rather than a thin film or a pointed wire. The sintered tungsten rhenium alloys tested, represent the first stage in a quest for high temperature materials that would be used as electrodes in thermionic energy converters.

Thermionic energy conversion is a method of converting heat into electricity without any intermediate steps. Some advantages of the thermionic energy converter are:

1. Absence of moving parts; therefore more stable.
2. High heat rejection temperature; hence suited for space applications where heat is rejected solely by radiation.
3. High temperature operation; consequently its possible use as a topping cycle in power generating plants where it can utilize the high temperature in the combustion chambers.
4. Small weight per unit power output.

In order to build a reliable thermionic energy converter for long term operation and with high conversion efficiency, the electrode materials have to be very carefully chosen.

Some basic characteristics for good emitter materials are:

1. High electron emission (i.e., low work function).
2. Low rate of deterioration and material emission to achieve long life and to minimize the deposition of the emitter material on the collector.
3. Low emissivity to reduce heat transfer by radiation from the emitter.
4. High temperature operation capabilities.

Pure tungsten, the most refractory metal, is an excellent candidate for the emitter material except that it is very brittle, therefore difficult to fabricate; and it begins to recrystallize below 40% of its melting point which makes manufacturing a difficult task. However, when rhenium is added to tungsten, it increases the ductility, increases the recrystallization temperature (up to about 3% rhenium and it stays about the same with any further addition) and gives greater creep resistance.

Four sintered tungsten base alloys with 3%, 10%, 25%, and 30% rhenium were fabricated for analysis. The main task was to determine the correlation between the effective work function and both sample composition and temperature. Some characteristics of interest of tungsten and rhenium are their melting points of 3640K and 3450K respectively; and their vapor pressures at 2000K of  $4 \times 10^{-12}$  torr and  $1 \times 10^{-10}$  torr, respectively.

The addition of rhenium should enhance the bare work function of tungsten. This assumption is based on the reported values of the bare work functions of polycrystalline tungsten (4.5eV) and that of polycrystalline rhenium (4.9eV). Higher bare work functions result in lower minimum cesiated work functions. For example, the minimum cesiated work function of polycrystalline tungsten is 1.6eV and that of polycrystalline rhenium is 1.45eV.

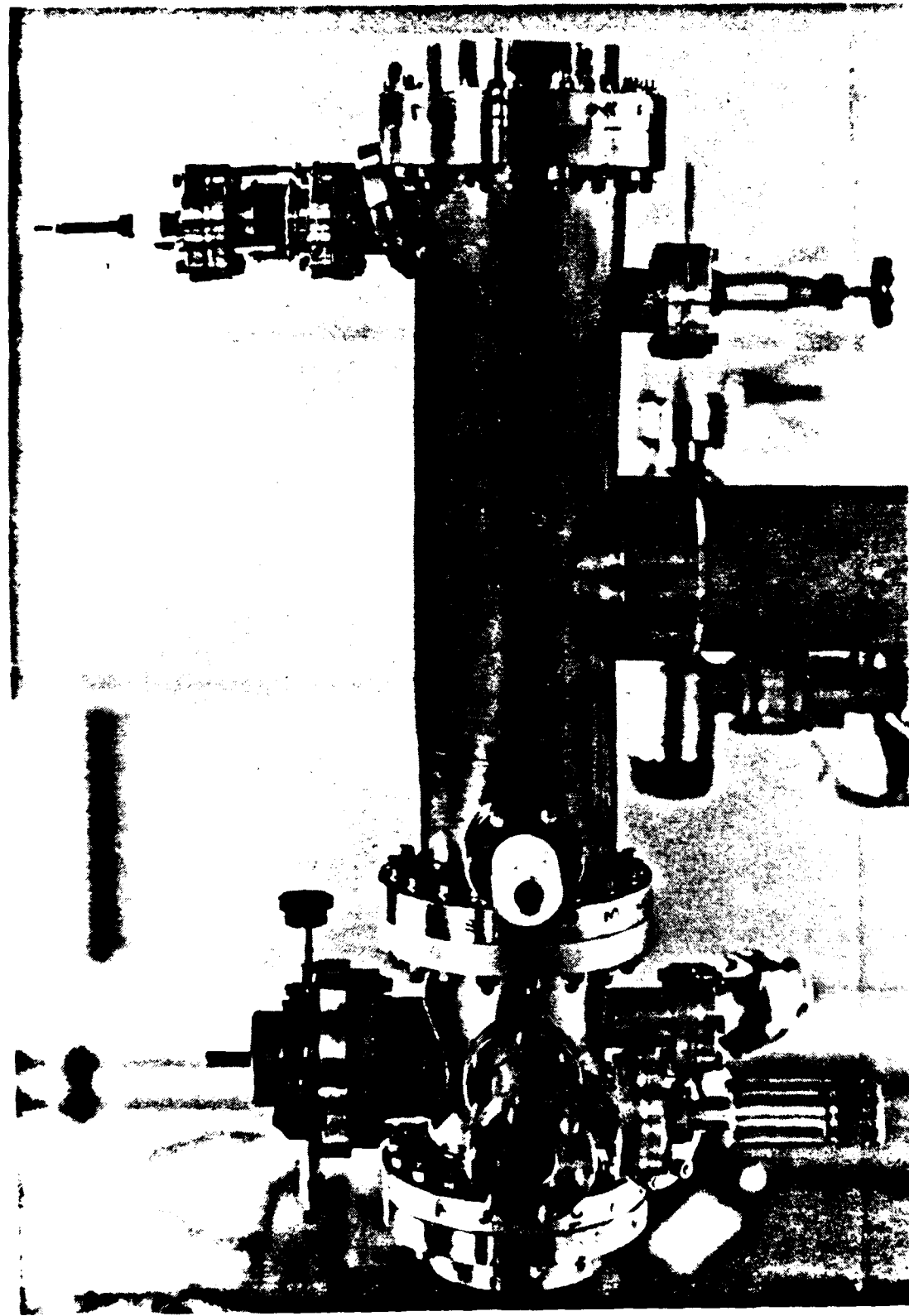


Figure 1.1 - Thermionic Emission Microscope

## Chapter 2

### THERMIONIC ELECTRON EMISSION

#### 2.1 Introduction

The phenomenon of thermionic emission is the emission of electrons and other charged particles from a metal surface which is at a temperature different from 0K and enclosed in a rarefied vapor or vacuum. In general though, for a given temperature, metal surfaces enclosed in a vacuum emit primarily electrons and a negligible amount of other particles such as positive ions.

When the metal is in equilibrium with the rarefied vapor, the net current of electrons emitted from the surface is zero, because they return and condense on the surface from which they were emitted. In the thermionic emission microscope, however, provisions are made to collect the electrons, so voltages along the microscope column are adjusted in such a fashion that the electron saturation current is obtained at the collector.

To a first approximation (Sommerfeld gas approximation), the structure of the metal is of no consequence when considering the motion of the electrons. At a given temperature  $T$ , the atoms vibrate about their equilibrium positions. The average number of free

electrons having a total energy between  $e$  and  $de$  is proportional to the Fermi factor  $F(e)$ . The Fermi factor is the probability of a particular state being occupied and is expressed by the Fermi function as:

$$F(e) = \frac{1}{1 + \exp[(e - e_f)/kt]}$$

where  $e_f$  is the Fermi energy and  $k$  is Boltzmann's constant. At absolute zero, all quantum levels up to Fermi level are occupied while levels at energies greater than Fermi energy are unoccupied. When considering the potential within a metal, one can assume the potential, or electron motive, defined as a scalar quantity whose negative gradient at any point equals the force exerted on an electron at that point, to be zero while the electron motive just outside the metal has a finite value eV. As was already mentioned, electrons occupy all states up to the Fermi level at 0K, and the energy required to lift an electron from the Fermi level to infinity is the work function ( $\phi$ ) of the metal (Figure 2.1) [5]. Infinity, in this case, is the distance away from the surface of the metal at which the "image" (+) charge in the metal left from the electron emission has no further effect upon the emitted electron.

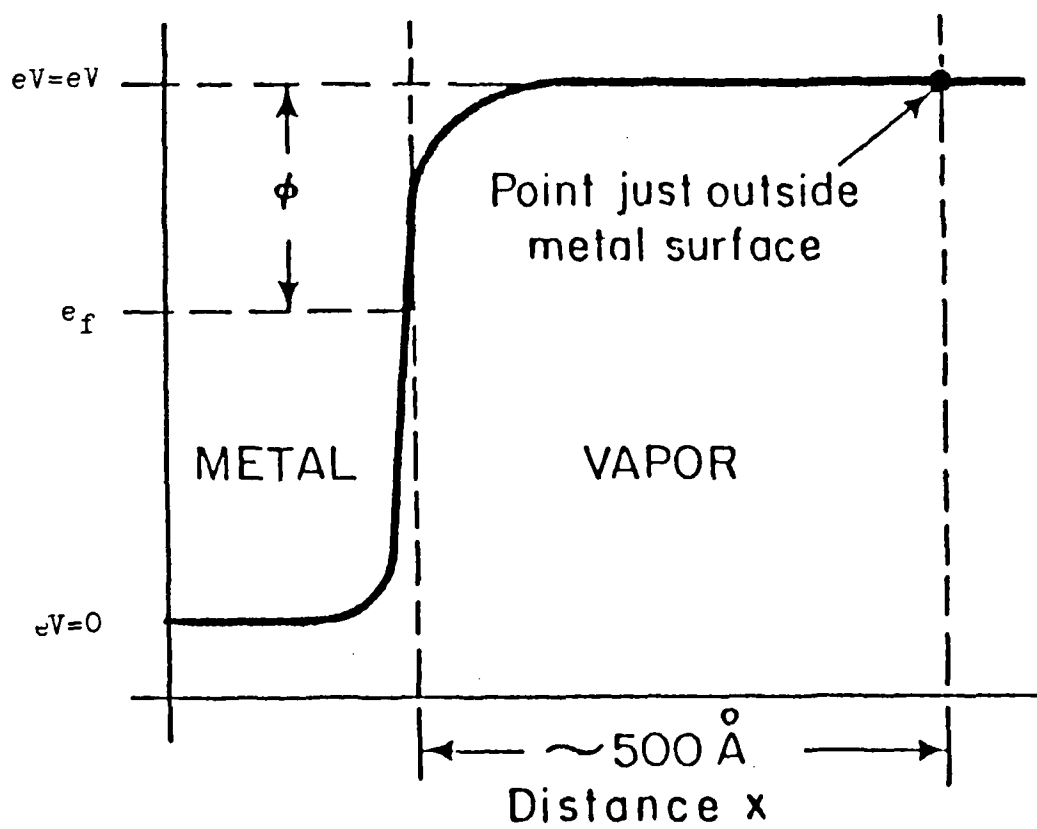


Figure 2.1 - Schematic of Electron Motive  
at a Metal-Vapor Interface

## 2.2 Work Function

The work function of a metal, as mentioned in the previous section, is the difference between the Fermi energy and the potential energy at "infinity". It is this amount of energy, expressed in electron-Volts (eV), which must be supplied to the electron in order for it to be emitted from the metal. In most cases, three categories of work functions are of interest. These are the true work function, the Richardson work function, and the effective work function. In this work, the effective work function is calculated from emission measurements, as it represents a consistent basis of information that can be obtained from a single measurement of the thermionic emission. The effective work function,  $\phi_e$ , is defined as the work function obtained by the direct substitution of the temperature, T, and emission current density,  $J_s$ , into the Richardson-Dushman equation with the constant, A, taken to be 120 Amp/cm<sup>2</sup>K<sup>2</sup> and the reflection coefficient assumed to be zero. When solving for the work function, the Richardson-Dushman equation can be expressed as

$$\phi_e = kT \ln(AT^2/J_s)$$

where k is Boltzmann's constant.

The work function values depend on crystallographic orientation of the metal, material composition, impurities, applied external fields and temperature.

In order to understand the meaning of that one material characteristic called work function and why researchers are investing so much time and effort in its determination, one has to understand the basic operating principles of a thermionic energy converter.

### 2.3 Thermionic Energy Converter

The thermionic energy converter consists of two electrodes, an emitter and a collector enclosed in a vacuum or a rarefied vapor (Figure 2.2) [5]. The work function of the emitter is greater than that of the collector (Figure 2.3) [5] due to the temperature difference between the emitter ( $\approx 2000K$ ) and the collector ( $\approx 1000K$ ).

When the emitter is supplied with sufficient energy from a high temperature source, the electrons from the top of the Fermi level obtain sufficient energy to escape from the metal, equal to the work function of the material plus some additional kinetic energy. Ideally, these electrons will move from the emitter to the collector giving up little or no energy at all. Once at the collector, the electrons give up their kinetic energy plus an amount of energy that is equal to the collector work function. This

energy is rejected as heat from the collector which is at a lower temperature than that of the emitter. This brings the emitted electrons to the Fermi level of the collector still at a higher energy level than where they started at the emitter Fermi level. It is this potential difference that is used to pass the electrons through an external load to perform work.

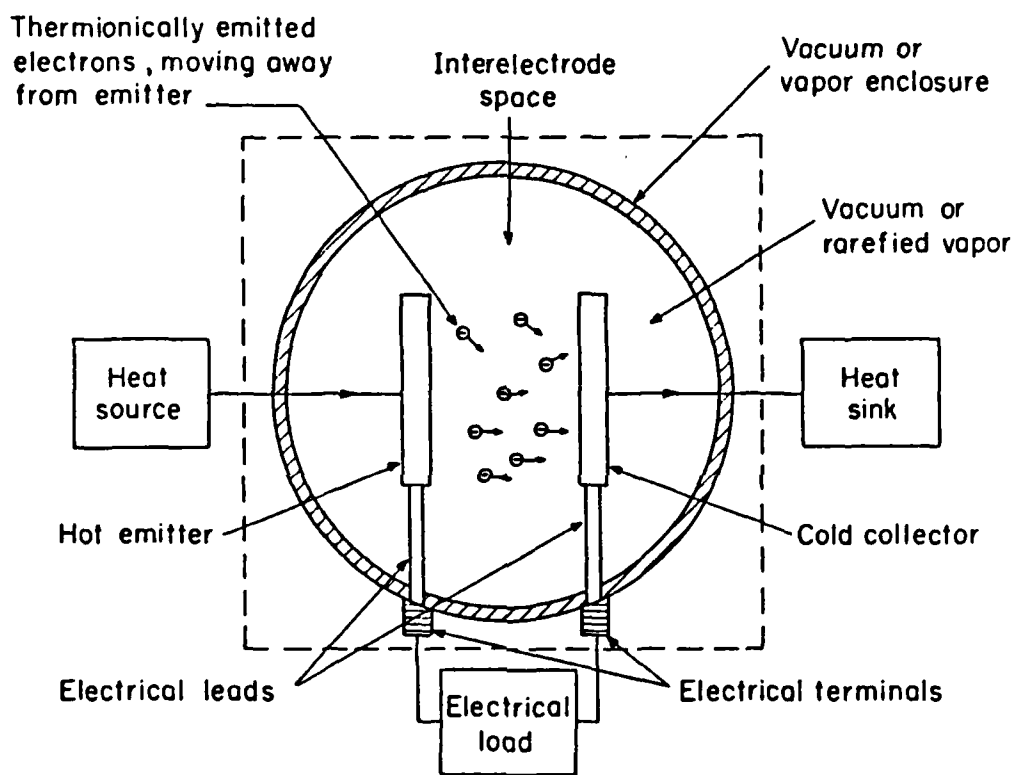


Figure 2.2 - Thermionic Energy Converter

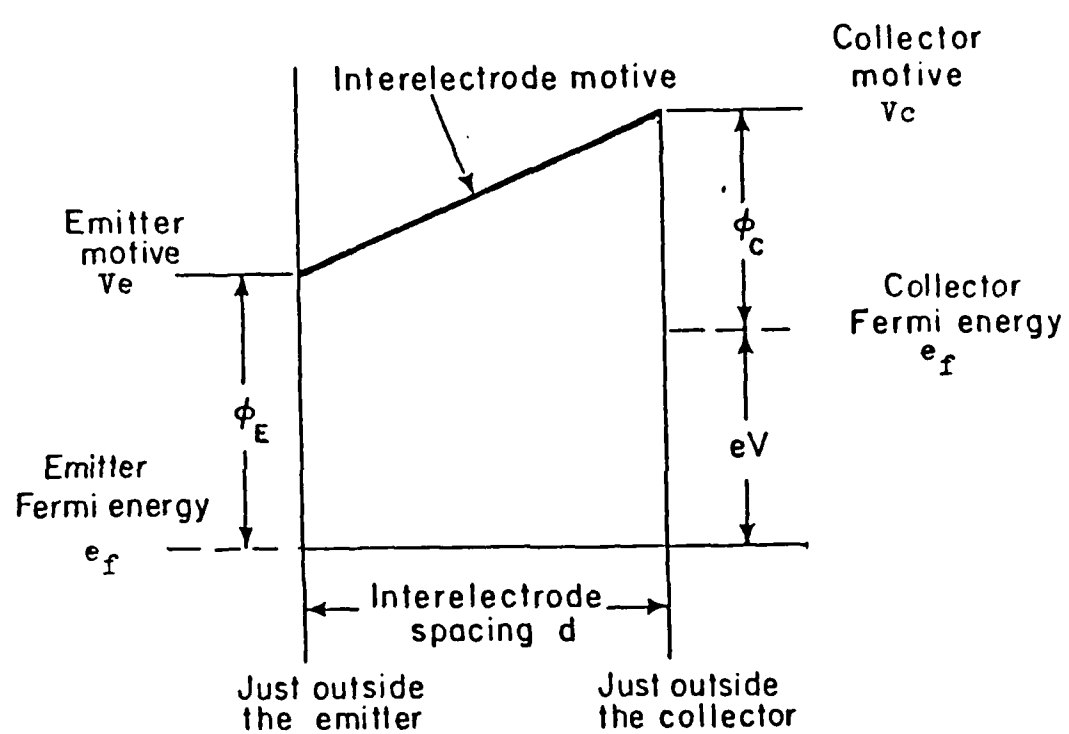


Figure 2.3 - Interelectrode Motive Diagram

#### 2.4 Effective Work Function Calculation

The effective work function is calculated from the Richardson-Dushman equation given in Section 2.2 where  $k$  and  $A$  are known,  $T$  is measured by optical pyrometry and  $J_s$  remains to be determined.

An equation for  $J_s$  can be derived from the analogy to light optics starting with the equation

$$I_i = \frac{I_s}{l^2} \cos\theta$$

where  $I_i$  and  $I_s$  are the radiant fluxes of illuminance from the image and the source respectively,  $l$  is the distance between the source and the image and  $\theta$  is the angle that a ray emitted from the source makes with the perpendicular to the image plane. In the case of the thermionic emission microscope  $\theta$  approaches zero, the magnification,  $M$ , is approximately equal to the distance from the lens to the screen, as the cathode is very close to the objective lens, and radiant intensity is analogous to current density. The first order equation for the calculation of saturation current density is therefore

$$J_s = \frac{IM^2}{Aa}$$

where  $I$  is the saturation emission current and  $Aa$  is the area of the screen aperture.

## Chapter 3

### EXPERIMENTAL APPARATUS

#### 3.1 Introduction

The thermionic emission microscope was originally designed at Xerox, Electro-Optical Systems Division, in 1966. Several parts were redesigned and some modifications were made in order to increase its accuracy and reliability. The microscope's main body is non-magnetic, 304 stainless steel, 0.12 inches thick. Basic dimensions are approximately 20 inches in length and 4.25 inches I.D. All microscope components were fabricated from materials that are capable of withstanding high temperatures and high vacuum operation. Copper gasket seals were used on all flanges and the view port seals were fused metal-to-glass.

The major components of the microscope are the sample (cathode) mounted on an x,y and z mechanism with a drive accuracy of  $\pm 0.001$  inches, lens element, phosphor screen and collector which is a part of the Faraday cage assembly. Figure 3.1 is an assembly drawing of the microscope showing the location of the above components.

This type of instrument differs from other similar devices by the fact that it does not use an external source of electrons such as an electron gun, but rather the sample (cathode) itself emits the electrons.

The microscope operates in conjunction with two vacuum pumps, an optical pyrometer, several power supplies and gauges which will be discussed in more detail in the next chapter.

A detailed description of the microscope's major components follows.

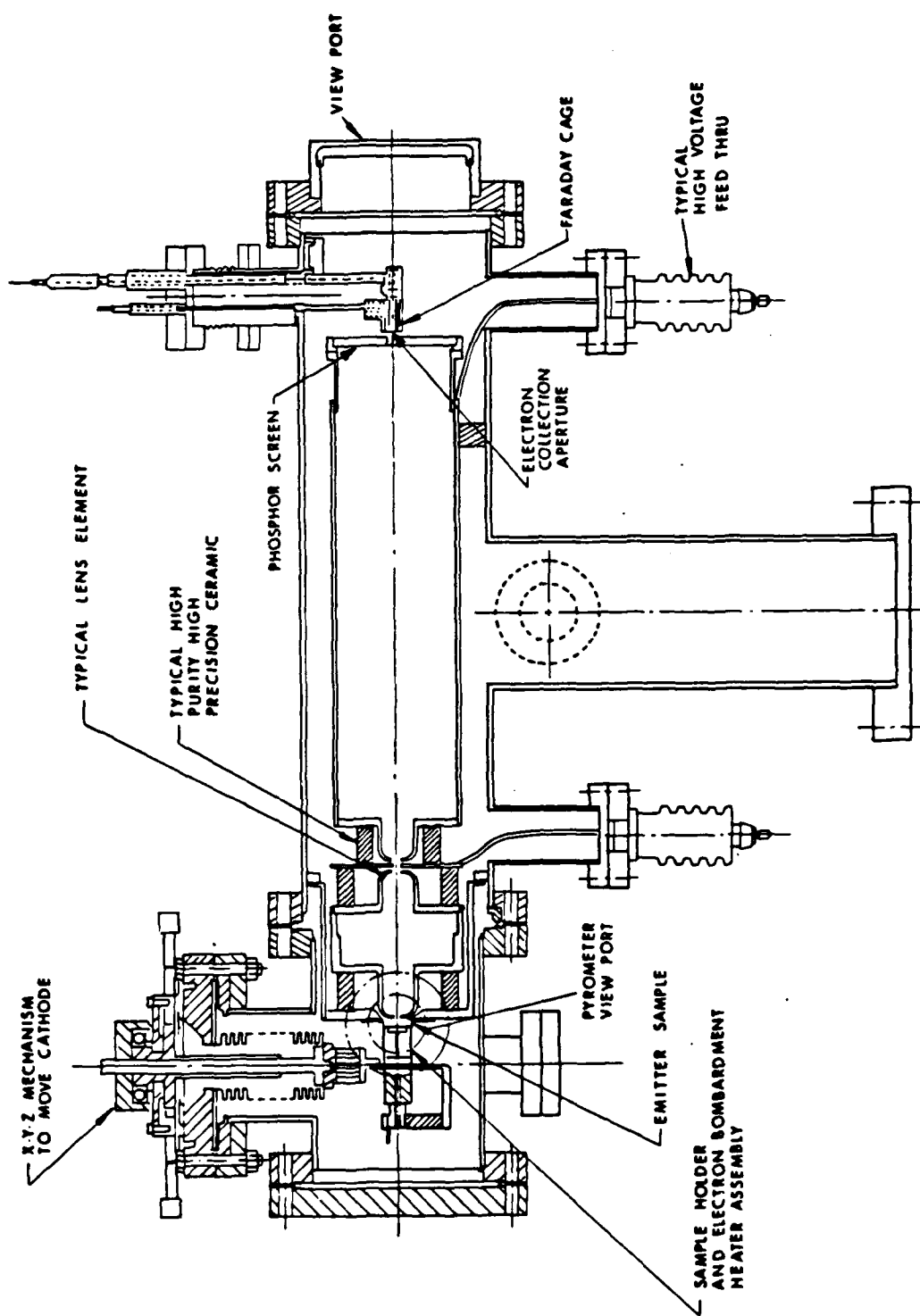


Figure 3.1 - Thermionic Emission Microscope Assembly and Components

### 3.2 Emitter Sample (Cathode)

A sample holder was designed to accommodate the relatively small samples (.375 inches diameter). The holder consists of a circular molybdenum plate to which a tantalum tube was press-fitted. A small circular rhenium plate was electron beam welded to the tantalum tube. The sample was fitted in a cavity at the center of the rhenium plate and locked in place by a tungsten rod. A notch formed on the face of the rhenium plate exposed the hohlraum for sample temperature measurements.

A fixture to hold a counterwound tungsten filament was connected by insulating ceramics to the molybdenum plate. The tungsten filament was located inside the tantalum tube directly behind the sample.

Electrical connections were provided to the tungsten filament and molybdenum plate for sample heating. The molybdenum plate was bolted to the x,y and z mechanism. This mechanism was used to scan the sample's surface and to focus and measure magnification. Figure 3.2 shows the emitter assembly.

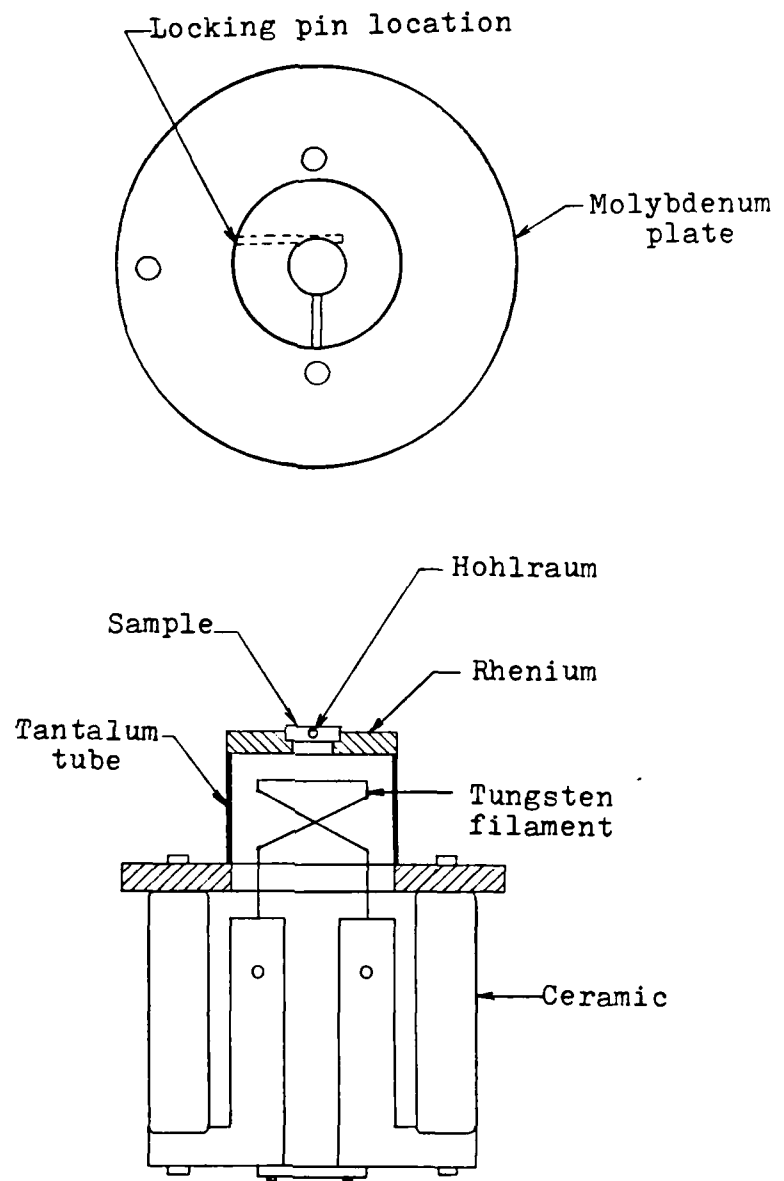


Figure 3.2 - Emitter Assembly

### 3.2 Lens and Screen Assembly

The first lens that the electrons encounter is a cathode objective immersion lens. This lens was made of arc-cast molybdenum and mounted on an arc cast molybdenum plate which was then mounted to the wall of the microscope and therefore kept at ground potential. The second lens is of the projection type and is made of stainless steel. This lens was insulated from the first lens by ceramics.

The projection lens was connected to the phosphor screen by a stainless steel drift tube. The screen was made of high purity glass coated with phosphor. A stainless steel insert was fitted in a hole at the center of the screen and electrically connected to the drift tube by two tantalum strips.

Electrons that emerge from the sample pass through the holes in the lenses, accelerate through the drift tube and are focused on the screen, providing an inverted and magnified image of the sample. Since the electrons that travel on the center line of the microscope are not deflected by the electrical field, they pass through the hole in the screen and are captured by the collector. Figure 3.3 is a diagram showing the assembly of the parts mentioned above.

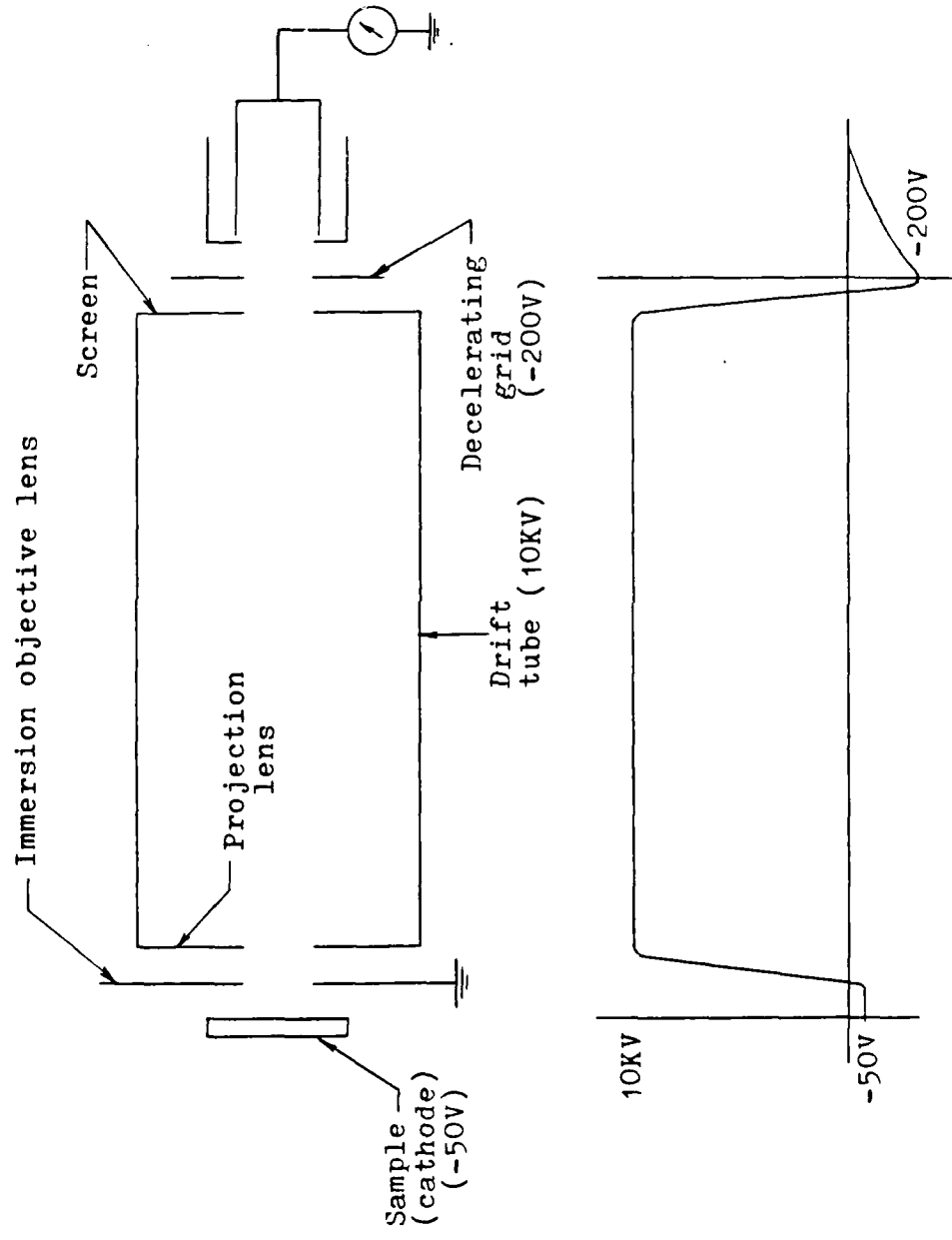


Figure 3.3 – Lens and Screen Assembly With Various Potentials Along the Column

### 3.4 Faraday Cage Assembly

The Faraday cage assembly was designed for more rigidity and welded bellows were incorporated into the design for external alignment capabilities.

The main parts of the Faraday cage are the decelerating grid (Figure 3.4), the guard ring (Figure 3.5) and a collector (Figure 3.6) which collects the electrons for subsequent emission measurements. All the above parts are electrically separated from each other by appropriate ceramic pieces and their assembly is shown in Figure 3.7. The ceramic parts had to be very carefully designed as the lava stone's linear dimensions increased by two percent when fired. The welded bellows (Figure 3.8) were positioned with the adjusting screws as shown.

Electrical connections to the Faraday cage were made via a feedthrough (Figure 3.9) that was designed and manufactured for this particular purpose. Figure 3.10 shows the entire Faraday cage assembly.

Electrons emerge with a high energy through the screen aperture and are first slowed down by the decelerating grid. The function of the decelerating grid is two-fold:

1. It prevents secondary electron production.
2. It refocuses the electron beam.

The guard ring eliminates any stray potentials or current leakages and isolates the collector. The last item that the electron beam encounters is the collector which was connected to a very sensitive electrometer capable of measuring currents in the  $10^{-13}$  amp range, with an accuracy of  $\pm 1\%$ .

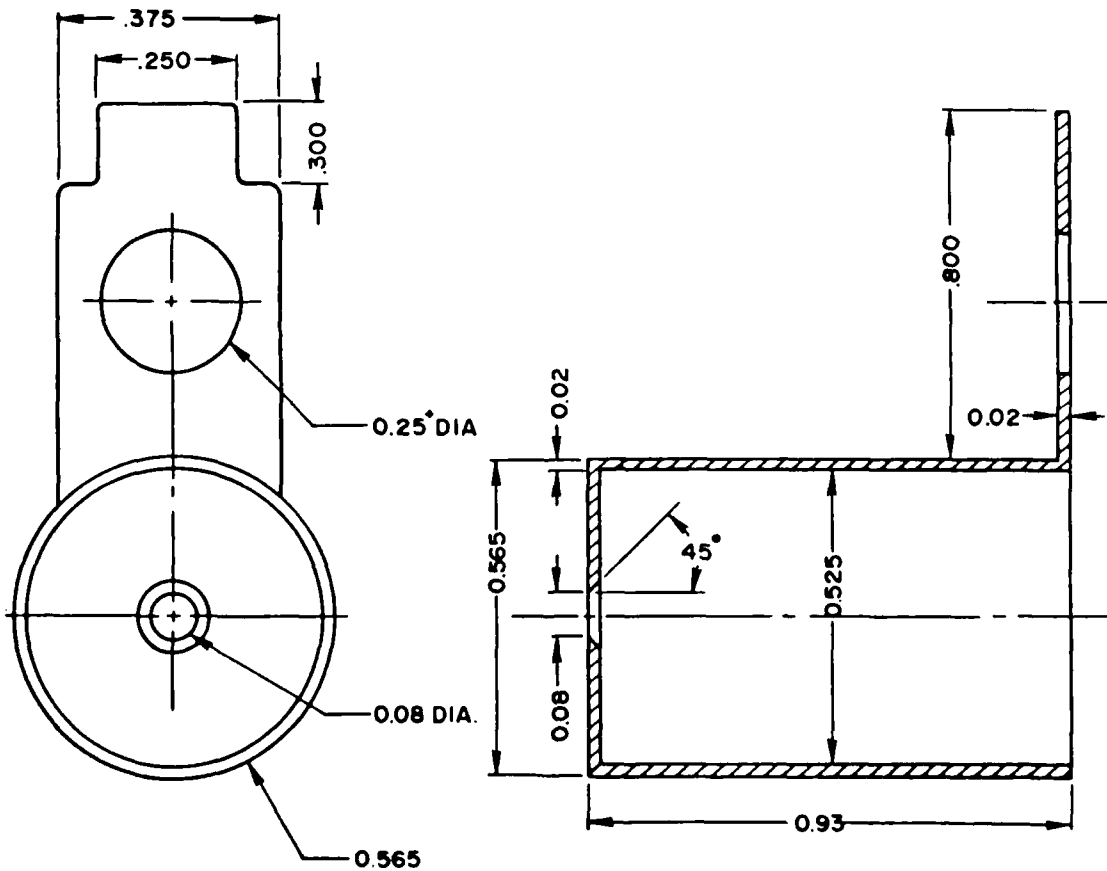


Figure 3.4 - Decelerating Grid

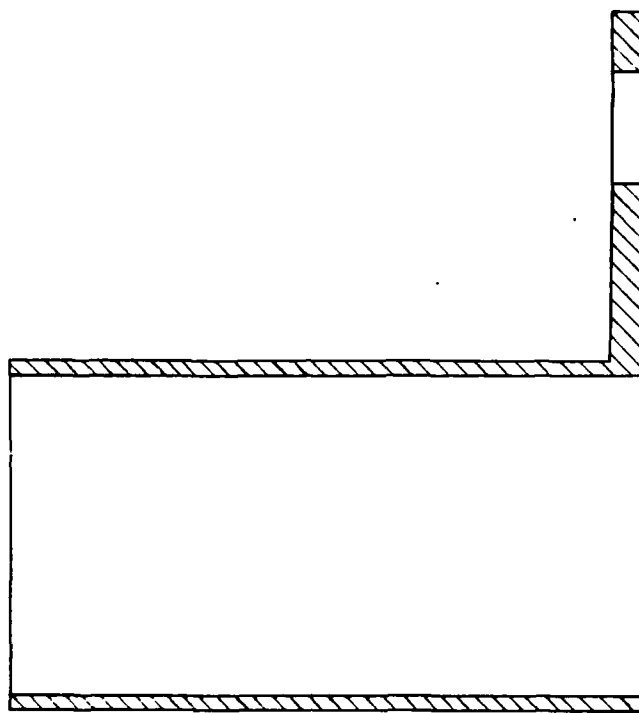


Figure 3.5 - Guard Ring

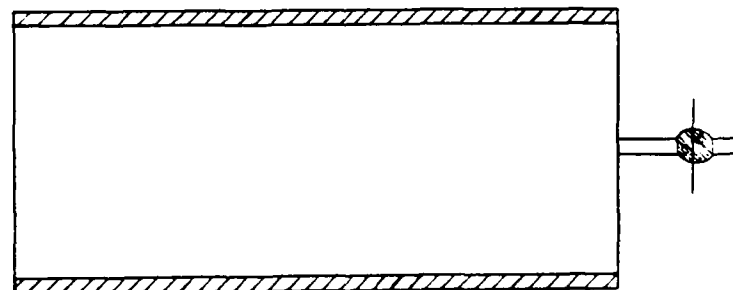


Figure 3.6 - Collector

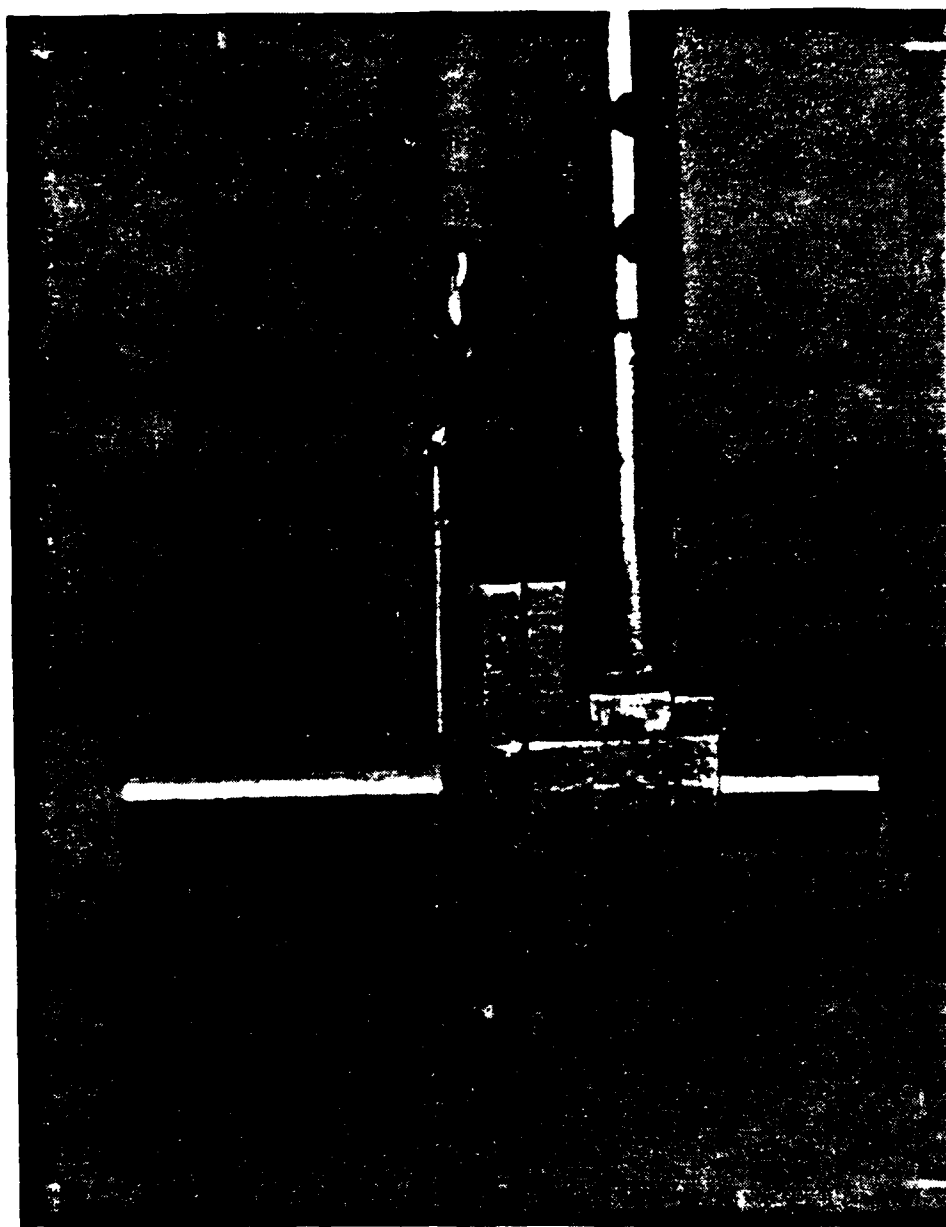


Figure 3.7 - Faraday Cage Assembly

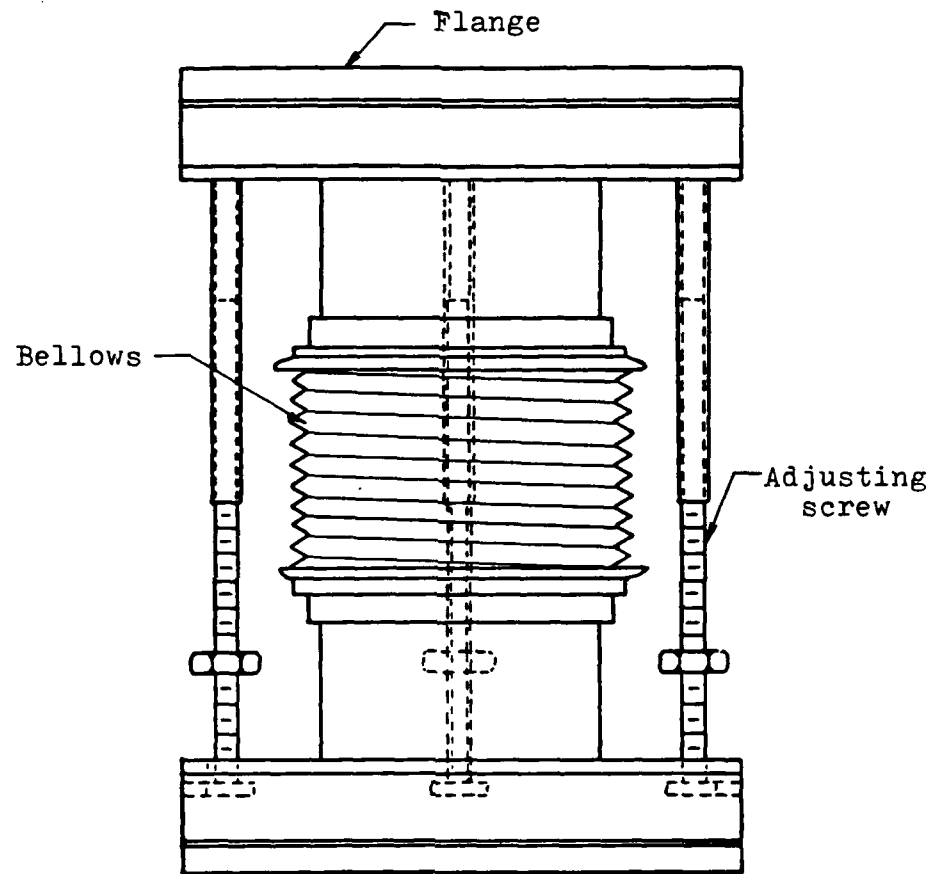


Figure 3.8 - Adjustable Welded Bellows

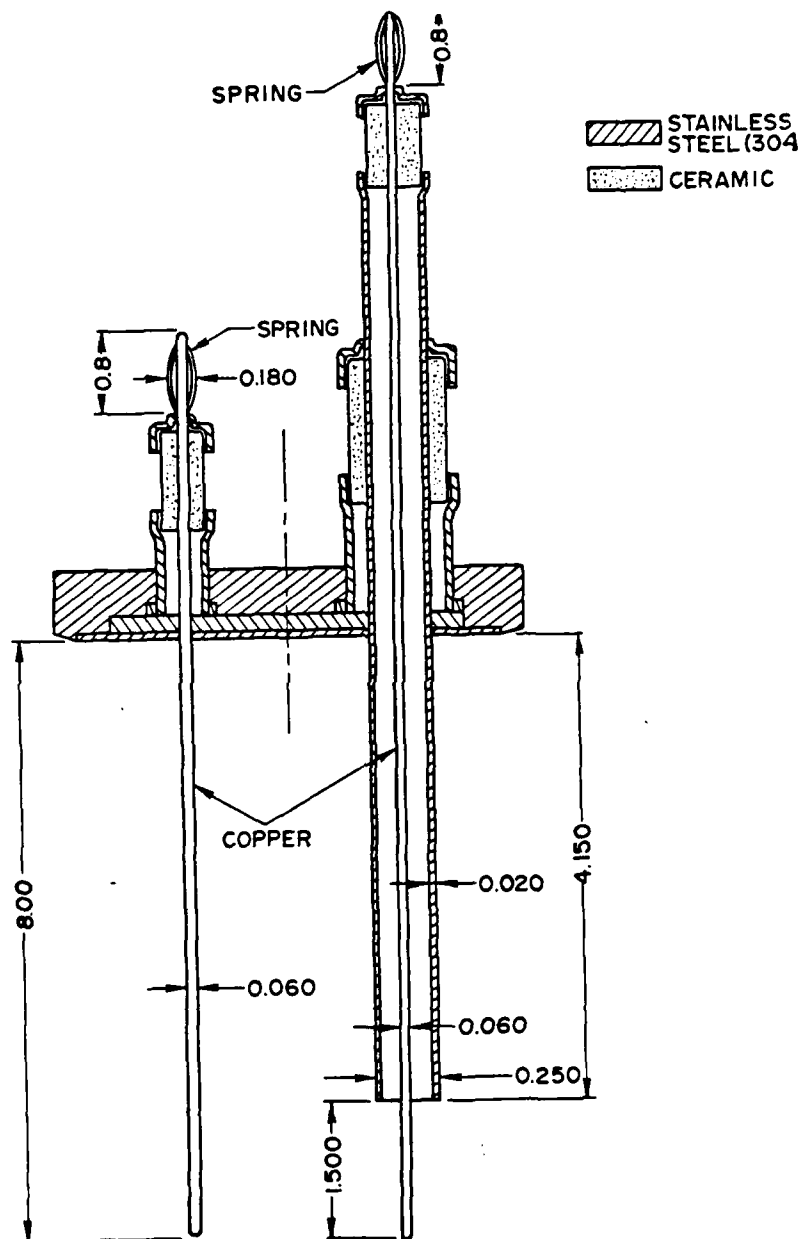


Figure 3.9 - Electrical Feedthrough

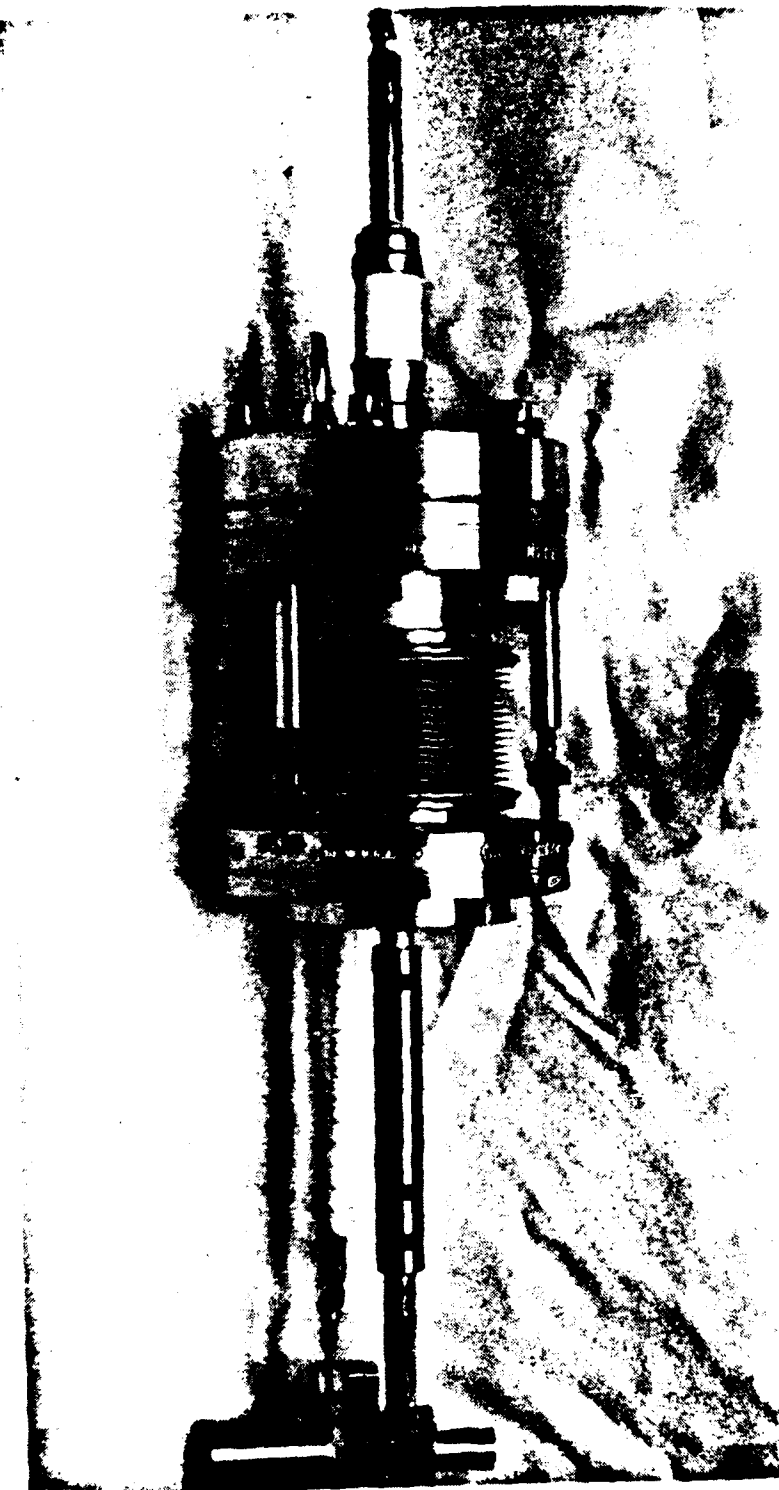


Figure 3.10 - Full Faraday Cage Assembly

Chapter 4  
EXPERIMENTAL PROCEDURE

**4.1 Introduction**

All internal parts of the microscope were ultrasonically cleaned in Oakite and then in acetone prior to final microscope assembly. Large parts were cleaned with hydrochloric acid and acetone. Parts were handled with rubber gloves to prevent their contamination. Any foreign particles or fingerprints interfere with the electron beam and increase pumpdown time.

Lenses, drift tube and screen assembly were bolted to the inside of the microscope. A small diameter, low power laser gun was used to align the above parts. This was a very important step that had to be done before final assembly of the microscope. The alignment was done by changing the position of the drift tube in such a way that the laser beam that entered through the lens assembly emerged through the screen aperture and was not obstructed on its way. Preliminary testing of the apparatus, proved that the cantilevered drift tube sagged during high temperature operation and axial alignment could not be maintained. A ceramic insert (Figure 4.1), whose purpose was to support the free end of the drift tube was designed, manufactured and fired.

Following alignment, the Faraday cage assembly was attached and fastened to the microscope's body. The decelerating grid, guard ring and collector assembly were connected to the electrical feedthrough from the inside as the opening of this location was too small and could not accommodate the large structure. At this point the collector was visually aligned with the screen aperture, at a distance of 0.06 inches from it.

The emitter assembly was the last part to be installed inside the microscope. The sample holder was attached to the x,y and z mechanism ensuring that the polished surface of the sample (see section on sample preparation) was parallel to the first grid of the lens assembly. The tungsten filament was positioned 0.03 inches behind the sample to compensate for the thermal expansion at operating temperatures.

After the installation of all the above parts, internal electrical connections to the Faraday cage, screen insert and emitter assembly were made. At this point the microscope was sealed off. All flanges were joined by tightening opposite bolts successively in order to prevent the copper gaskets from warping. The torque requirements for bolts are 16 ft-lbs on the small flanges and 26 ft-lbs on the large flanges.

The next step was to evacuate the system (see section 4.3). When the required vacuum was reached, external electrical connections were made and the microscope was ready for testing. Supporting instrumentation is described in section 4.4.

In the thermionic emission technique, the sample is heated by electron bombardment from a hot counterwound tungsten filament up to temperatures at which there is an appreciable electron emission from its surface. For sample temperature measurements, see section 4.5. The electrons are focused through a lens arrangement and accelerated towards a fluorescent screen, providing a magnified image of the surface examined. The microscope was operated in such a fashion that the light intensity emitted by a certain region of the image on the phosphor screen was directly proportional to the electron current emitted by the corresponding region on the sample's surface and inversely proportional to its work function. For example, a grain with a high work function has a relatively low electron emission and will appear as a dark area on the screen. The electrons that emerged from the screen aperture were collected in order to measure the current for purposes of work function calculations.

Before testing the tungsten rhenium samples, the microscope was calibrated with a known rhenium sample. Grains 1 and 4 (Figure 4.2) were tested and their effective work function at a temperature of 2053K were calculated to be 5.22eV and 4.90eV, respectively. These results are within experimental error ( $\pm 0.04\text{eV}$ ) when compared to the original results of 5.26eV and 4.92eV reported by Jacobson and Campbell [9].

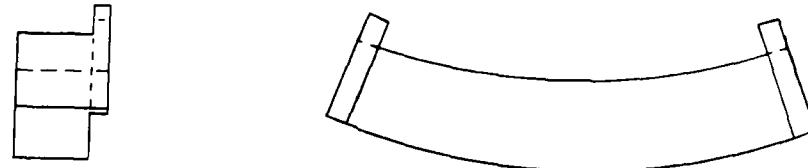


Figure 4.1 - Ceramic Insert

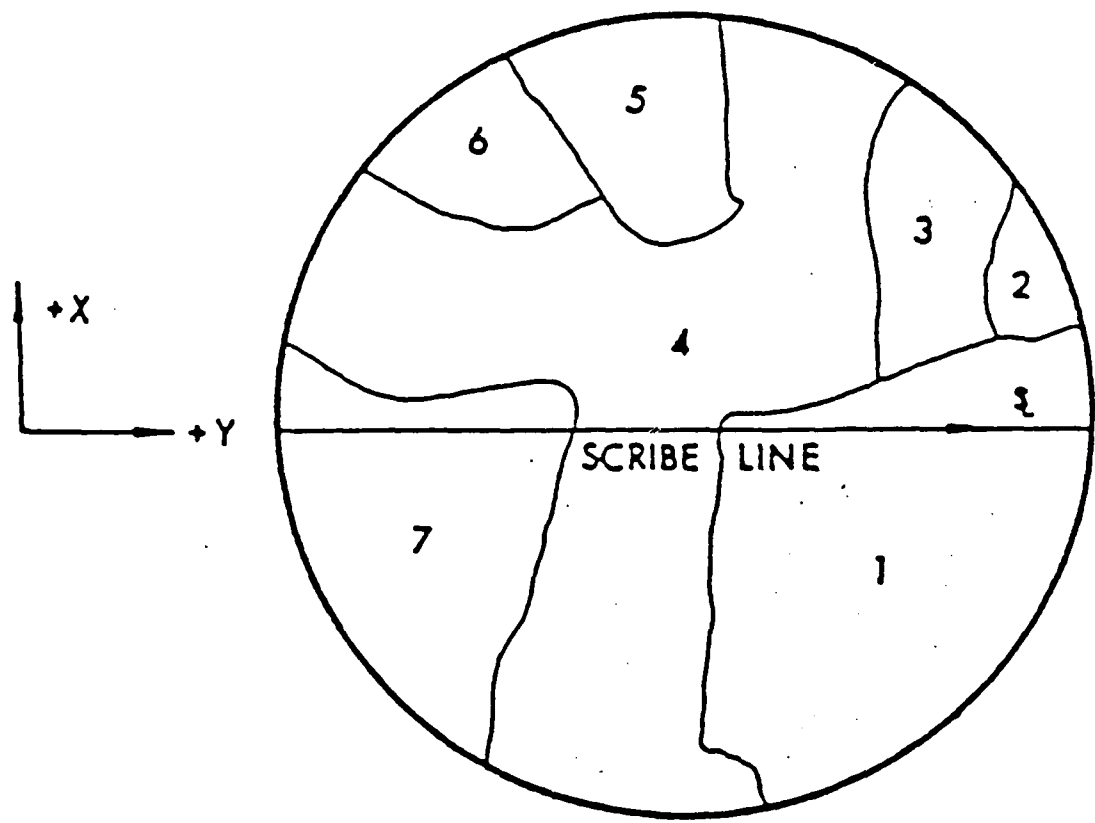


Figure 4.2 - Rhenium Sample Used for Calibration

#### 4.2 Sample Preparation

The samples tested were tungsten based alloys with 3%, 10%, 25%, and 30% rhenium. The alloys were sintered from tungsten and rhenium powders and were supplied by Rhenium Alloys, Inc., (1329 Taylor Street, Box 245, Elyria, Ohio 44035).

The original sintered material came in button form, roughly 0.4 inches in diameter and 0.5 inches long. All samples were turned down to .375 inches in diameter and .100 inches thick. The surface finish was achieved with an Electrical Discharge Machine (EDM). The EDM was also used to drill the hohlraum on the circumference of the sample parallel to its surface. This hole has a ratio of diameter to depth of 1:10 so that it approximates a black body. In this case, the hohlraum was 0.020 inches in diameter and 0.200 inches deep. The EDM was further used to make a groove perpendicular to the hohlraum to lock the sample in place with a tungsten rod. All samples were polished with emery paper down to grit 600 and lapped with Alumina slurry down to 0.05  $\mu\text{m}$ . Before insertion into the microscope, the samples were ultrasonically cleaned in Oakite (HD126), rinsed with distilled water and ultrasonically cleaned in acetone. Lines were scribed on the polished surface to identify grain location. Figure 4.3 shows a typical sample.

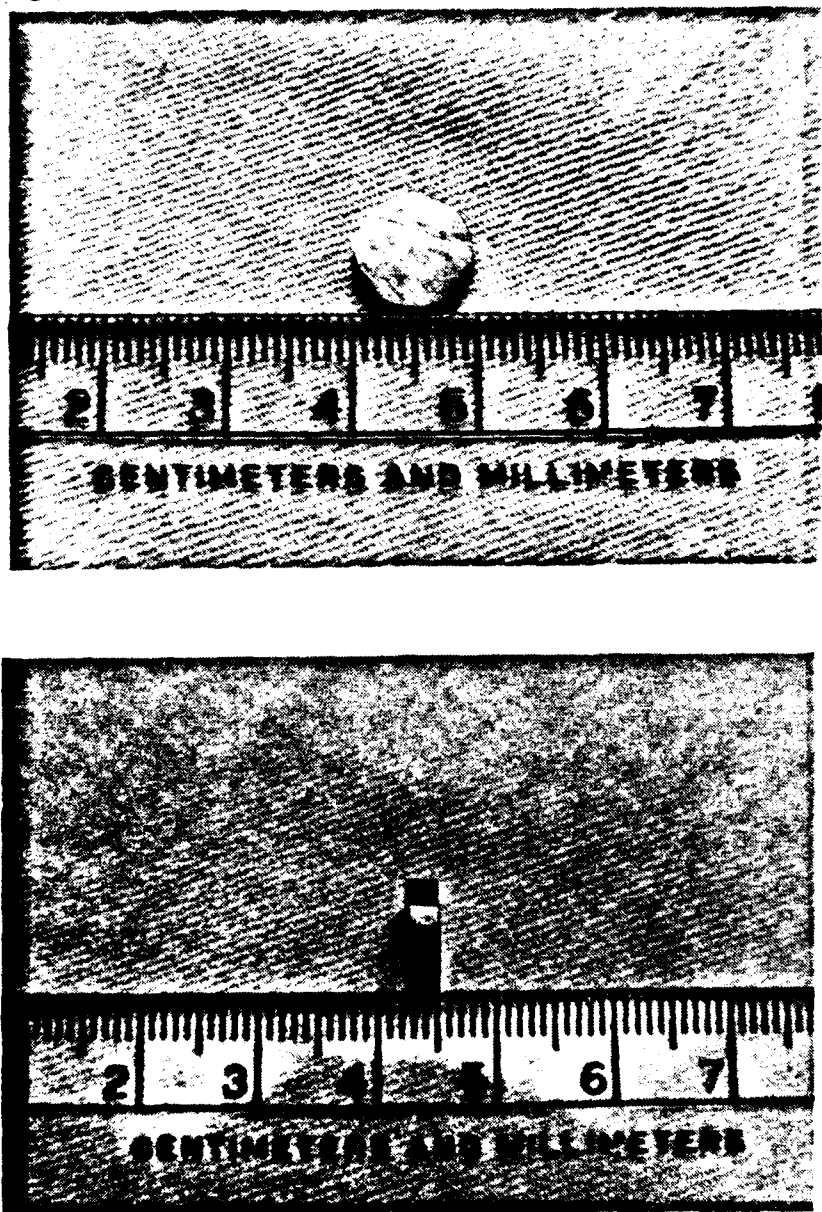
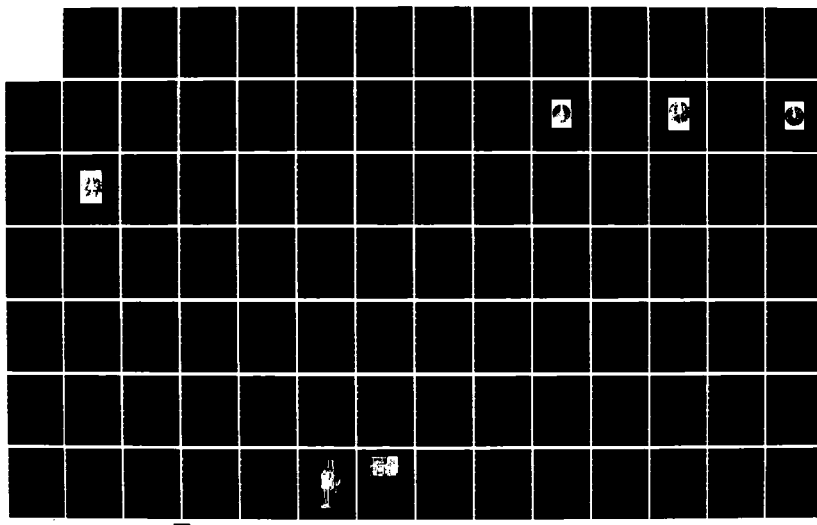
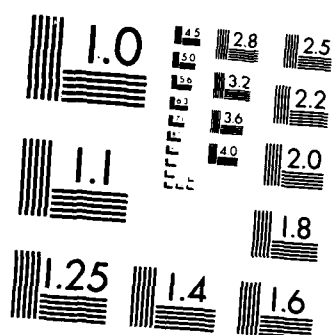


Figure 4.3 - Typical Sample

AD-A173 245 INVESTIGATION OF MATERIAL PROBLEMS FOR HIGH TEMPERATURE 2/5  
HIGH POWER SPACE. (U) ARIZONA STATE UNIV TEMPE COLL OF  
ENGINEERING AND APPLIED SCIE. D L JACOBSON ET AL.  
UNCLASSIFIED JUL 86 AFOSR-TR-86-0819 AFOSR-83-0067 F/G 11/6 NL





MICROCOPY RESOLUTION TEST CHART  
NATIONAL BUREAU OF STANDARDS 1963 A

#### 4.3 Vacuum Generation

Vacuum was achieved in two stages by two different pumps.

The first stage, or the roughing stage, brought the pressure from atmospheric down to about  $10^{-2}$  torr. For this stage, a sorption pump was used. This pump was chosen to eliminate possible back streaming of oil. In addition, the sorption pump has no moving parts and requires no electrical power.

The roughing pump was connected to the system by a manual stainless steel valve with a viton main seal. The entire roughing manifold was isolated from the system by a metal valve with copper gaskets.

The sorption pump works according to the principle of the physical adsorption of gases at the surface of molecular sieve materials. These materials have a surface area on the order of  $10^3 \text{ m}^2$  per gram, which explains the large number of molecules that can be adsorbed as a monolayer on their surface. The adsorption of the gases is dependent upon the temperature. Therefore, the pump was baked overnight every three or four pumpdowns in order to get rid of the adsorbed gases and water vapor. In the pumpdown stage, the sorption pump was immersed in liquid nitrogen. After the pump and the molecular sieve material

were brought down to the temperature of the liquid nitrogen (i.e., the liquid nitrogen stopped its vigorous boiling), the roughing valve was opened. Roughing pressure was monitored with a thermocouple gauge.

The second stage increased the vacuum to the  $10^{-9}$  torr range. For this stage, a 140 liters per second Vac-Ion pump was used.

This pump does not require a continuously operating backing pump, therefore, the particular choice of the roughing stage. The Vac-Ion pump operates by ionizing the gas particles which in turn impinge upon the cathode and sputter the cathode material (titanium). The high energy ionized gas particles enter deep into the electrode surface where they are absorbed by ion implantation.

The Vac-Ion pump was activated when the roughing pressure fell to  $10^{-2}$  torr (10-15 minutes). Initially, a bluish glow could be seen and the pump body warmed up slightly. When the glow disappeared and the pump cooled down, the roughing manifold including the thermocouple gauge was valved off.

When the pressure was in the  $10^{-7}$  torr range, the microscope was baked at approximately  $200^{\circ}\text{C}$  with infrared lamps inside an aluminum enclosure designed specifically for this purpose. Baking was done in order to degas the interior of the microscope. After experimenting with the new enclosure it was found that a bakeout of 8-10 hours was sufficient for the system to again reach  $10^{-7}$  torr at which point the heat was removed. When the system was again at  $10^{-7}$  torr, the heat was removed. After the system cooled down, it achieved an ultra-high vacuum of  $10^{-9}$  torr.

The Vac-Ion pump maintained the vacuum throughout the experiment. The pressure given by the pump control unit indicates the pressure in the pump. A nude ionization gauge, installed closer to the sample, provided more accurate pressure measurements in the microscope head. This pressure was usually slightly higher when the sample was heated up.

If the system was filled and purged with nitrogen between sample changes, the pumpdown time was reduced considerably as the nitrogen prevented water molecules from adhering to the surfaces exposed to the vacuum.

#### 4.4 Instrumentation and Technique

Several power supplies and two electrometers supported the apparatus during its operation. An electrical schematic is given in Figure 4.4.

Before electrical connections were made, the system was thoroughly checked to ensure that the filament and the sample were not grounded or in contact. It was also checked to ensure that the drift tube was not grounded and that the various parts of the Faraday cage did not touch each other or the screen insert.

The filament was connected to the NJE CR 18-30 power supply and 16 amps were passed through it. The tungsten filament was the source of electrons from which the sample was bombarded. The Kilovolt 0-1500V power supply was connected between the filament and the sample and supplied the bombarding voltage for sample heating. When samples were changed, the relative location of the filament to the sample was not altered, therefore, bombarding voltages were easily correlated to sample temperatures. Potentials between 250-500 volts were needed; the higher the potential, the higher the sample's temperature. The Fluke 407D was used to apply a small negative voltage (-50V) to the sample in order to overcome the space charge barrier and repel the electrons from its surface. A large electric

field was not applied to the sample as this would have altered its electron emission. The potential of -50V applied at the sample was chosen as this was the value at which saturation occurred (Figure 4.5). The Sorenson 1030-20 0-30kV power supply was connected to the drift tube and further to the screen insert by two tantalum strips which provided a symmetrical accelerating field. The voltage was adjusted for a comfortable brightness and was usually around 10kV. Electrons that emerge from the screen aperture do so with a high energy. The HP-890A, 0-320V power supply was connected to the decelerating grid and was used to apply a negative voltage (-200V) to decelerate the electrons and refocus them. This particular value of -200V was also chosen for saturation considerations (Figure 4.6). The Keithly 610C Electrometer was connected to the guard ring so as to match its resistance to that of the collector. The Keithly 642 digital electrometer which has an accuracy of +1% in the range of currents measured was connected to the collector. The bellows were adjusted in such a fashion so as to maximize the current reading. Extreme care was taken while moving the Faraday cage so that it would not touch the anode (screen insert). A copper screen was built around the Faraday cage feedthrough to prevent stray fields from affecting the current readings.

Before taking any data, the microscope was allowed to attain thermal equilibrium. This was usually taken as the time it took the current readings to stabilize. A shielded co-axial cable connected the Keithly 642 to the collector and the instrument was kept at a distance of three feet as it exhibited large fluctuations when close to the microscope's body.

The x,y and z mechanism was adjusted at this point to focus the image on the screen and to scan the sample's surface. Scanning was necessary in order to obtain readings from several grains located close to the center of the sample so as not to measure the emission from the rhenium disc in which the sample was held. The built-in micrometer assisted in determining the magnification. This was done by moving a certain feature across the screen through its center and then dividing the screen's diameter by the micrometer reading. Cool air from a large fan was passed across the head of the microscope to prevent the x,y and z mechanism from jamming during high temperature operation due to dryout of the lubrication.

In order to get reliable results the magnification was checked periodically, many values of temperature were also taken in order to get an average temperature reading for a particular grain and several current readings were taken for each grain of the polycrystalline samples. This last task became almost impossible with decreasing grain size.

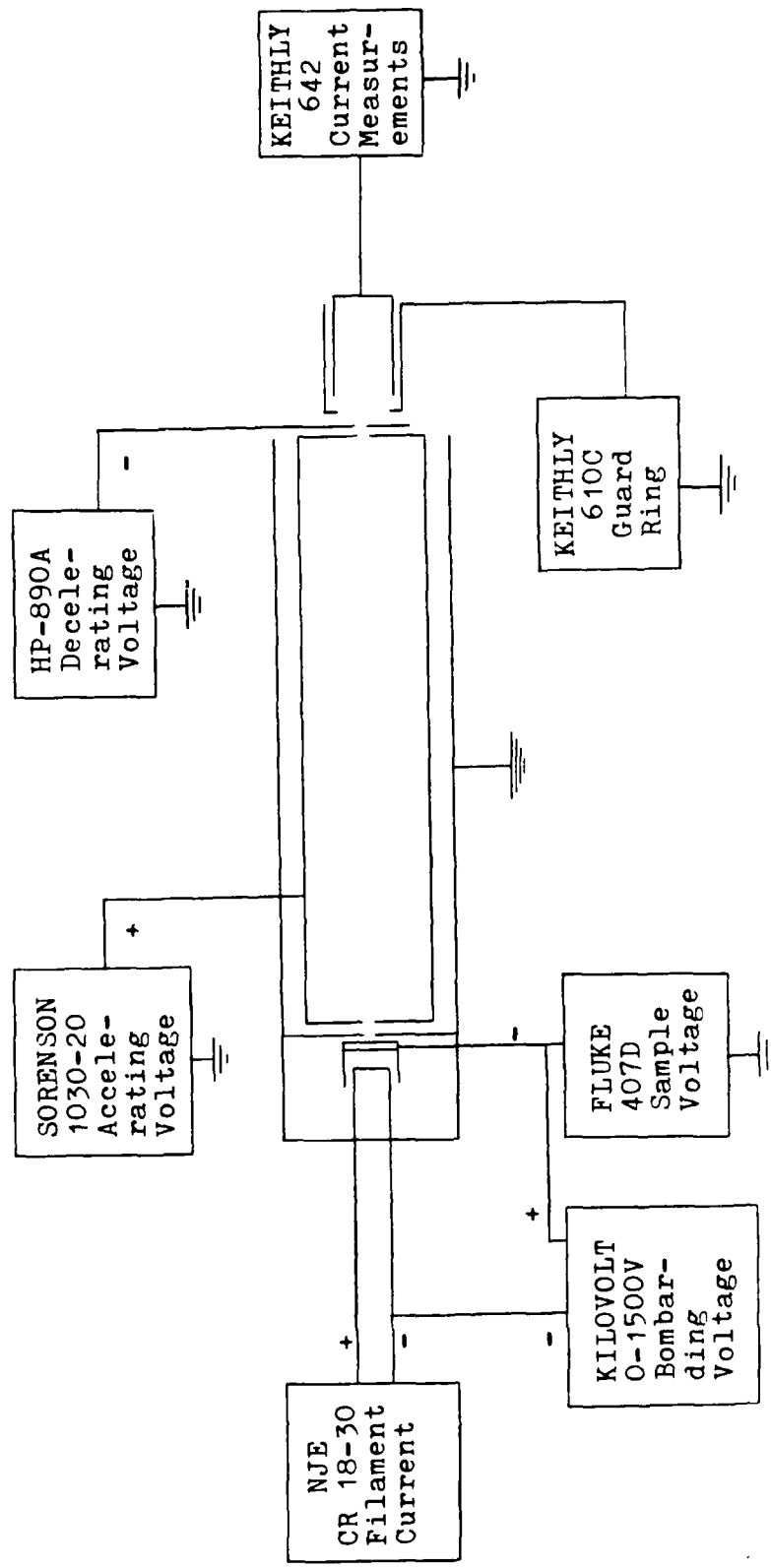


Figure 4.4 - Electrical Schematic

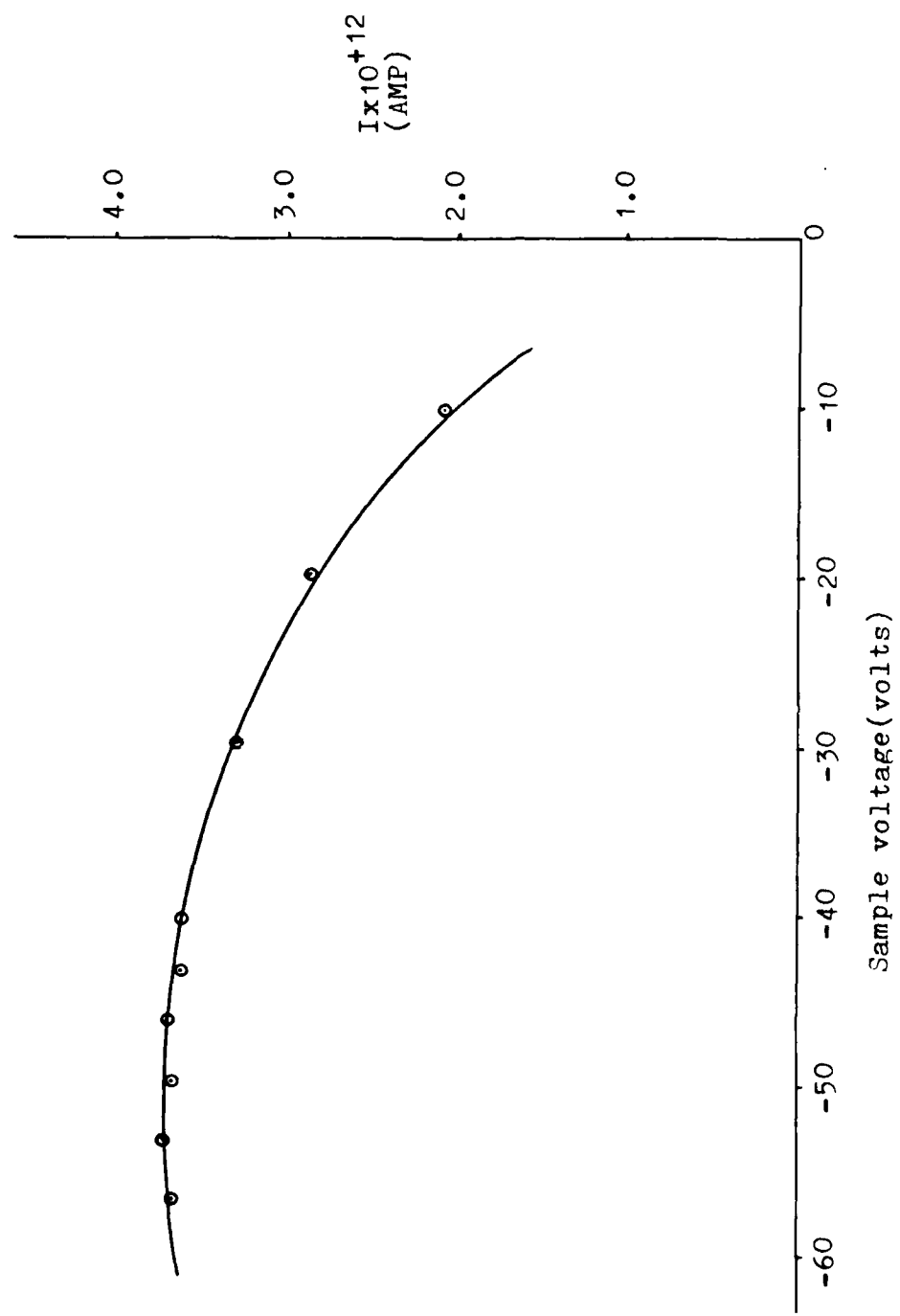


Figure 4.5 - Emission Current vs. Sample Voltage

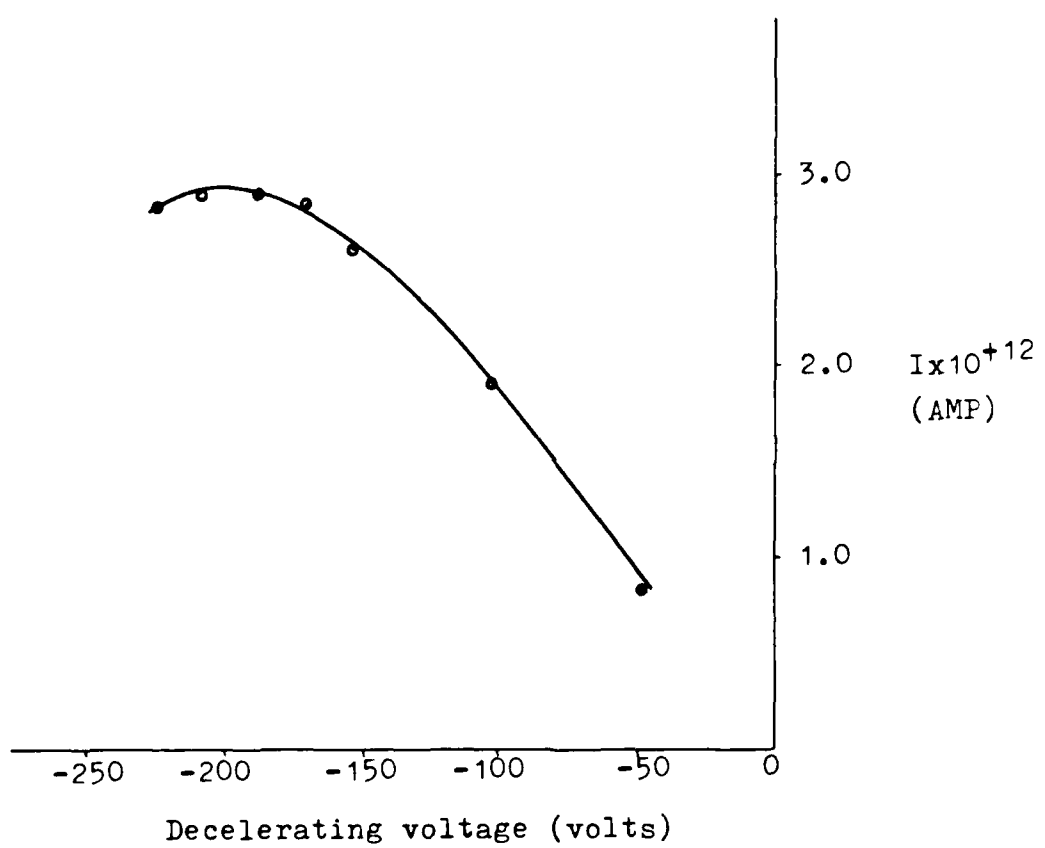


Figure 4.6 - Emission Current VS. Decelerating Voltage

#### 4.5 Temperature Measurements

Sample temperatures were determined with a micro-optical pyrometer. As the sample is at a negative potential, the circuitry for employing a thermocouple would be quite complicated; therefore, the choice of the optical technique.

In order to obtain accurate results, the pyrometer was first calibrated against a tungsten ribbon filament lamp which was in turn calibrated by the National Bureau of Standards (NBS). A table of filament temperatures versus lamp current was also provided by NBS. This lamp was contained within a box built to approximate a black body.

##### 1. Calibration Procedure

After the determination of focal distance and object size at focal distance, an auxiliary objective lens was selected. The one inch saphire view port was removed from the microscope and placed between the NBS lamp and the pyrometer. The lamp current was adjusted using the circuit described in Figure 4.7 and the filament temperature was taken as the true temperature.

The pyrometer was connected to a battery through an ammeter calibrated in degrees Celsius (Figure 4.8).

The pyrometer filament was focused at the center of the tungsten filament across from the notch. The current through the pyrometer lamp filament was set by adjusting the rheostat in the telescope until a blend (colorwise) was made between the apex of the pyrometer lamp filament and the NBS lamp filament. At this point, the pyrometer reading was recorded. This procedure was repeated at various NBS lamp currents thus producing a calibration curve for the pyrometer (Figure 4.9). The two different curves represented in Figure 4.9 correspond to the respective temperature scales on the ammeter.

With the exception of the first two readings, pyrometer readings were all lower than the true temperature.

## 2. Sample Temperature Measurement Procedure

The pyrometer was operated in a similar manner as in the calibration procedure. The target in this case was the hohlraum drilled in the side of the sample. The hohlraum has a diameter to depth ratio of 1:10 and so it approximates a black body.

According to NBS, the maximum uncertainty of the temperature values around working temperatures for thermionic emission is  $\pm 3^{\circ}\text{C}$ . The pyrometer has a reproducibility of  $\pm 2^{\circ}\text{C}$  around the same temperature range. The accuracy, therefore, was at worst  $\pm 5^{\circ}\text{C}$ .

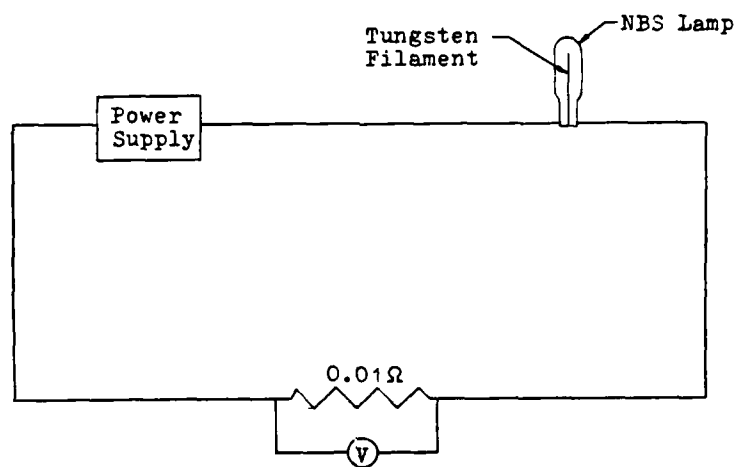


Figure 4.7 - NBS Lamp Circuit

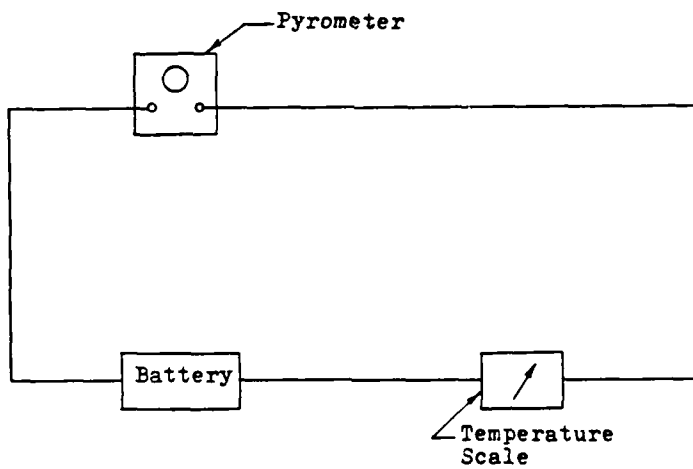


Figure 4.8 - Pyrometer Circuit

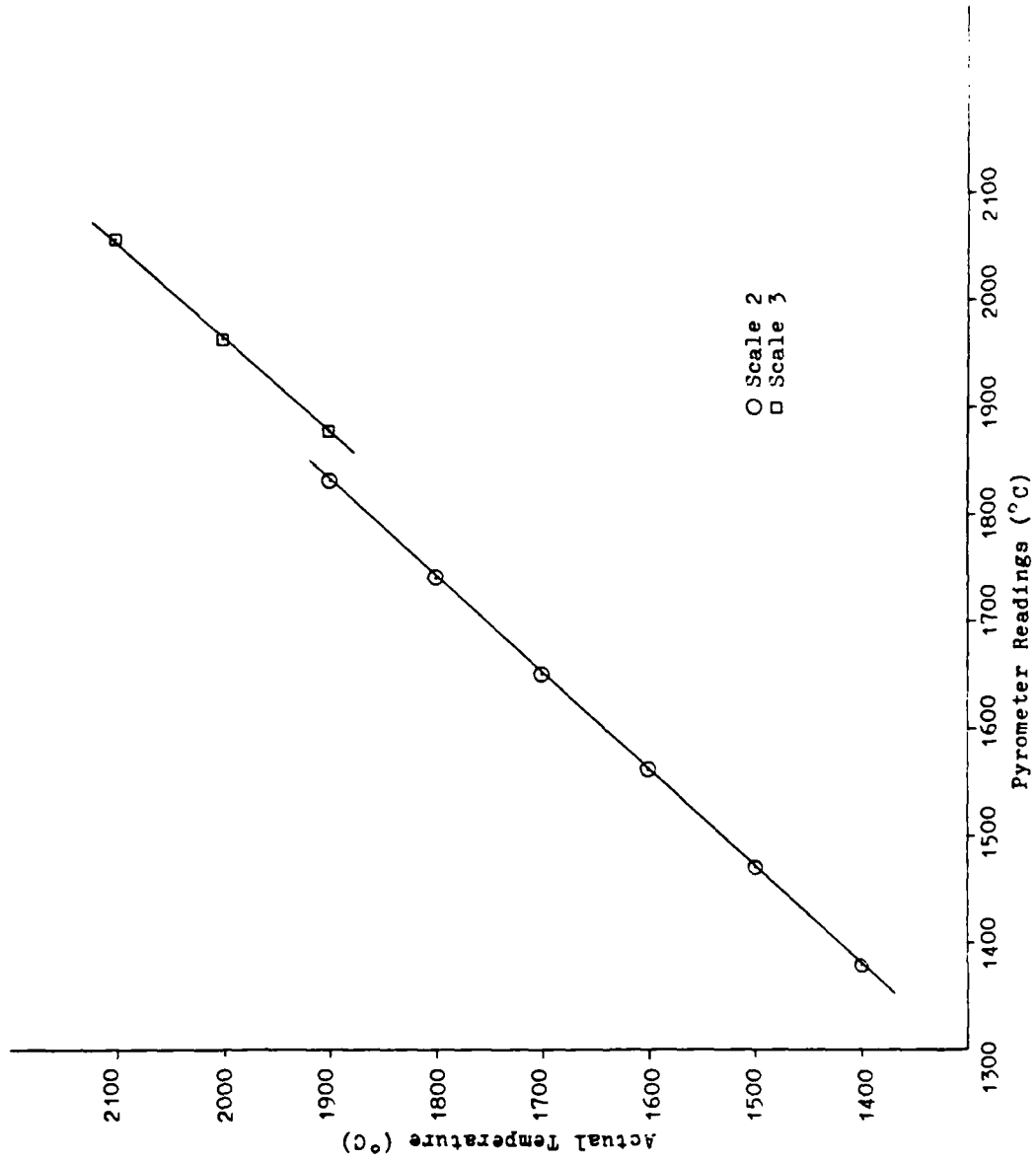


Figure 4.9 - Pyrometer Calibration Curve

#### 4.6 Safety Precautions

As always when one works with lethal voltages and currents much care has to be taken.

When power supplies were adjusted, the operator stood on rubber mats and avoided touching ground. The microscope body and all the other instruments were well grounded. Protective covers were placed on high voltage inputs.

The apparatus was tested for x-ray emission and values below 0.1 mR/hour were recorded. These values were considered to be safe. If the microscope is operated at higher accelerating voltages, lead glass should be used instead of the existing view ports.

## Chapter 5

### RESULTS

#### 5.1 Introduction

Four sintered tungsten base alloys with 3%, 10%, 25% and 30% rhenium were tested. The tungsten was of commercial purity and the rhenium was 99.9999% pure. Results from analysis on the original powders in a mass spectrometer by the supplier are given in Table 5.1.

The powders were sintered in an ultra-pure hydrogen atmosphere at a temperature of about 2550°C for 2.5 hours under a pressure of 30,000 psi. The sintered materials were also cooled in a reducing hydrogen atmosphere. The process was done in a molybdenum-lined furnace.

A small sample of each alloy was analyzed by Jim Clark from the Chemistry Department at Arizona State University with an electron microprobe. Results of this analysis are given in Table 5.2.

All samples were metallographically polished as described in Section 4.2 and then annealed for 12 hours in a vacuum of  $6 \times 10^{-8}$  torr to assure recrystallization and provide enough time to allow a stable grain structure.

Electron emission measurements were averaged for each grain tested, unless the size of the grain posed a limitation. Several grains were tested for each material and the results were averaged at each temperature. The area tested represented about 5% of the entire sample surface. The temperature was continuously monitored to obtain an average value for the entire duration of the test.

Table 5.1 - Spectrographic Analysis

<u>Tungsten Powder</u>		<u>Rhenium Powder</u>	
Element	ppm	Element*	ppm
Al	<1.0	Cu	8.0
Ca	<1.0	Fe	<1.0
Cr	<1.0	Na	<1.0
Cu	<1.0		
Fe	4.0		
K	<10.0		
Mg	<1.0		
Mn	<1.0		
Mo	10.0		
Na	9.0		
Ni	4.0		
Si	<1.0		
Sn	<1.0		

\* Evidence of other elements was not detected.

Table 5.2 - Results of Electron Microprobe Analysis

<u>Alloy</u>	<u>Elements</u>	Concentrations at Different Positions				
		1	2	3	4	5
W-3%Re	W	.968	.987	.926	.973	.991
	Re	.033	.016	.057	.023	.016
	Total	1.001	1.003	.983	.996	1.007
W-10%Re	W	.874	.888	.814	.880	.855
	Re	.082	.062	.137	.075	.105
	Total	.956	.950	.951	.955	.960
W-25%Re	W	.733	.736	.765	.777	.718
	Re	.255	.253	.213	.252	.260
	Total	.988	.989	.983	1.029	.978
W-30%Re	W	.701	.736	.730	.712	.737
	Re	.280	.250	.266	.269	.246
	Total	.981	.986	.996	.981	.983

## 5.2 Tabulated Results

This section presents the results tabulated in order of increasing rhenium percentages in the sample. Each table is accompanied with an emission micrograph of the corresponding sample showing the grains which were tested.

Actual temperatures were obtained from Figure 4.9. Saturation current density is also included. The magnification, 97X, did not change during the testing of all the alloys. This is not surprising as the sizes and distances between microscope components were not changed, and the sample voltage was not altered during the course of the experiment.

The experimental error in work function computation was determined to be  $\pm 0.04\text{eV}$  based on experimental accuracies from the measurements of emission current ( $\pm 1\%$ ), temperature ( $\pm 5\text{ K}$ ) and magnification ( $\pm 3\%$ ).

Five grains were chosen ranging from very bright to very dark in order to get a true average for the effective work function. An effort was made to look for large grains in order to allow scanning of the grain itself, but this was not possible in all cases.

Tables 5.3 through 5.6 contain the experimental data on the four tungsten rhenium alloys tested, showing the average effective work function for each grain. Table 5.7 gives a summary of the average effective work function of each sample at appropriate temperatures. The value of the emission constant, A, in the Richardson-Dushman equation was taken as 120 Amp/cm<sup>2</sup>K<sup>2</sup>.

Table 5.3 - Emission Results for Sample I - W, 3%Re\*

Magnification = 97X  
 Vacuum =  $6 \times 10^{-8}$  torr or better

<u>Grain #</u>	<u>T</u> (K)	<u>I</u> (amp)	<u>J<sub>s</sub></u> (amp/cm <sup>2</sup> )	<u>Φe**</u> (eV)
1	1951	6.285E-11	7.294E-5	4.95
2	1951	6.986E-11	8.108E-5	4.94
3	1951	8.337E-11	9.676E-5	4.91
4	1951	1.425E-10	1.654E-4	4.82
5	1951	2.023E-10	2.349E-4	4.76
1	2062	1.586E-10	1.841E-4	5.09
2	2062	3.723E-10	4.321E-4	4.94
3	2062	4.123E-10	4.785E-4	4.92
4	2062	6.868E-10	7.971E-4	4.83
5	2062	7.631E-10	8.856E-4	4.81
1	2168	6.743E-10	7.826E-4	5.10
2	2168	1.125E-9	1.306E-3	5.01
3	2168	1.305E-9	1.514E-3	4.98
4	2168	1.773E-9	2.058E-3	4.92
5	2168	2.591E-9	3.007E-3	4.85
1	2236	1.509E-9	1.751E-3	5.12
2	2236	1.891E-9	2.195E-3	5.07
3	2236	2.516E-9	2.920E-3	5.02
4	2236	3.197E-9	3.710E-3	4.97
5	2236	4.652E-9	5.399E-3	4.90
1	2361	6.916E-9	8.026E-3	5.12
2	2361	8.950E-9	1.039E-2	5.06
3	2361	1.362E-8	1.581E-2	4.98
4	2361	1.391E-8	1.614E-2	4.97
5	2361	1.537E-8	1.784E-2	4.95

\* Based on less than 5% of cathode area

\*\* Experimental error  $\pm 0.04\text{eV}$



Figure 5.1 Emission Micrograph of W, 3%Re (T=1951 K)

Table 5.4 - Emission Results for Sample II - W, 10%Re\*

Magnification = 97X  
 Vacuum =  $6 \times 10^{-8}$  torr or better

<u>Grain #</u>	<u>T</u> ( <u>K</u> )	<u>I</u> (amp)	<u>J<sub>s</sub></u> (amp/cm <sup>2</sup> )	<u>Øe**</u> (eV)
1	1946	2.386E-10	2.769E-4	4.72
2	1946	7.542E-11	8.753E-5	4.91
3	1946	1.089E-10	1.264E-4	4.85
4	1946	1.394E-10	1.618E-4	4.81
5	1946	2.215E-10	2.571E-4	4.73
1	2051	1.783E-9	2.069E-3	4.63
2	2051	7.510E-11	8.716E-5	5.19
3	2051	5.182E-10	6.014E-4	4.85
4	2051	7.926E-10	9.199E-4	4.78
5	2051	1.282E-9	1.488E-3	4.69
1	2162	6.752E-9	7.836E-3	4.66
2	2162	2.121E-10	2.462E-4	5.30
3	2162	2.621E-9	3.042E-3	4.83
4	2162	3.809E-9	4.421E-3	4.76
5	2162	5.421E-9	6.291E-3	4.70
1	2224	1.245E-8	1.445E-2	4.68
2	2224	7.890E-10	9.157E-4	5.21
3	2224	4.782E-9	5.550E-3	4.87
4	2224	6.804E-9	7.896E-3	4.80
5	2224	9.685E-9	1.124E-3	4.73
1	2339	3.589E-8	4.165E-2	4.73
2	2339	3.110E-9	3.609E-3	5.22
3	2339	1.796E-8	2.084E-2	4.87
4	2339	2.497E-8	2.898E-2	4.81
5	2339	2.632E-8	3.055E-2	4.80

\* Based on less than 5% of cathode area

\*\* Experimental error  $\pm 0.04\text{eV}$



Figure 5.2 - Emission Micrograph of W, 10%Re (T=1946 K)

Table 5.5 - Emission Results for Sample III - W, 25%Re\*

Magnification = 97X  
 Vacuum =  $6 \times 10^{-8}$  torr or better

<u>Grain #</u>	<u>T</u> (K)	<u>I</u> (amp)	<u>J<sub>s</sub></u> (amp/cm <sup>2</sup> )	<u>Φe**</u> (eV)
1	1951	4.345E-11	5.043E-5	5.02
2	1951	2.535E-10	2.942E-4	4.72
3	1951	1.795E-10	2.083E-4	4.78
4	1951	4.260E-11	4.944E-5	5.02
5	1951	1.605E-11	1.863E-5	5.18
1	2037	1.060E-10	1.230E-4	5.09
2	2037	7.982E-10	9.264E-4	4.74
3	2037	6.688E-10	7.762E-4	4.77
4	2037	1.102E-10	1.279E-4	5.09
5	2037	8.675E-11	1.007E-4	5.13
1	2148	4.405E-10	5.112E-4	5.13
2	2148	3.968E-9	4.605E-3	4.72
3	2148	2.944E-9	3.417E-3	4.78
4	2148	7.395E-10	8.582E-4	5.03
5	2148	2.594E-10	3.011E-4	5.23
1	2259	2.295E-9	2.664E-3	5.09
2	2259	1.222E-8	1.418E-2	4.77
3	2259	8.910E-9	1.034E-2	4.83
4	2259	3.022E-9	3.507E-3	5.04
5	2259	1.193E-9	1.384E-3	5.22
1	2339	2.792E-9	3.240E-3	5.25
2	2339	2.214E-8	2.569E-2	4.83
3	2339	1.308E-8	1.518E-2	4.94
4	2339	3.850E-9	4.468E-3	5.18
5	2339	1.219E-8	1.415E-2	4.95

\* Based on less than 5% of cathode area

\*\* Experimental error  $\pm 0.04\text{eV}$



Figure 5.3 - Emission Micrograph of W, 25%Re (T=1951 K)

Table 5.6 - Emission Results for Sample IV - W, 30%Re\*

Magnification = 97X  
 Vacuum =  $6 \times 10^{-8}$  torr or better

<u>Grain #</u>	<u>T</u> (K)	<u>I</u> (amp)	<u>J<sub>s</sub></u> (amp/cm <sup>2</sup> )	<u>Φe**</u> (eV)
1	1946	1.072E-10	1.244E-4	4.85
2	1946	1.036E-12	1.202E-5	5.24
3	1946	5.718E-11	6.636E-5	4.96
4	1946	4.235E-11	4.915E-5	5.01
5	1946	1.867E-11	2.167E-5	5.14
1	2051	5.434E-10	6.306E-4	4.84
2	2051	5.360E-10	6.209E-5	5.25
3	2051	2.217E-10	2.573E-4	5.00
4	2051	2.735E-10	3.174E-4	4.97
5	2051	9.818E-11	1.139E-4	5.15
1	2170	2.501E-9	2.901E-3	4.86
2	2170	2.525E-10	2.930E-4	5.29
3	2170	1.567E-9	1.819E-3	4.95
4	2170	1.193E-9	1.384E-3	5.00
5	2170	6.001E-10	6.963E-4	5.13
1	2224	3.542E-9	4.111E-3	4.92
2	2224	5.810E-10	6.743E-4	5.27
3	2224	1.843E-9	2.139E-3	5.05
4	2224	1.530E-9	1.776E-3	5.09
5	2224	1.265E-9	1.468E-3	5.12
1	2350	1.848E-8	2.144E-2	4.89
2	2350	1.714E-9	1.989E-3	5.37
3	2350	1.114E-8	1.292E-2	4.99
4	2350	9.424E-9	1.094E-2	5.03
5	2350	5.051E-9	5.862E-3	5.15

\* Based on less than 5% of cathode area

\*\* Experimental error  $\pm 0.04$ eV



Figure 5.4 - Emission Micrograph of W,30%Re (T=1946 K)

Table 5.7 - Summary of  $\bar{\phi}_e$  Measurements\*

<u>Sample</u>	T (K)	$\bar{\phi}_e^{**}$ (eV)
W, 3%Re	1951	4.87
	2062	4.92
	2168	4.97
	2236	5.02
	2361	5.02
W, 10%Re	1946	4.80
	2051	4.83
	2162	4.85
	2224	4.86
	2339	4.89
W, 25%Re	1951	4.94
	2037	4.96
	2148	4.98
	2259	4.99
	2339	5.03
W, 30%Re	1946	5.04
	2051	5.04
	2170	5.05
	2224	5.09
	2350	5.09

\* Based on less than 5% of cathode area

\*\* Experimental error  $\pm 0.04\text{eV}$

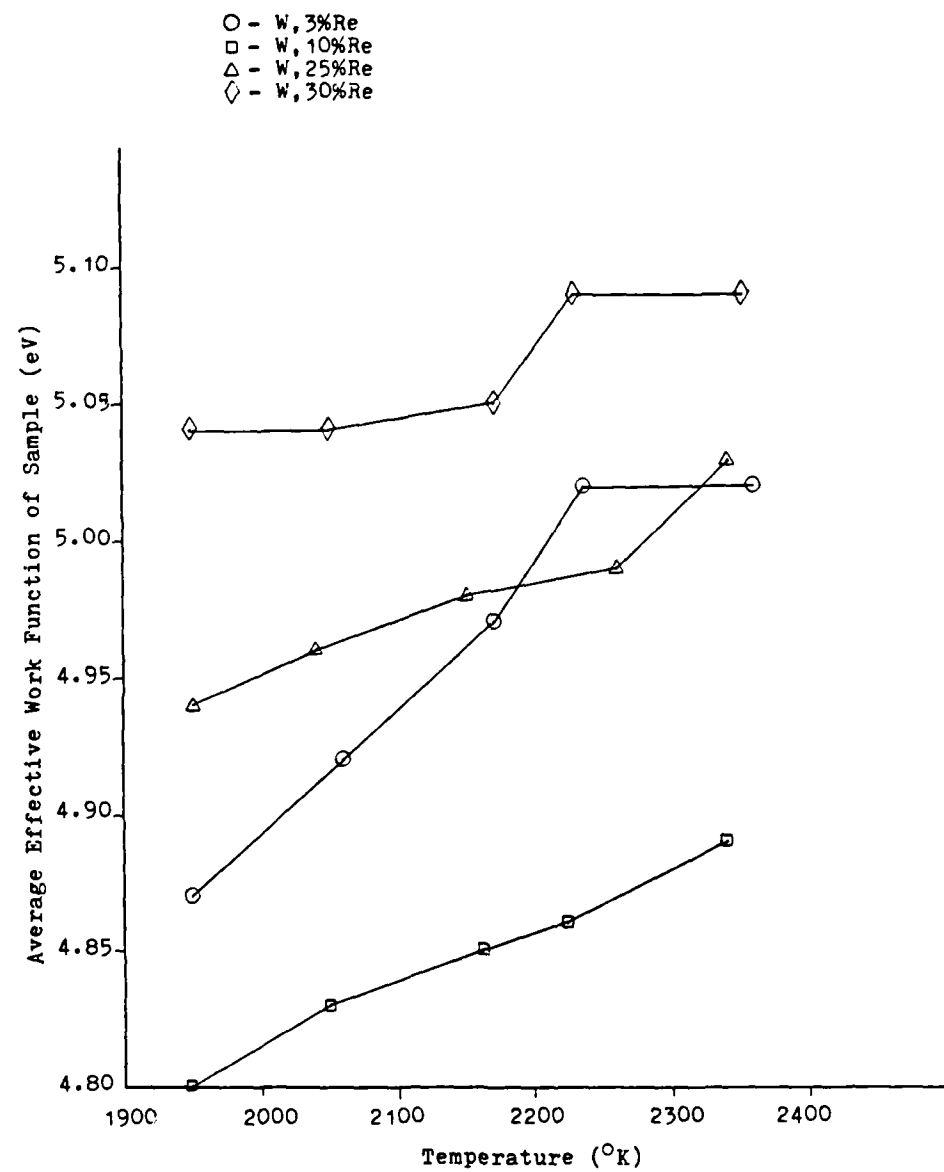


Figure 5.5 - Temperature Dependence of  $\bar{\phi}_e$

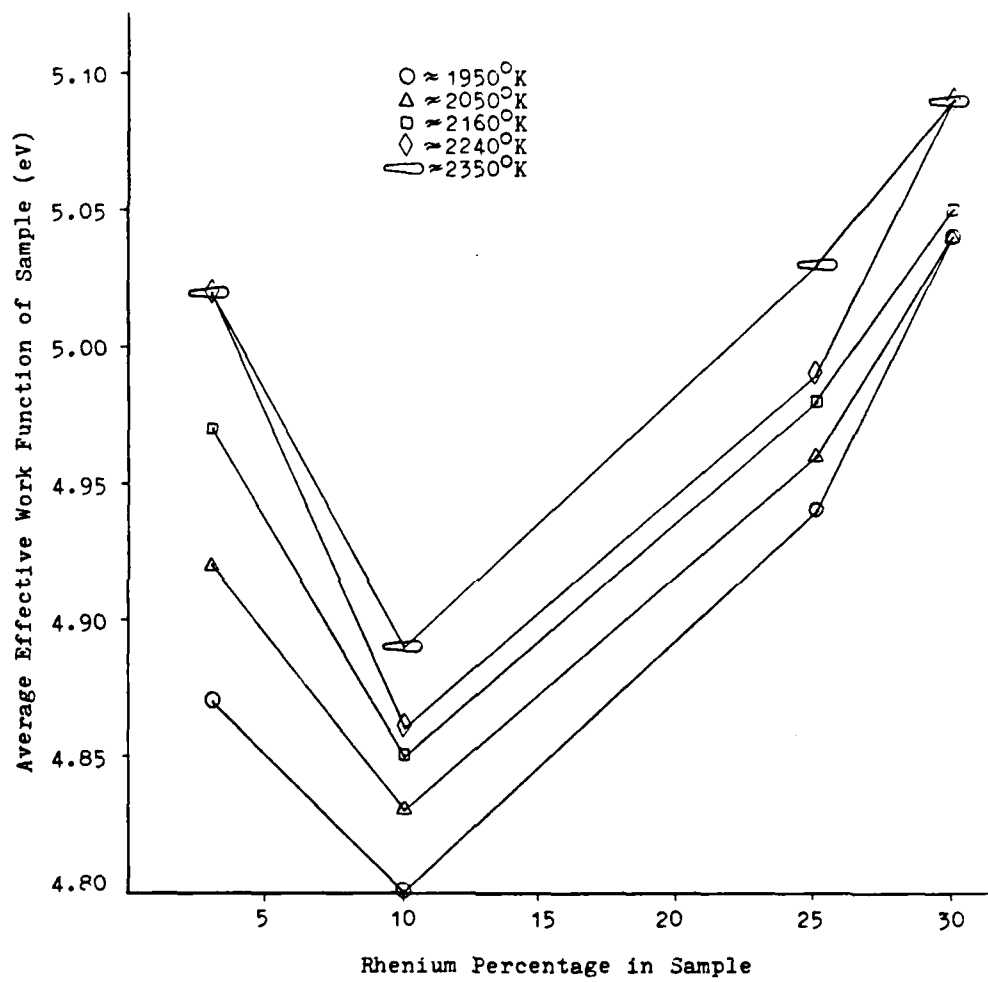


Figure 5.6 - Variation of  $\overline{\phi_e}$  With Alloy Composition

### 5.3 Discussion

From the tables and figures presented in the previous section, it can be seen that the general trend is of increasing values of effective work function with increasing temperatures. Hatsopoulos and Gyftopoulos [5] introduce a relation which presents  $\phi$  as a function of temperature. In this case, the results would fit the equation with a positive temperature coefficient (slope), and the work function could be calculated theoretically if its value at absolute zero was known. The above reference shows the temperature coefficients of tungsten and rhenium to be  $5.1701 \times 10^{-5}$  and  $3.4467 \times 10^{-5}$  respectively.

Grain sizes were observed to decrease on the average with increasing rhenium content. Various elements behave in different ways, but in this case, it seems that adding the alloying element, rhenium, to tungsten, inhibits grain growth in the lattice. This is probably due to the strain that the rhenium atoms introduce in the structure by migrating to grain boundaries and hindering their motion.

In general, it can be deduced from the results that the average effective work function increases with low and high rhenium concentrations exhibiting a minimum at 10% Re. This result was expected as the effective work function of polycrystalline rhenium is higher (4.9eV) than that of polycrystalline tungsten (4.5eV). The effective work

functions of selected orientations, though, are quite different such as 5.00eV for (110) tungsten and 5.51eV for (0001) Rhenium. Sample II of W,10%Re though, has a lower effective work function on the average than Sample I which has only 3% rhenium. Other researchers [8] reported a similar drop in the effective work function. Another phenomenon is the relatively high effective work function calculated for Sample IV of W,30%Re, considering the  $\phi_e$  of the polycrystalline elements present in the alloy.

In order to explain some of the problems faced when measuring various parameters under the conditions presented in this work, they will be divided into three categories.

1. Instrumentation: The accuracies of some instruments were given at the beginning of the chapter from which an experimental error for the effective work function of  $\pm 0.04\text{eV}$  was calculated. Other aspects of instrument limitations are the fluctuations in the output of the power supplies which caused fluctuations in sample temperature, sample voltage, accelerating voltage and decelerating voltage. The digital electrometer being such a sensitive instrument also suffered from small variations in emission current readings.

2. High Temperature Phenomena: At high temperatures (2400K and above) the system was not stable. This fact was deduced from the large fluctuations of the electrometer and the poor image on the phosphor screen. At high temperatures there are grooves formed on the surfaces where grain boundaries intersect the specimen surface. This phenomenon is called thermal grooving, and it exposes a larger array of crystallographic orientations which may alter the calculated average effective work function. A third aspect is that of electron cooling of the sample surface. This phenomenon produces a temperature gradient between the surface and the bulk of the material which causes inaccuracies in work function calculations.

3. Sample Preparation: As can be seen from Table 5.2, Samples I and II, with 3%Re and 10%Re respectively, are not homogeneous. This can cause large differences in electron emission from one area of the sample to another. The samples exhibited irregular surfaces even after a mirror polish; probably due to the sintering process. Surface irregularities cause distortions as they can behave

like diverging or converging lenses. Impurities are the last aspect of sample preparation which have a marked influence on the value of the effective work function of the sample in question. Some impurities have lower work functions than the base material such as  $W_2C$  and WC with 2.60eV and 3.60eV, respectively. Some impurities have higher work functions than the base materials such as  $WO_2$  with 4.96eV.

## Chapter 6

### CONCLUSIONS AND RECOMMENDATIONS

#### 6.1 Conclusions

The electron emission results presented in the previous chapter were for the most part in agreement with the expectations and with previous studies done on similar alloys. Jacobson [8] reported the values of tungsten with 5% and 15% rhenium to have effective work functions of 4.87eV at 1953K and 4.80eV at 2053K, respectively. The correlation between the effective work function and both sample composition and temperature was determined. The trend was of increasing effective work function at low and high rhenium concentrations with a minimum at 10% Re, and increasing effective work function with increasing sample temperature.

The alloying element, rhenium, proved indeed to enhance the effective work function of tungsten and the thermionic emission microscope was an excellent tool for a quantitative evaluation of this material characteristic.

If the alloying element does produce a material which is easier to fabricate and more ductile with higher resistance to creep and recrystallization and with a high stable work function, the alloy should be considered as an alternative to processes such as single crystal production.

## 6.2 Recommendations

Additional studies should be done on the samples tested with the vacuum emission vehicle in order to compare to the results obtained here with the emission microscope. Additional alloys with different percentages of rhenium should also be tested in order to study the effective work function variation with composition, and to determine if the minimum observed at 10% Re is consistent. The increase in the effective work function with decreasing composition below 10% should be researched further in order to understand the phenomenon.

Some modifications to the thermionic emission microscope should be made in future experimental work in order to tip the scale in favor of pure research.

The existing phosphor screen is deteriorating. Three new screens were recoated; two with the same type of material as the existing screen and one with type P-20 electronic phosphor. It is advisable to replace the existing screen and try both kinds of coatings available.

A leak was detected in the welded bellows assembly of the Faraday cage. A new welded bellows was designed and manufactured. The old bellows should be replaced before any further testing and would definitely improve the vacuum in the system.

A new sample holder should be designed for better alignment of the sample surface. If possible, two sample holders should be manufactured in order to shorten sample replacement time.

Vacuum near the hot sample is measured by the nude ionization gauge to be one order of magnitude higher than that measured by the pump power supply. This can be corrected by the use of another Vac-Ion pump attached closer to the sample. Assuming no leaks, this would be an extreme improvement and would solve problems such as electrical breakdown.

An aluminum enclosure similar to the one built for the microscope should be built for the Vac-Ion pump. This would help degas the walls of the pump and improve the vacuum.

## REFERENCES

- (1) S. W. Angrist, "Direct Energy Conversion," Allyn and Bacon, Inc., Boston, 1976.
- (2) V. D. Booth, "Physical and Mechanical Properties of Tungsten and Tungsten Base Alloys," DMIC Report 127, 1960.
- (3) E. Eichen, "Thermionic Emission Microscopy," Metallurgical Society Conference, 1965, V. 38, pp. 167-216.
- (4) W. L. Grube and S. R. Rouse, "Thermionic Emission Microscopy - Applications," Metallurgical Society Conferences, 1965, V. 38, pp. 313-345.
- (5) G. N. Hatsopoulos and E. P. Gyftopoulos, "Thermionic Energy Conversion," The MIT Press, Cambridge, Massachusetts, 1979, V. I and II.
- (6) E. B. Hensley, "Thermionic Emission Constants and Their Interpretation," Journal of Applied Physics, November 2, 1961, V. 32.
- (7) D. L. Jacobson, "Thermionic Research and Development Program," EOS Final Report 7118, 1968, pp. 36-59.
- (8) D. L. Jacobson, "Emission Characteristics of Some Dilute Tungsten Alloys," Metallurgical Transactions, 1972, V. 3, pp. 1263-1268.
- (9) D. L. Jacobson and A. E. Campbell, "Effective Work Function Determinations of Rhenium and Molybdenum," IEEE Conference Record of 1968, Thermionic Conversion Specialist Conference, October 21-23, 1968, pp. 1-9.
- (10) D. L. Jacobson and A. E. Campbell, "Molybdenum Work Function Determined by Electron Emission Microscopy Transactions," 1971, V. 2, pp. 3063-3066.
- (11) J. E. Jaskie, "Thermionic Emission and Surface Composition of the Lanthanum - Boron and Yttrium-Boron Systems," Arizona State University, 1981.
- (12) C. V. Landrith, "Thermionic Emission Microscopy of Polycrystalline Molybdenum," M. S. Thesis, Arizona State University, 1982.

## REFERENCES (continued)

- (13) Leybold and Heraeus, "Product and Vacuum Technology Reference Book."
- (14) W. R. Martini, "Energy Conversion in the Long Run," 13th IECEC, 1978.
- (15) J. F. Morris, "High Power Densities from High-Temperature Material Interactions," AIAA 16th Thermophysics Conference, 1981.
- (16) J. F. Morris, "Space Nuclear-Reaction Questions," 18th IECEC, August 21-26, 1983.
- (17) Raser Associates, Inc., "Advanced Thermionic Energy Conversion," July - September, 1979.
- (18) R. E. Reed-Hill, "Physical Metallurgy Principles," 1973, 2nd edition.
- (19) G. D. Rieck, "Tungsten and Its Components," Pergamon Press, 1967.
- (20) E. M. Savitskii, M. A. Tylkina, and K. B. Povarova, "Rhenium Alloys," Israel Program for Scientific Translation, Ltd., 1970.
- (21) A. Subramanian, "Thermionic Emission Microscopy of Mo - La CrO<sub>3</sub> and LaB<sub>6</sub>," M. S. Thesis, Arizona State University, 1984.
- (22) J. D. Verhoeven, "Fundamentals of Physical Metallurgy," John Wiley and Sons, 1975.
- (23) S. W. H. Yih and C. T. Wang, "Tungsten - Sources, Metallurgy, Properties and Applications," Plenum Press, N.Y. and London, 1979.

**SECTION 4**

**INVESTIGATION OF SINTERED TUNGSTEN, RHENIUM ADDITIVE  
ALLOYS FOR HIGH TEMPERATURE SPACE APPLICATIONS**

3 1 2 3 4

5 6 7 8 9

10 11 12 13

14 15 16 17

18 19 20 21

22 23 24 25

26 27 28 29

30 31 32 33

34 35 36 37

38 39 40 41

42 43 44 45

## ABSTRACT

In the quest to obtain enhanced bare work functions and increase their utility for thermionic energy conversion in future space applications, four tungsten, rhenium alloys (W-3%Re, W-10%Re, W-25%Re, W-30%Re) were tested and found to have effective work functions of  $4.87 \pm 0.04\text{eV.}$ ,  $4.80 \pm 0.04\text{eV.}$ ,  $4.94 \pm 0.04\text{eV.}$  and  $5.04 \pm 0.04\text{eV.}$ , respectively at an operating temperature of 1950 K. Tests were conducted at progressively increasing temperatures up to 2350 K and the effective work functions were found to increase uniformly with temperature. The effect of adding 1%  $\text{ThO}_2$ , to each one of the above mentioned alloys (W, W-10%Re, W-25%Re, W-30%Re) was to marginally increase the work functions to  $4.83 \pm 0.04\text{eV.}$ ,  $4.82 \pm 0.04\text{eV.}$ ,  $4.96 \pm 0.04\text{eV.}$  and  $5.06 \pm 0.04\text{eV.}$ , respectively. The work functions exhibited trends similar to that of the W,Re alloys, with increase in temperature and rhenium content.

Normal spectral emissivities of W, W-3%Re, W-25%Re and W-30%Re were evaluated with a sophisticated photon counting pyrometer. At 1400 K these alloys were found to have emissivities of 0.599, 0.521, 0.476 and 0.610 respectively and in each case the values decreased with increase in operating temperature. W,25%Re had the lowest and most stable values in the range of temperatures (1400 K to 2500 K) tested. The thoriated samples exhibited the same behavior as the W, Re samples but were observed to be more stable. At 1420 K these alloys were found to have emissivities of the order of 0.525, 0.449, 0.410, 0.422 and 0.473, which were generally lower and better suited for TEC application.

The one-hour recrystallization temperature for pure sintered W was determined to be 1650 K whereas that for the other W,Re alloys was about 1850 K. The recrystallized grain sizes for the four samples with increasing rhenium content, were 62  $\mu\text{m}$ , 51  $\mu\text{m}$ , 32  $\mu\text{m}$  and 34  $\mu\text{m}$  respectively. Addition of 1% thoria increased the recrystallization temperature of W, to 1810 K and that of W,25Re to 2100 K. The alloys were found to have coarse as well as fine thoria particles distributed in them.

A high temperature, high vacuum mechanical testing system was designed, fabricated and installed to determine elevated temperature tensile properties for the W,Re and W,Re, $\text{ThO}_2$ , samples. Due to fabrication and instrumentation problems, the tests could not be completed. However, the expected results are discussed.

## TABLE OF CONTENTS

	Page
<b>LIST OF TABLES .....</b>	<b>x</b>
<b>LIST OF FIGURES .....</b>	<b>xi</b>
<b>NOMENCLATURE .....</b>	<b>xv</b>
<b>1. INTRODUCTION .....</b>	<b>1</b>
1.1 Projected space requirements for high temperature materials .....	1
1.2 Characteristics of ultimate space materials .....	2
1.2.1 The primary components tungsten and rhenium .....	4
1.2.2 The additive thoria .....	5
1.3 Proposed research on tungsten, rhenium additive alloys .....	8
1.3.1 Scientific approach and merits of the proposed research .....	9
<b>2. THERMIONIC EMISSION CHARACTERISTICS OF W,Re AND THORIATED W,Re ALLOYS .....</b>	<b>11</b>
2.1 Fundamentals of thermionic emission microscopy .....	11
2.1.1 Thermionic emission and work function .....	12
2.1.2 Work function evaluation with the thermionic emission microscope .....	14
2.1.3 Objectives of the research on thermionic emission .....	14
2.2 Literature survey .....	15
2.3 Material characterization and sample preparation .....	17
2.3.1 Mass spectrometer analysis, electron microprobe analysis and x-ray spectrometer analysis .....	18
2.3.2 Thermionic emission sample preparation, fabrication and mounting .....	22
2.4 Description of apparatus used .....	24
2.4.1 The vacuum system .....	26
2.4.2 The sample heating system .....	26
2.4.3 Thermionic emission and collection .....	26
2.4.3.1 Electrical schematic and potential distribution .....	27
2.4.3.2 Sample voltage and decelerating voltage for saturated emission .....	27
2.4.3.3 Faraday cage assembly and modifications ...	30
2.4.4 Temperature measurement system .....	32
2.4.4.1 Optical pyrometer calibration .....	32
2.5 Experimental procedure .....	36
2.5.1 Vacuum annealing for grain size stability .....	36
2.5.2 Measurements for work function evaluation .....	38

TABLE OF CONTENTS (Continued)

	Page
2.6 Results and discussion .....	39
2.6.1 Effective work functions of W,Re alloys .....	39
2.6.2 Effective work functions of thoriated W,Re alloys .....	55
<b>3. EFFECT OF TEMPERATURE ON THE EMISSIVITY OF W,Re AND THORIATED W,Re ALLOYS .....</b>	<b>63</b>
3.1 Introduction to elevated temperature emissivity measurement .....	63
3.1.1 Theory of operation of the photon counting pyrometer .....	66
3.1.2 Temperature and emissivity evaluation .....	68
3.1.3 Primary objectives on emissivity evaluation .....	70
3.2 Sample characterization and preparation .....	70
3.2.1 Electron microprobe analysis .....	70
3.2.2 Sample fabrication and mounting details .....	72
3.3 Experimental set up for emissivity measurement .....	72
3.3.1 The vacuum and electron bombardment systems .....	75
3.3.2 Temperature measurement with the photon counter ...	75
3.4 Operating procedure .....	77
3.5 Results and discussion .....	80
3.5.1 Variation of normal spectral emissivity with temperature and rhenium content .....	83
3.5.2 Effect of alloying sintered W,Re with thoria .....	87
<b>4. RECRYSTALLIZATION AND GRAIN GROWTH CHARACTERISTICS OF SINTERED W,Re AND THORIATED W,Re ALLOYS .....</b>	<b>91</b>
4.1 A brief introduction to elevated temperature softening .....	91
4.2 Literature review .....	92
4.3 Experimental set up for vacuum annealing .....	94
4.3.1 Sample preparation and associated metallography .....	96
4.3.2 Vacuum annealing of specimen .....	96
4.4 Results and discussion .....	97
4.4.1 Variation of microhardness of tungsten with elevated temperature and rhenium content .....	100
4.4.2 Recrystallization and grain growth of sintered tungsten, rhenium .....	104
4.4.3 Variation of microhardness of thoriated tungsten, with elevated temperature and rhenium content ....	107
4.4.4 Recrystallization and grain growth of thoriated tungsten, rhenium .....	110

TABLE OF CONTENTS (Continued)

	Page
5. HIGH TEMPERATURE, HIGH VACUUM MECHANICAL TESTING OF W,Re AND W,Re,ThO <sub>2</sub> ALLOYS .....	117
5.1 High temperature mechanical testing .....	118
5.1.1 Mechanical properties in elevated temperature tensile testing .....	118
5.1.2 Objectives of the research on tensile testing .....	119
5.2 Literature survey on elevated temperature testing of refractory materials .....	120
5.3 Design and fabrication of the high temperature, high vacuum tensile stages .....	123
5.3.1 The external stage .....	123
5.3.2 The internal stage .....	129
5.3.3 Fabrication and preparation of the tensile test specimen .....	132
5.4 General instrumentation .....	134
5.4.1 The ion pump vacuum system .....	134
5.4.2 The sample heating system .....	137
5.4.3 The temperature measurement system .....	138
5.4.3.1 Calibration of photon counter and optical pyrometer .....	138
5.5 Experimental procedure .....	140
5.6 Results and discussion .....	142
6. FACILITY DEVELOPMENT .....	150
7. GENERAL CONCLUSIONS .....	154
8. RECOMMENDATIONS FOR FUTURE RESEARCH ACTIVITY .....	157
REFERENCES .....	160
Appendix-1 Details of the components of the system for thermionic emission microscopy .....	165
Appendix-2 Some technical data on the thermionic emission microscope .....	166
Appendix-3 Details of the various components of the emissivity measurement system .....	167

LIST OF TABLES

Table		Page
1	Department of Defense potential high power requirements .....	3
2	List of high melting, low vaporizing materials .....	3
3	Mass spectrometer analysis of the powders used in preparing W,Re alloys .....	19
4	Results of electron microprobe analysis .....	19
5	Emission results for W,3% Re and W,10% Re samples .....	40
6	Emission results for W,25% Re and W,30% Re samples .....	41
7	Emission results for W,1% ThO <sub>2</sub> and W,10% Re, 1% ThO <sub>2</sub> samples .....	42
8	Emission results for W,25% Re, 1% ThO <sub>2</sub> , and W,30% Re, 1% ThO <sub>2</sub> samples .....	43
9	Constant parameters in evaluating emissivity .....	71
10	Results of electron microprobe analysis (emissivity studies) .....	71
11	Typical power supply ranges to heat the sample to various temperatures .....	79
12	Temperatures of hohlraum and surface and emissivity values ..	81
13	Temperatures of hohlraum and surface and emissivity values for thoriated tungsten, rhenium .....	82
14	Specimen temperature and microhardness values for tungsten, rhenium .....	98
15	Specimen temperature and microhardness values for thoriated tungsten, rhenium .....	99
16	Mechanical properties in conventional mechanical testing ....	124
17	Important properties of Inconel 750X and ceramic AD-998 .....	133
18	High temperature tensile properties of W,Re,ThO <sub>2</sub> alloys [60] .....	145
19	High temperature tensile properties of other solid-solution alloys of interest .....	147

LIST OF FIGURES

Figure	Page
1 Stability relationships of refractory oxides .....	7
2 Change in microstructure of a pure tungsten filament heated by alternating current .....	7
3 Operating principle of a thermionic energy converter .....	13
4 Schematic view of the potential field of metal .....	13
5 Output for chemical analysis by x-ray spectrometry of pure tungsten .....	20
6 Output for chemical analysis by x-ray spectrometry of tungsten, 10% rhenium .....	20
7 Output for chemical analysis by x-ray spectrometry of tungsten, 25% rhenium .....	21
8 Output for chemical analysis by x-ray spectrometry of tungsten, 30% rhenium .....	21
9 Details of electrical discharge machining .....	23
10 Emitter assembly with sample and filament .....	23
11 Experimental layout for thermionic emission .....	25
12 Block diagram for the movement of electrons .....	28
13 Electrical schematic for thermionic emission .....	28
14 Potential distribution along the longitudinal axis of the microscope .....	29
15 Variation of emission current with sample voltage .....	31
16 Variation of emission current with decelerating voltage .....	31
17 Components of the Faraday cage assembly .....	33
18 Complete assembly with bellows system and feedthroughs .....	34
19 Temperature measurement with the optical pyrometer .....	35
20 Electrical circuits for pyrometer calibration .....	35

LIST OF FIGURES (Continued)

Figure		Page
21	Plot of actual temperature versus measured temperature .....	37
22	Grain growth history for W,3% Re and W,10% Re samples .....	44
23	Grain growth history for W,25% Re and W,30% Re samples .....	45
24	Summary of work function measurements for W,3% Re .....	47
25	Summary of work function measurements for W,10% Re .....	48
26	Summary of work function measurements for W,25%Re .....	49
27	Summary of work function measurements for W,30% Re .....	50
28	Variation of average effective work function with sample temperature .....	51
29	Variation of work function parameter with rhenium content ...	53
30	Variation of average effective work function with rhenium content .....	54
31	Summary of work function measurements for W,1% ThO <sub>2</sub> .....	56
32	Summary of work function measurements for W,10% Re, 1% ThO <sub>2</sub> .....	57
33	Summary of work function measurements for W,25% Re, 1% ThO <sub>2</sub> .....	58
34	Summary of work function measurments for W,30% Re, 1% ThO <sub>2</sub> .....	59
35	Variation of average effective work function with sample temperature, for thoriated W,Re .....	60
36	Variation of average effective work function with rhenium content for thoriated W,Re .....	62
37	Schematic of the photon counting pyrometer .....	67
38	The photon counting pyrometer .....	67
39	Cross section of the sample assembly .....	73
40	Steel frame to support sample holder, with filament assembly .....	73

LIST OF FIGURES (Continued)

Figure		Page
41	Schematic of the experimental set up for emissivity measurement .....	74
42	High voltage power supply for electron bombardment .....	76
43	Sample being heated in the bell jar .....	76
44	Temperature measurement using photon counter .....	78
45	Printer, timer-counter and discriminator controls for the photon counter .....	78
46	Variation of spectral emissivity of tungsten, rhenium at elevated temperatures .....	84
47	Variation of spectral emissivity of tungsten with the addition of rhenium .....	86
48	Variation of spectral emissivity of thoriated tungsten, rhenium at elevated temperatures .....	88
49	Variation of spectral emissivity of thoriated tungsten, with the addition of rhenium .....	89
50	Experimental set up for recrystallization studies .....	95
51	Effect of elevated temperatures on the microhardness of tungsten, rhenium .....	101
52	Variation of microhardness of tungsten with the addition of rhenium .....	103
53	Microstructures of recrystallized W,25at.% Re and W,30at.% Re samples after annealing at the temperatures indicated .....	105
54	Microstructures of the different samples after annealing for 1 hour at 2500°K .....	106
55	Recrystallization effects of alloying tungsten with rhenium .....	108
56	Effect of elevated temperatures on the microhardness of thoriated tungsten, rhenium .....	109
57	Variation of the microhardness of thoriated tungsten with the addition of rhenium .....	111

LIST OF FIGURES (Continued)

Figure		Page
58	Microstructures of recrystallized W,25% Re, 1% ThO <sub>2</sub> and W,30% Re, 1% ThO <sub>2</sub> samples after annealing .....	113
59	Microstructures of different thoriated samples after annealing for one hour at 2500 K .....	114
60	Recrystallization effects of alloying tungsten with rhenium and thoria .....	116
61	The high temperature, high vacuum tensile testing system ....	124
62	Experimental layout for high temperature mechanical testing .....	125
63	The external part of the high temperature stage .....	126
64	Parts of the external heating stage .....	127
65	Other parts of the external heating stage .....	128
66	Partial cross sectional view of the internal stage .....	130
67	The various parts of the internal stage and their assembly ..	131
68	Configuration of tensile test specimen .....	135
69	Fixture for holding the specimen in the EDM .....	135
70	Electrical schematic for electropolishing .....	136
71	Finished product ready for testing .....	136
72	Calibration of photon counter/optical pyrometer .....	139
73	Various steps involved in the fabrication of the tensile test specimen .....	143
74	Stages at which the samples failed during fabrication .....	143
75	Schematic of the zone refining system components .....	151
76	The zone refining system with power supply .....	152
77	The zone refining chamber with the electron gun .....	153

## NOMENCLATURE

e - Energy of an ejected electron  
 $e_{\lambda b}$  - Emissive power  
f - Volume fraction of thoria particles  
 $f(e)$  - Fermi function  
h - Planck's constant  
k - Boltzmann constant  
 $r_t$  - Radius of thoria particles  
A - Attenuation factor  
 $A_1$  - Constant in R-D equation ( $120 \text{ Amps/cm}^2\text{K}^2$ )  
 $A_c$  - Area of aperture at the centre of the collecting plane  
 $C_1$  - Planck's first constant  
 $C_2$  - Planck's second constant  
E - Energy level of a given energy state  
 $E_c$  - Corrected count rate  
 $E_f$  - Fermi energy  
 $E_h$  - Observed count rate of hohlraum at  $T_h$   
 $E_{hc}$  - Corrected count rate of hohlraum at  $T_h$   
 $E_n$  - Count rate after 'n' filters  
 $E_o$  - Count rate at temperature  $T_o$   
 $E_s$  - Observed count rate of surface at  $T_s$   
 $E_{sc}$  - Corrected count rate of surface at  $T_s$   
I - Current measured by the electrometer  
 $J_o$  - Current density

## NOMENCLATURE (Continued)

$K_{max}$  - Maximum available energy of ejected electron  
 $M$  - Magnification  
 $P$  - Work function parameter  
 $R_e$  - Limiting grain size  
 $T$  - Absolute temperature in K  
 $T_h$  - Absolute temperature of hohlraum  
 $T_o$  - Melting point of copper  
 $T_s$  - Temperature of surface  
 $V$  - Finite value of potential outside the metal  
 $\alpha$  - Contact angle of second phase particles  
 $\epsilon$  - Emissivity  
 $\epsilon_\lambda^1$  - Normal spectral emissivity  
 $\gamma$  - Dead time of counter circuits  
 $\lambda$  - Wavelength of thermal radiation  
 $v$  - Frequency of light waves  
 $\phi$  - Work function of parent metal.  
 $\phi_e$  - Effective work function  
 $\sigma_e$  - Effective stress component of the flow stress  
 $\sigma_i$  - Internal stress component of the flow stress

## 1. INTRODUCTION

There are a variety of potential missions, such as space based manufacturing, high capacity communications, outer planetary orbiters and lunar and planetary bases that appear to demand compact high power, very long life power units which are independent of sunlight. In general, the most intensive energy processing in any spacecraft occurs in the source and conversion systems for primary space power. There, higher temperatures translate into less weight, greater capability and increased mobility essential, particularly in military missions.

### 1.1 Projected space requirements for high temperature materials

Cohen [11] presents a tabulation of potential high power requirements for the U.S. national defense. For space based systems, high power levels must be achieved at significantly higher values of specific power (W/kg) and energy (W-Hr/Kg) than are presently available to satisfy defense needs for survivability. Table 1 gives a list of the potential high power requirements.

The Soviet development of Space Nuclear Reactors [39] (SNR's) aims at military goals. The USSR-SNR program is aimed at achieving prime power sources at Megawatt levels and beyond and quite obviously the US-SNR program is also expected to follow suit and develop these high energy source systems for defense utilization. Development of these high temperature, high power space energy conversion systems would definitely pose critical material problems.

Accordingly, ultimate alloys are extremely important and almost mandatory for future orbital power systems technology requirements [43].

If there is a single general trend that applies to the various combinations of heat sources and conversion methods, it is the one toward higher source temperature and higher sink temperature and consequently lighter weight systems. Higher sources and sink temperatures means developing materials with superior properties at high temperatures and for this, high temperature materials data is of prime importance. This emphasizes anticipating and solving material problems for high temperature space applications.

### 1.2 Characteristics of ultimate space materials

At high temperatures, ceramic materials become more electrically conductive and this precludes their effective use to transfer heat to energy converters while blocking electric transport. Even when solid insulators function adequately at high temperatures, their comparative mechanical intransigence limits the fabricability and service adaptability. Thus refractory alloys must in general accommodate ceramics as well as themselves to system fabrication and service requirements. However, refractory alloys suffer from ductility deficiencies and recrystallization effects. Other complications arise from intensified influences of high temperatures and hard vacuum on strength, creep, diffusion, segregation, chemical reaction, vaporization and other thermophysical phenomena.

To start with we can examine the highest melting, least vaporizing metals listed in Table 2.

Table 1. Department of Defense potential high power requirements.

APPLICATIONS	POWER LEVEL
SPACE-BASED RADARS	5 TO 400 KW
SURVEILLANCE	30 TO 100 KW
COMMUNICATIONS	100 KW
OTV (NEP)	>100 KW
JAMMERS	70 TO 200 KW
LASERS	10 TO 100 MW PULSED
PARTICLE BEAMS	10 TO 100'S MW PULSED
ADVANCED CONCEPTS	1 TO 100'S MW PULSED

Table 2. List of high melting, low vaporizing materials.

ATOMIC NUMBER	MATERIAL (SYMBOL)	APPROXIMATE MELTING POINT, °K	APPROXIMATE VAPOR PRESSURE AT 2000°K, TORR
40	ZIRCONIUM (Zr)	2130	$2 \times 10^{-6}$
41	NIOBIUM (Nb)	2760	$5 \times 10^{-9}$
42	MOLYBDENUM (Mo)	2890	$2 \times 10^{-7}$
43	TECHNETIUM (Tc)	2400	$3 \times 10^{-6}$
44	RUTHENIUM (Ru)	2700	$1 \times 10^{-6}$
72	HAFNIUM (Hf)	2400	$2 \times 10^{-6}$
73	TANTALUM (Ta)	3270	$5 \times 10^{-11}$
74	TUNGSTEN (W)	3640	$4 \times 10^{-12}$
75	RHENIUM (Re)	3450	$1 \times 10^{-10}$
76	OSMIUM (Re)	3320	$< 3 \times 10^{-10}$
77	IRIDIUM (Ir)	2720	$2 \times 10^{-7}$
90	THORIUM (Th)	1960	$3 \times 10^{-6}$
	ALUMINA ( $\text{Al}_2\text{O}_3$ )	2320	$6 \times 10^{-6}$
	THORIA ( $\text{ThO}_2$ )	3490	APPROXIMATELY EQUAL "HIGHEST OF THE OXIDES" TO THAT OF MOLYBDENUM
	HAFNIUM CARBIDE (HfC)	4120	OVER TWO ORDERS OF MAGNITUDE LOWER THAN THAT OF MOLYBDENUM, NEARLY FOUR WITH EXCESS CARBON

### 1.2.1 The primary components tungsten and rhenium

Tungsten is the most refractory metal. It is a body centered cubic element with a 2000 K vapor pressure of  $4 \times 10^{-12}$  torr and a melting point of 3683 K. Its ductile to brittle transition occurs well above room temperature and it begins to recrystallize below 40% of its melting point which further complicates manufacturing and service. Even today, brittleness and difficult fabricability often overshadow the peerless high temperature properties of tungsten.

Rhenium, another refractory element is a metal whose strength apparently is the only one among the metals to approach or exceed those of tungsten. It is quite ductile in contrast to tungsten but exhibits extremely high work hardenability with very little deformation, often requiring repeated vacuum annealing during fabrication. However in combination with rhenium, tungsten becomes fabricable, ductile even after welding and improves in resistance to creep and recrystallization. Rhenium has a higher density (21.0 gms/cc) than tungsten (19.3 gms/cc) and a melting point of 3453 K with an atomic radius (1.37A) close to that of tungsten. With a solubility of approximately 26.5%, rhenium is a very interesting solute for tungsten. The fact that rhenium additions in small quantities soften and increase the ductility of tungsten, is attributed to the formation of a complex oxide with appreciable surface tension. This oxide agglomerates into round globules instead of wetting grain boundaries and in the process, gives the alloy high intergranular strength and ductility. This is discussed in detail in a later section.

### 1.2.2 The additive thoria

Interstitial impurities generally tend to diminish ductility, but some of them can produce beneficially dispersed refractory products through reactions with low pressure vapor getters such as thorium and hafnium. Thorium is the best getter for oxygen. The proposal to add thoria to tungsten, rhenium alloys was initiated when it was found that the unactivated thoria had a bare work function of 6.3 eV. and a cesiated work function of 1.0 eV. Great gains in ductility, hot strength and recrystallization resistance for thoria additions to tungsten, rhenium ultralloys have already received attention. Particle dispersions strongly influence mobility of grain boundaries and subboundaries, redistribution of dislocations and other effects that affect the formation of recrystallization nuclei and initial growth. The dispersed particles such as thoria change recrystallization temperatures as complex functions of the size, spacing, concentration, stability and other variables of microstructural interaction. As shown in Figure 1 [35], thoria is a very stable oxide which has a melting point of 3573 K. Thoriated tungsten is generally obtained by flashing a tungsten filament containing 0.5 to 1.5% thoria at a high temperature (2700 K) which reduces some of the oxide to metallic thorium. This is then followed by heating at 2100-2200 K, thus causing diffusion of thorium to the surface where it forms a monatomic layer which possesses much higher electron emission than pure tungsten. At temperatures above 2000 K the thorium evaporates at a rate which exceeds the diffusion to the surface with a resultant decrease in electron emissivity.

The effect of adding thoria to tungsten can be appreciated if one considers the change in microstructure of a pure tungsten filament heated by alternating current, shown in Figure 2 [64]. When large grains extend across the filament, it becomes very brittle and breaks apart under the stresses produced by the thermal expansion on heating and cooling. However, if randomly distributed second phase particles of thoria are doped into the tungsten, the grain growth is limited. As a result, there is a limiting grain size which prevents the failure of tungsten filaments by brittle fracture.

If the volume fraction of thoria particles is "f", the number of particles intercepted by an area of  $1 \text{ cm}^2$  is given by,

$$\text{No. of particles} = 3f/2\pi r_t^2 \quad (1)$$

force restraining grain boundary

$$\text{motion} = 3f\pi r_t Y(1+\cos\alpha) \quad (2)$$

When the force balances the pressure force due to curvature, grain growth stops and a limiting grain size is obtained as

$$R_l = [4r_t/3f(1+\cos\alpha)] \quad (3)$$

This is based on the assumption that the interfaces are spherical of radius  $R_l$ . Thus we see that the limiting grain size depends upon the volume fraction, the radius and the contact angle "a" of the second phase particles.

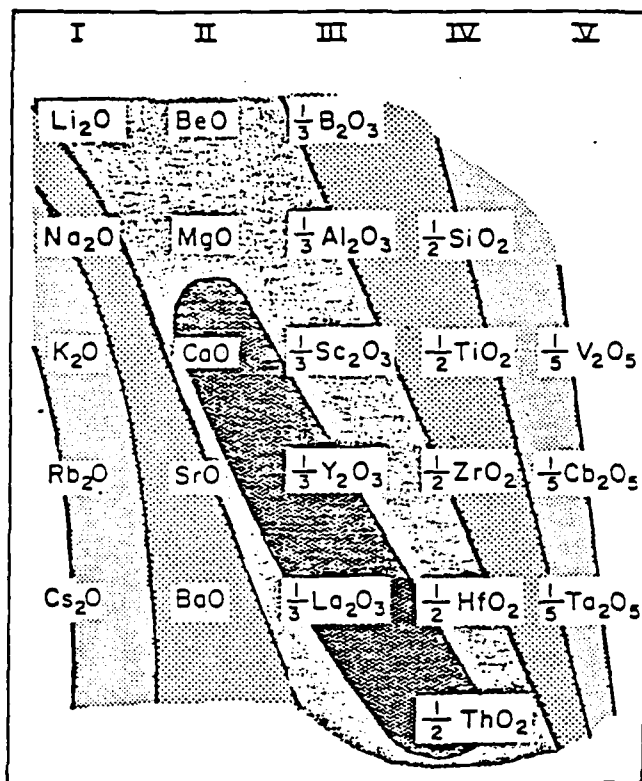


Figure 1. Stability relationships of refractory oxides.

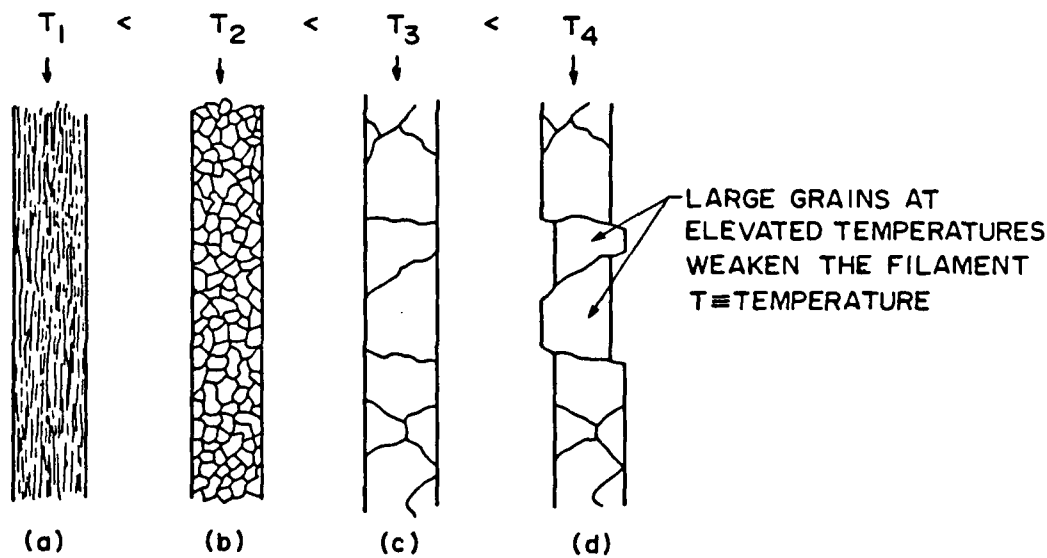


Figure 2. Change in microstructure of a pure tungsten filament heated by alternating current.

### 1.3 Proposed research on tungsten, rhenium additive alloys

It has already been established that rhenium percentages between two and five, at about ten and near twenty-five in tungsten alloys maximizes ductility locally and tungsten, 25% rhenium offers higher creep strength than tungsten to over 1873 K. Additions of thoria and hafnium carbide in the order of 1 and 0.3% respectively, further increase creep strengths, ductilities and recrystallization temperatures of tungsten, rhenium alloys. Thus, parametric evaluations of tungsten with, 3, 10, 25 and 30% rhenium, each in turn modified initially with 1% thoria and later, with 0.3% hafnium carbide, were used as the basis for the research work.

Until 1975, data on pure tungsten, rhenium alloys prepared by powder metallurgy were lacking. But investigators still resorted to powder metallurgy techniques as it was the only practical method of producing tungsten alloys containing a thoria dispersion. Fusion processes such as electron beam melting or arc casting would be beneficial because the impurity concentrations in such alloys are low, but the prohibitive cost and the fact that thoria decomposes at the melting temperature of tungsten and its dilute alloys, prevent them from being used for making tungsten, rhenium, thoria alloys. Further, sintered samples have a small grain size and this reduces recrystallization processes with the surface impurities of oxygen, nitrogen and carbon forming resistance to diffusion and grain growth. As a result, it was decided that sintered tungsten with 3, 10, 25 and 30% rhenium, would be investigated in the thermionic microscope, the emissivity measurement apparatus and the high temperature mechanical

testing facility. This would then be followed up with identical investigations on each of the above mentioned alloys with 1% thoria added to it.

### 1.3.1 Scientific approach and merits of the proposed research

Recrystallization, ductility, mechanical strength, work function, spectral emissivity and compositional stability were some of the characteristics that were considered that were vital to high temperature energy converters. Techniques for producing and sustaining the desired properties were investigated from a microscopic, mechanistic point of view. As there was limited experimental information available for such systems, a baseline system was examined in order to test the experimental models developed. It was proposed to add getters like thorium and hafnium to react with oxygen and carbon and improve high temperature strength, ductility and recrystallization. A better understanding of high temperature thermal, thermionic, mechanical and metallurgical behavior of refractory alloys, was considered crucially essential for overcoming the material problems for high temperature, high power space energy conversion systems.

High temperature phenomena are often only inferred through room temperature observations following high temperature treatment. The present research activity is a real time investigation of high temperature surface characteristics and electron emission to obtain information on complex transport and reaction mechanisms. Some very enlightening information was expected from observing high temperature size and surface composition changes of grains in sintered samples of

tungsten, rhenium with appropriate additions. The primary additive (rhenium) reduces and controls embrittlement and recrystallization. The gettering additive (thorium) affects the base metal ductility and recrystallization by producing very stable oxides and carbides.

## 2. THERMIONIC EMISSION CHARACTERISTICS OF W,Re AND THORIATED W,Re ALLOYS

This section deals with the information on research pertaining to the thermionic emission microscopy of W,Re and thoriated W,Re alloys. The theory of electron emission and work function evaluation is discussed and a sequential procedure for all the research activities involved has been established.

### 2.1 Fundamentals of thermionic emission microscopy

Thermionic emission microscopy is a form of electron microscopy where the specimen itself serves as a source of electrons. Electrons emitted from the surface of a heated flat bulk specimen is focused through a suitable lens system and then projected at a useful magnification onto a fluorescent screen. The result is a metallographic type image of the kind usually associated with optical microscopy. The design and operation of a thermionic emission microscope requires coordination of two physical processes. The first process is electron emission from a specimen, while the second involves the formation of an image with these electrons. The two major characteristics that exemplify the usefulness of the thermionic emission microscope as a research tool are; a) the fact that it represents a magnification range which bridges that between optical microscopy and the more conventional types of electron microscopy, and b) it is more suited to elevated temperature operation than other forms of microscopy. A schematic of the principle of operation of a thermionic energy converter is presented in Figure 3 [44].

### 2.1.1 Thermionic emission and work function.

The Sommerfield model for the behavior of electrons in a metal provides the simplest view of the theory of operation of a thermionic emission microscope. This is indicated schematically in Figure 4 [17]. Here, it can be seen that the potential within the metal is assumed zero while that outside the metal is given some finite value,  $V$ . According to this model, electrons can occupy energy states within the metal up to the level  $E_f$ , the Fermi energy. The probability that a particular state is occupied is given by the Fermi function,

$$f(E) = \{1/\exp[(E-E_f)/kT] + 1\} \quad (4)$$

For  $E < E_f$  and

$$T = 0 \text{ K}, f(E) = [1/(e^{-\infty} + 1)] = [1/1] = 1 \quad (5)$$

This means that all quantum states are occupied at absolute zero while all quantum states at energies greater than  $E_f$  are unoccupied.

The energy difference between the Fermi energy and the potential to infinity outside of the metal is the "work function" ( $\phi$ ) of the metal. Either an electron absorbs a quantum of energy or it does not. The energy  $E$  of a photon is proportional to the frequency of the light or

$$E = h\nu \quad (6)$$

If an electron is given an amount of energy  $h\nu$ , then in order to escape from the metal, it must use up an amount  $e.\phi$  of this energy. The maximum energy an electron can have left after it gets out of the surface is

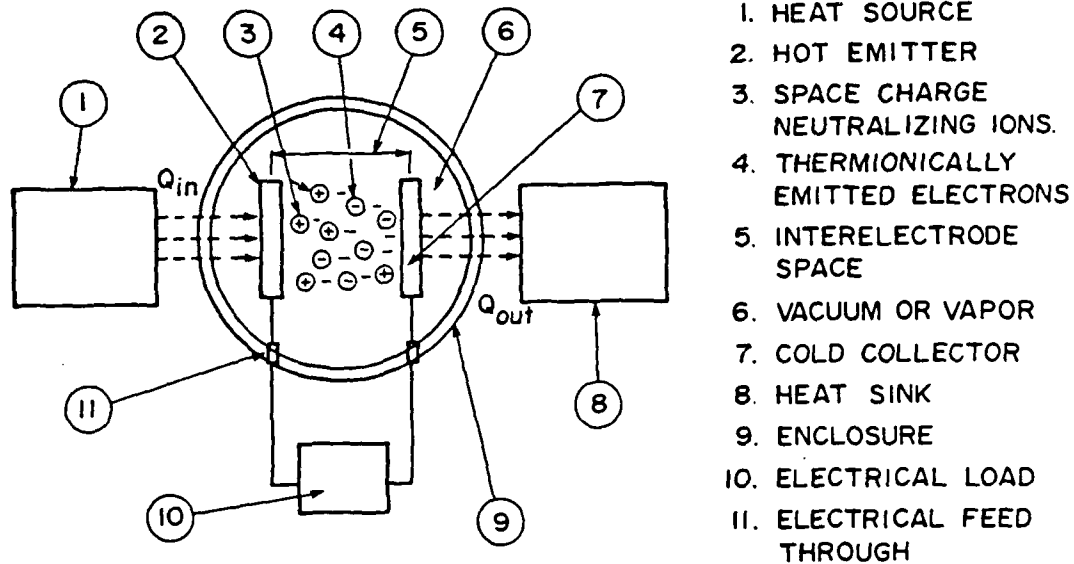


Figure 3. Operating principle of a thermionic energy converter.

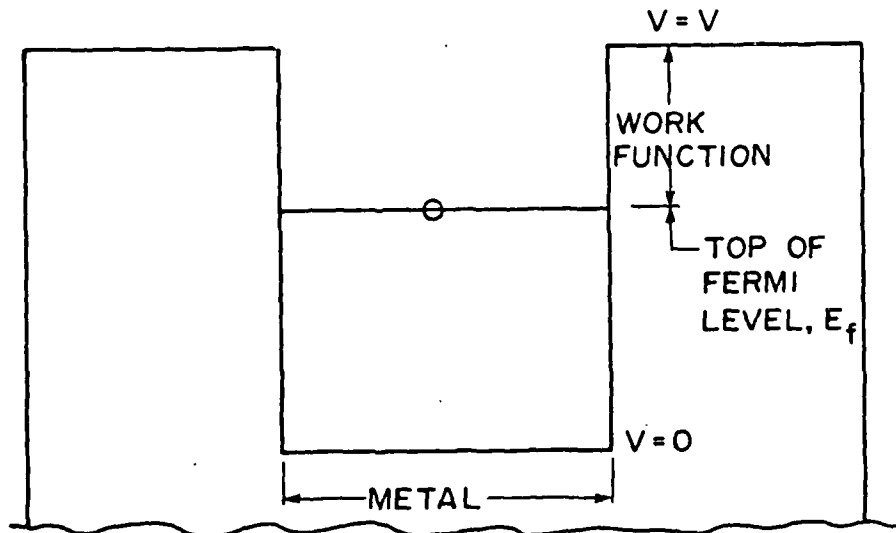


Figure 4. Schematic view of the potential field of metal.

$$K_{\max} = h\nu - e\phi \quad (7)$$

and this surfaces as the kinetic energy of the emerging particle.

### 2.1.2 Work function evaluation with the thermionic emission microscope

The thermionic emission microscope is a device which is used to measure the electron emission from individual grains of a heated sample. Basically, the sample which is heated by the bombardment of electrons from a tungsten filament, gives out electrons from the surface and these electrons are focused on a phosphor screen by the application of a large positive potential difference. The phosphor screen displays the fine grain structure for visual observation and subsequent emission micrograph documentation. Some of the electrons are allowed to pass through a small aperture in the phosphor screen and impinge on a Faraday collector that registers the electron flow in terms of a current flow. The Faraday collector current can then be related to the sample electron current density by the following equation;

$$J_o = [(I.M^2)/A_c] \quad (8)$$

The current density  $J_o$  can then be used to calculate the effective work function ( $\phi_e$ ) from the well known Richardson-Dushman equation,

$$J_o = A_1 T^2 \exp[-\phi_e/kT] \quad (9)$$

### 2.1.3 Objectives of the research on thermionic emission

The objectives of the research on thermionic emission were to:

- a) Fabricate sintered alloys of tungsten with 3at%, 10at%, 25at% and 30at% of rhenium with a diameter of at least 1.00 cms. and a porosity of less than 10 percent.
- b) Perform thermionic emission microscope examinations of the samples in a), above at 1900 to 2500 K in suitable intervals.
- c) For each test,
  - i) Observe grain size, grain growth and document by photographic enlargements.
  - ii) Measure emission of grains in the thermionic microscope and calculate the work function.
  - iii) Perform emission scans of surfaces to determine work function variation from grain to grain.
- d) Repeat a), b) and c) above for each one of the tungsten, rhenium alloys with an addition of 1 percent thoria.

## 2.2 Literature survey

E. Eichen [18] who has spent a considerable amount of time and effort in reviewing the work done on thermionic emission has compiled a list of applications of the thermionic emission microscope. From his compilations it is observed that it is a very useful tool and is capable of doing a lot more than provide work function data of refractory metals and alloys. Evaluation of the work functions of materials using electron emission was compiled by Michaelson [42] who indicated that refractory materials such as rhenium, osmium, iridium etc., had higher work functions than polycrystalline tungsten. However Brown et al. [9] found that different faces of a tungsten single crystal also exhibited work functions ( $4.59 \pm 0.2\text{eV}$ ) that were higher than that of

polycrystalline tungsten (4.50eV). With time, the applications of the technique were extended to phase transformations [19] which included both polymorphic transformations and precipitation from solid solution, in metallic and non-metallic systems. Heidenreich [28] proved that the thermionic emission microscope could be used for the direct observation of transformations in plain carbon steels at temperatures above 900 K.

Sandor [57] directed his efforts toward the conception of a theoretical basis which would permit reconciliation of all the phenomena observed during the thermionic emission microscopy of barium coated polycrystalline nickel. Forgacs [21] and his colleagues developed a temperature recording system for their thermionic emission microscope and with the known temperature of metallurgical phase transformation, determined the accuracy to be  $\pm 5$  K.

Active research, evaluating refractory materials for thermionic energy conversion applications, has been taking place since the late sixties when Savitski et. al. [59] determined the electron work function for different planes of molybdenum single crystals. They observed work functions of  $4.9 \pm 0.07$ eV for the (110) plane and  $4.35 \pm 0.07$ eV. for the (100) plane. Protopov [49] and others measured the work functions of four orientations of a molybdenum single crystal and three orientations of a tantalum single crystal and produced results consistent with former investigations. Jacobson et al. [30, 31, 29, 32, 33] have contributed information on the work functions of various refractory materials which have potential applications in high temperature thermionic energy converters. The (1010) crystallographic orientation of rhenium was found to have an effective work function of 5.26 eV. and (110) single

crystal molybdenum was found to have an effective work function of 4.90 eV. Correlations between the effective work function and crystallographic orientation were developed. Effective work functions of nine tungsten-base alloys were determined, some of which exhibited anomalous emission areas with exceptionally high bare work functions, even though alloying additions were in very small quantities. Lanthanum hexaboride was also tested in the thermionic emission microscope, and produced a work function of  $4.29 \pm 0.04$  eV.

The literature considered so far refer to work function evaluations of individual grains of a refractory metal or alloy in the thermionic emission microscope. However the average work function of the entire surface of a sample can be obtained in a vacuum emission vehicle but in this device, one cannot observe the specimen surface on a fluorescent screen as in the thermionic emission microscope.

### 2.3 Material characterization and sample preparation.

The materials fabricated for testing in the thermionic emission microscope were procured from Rhenium Alloys Inc., Cleveland, Ohio. The tungsten, rhenium alloys with 3%, 10%, 25% and 30% rhenium were sintered from tungsten and rhenium powder. A mass spectrometer spectrographic analysis was carried out before sintering. The alloys were fabricated at a pressure of  $2.07 \times 10^{-8}$  N/m<sup>2</sup> and a temperature of 2500 K. The process was carried out in a reducing atmosphere of ultrapure hydrogen. The furnace used for this purpose had a lining of molybdenum to withstand the high temperature. The rhenium powder was 99.9999% pure and the tungsten powder was of commercial purity.

### 2.3.1 Mass spectrometer analysis, electron microprobe analysis and x-ray spectrometer analysis

In order to check the purity level of the powders constituting the tungsten, rhenium alloys, a mass spectrometer spectrographic analysis was carried out on each of the tungsten and rhenium powders. The results of this analysis is indicated in Table 3. The impurities were all found to be at acceptable levels. The table also indicates the source of this spectrographic analysis.

After the samples were sintered to the desired configuration they were subjected to electron microprobe analysis and a chemical analysis by x-ray spectrometry. A small portion of each sample was observed, at different locations, in the electron microprobe facility in order to check the homogeneity of the as-received material. The results of the analysis, as indicated in Table 4, reveals that the alloys with lower percentages of rhenium were inhomogeneous and suitable measures were being taken to improve the homogeneity on sintering.

The chemical analysis by x-ray spectrometry gave a qualitative measure of the chemical composition of the major constituents. Figures 5 through 8 are typical outputs of the x-ray spectrometer tests representing the various peaks for the various tungsten, rhenium alloys. The chromium peaks are present because a target of chromium was used in the tests.

Table 3. Mass spectrometer analysis of the powders used in preparing W-Re alloys.

	Elements (Spectrographic analysis) ppm												
	Al	Ca	Cr	Cu	Fe	K	Mg	Mn	Mo	Na	Ni	Si	Sn
Tungsten*	<1	<1	<1	<1	4	<10	<1	<1	10	9	4	<1	<1
Rhenium**	-	-	-	<1	8	-	-	-	-	<1	-	-	-

Table 4. Results of electron microprobe analysis.

Alloy	Elements	Concentrations at Difference Positions				
		1	2	3	4	5
W-3%Re	W	.968	.987	.926	.973	.991
	Re	.033	.016	.057	.023	.016
	Total	1.001	1.003	.983	.996	1.007
W-10%Re	W	.874	.888	.814	.880	.855
	Re	.082	.062	.137	.075	.105
	Total	.956	.950	.951	.955	.960
W-25%Re	W	.733	.736	.765	.777	.718
	Re	.255	.253	.213	.252	.260
	Total	.988	.989	.983	1.029	.978
W-30%Re	W	.701	.736	.730	.712	.737
	Re	.280	.250	.266	.269	.246
	Total	.981	.986	.996	.981	.983

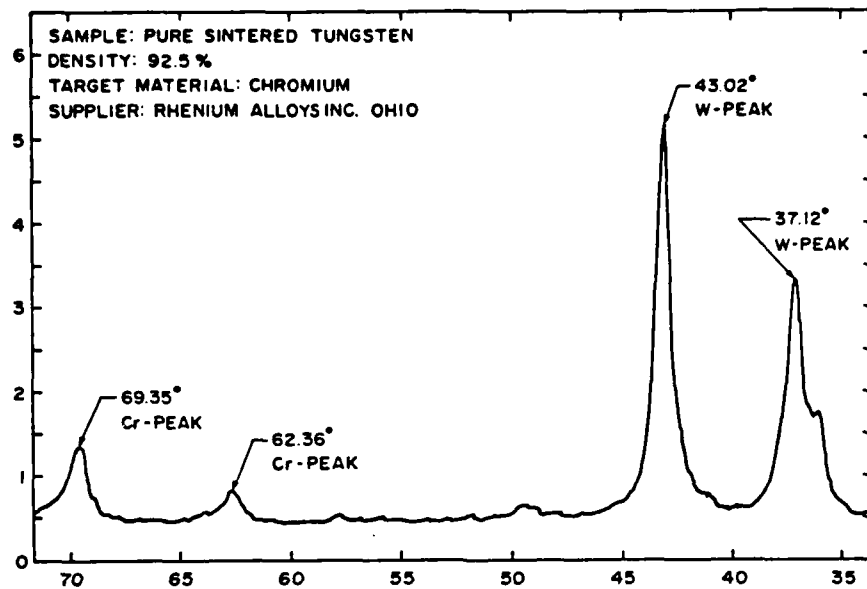


Figure 5. Output for chemical analysis by x-ray spectrometry of pure tungsten.

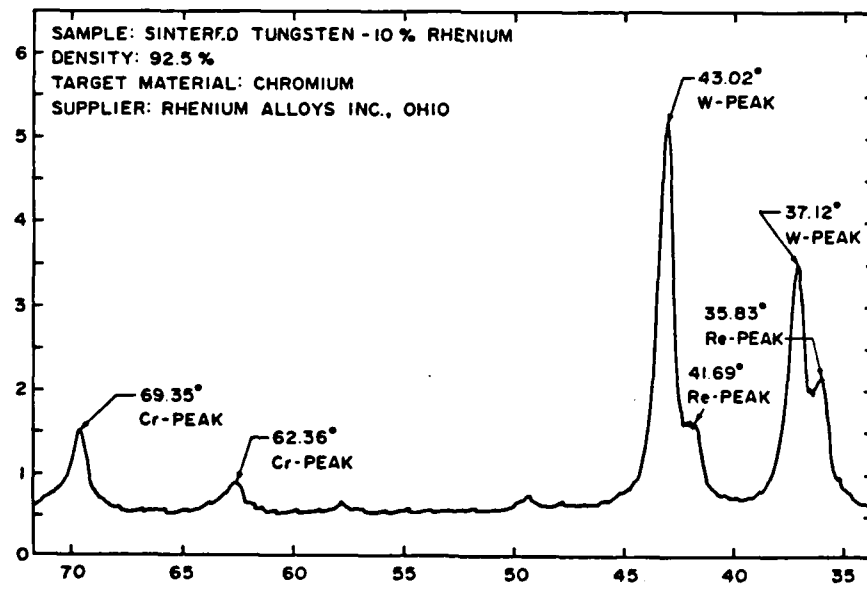


Figure 6. Output for chemical analysis by x-ray spectrometry of tungsten, 10% rhenium.

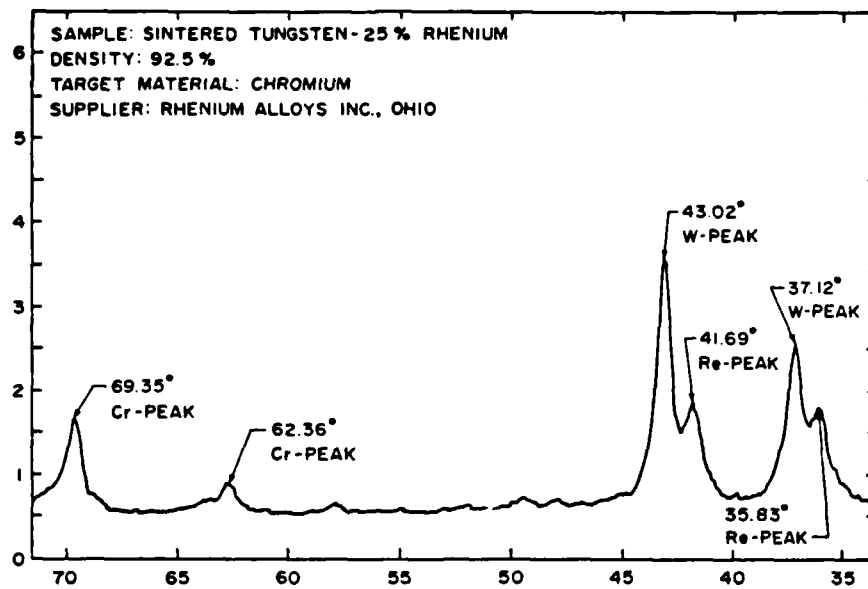


Figure 7. Output for chemical analysis by x-ray spectrometry of tungsten, 25% rhenium.

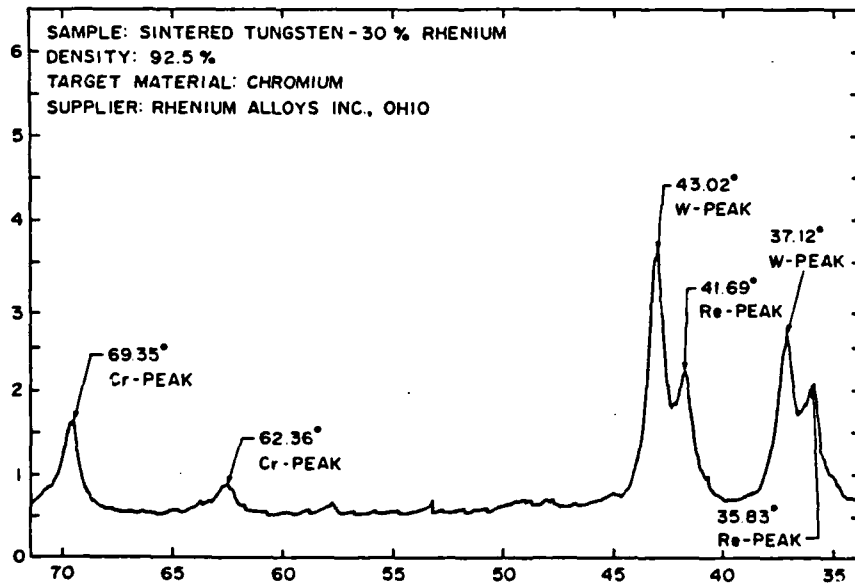


Figure 8. Output for chemical analysis by x-ray spectrometry of tungsten, 30% rhenium.

### 2.3.2 Thermionic emission sample preparation, fabrication and mounting.

The material which was originally in button form, roughly 10.20 mm. in diameter and 12.70mm. in length was first machined to 9.80 mm using a four-faceted tungsten carbide cutting tool. Because of the brittle nature of the alloys, the machined surface had a lot of dents due to particles chipping off from the surface. The surface was eventually finished (Figure 9) on the electrical discharge machine, with a copper-tungsten electrode, to a final diameter of 9.60 mm. The rod was then sliced, using a special diamond cutting wheel, to the final sample configuration of a disc with a diameter of 9.60 mm and a thickness of 2.60 mm. The electrical discharge machine was once again used to drill the hohlraum (or black enclosure) which had a diameter of 0.70 mm and a length of 7.00 mm thereby satisfying the condition for an isothermal enclosure, of having a 10:1 length to diameter ratio.

The emitting surface of each sample was polished with 240, 300, 420 and 600 grit carborundum wet/dry paper and then lapped with 3  $\mu\text{m}$ ., 0.1  $\mu\text{m}$ , and 0.05  $\mu\text{m}$ . alumina slurries, to get a mirror finish. Each sample was then thoroughly cleaned by ultrasonic cleaning in Oakite-HD 126, deionized water and acetone before being mounted in the tantalum holder shown in Figure 10, along with the rest of the emitter assembly. The sample was held in position by a tungsten pin passing through the holder. The holder which was electron beam welded to a molybdenum plate had a groove that exposed the hohlraum to be viewed by the optical pyrometer.

The emitter assembly, designed to accommodate the sample consisted of a circular molybdenum plate to which a tantalum tube was electron

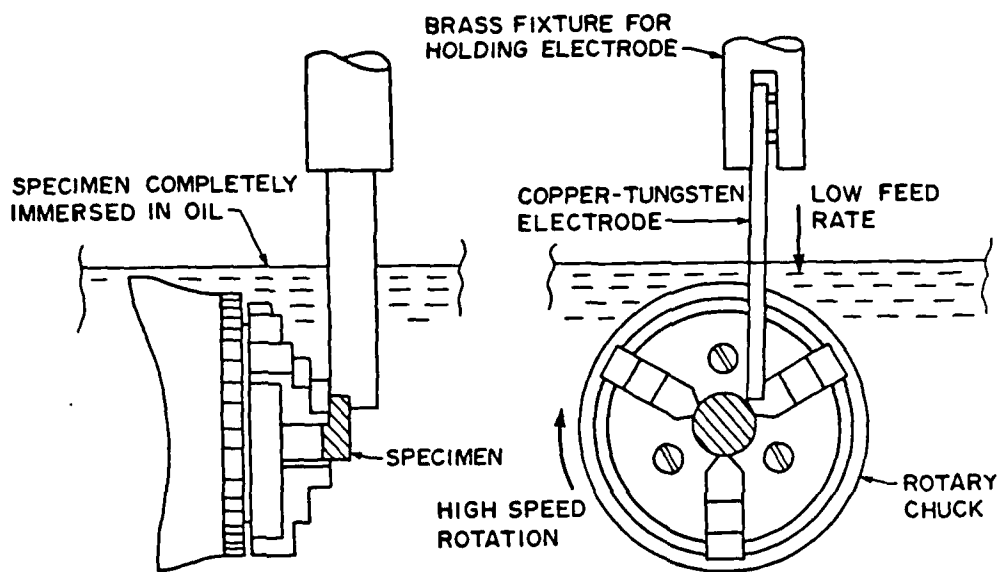


Figure 9. Details of electrical discharge machining.

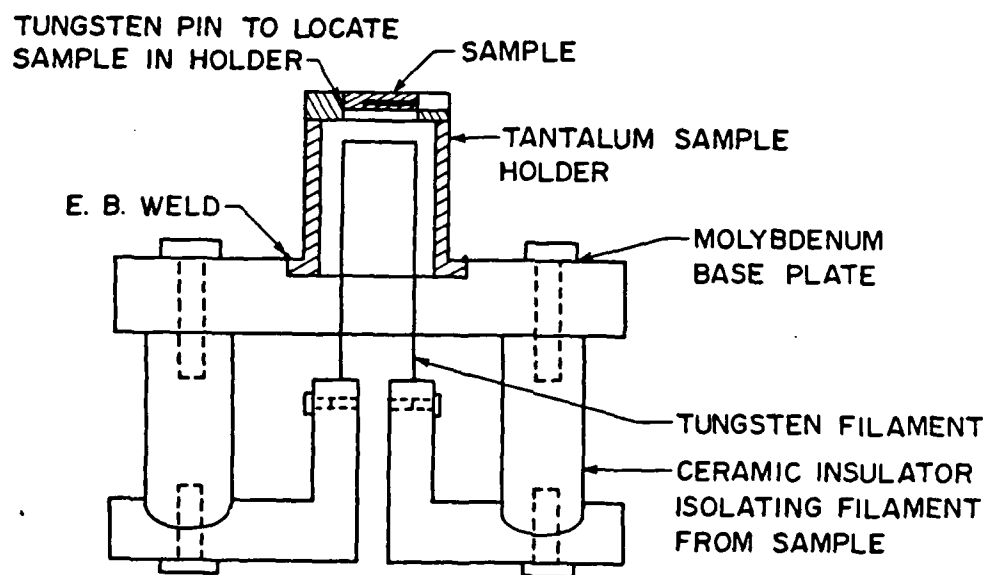


Figure 10. Emitter assembly with sample and filament.

beam welded to withstand the high temperatures. The molybdenum plate was in turn connected to the fixture, for holding the tungsten filament, with ceramic insulators thereby isolating the filament from the sample. Extreme caution was exercised in locating the filament below the sample, as the filament thermally expands when heated to high temperatures and this might lead to a short circuit between the sample and the filament. The molybdenum plate was also fastened to the x,y,z mechanism at the head of the microscope so that the sample could be manipulated in all three directions for magnification measurements as well as image scanning.

#### 2.4 Description of apparatus used

The thermionic emission microscope was originally designed at the Electro Optical Systems Division of "XEROX" in 1966. However, it has been subjected to a series of modifications in order to enhance its performance. The microscope and its accessories, shown in Figure 11, essentially consists of an electron source that is heated in the neighborhood of 1750 to 2250 K with a tungsten filament. The electrons emitted from the surface are drawn, through a system of lenses and drift tube, to the Faraday collector by the imposition of suitable potentials. The electrons collected at the Faraday cage are allowed to pass through an electrometer which measures currents of the order of  $10^{-11}$  to  $10^{-14}$  amps. The device is operated with a vacuum of  $10^{-9}$  torr and the temperature of the specimen is measured with a calibrated optical pyrometer. There is a phosphor screen at the end of the drift tube

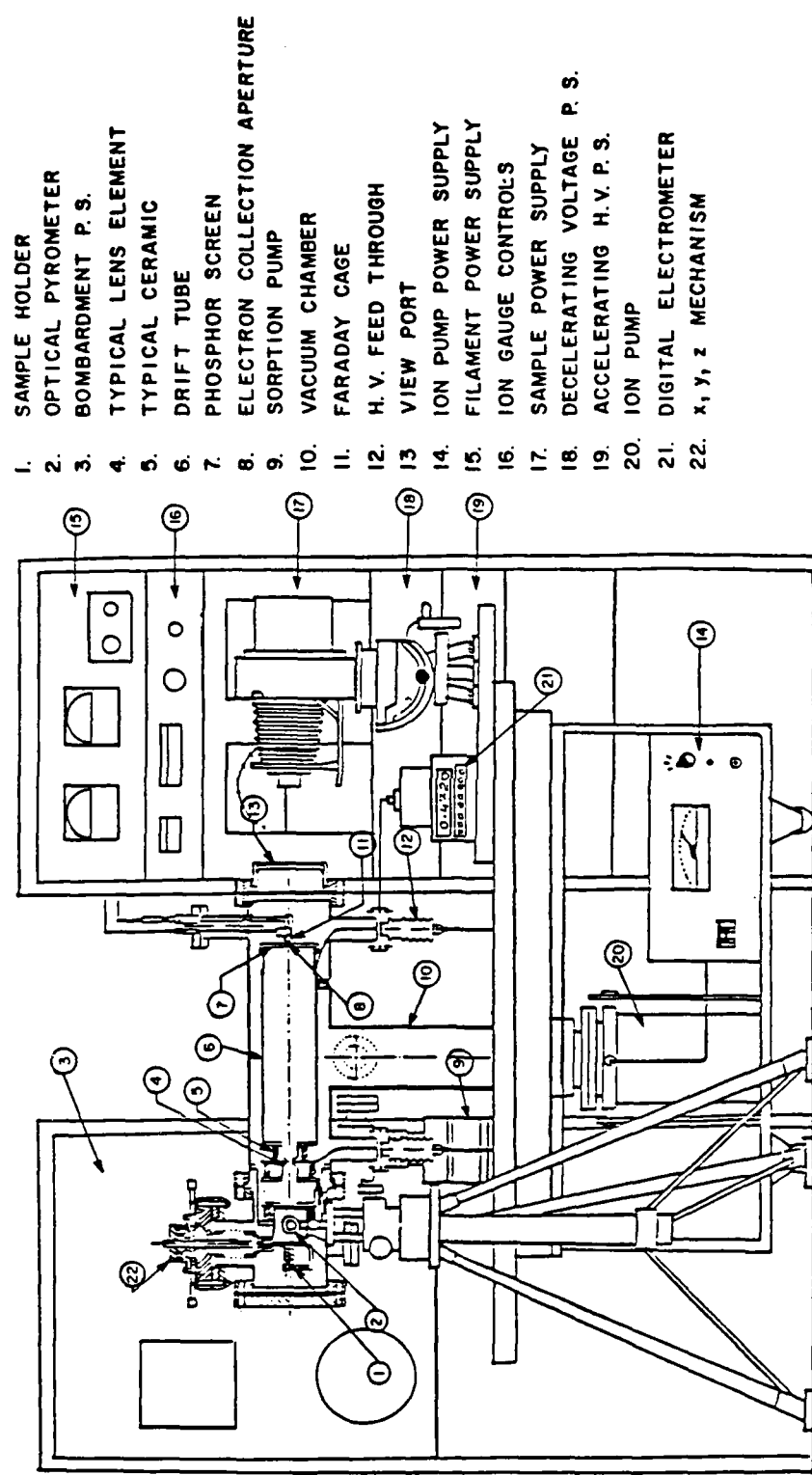


Figure 11. Experimental layout for thermionic emission.

which allows real time grain boundary movements to be observed during the test.

The entire set up can be divided into four categories based on their respective functions. These are:

#### 2.4.1 The vacuum system

The performance of the thermionic emission microscope is similar to that of an electron gun necessitating the presence of a vacuum in order to eliminate particle interference with the electron beam and at the same time minimize oxidation of the sample by contaminants at elevated temperatures. A sorption roughing pump was used to bring the vacuum level down to the  $10^{-2}$  torr range, while an ion pump reduced the pressure to better than  $10^{-6}$  torr. A thermocouple gauge measured the rough vacuum while an ionization gauge measured the high vacuum.

#### 2.4.2 The sample heating system

The sample was heated by electron bombardment, shown in Figure 10. An alternating current power supply was used to heat the filament. A potential difference imposed between the sample and the filament produces the electron bombardment for heating.

#### 2.4.3 Thermionic emission and collection

Figure 12 depicts a block diagram indicating the movement of electrons from the emitter (sample) to the collector (Faraday cage). Electrons given out by the heated sample pass through a system of objective immersion electrostatic lenses and a drift tube before striking the phosphor screen and producing an inverted image of the

sample. A small hole in the screen allows a portion of the electrons to be transmitted to the Faraday cage to give a measure of the current density.

#### 2.4.3.1 Electrical schematic and potential distribution.

The electrical circuit for the system is shown in Figure 13 where the emitter assembly was connected to a three pronged electrical feedthrough by copper wires that were capable of supporting a current of at least 20 amps. A NJE 15V, 20A, power supply provided the necessary power to the filament. A 1500 volts bombardment heating supply was connected across the negative filament lead and the sample lead. A Sorenson 30 KV, high voltage power supply provided a symmetrical high positive voltage to the lens and screen assembly to accelerate the electrons. The Fluke 407D supplied the necessary small negative voltage to the sample while the decelerating grid received its power from a HP, 320V power supply. The inner Faraday cage was connected to the electrometer and the guard ring was connected to an inactive electrometer to match the resistances in the inner and outer cups. The potential distribution along the longitudinal axis of the microscope is presented in Figure 14.

#### 2.4.3.2 Sample voltage and decelerating voltage for saturated emission.

In order to improve the efficiency of electron emission from the sample, it is necessary to overcome the space charge barrier at its surface. This was easily overcome by applying a small negative potential that penetrated the space charge barrier and repelled the electrons from its surface. The actual value of this potential was

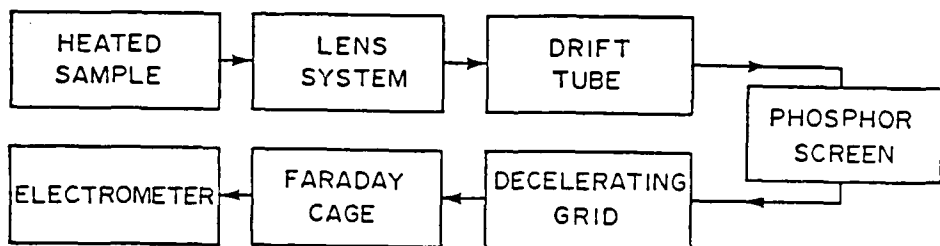


Figure 12. Block diagram for the movement of electrons.

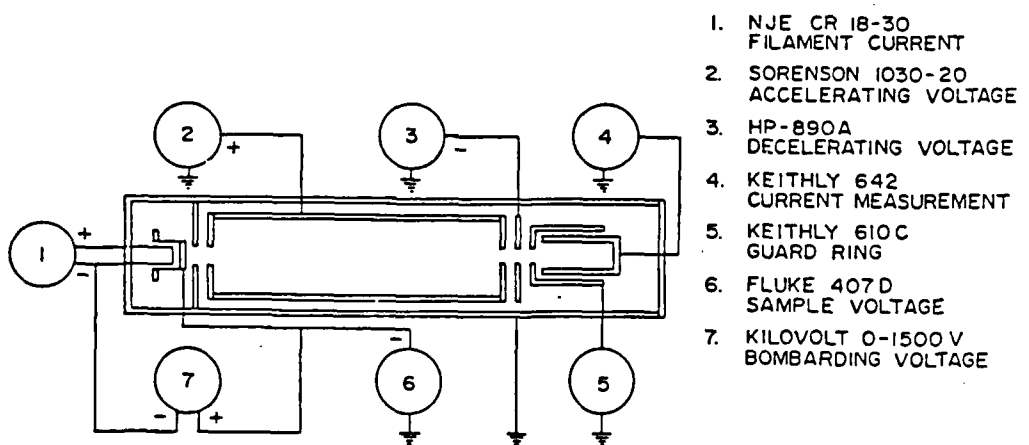


Figure 13. Electrical schematic for thermionic emission.

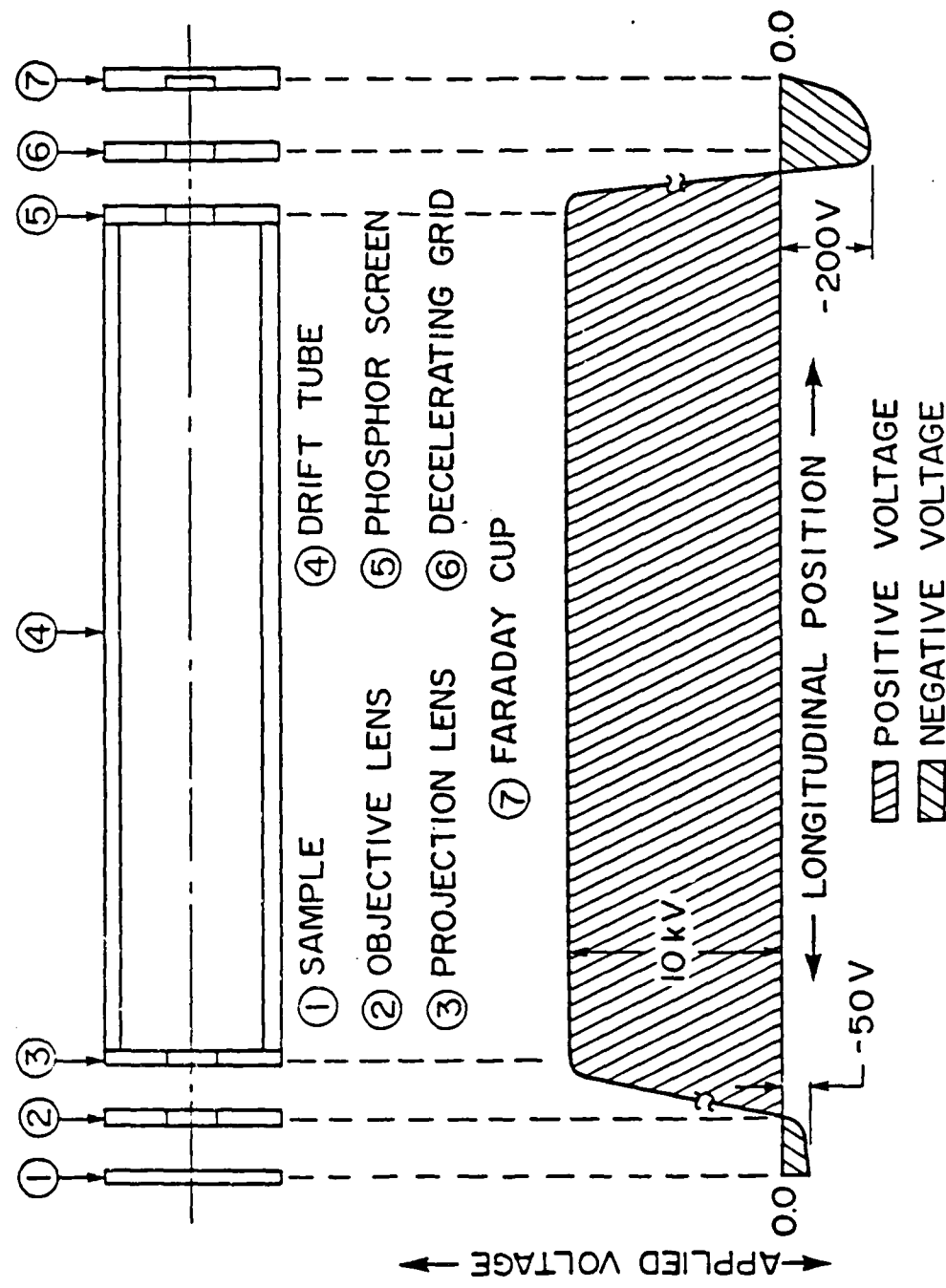


Figure 14. Potential distribution along the longitudinal axis of the microscope.

arrived at by gradually increasing the sample voltage from zero volts and observing the electron emission current at various stages while the sample was heated up to its operating temperature. The results of this test have been plotted in Figure 15 where it can be seen that the saturated emission occurs at a sample voltage of -50 volts.

Electrons that pass through the screen aperture are extremely high energy electrons which, if not taken care of, would result in secondary electron emission and an improperly focused electron beam both of which would introduce an error in the measurements at the collector. The decelerating grid, with a negative potential on it, slows down the electrons and minimizes the effects mentioned above. Again, in this case, the variation of sample electron emission with decelerating voltage was studied to arrive at a value of -200 volts for saturated emission. The plot for this study is indicated in Figure 16.

#### 2.4.3.3 Faraday cage assembly and modifications

All the major parts of the Faraday cage assembly viz. the decelerating grid, the guard ring and the Faraday cup were electrically separated by suitable ceramic insulations. The decelerating grid prevents secondary electron emission and refocuses the electron beam. The guard ring eliminates stray electric and magnetic fields and prevents current leakage around the collector. The Faraday cup collects the electrons and transmits it to the electrometer in a coaxial cable through a system of adjustable bellows and dual current feedthroughs. The bellows was used to move the collector around, without touching the screen insert, in order to get maximum current throughput. The

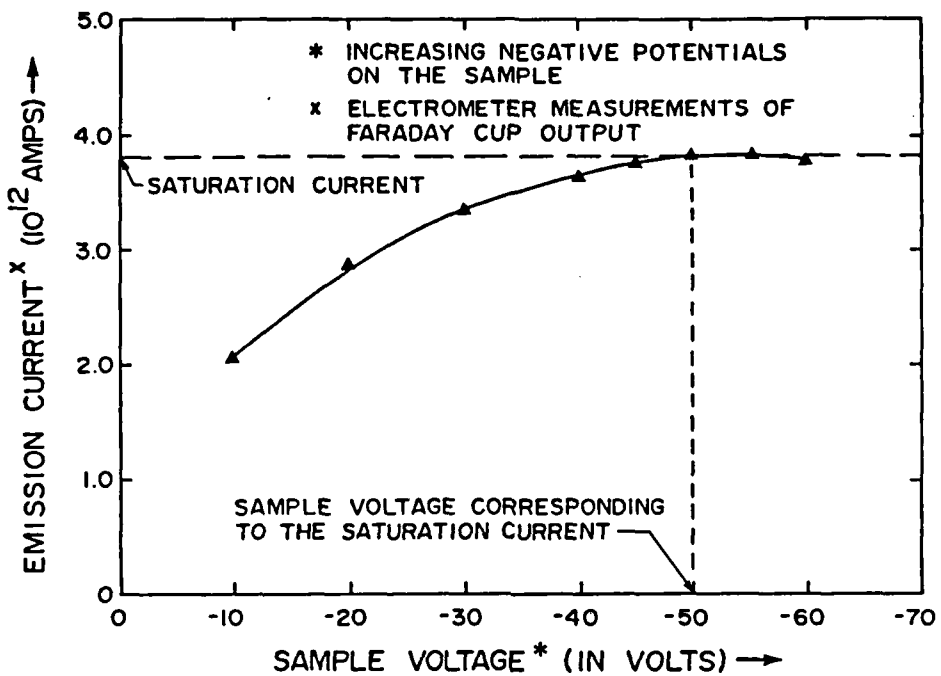


Figure 15. Variation of emission current with sample voltage.

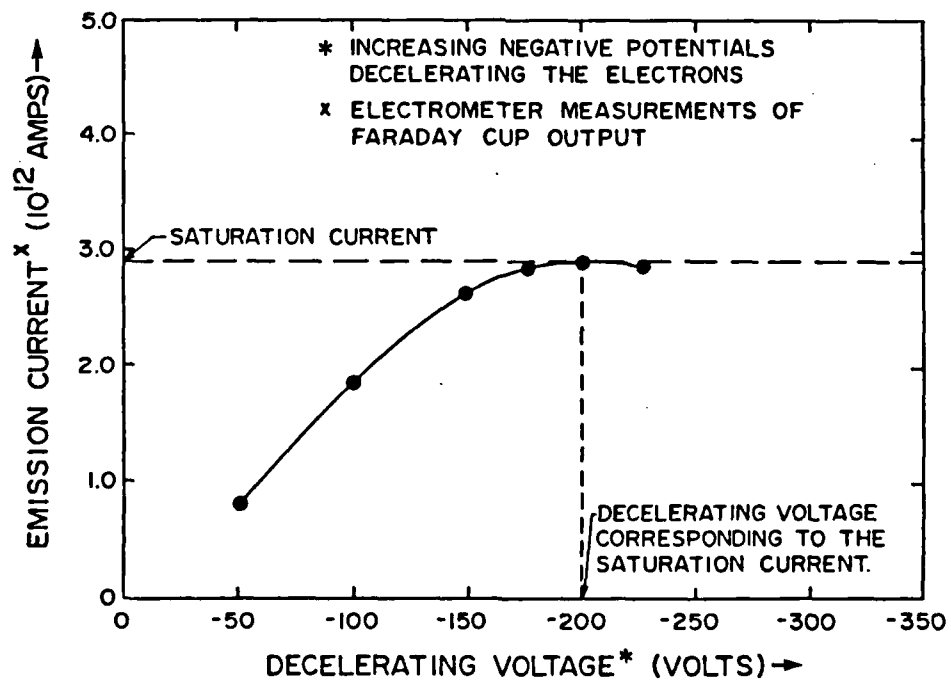


Figure 16. Variation of emission current with decelerating voltage.

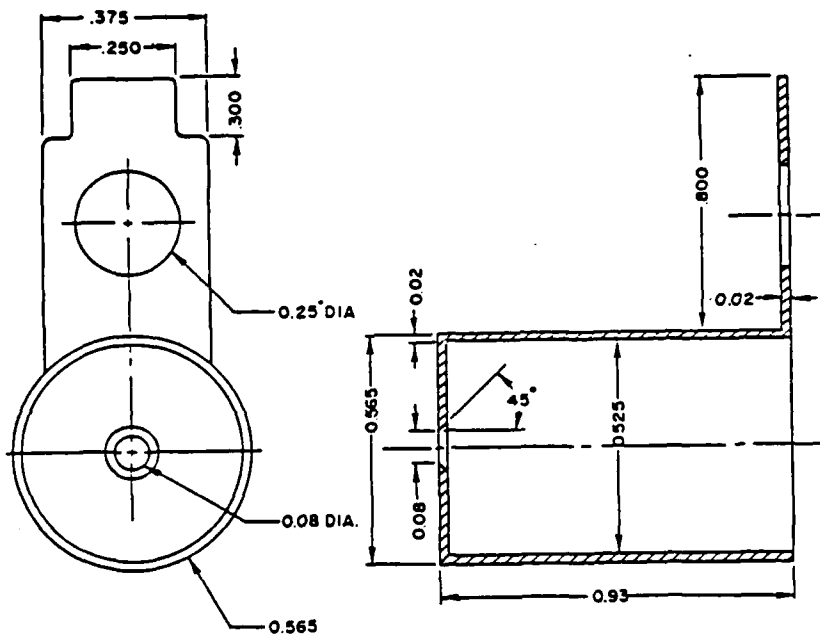
components of the Faraday cage assembly are shown in Figure 17 [61] and Figure 18 [61] is a photograph of the entire assembly along with the adjustable bellows and the dual current feedthrough which was specially designed and constructed for this application. A copper screen was built around the collector feedthrough to further prevent stray electric and magnetic fields from affecting the current readings in the electrometer.

#### 2.4.4 Temperature measurement system

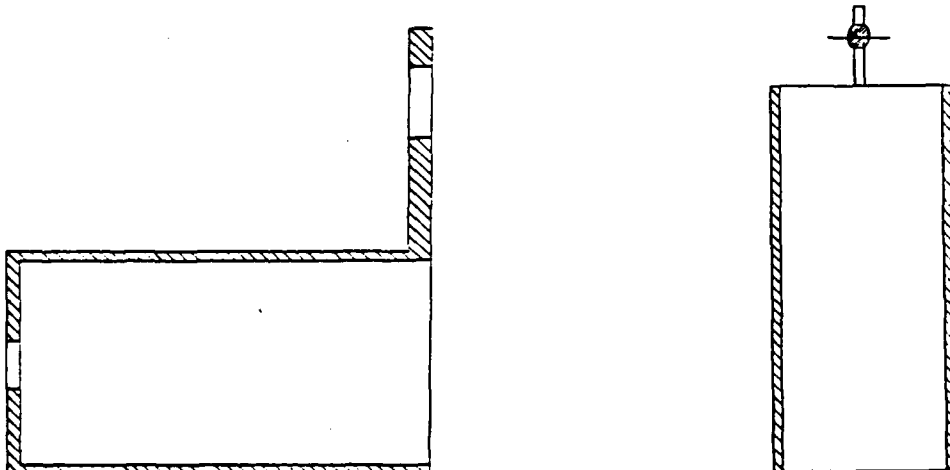
Because of the high temperatures involved and the fact that the sample was electrically hot, it was impossible to use a sensor that relies on contact to produce temperature output. Thus an optical pyrometer was used for measuring specimen temperatures. This was done by comparing the intensity of the filament in the calibrated pyrometer with that of the hohlraum on the side of the sample. However, the hohlraum was viewed through a system of neutral density filters in the pyrometer and a sapphire viewport and thus it was essential to calibrate the pyrometer with a constant temperature source. Figure 19 is a photograph of the optical pyrometer being directed towards the heated sample through the viewport.

##### 2.4.4.1 Optical pyrometer calibration

The optical pyrometer was calibrated with a constant temperature NBS (calibrated) tungsten ribbon filament lamp with a notch in the centre to locate and compare filament intensities. The sapphire viewport was placed between the pyrometer and the lamp. The electrical circuit for calibration is shown in Figure 20 and the results of the



Decelerating grid



Guard ring

Faraday cup

Figure 17. Components of the Faraday cage assembly.

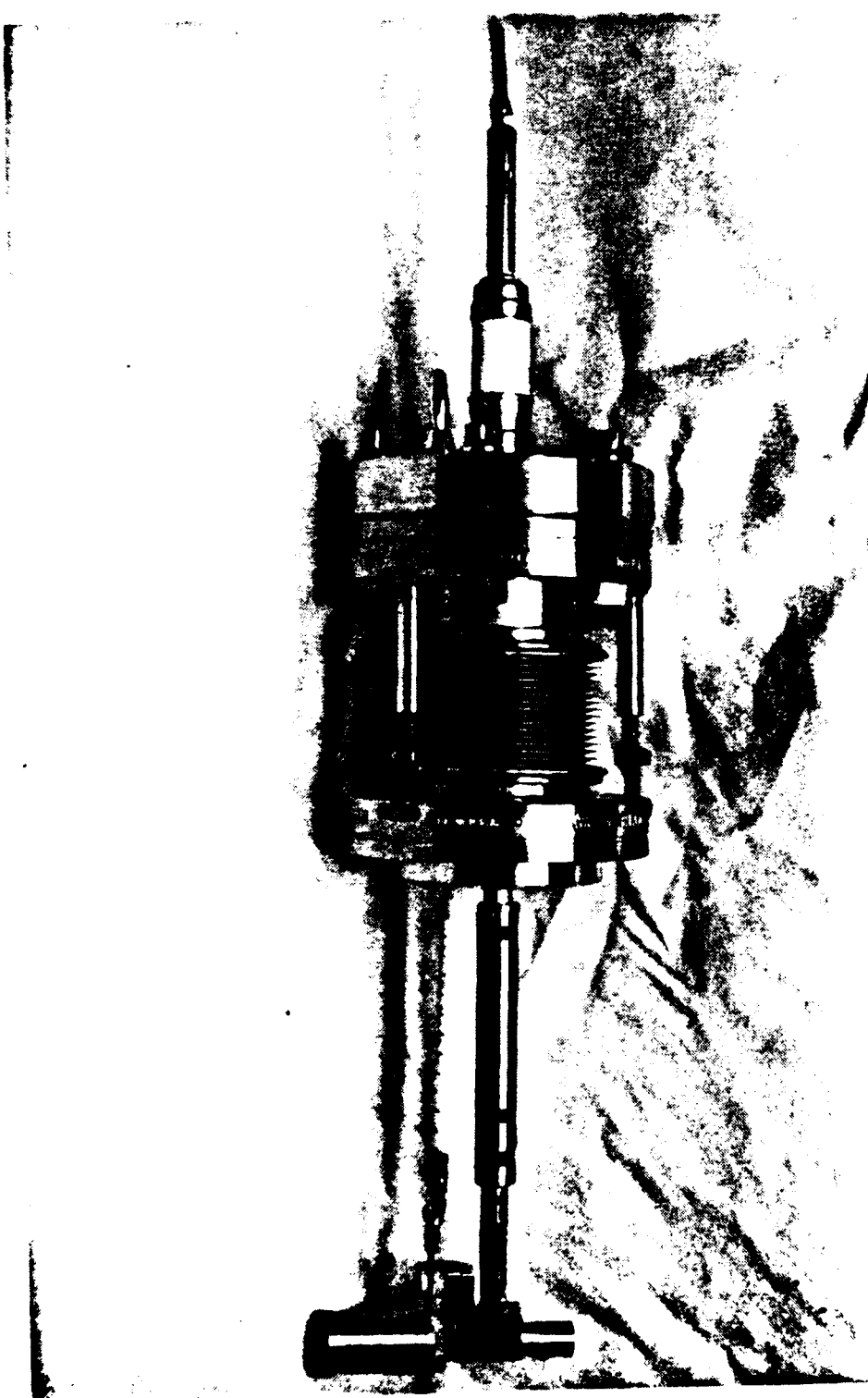


Figure 18. Complete assembly with bellows system and feedthroughs.

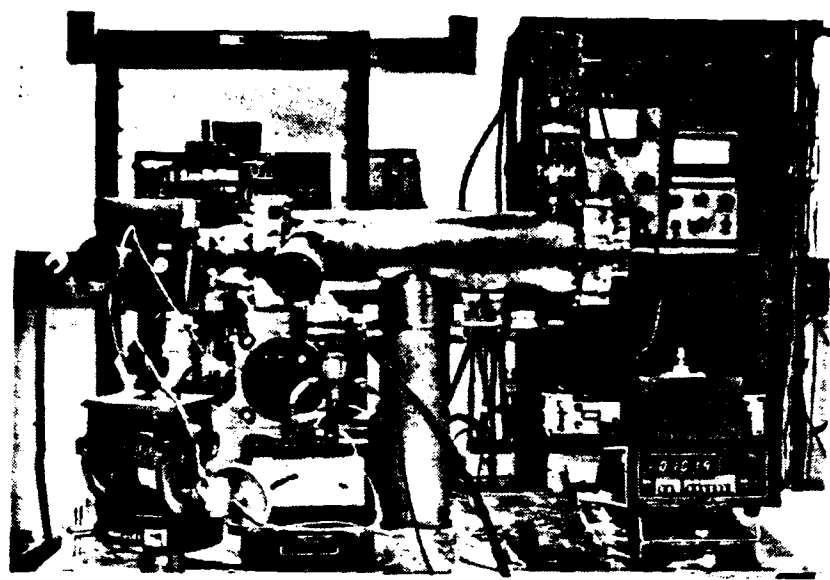


Figure 19. Temperature measurement with the optical pyrometer.

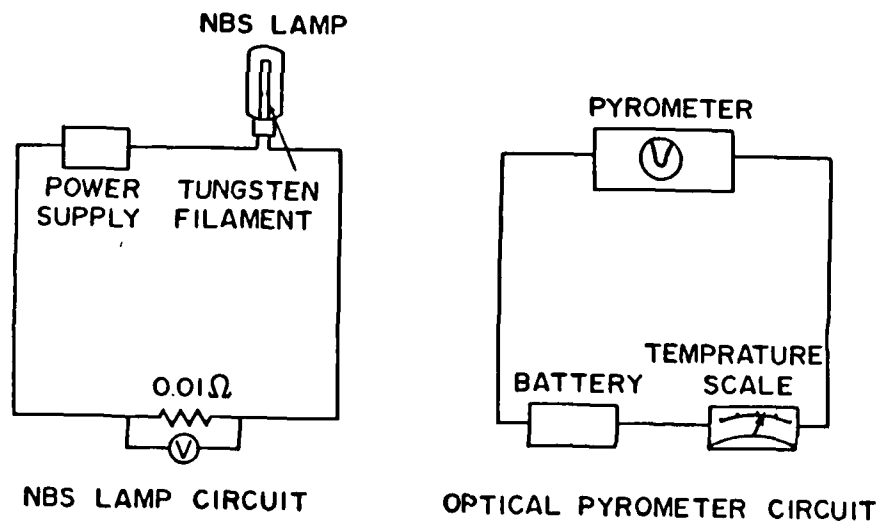


Figure 20. Electrical circuits for pyrometer calibration.

calibration are plotted in Figure 21. The details of all the components of the system are given in Appendix - 1 and some technical data on the thermionic emission microscope is presented in Appendix - 2.

## 2.5 Experimental procedure

The first part of the procedure was to assemble the various components of the microscope. The lenses, drift tube and screen assembly were bolted to the inside of the microscope, after being thoroughly cleaned in Oakite-HD 126, acetone, and finally deionized water. A small diameter, low power laser gun was used to align all the parts in the path of the electrons. The Faraday cage assembly along with the bellows and electrodes, was then bolted onto the microscope. The emitter assembly was the last part to be installed inside the microscope. The rest of the procedure consists of conducting the test in two stages. The first stage was the vacuum annealing stage to study the grain growth characteristics and establish stability of grain size and the second stage was the work function measurement of selected grains at various temperatures.

### 2.5.1 Vacuum annealing for grain size stability

For vacuum annealing, the sample was cleaned, fixed in the emitter assembly and then mounted in the head of the microscope. The microscope was then sealed and the sorption pump activated with liquid nitrogen for preliminary roughing. When a roughing vacuum of  $3 \times 10^{-3}$  torr was attained, the vac-ion pump was started. A glow appeared in the microscope, but its intensity decreased and finally disappeared after the sorption pump was isolated. The entire microscope assembly was then

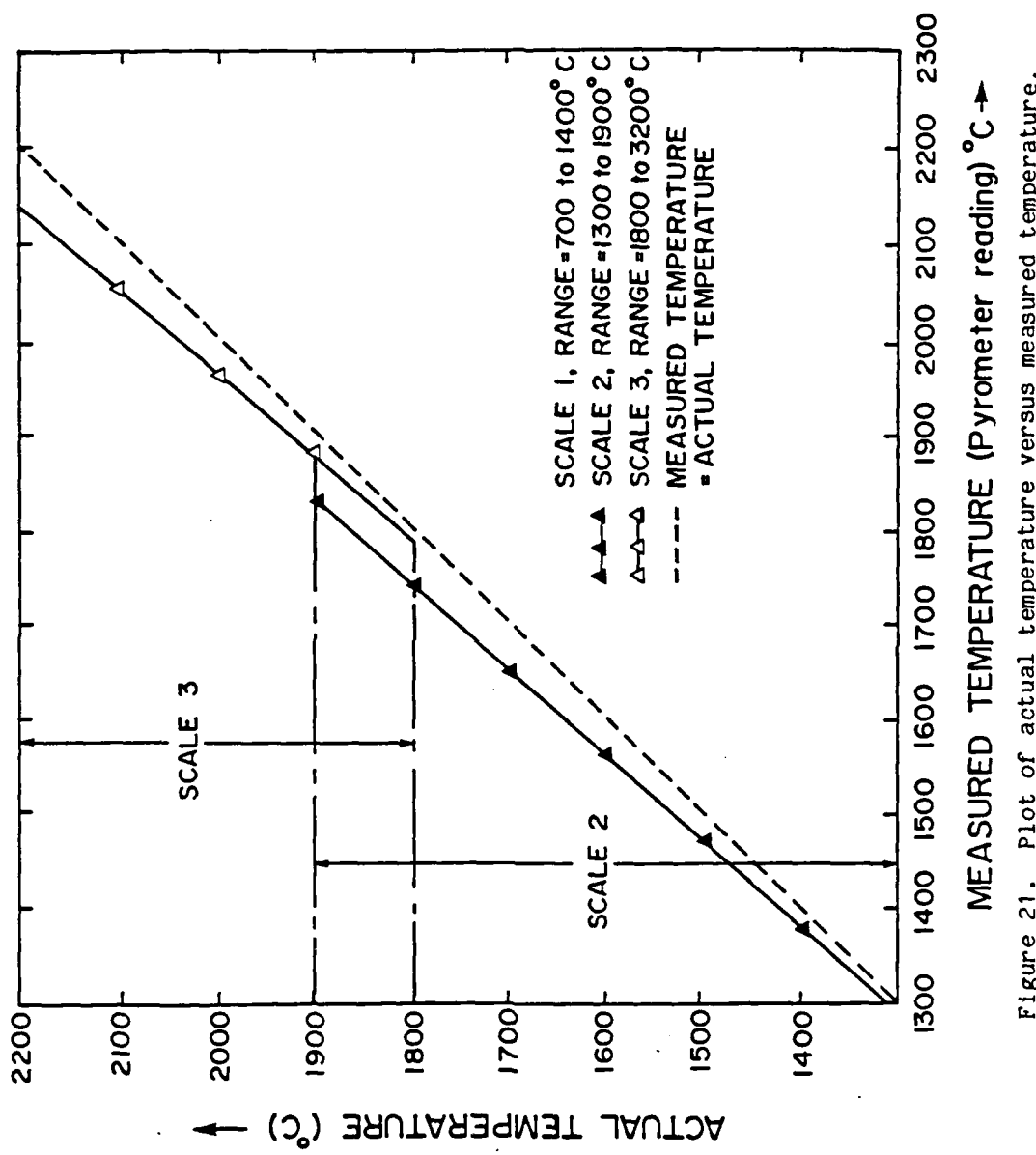


Figure 21. Plot of actual temperature versus measured temperature.

baked at 473 K to produce an ultimate vacuum of  $5 \times 10^{-9}$  torr. At this stage, all the electrical connections were made and the filament heated up with an a.c. power supply of 16 amps. The sample was then heated up with a bombardment current of about 300 ma. and brought to the required temperature of 2000 K. The sample voltage, the decelerating voltage and the accelerating voltage of 10 kV were imposed to bring the electrons and form an illuminated image on the phosphor screen. The image clarity was improved by manipulating the x,y,z mechanism. A camera was set up to take pictures of a particular grain on the image. Pictures were taken at thirty minute intervals for twelve hours when grain size stability was observed.

#### 2.5.2 Measurements for work function evaluation

The Faraday cage and electrometer connections were then made for work function evaluation. A suitable area on the image, with five grains of varying intensities was chosen and focused for emission measurement. The sample was heated to 1950 K and current measurements were made by moving the image such that the Faraday cup was directed towards the grain of interest. At the end of each test the magnification of the image was determined by using the movement of a distinct feature, at the centre of the image, from one end to the other. This was repeated at temperatures of 2050 K, 2150 K, 2240 K and 2350 K. The respective work functions were then evaluated using the emission current, the magnification and the Richardson-Dushman Equation. The entire procedure was repeated for the thoriated tungsten, rhenium alloys.

## 2.6 Results and discussion

Table 5 and Table 6 represent the emission results for the tungsten, rhenium samples and those for the thoriated tungsten, rhenium are provided in Table 7 and Table 8. Each sample was observed while it was being vacuum annealed at 2000 K, and emission micrographs recorded to study the kinetics of grain growth, on the same lines as Rouze [55] and Nutting [46]. However it was found that the grains under consideration had already assumed a fairly steady state and no appreciable growth was detected as shown in Figure 22 and Figure 23. This indicated that the structure of each sample had stabilized which is necessary for work function measurements that are very sensitive to factors affecting the surface of the sample. It was also found that the recrystallized grain size decreased with increasing rhenium content. This indicates that the addition of rhenium delays the recrystallization of tungsten, by promoting twinning during deformation [14]. Rhenium is believed to lower the lattice resistance to dislocation of the parent metal, resulting in solid solution softening of b.c.c. metals. Excess rhenium above the solubility limit (27%) in tungsten does not inhibit recrystallization as does lower percentages. This procedure intended for the study of grain growth kinetics was not carried out for the thoriated samples.

### 2.6.1 Effective work functions of W,Re alloys

The work function, as depicted by Michaelson [42] is a periodic function of atomic number. It is for this reason that we find a large difference in the effective work functions of polycrystalline tungsten

Table 5. Emission results for W, 3% Re and W, 10% Re samples.

Grain No.	Temperature in °K	Electrometer Rdg. (Amps)	Current Density A/cm <sup>2</sup>	Work function	Temperature in °K	Electrometer Rdg. (Amps)	Current density A/cm <sup>2</sup>	Work function
1	1951	6.205E-11	7.294E-5	4.95	1946	2.386E-10	2.769E-4	4.72
2	1951	6.986E-11	8.108E-5	4.94	1946	7.512E-11	8.753E-5	4.91
3	1951	8.337E-11	9.676E-5	4.91	1946	1.089E-10	1.264E-4	4.85
4	1951	1.425E-10	1.654E-4	4.82	1946	1.394E-10	1.618E-4	4.81
5	1951	2.023E-10	2.349E-4	4.76	1946	2.215E-10	2.571E-4	4.73
1	2062	1.586E-10	1.811E-4	5.09	2051	1.783E-9	2.069E-3	4.63
2	2062	3.723E-10	4.321E-4	4.94	2051	7.510E-11	8.716E-5	5.19
3	2062	4.123E-10	4.785E-4	4.92	2051	5.182E-10	6.014E-4	4.85
4	2062	6.868E-10	7.971E-4	4.83	2051	4.926E-10	9.199E-4	4.78
5	2062	7.631E-10	8.856E-4	4.81	2051	1.282E-9	1.488E-3	4.69
1	2168	6.743E-10	7.826E-4	5.10	2162	6.752E-9	7.836E-3	4.66
2	2168	1.125E-9	1.306E-3	5.01	2162	2.121E-10	2.462E-4	5.30
3	2168	1.305E-9	1.514E-3	4.98	2162	2.621E-9	3.012E-3	4.83
4	2168	1.773E-9	2.058E-3	4.92	2162	3.809E-9	4.421E-3	4.76
5	2168	2.591E-9	3.007E-3	4.85	2162	5.421E-9	6.291E-3	4.70
1	2236	1.509E-9	1.751E-3	5.12	2221	1.2415E-8	1.4715E-2	4.68
2	2236	1.891E-9	2.195E-3	5.07	2221	7.890E-10	9.157E-4	5.21
3	2236	2.516E-9	2.920E-3	5.02	2221	4.782E-9	5.550E-3	4.87
4	2236	3.197E-9	3.710E-3	4.97	2221	6.804E-9	7.896E-3	4.80
5	2236	4.652E-9	5.399E-3	4.90	2221	9.685E-9	1.124E-3	4.73
1	2361	6.916E-9	8.026E-3	5.12	2339	3.589E-8	4.165E-2	4.73
2	2361	8.950E-9	1.039E-2	5.06	2339	3.110E-9	3.609E-3	5.22
3	2361	1.362E-8	1.581E-2	4.98	2339	1.796E-8	2.084E-2	4.84
4	2361	1.391E-8	1.614E-2	4.97	2339	2.197E-8	2.898E-2	4.81
5	2361	1.537E-8	1.784E-2	4.95	2339	2.632E-8	3.055E-2	4.80

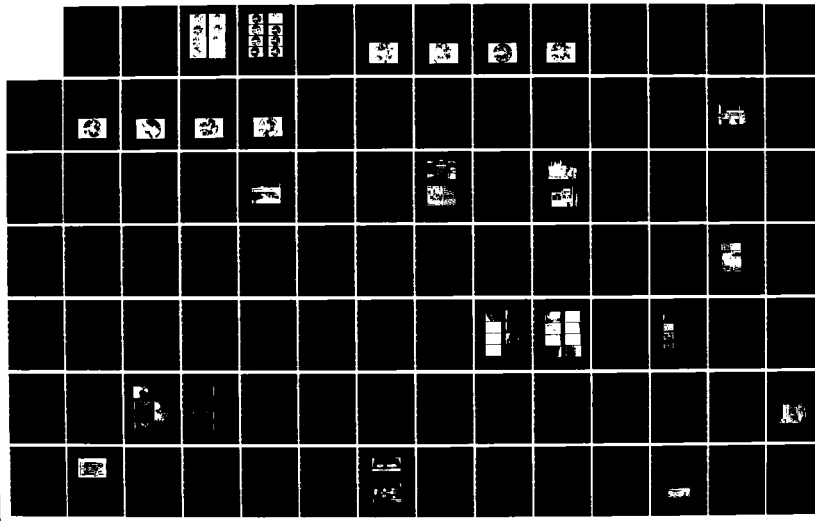
Table 6. Emission results for W,25% Re and W,30% Re samples.

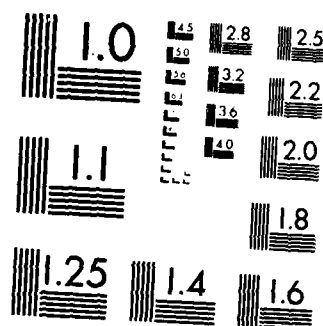
Grain No.	Temperature in °K	Electrometer Rdg. (Amps)	Current Density A/cm <sup>2</sup>	Work function	Temperature in °K	Electrometer Rdg. (Amps)	Current density A/cm <sup>2</sup>	Work function
1	1951	4.315E-11	5.0E-5	5.02	1916	1.072E-10	1.24E-4	4.85
2	1951	2.535E-10	1.912E-4	4.72	1916	1.036E-12	1.202E-5	5.24
3	1951	1.795E-10	2.083E-4	4.78	1916	5.718E-11	6.639E-5	4.96
4	1951	1.260E-11	4.914E-5	5.02	1916	1.235E-11	4.915E-5	5.01
5	1951	1.605E-11	1.863E-5	5.18	1916	1.867E-11	2.167E-5	5.14
1	2037	1.060E-10	1.230E-4	5.09	2051	5.534E-10	6.366E-4	4.84
2	2037	7.982E-10	9.261E-4	4.74	2051	5.360E-10	6.209E-5	5.25
3	2027	1.102E-10	1.279E-4	5.09	2051	2.735E-10	2.573E-4	5.00
4	2037	1.102E-10	1.279E-4	5.09	2051	2.735E-10	3.171E-4	4.97
5	2037	8.675E-11	1.007E-4	5.13	2051	9.818E-11	1.139E-4	5.15
1	2148	4.105E-10	5.112E-4	5.13	2170	2.501E-9	2.901E-3	4.86
2	2148	3.968E-9	4.605E-3	4.72	2170	2.575E-10	2.930E-4	5.29
3	2148	2.911E-9	3.417E-3	4.78	2170	1.567E-9	1.819E-3	4.95
4	2148	7.395E-10	8.582E-4	5.03	2170	1.193E-9	1.384E-3	5.00
5	2148	2.591E-10	3.011E-4	5.23	2170	6.001E-10	6.963E-4	5.13
1	2259	2.295E-9	2.666E-3	5.09	2224	3.512E-9	4.111E-3	4.92
2	2259	1.222E-8	1.418E-2	4.77	2224	5.810E-10	6.743E-4	5.27
3	2259	8.910E-9	1.034E-2	4.83	2224	1.813E-9	2.139E-3	5.05
4	2259	3.022E-9	3.507E-3	5.04	2224	1.530E-9	1.776E-3	5.09
5	2259	1.193E-9	1.384E-3	5.22	2224	1.265E-9	1.463E-3	5.12
1	2339	2.792E-9	3.210E-3	5.25	2350	1.010E-8	2.144E-2	4.89
2	2339	2.214E-8	2.569E-2	4.83	2350	1.714E-9	1.909E-3	5.34
3	2339	1.308E-8	1.518E-2	4.94	2350	1.114E-8	1.292E-2	4.99
4	2339	3.050E-9	4.468E-3	5.18	2350	9.124E-9	1.091E-2	5.03
5	2339	1.219E-8	1.415E-2	4.95	2350	5.051E-9	5.862E-3	5.15

Table 7. Emission results for W, 1%ThO<sub>2</sub> and W, 10%Re, 1%ThO<sub>2</sub> samples.

Grain No.	Temperature in °K	Electrometer Rdg. (Amps)	Current Density A/cm <sup>2</sup>	Work function	Temperature in °K	Electrometer Rdg. (Amps)	Current density A/cm <sup>2</sup>	Work function
1	1933	1.117E-10	1.296E-4	4.807	1933	1.893E-9	2.197E-3	4.336
2	1933	1.065E-10	1.236E-4	4.815	1933	1.034E-10	8.753E-5	4.820
3	1933	9.616E-10	1.116E-4	4.832	1933	8.892E-11	1.032E-4	4.845
4	1933	8.892E-11	1.032E-4	4.845	1933	1.394E-10	5.021E-5	4.965
5	1933	8.331E-11	9.662E-5	4.856	1933	2.215E-10	1.823E-5	5.134
1	2043	6.323E-10	7.338E-4	4.795	2043	9.574E-10	1.111E-3	4.722
2	2043	5.709E-10	6.625E-4	4.813	2043	8.401E-10	9.452E-4	4.745
3	2043	4.897E-10	5.682E-4	4.840	2043	4.599E-10	5.338E-4	4.851
4	2043	4.316E-10	5.011E-4	4.861	2043	2.131E-10	2.821E-4	4.963
5	2043	3.462E-10	4.017E-4	4.901	2043	1.929E-10	2.237E-4	5.004
1	2153	2.735E-19	3.171E-3	4.801	2153	1.503E-8	1.745E-2	4.485
2	2153	2.327E-9	2.701E-3	4.831	2153	3.321E-9	3.851E-3	4.765
3	2153	1.815E-9	2.141E-3	4.874	2153	1.601E-9	1.861E-3	4.900
4	2153	1.479E-9	1.717E-3	4.915	2153	5.332E-10	6.195E-4	5.104
5	2153	1.159E-9	1.345E-3	4.960	2153	2.691E-10	3.123E-4	5.231
1	2243	1.331E-8	1.544E-2	4.712	2243	1.769E-8	2.053E-2	4.654
2	2243	5.406E-9	6.274E-3	4.886	2243	5.028E-9	5.836E-3	4.900
3	2243	5.110E-9	5.989E-3	4.895	2243	4.875E-9	5.657E-3	4.906
4	2243	3.255E-9	3.778E-3	4.984	2243	2.981E-9	3.460E-3	5.001
5	2243	2.950E-9	3.424E-3	5.003	2243	1.719E-9	2.030E-3	5.104
1	2353	2.638E-8	3.119E-2	4.820	2353	2.039E-8	2.367E-2	4.876
2	2353	1.724E-9	2.001E-2	4.910	2353	1.989E-8	2.319E-2	4.881
3	2353	1.5322E-8	1.819E-2	4.926	2353	1.617E-8	1.877E-2	4.923
4	2353	1.465E-8	1.700E-2	4.913	2353	1.487E-8	1.726E-2	4.910
5	2353	1.311E-8	1.556E-2	4.961	2353	5.823E-9	6.758E-3	5.130

AD-A173 245 INVESTIGATION OF MATERIAL PROBLEMS FOR HIGH TEMPERATURE 3/9  
HIGH POWER SPACE. (U) ARIZONA STATE UNIV TEMPE COLL OF  
ENGINEERING AND APPLIED SCIE. D L JACOBSON ET AL.  
UNCLASSIFIED JUL 86 AFOSR-TR-86-0819 AFOSR-83-0867 F/G 11/6 NL





MICROCOPY RESOLUTION TEST CHART  
NATIONAL BUREAU OF STANDARDS 1963-A

Table 8. Emission results for W,25% Re, 1%ThO<sub>2</sub>, and W,30%Re, 1%ThO<sub>2</sub> samples.

Grain No.	Temperature in °K	Electrometer Rdg. (Amps)	Current Density A/cm <sup>2</sup>	Work function	Temperature in °K	Electrometer Rdg. (Amps)	Current density A/cm <sup>2</sup>	Work function
1	1933	7.301E-11	8.473E-5	4.878	1933	6.592E-11	7.651E-5	4.895
2	1933	6.793E-11	7.882E-5	4.890	1933	3.933E-11	4.567E-5	4.981
3	1933	4.625E-11	5.361E-5	4.954	1933	2.491E-11	2.891E-5	5.057
4	1933	4.101E-11	4.759E-5	4.974	1933	1.588E-11	1.842E-5	5.132
5	1933	1.551E-11	1.812E-5	5.135	1933	8.055E-12	9.315E-5	5.245
1	2043	8.259E-10	9.585E-4	4.748	2043	1.75E-10	2.031E-4	5.021
2	2043	4.013E-10	4.657E-4	4.875	2043	1.411E-10	1.637E-4	5.059
3	2043	2.088E-10	2.422E-4	4.990	2043	1.363E-10	1.582E-4	5.065
4	2043	1.092E-10	1.267E-4	5.104	2043	1.318E-10	1.529E-4	5.071
5	2043	5.879E-11	6.82E-5	5.213	2043	1.245E-10	1.441E-4	5.081
1	2153	2.578E-9	2.991E-3	4.812	2153	7.661E-10	8.891E-4	5.037
2	2153	1.786E-9	2.073E-3	4.880	2153	6.242E-10	7.243E-4	5.075
3	2153	1.003E-9	1.164E-3	4.987	2153	6.043E-10	7.013E-4	5.081
4	2153	4.349E-10	5.047E-4	5.142	2153	5.757E-10	6.682E-4	5.090
5	2153	3.113E-10	3.612E-4	5.204	2153	5.51348E-10	6.398E-4	5.098
1	2243	5.965E-9	6.923E-3	4.867	2243	3.044E-9	3.532E-3	4.997
2	2243	3.783E-9	4.390E-3	4.955	2243	1.960E-9	2.275E-3	5.082
3	2243	3.028E-9	3.514E-3	4.998	2243	1.767E-9	2.051E-3	5.102
4	2243	2.702E-9	3.136E-3	5.020	2243	1.740E-9	2.020E-3	5.105
5	2243	1.011E-9	1.173E-3	5.210	2243	1.498E-9	1.738E-3	5.134
1	2353	1.334E-8	1.548E-2	4.962	2353	1.139E-8	1.322E-2	4.994
2	2353	1.197E-8	1.389E-2	4.984	2353	8.514E-9	9.881E-3	5.053
3	2353	1.042E-8	1.210E-2	5.012	2353	7.128E-9	8.273E-3	5.089
4	2353	9.921E-9	1.115E-2	5.022	2353	6.523E-9	7.571E-3	5.107
5	2353	5.7943E-9	6.725E-3	5.131	2353	3.885E-9	4.509E-3	5.212

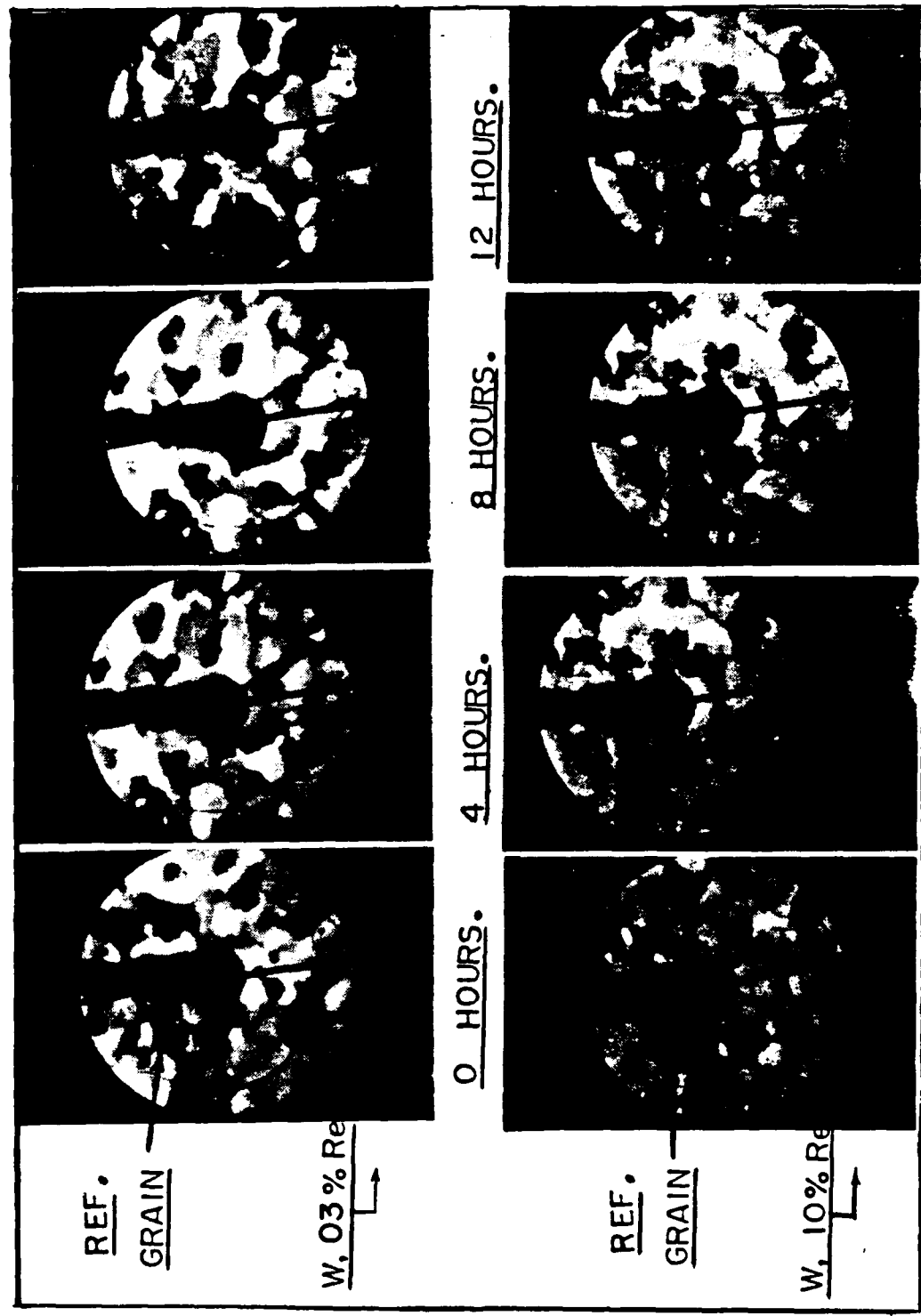


Figure 22. Grain growth history for W-3% Re and W-10% Re samples.

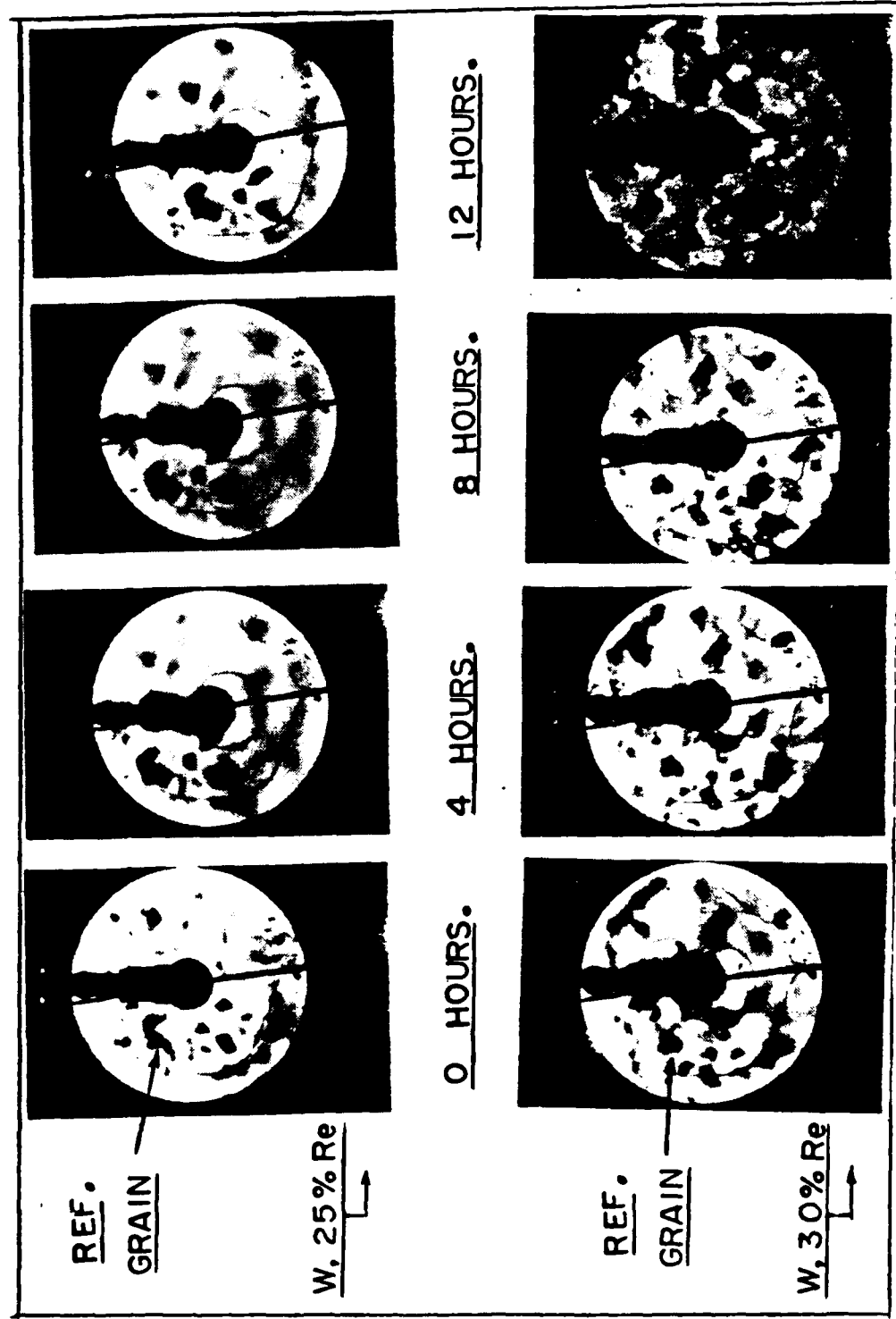


Figure 23. Grain growth history for W,25% Re and W,30% Re samples.

( $\phi = 4.5\text{eV}$ ) and polycrystalline rhenium ( $\phi = 4.9\text{eV}$ ) even though the difference in atomic number is just one. From the results obtained we notice that some of the values for average effective work function do exceed  $4.9\text{eV.}$ , but this arises from the fact that the representative grains have different orientations and work function is a strong function of crystal orientation. The authenticity of the values obtained was derived from the fact that the measurements were calibrated with a rhenium sample originally tested by Jacobson [31]. The repeat tests revealed a work function that was well within the experimental error limitations of  $\pm 0.04\text{eV}$ . This error limit was determined by combining the experimental accuracies from the measurements of electron current, temperature, area and electric field.

Figure 24 is a summary of the emission test on W,3% Re. The emission micrograph has five grains numbered in order of decreasing or increasing intensities corresponding to increasing or decreasing work functions. The grains represent the average intensities on the image and are considered to be a representative of the entire surface even though they actually cover less than five percent of the emitter area. At a given temperature, there were five current readings recorded, corresponding to the five grains and the average of these readings is shown in this table. Further, the average effective work function increases with increase in operating temperature, as expected from the R-D equation. Figures 25 through 27 are similar summaries for the W,10% Re, the W,25% Re and the W,30% Re samples.

Figure 28 is the variation of average effective work function with operating temperature. As can be seen, the work function in each case,

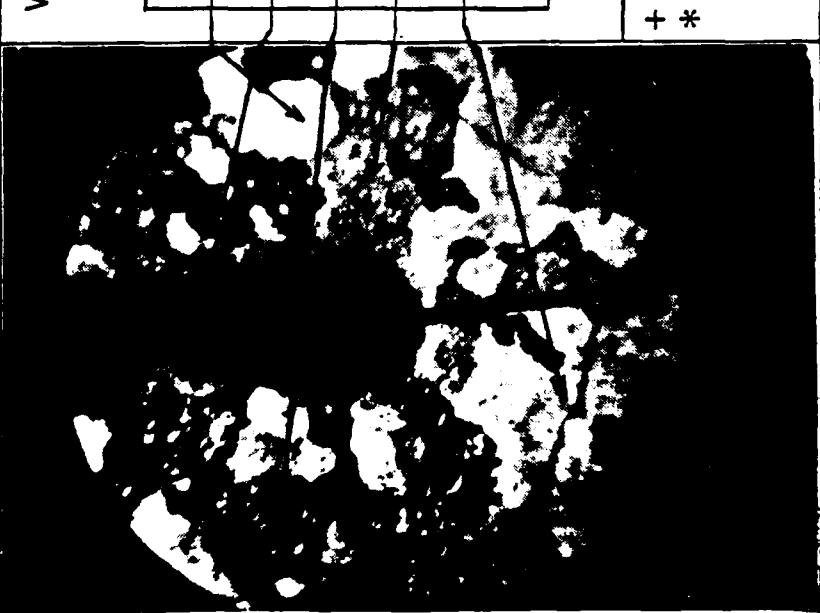
EXPT. NO.	EMISSION MICROGRAPH (WITH GRAIN NUMBERS)	SAMPLE <sup>+</sup>	ACTUAL TEMPERATURE (°K)	EFFECTIVE WORK FUNCTION* (eV)
	W, 3% Re	1951	4.84	
		2062	4.92	
		2168	4.97	
		2236	5.02	
		2361	5.02	

(1) (2) (3) (4) (5)



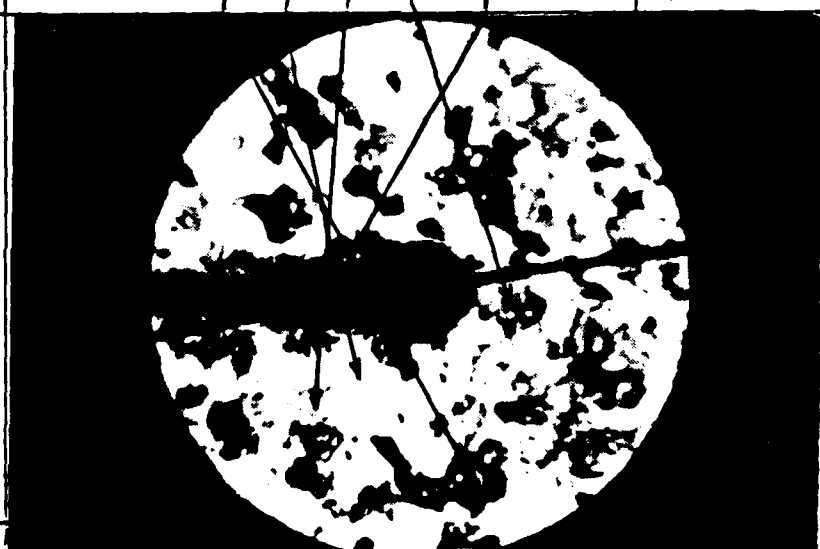
+ BASED ON LESS THAN 5 % OF CATHODE AREA  
\* EXPERIMENTAL ERROR IS  $\pm 0.04$  eV  
MAGNIFICATION = 97 X  
EXPERIMENTAL VACUUM = BETTER THAN  $5 \times 10^{-8}$  TORR.

Figure 24. Summary of work function measurements for W, 3% Re.

EXPT. NO.	EMISSION MICROGRAPH (WITH GRAIN NUMBERS)	SAMPLE <sup>+</sup>	ACTUAL TEMPERATURE (°K)	EFFECTIVE WORK FUNCTION* (eV)
2		W, 10% Re	1946	4.80
			2051	4.83
			2162	4.85
			2224	4.86
			2339	4.89

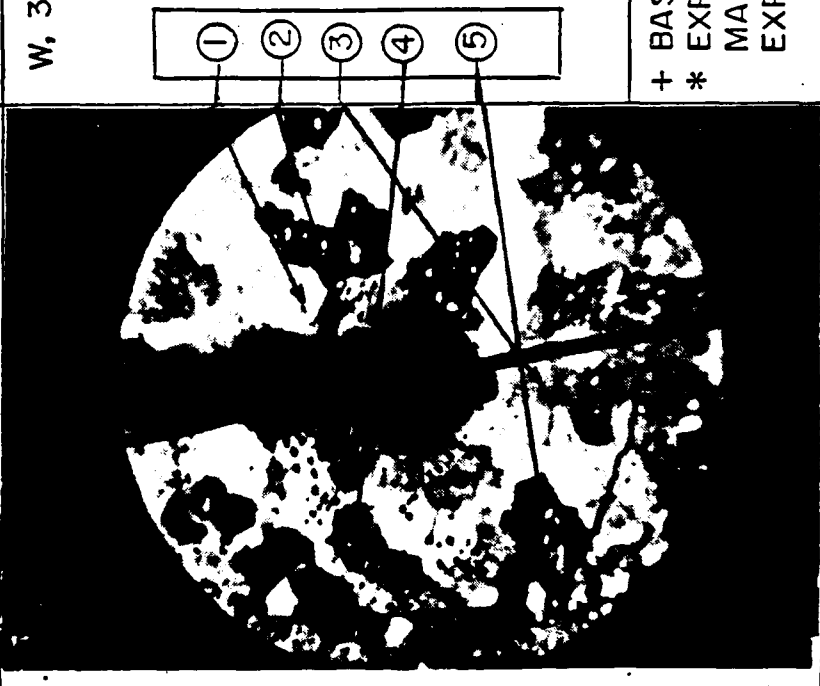
+ BASED ON LESS THAN 5% OF CATHODE AREA  
 \* EXPERIMENTAL ERROR IS  $\pm 0.04$  eV  
 MAGNIFICATION = 97 X  
 EXPERIMENTAL VACUUM = BETTER THAN  $5 \times 10^{-8}$  TORR.

Figure 25. Summary of work function measurements for W, 10% Re.

EXPT. NO.	EMISSION MICROGRAPH (WITH GRAIN NUMBERS)	SAMPLE + W, 25% Re	ACTUAL TEMPERATURE (°K)	EFFECTIVE WORK FUNCTION* (eV)
3.		1951	4.94	
		2034	4.96	
		2148	4.98	
		2259	4.99	
		2339	5.03	

+ BASED ON LESS THAN 5% OF CATHODE AREA  
 \* EXPERIMENTAL ERROR IS  $\pm 0.04$  eV  
 MAGNIFICATION = 97 X  
 EXPERIMENTAL VACUUM = BETTER THAN  $5 \times 10^{-8}$  TORR.

Figure 26. Summary of work function measurements for W,25% Re.

EXPT. NO.	EMISSION MICROGRAPH (WITH GRAIN NUMBERS)	SAMPLE + W, 30% Re	ACTUAL TEMPERATURE (°K)	EFFECTIVE WORK FUNCTION* (eV)
4.		1946	5.04	
		2051	5.04	
		2170	5.05	
		2224	5.09	
		2350	5.09	

+ BASED ON LESS THAN 5% OF CATHODE AREA  
 \* EXPERIMENTAL ERROR IS  $\pm 0.04$  eV  
 MAGNIFICATION = 97 X  
 EXPERIMENTAL VACUUM = BETTER THAN  $5 \times 10^{-8}$  TORR.

Figure 27. Summary of work function measurements for W, 30% Re.

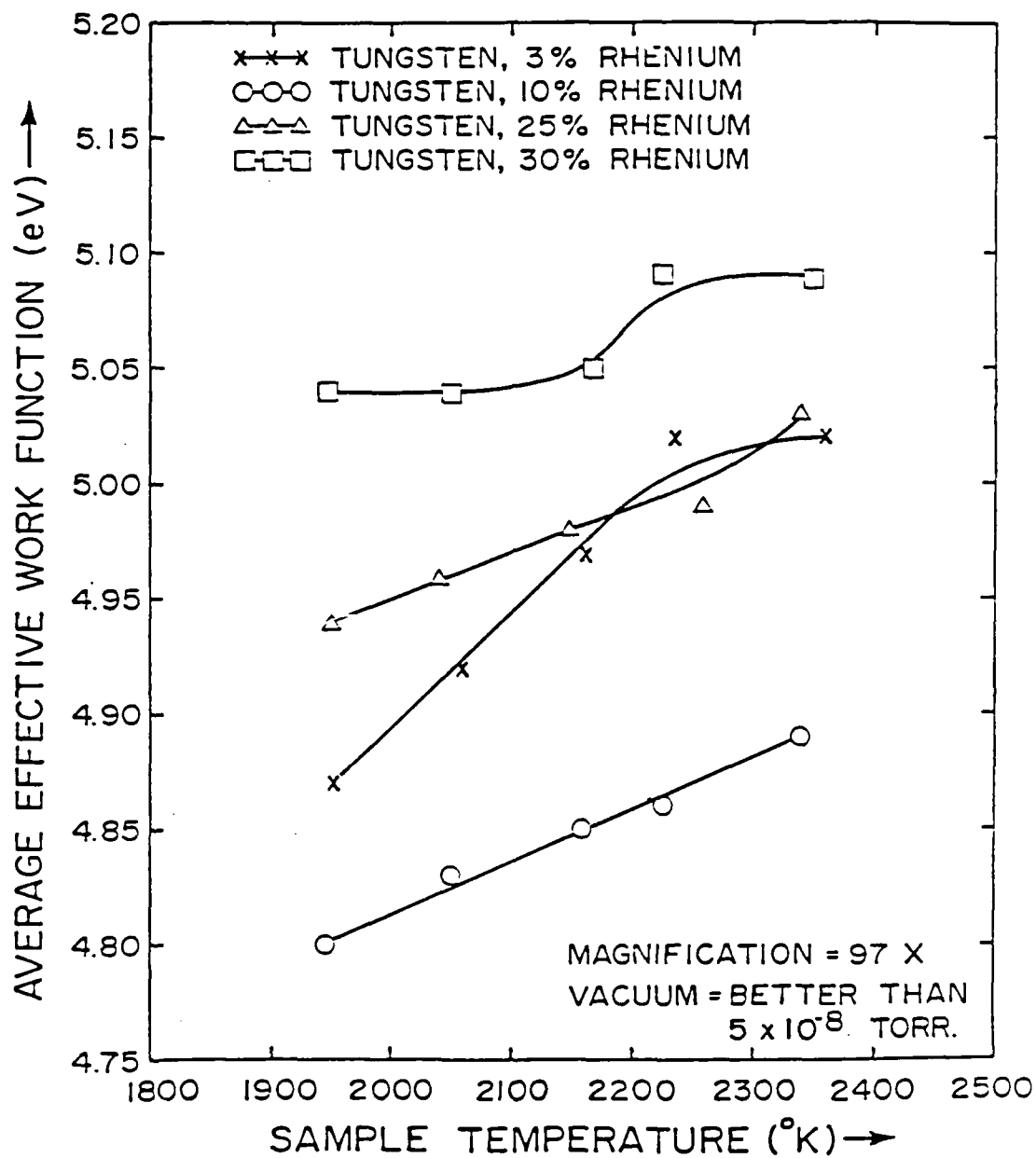


Figure 28. Variation of average effective work function with sample temperature.

increases with temperature, the maximum increase being registered by the W,3% Re sample and the minimum increase, by the W,30% Re. However Figure 29 is a more appropriate variation as the work function parameter P, takes into consideration the temperature as well as the work function between the upper and lower temperature limits. Here we see that the rate of increase of work function with temperature is almost the same for the W,3% Re, the W,10% Re and the W,25% Re samples but it trails the temperature quite a bit, for the W,30% Re sample. This could be due to the presence of a second phase of rhenium which has a solubility limit of 27% in tungsten. These results could well be used as an initial step in studying the diffusivity of rhenium in tungsten.

Figure 30 shows the variation of average effective work function with rhenium content in tungsten. Beyond 10% Re, the work function increases with rhenium content and this could be expected as the work function of pure tungsten is lower than that of pure rhenium. However, there is a decrease in work function in the 3% Re to 10% Re range, a behavior which was observed in an earlier investigation by Jacobson [29]. This anomalous behavior is similar to that of other properties of W,Re, such as microhardness, spectral emissivity, electrical resistivity, etc. investigated earlier, in that they all exhibit minimum values at around 5% Re. This has been attributed to the change in ductility at this percentage of rhenium and it would certainly prove to be enlightening to study the effect of ductility on the average effective work function of sintered W,Re alloys.

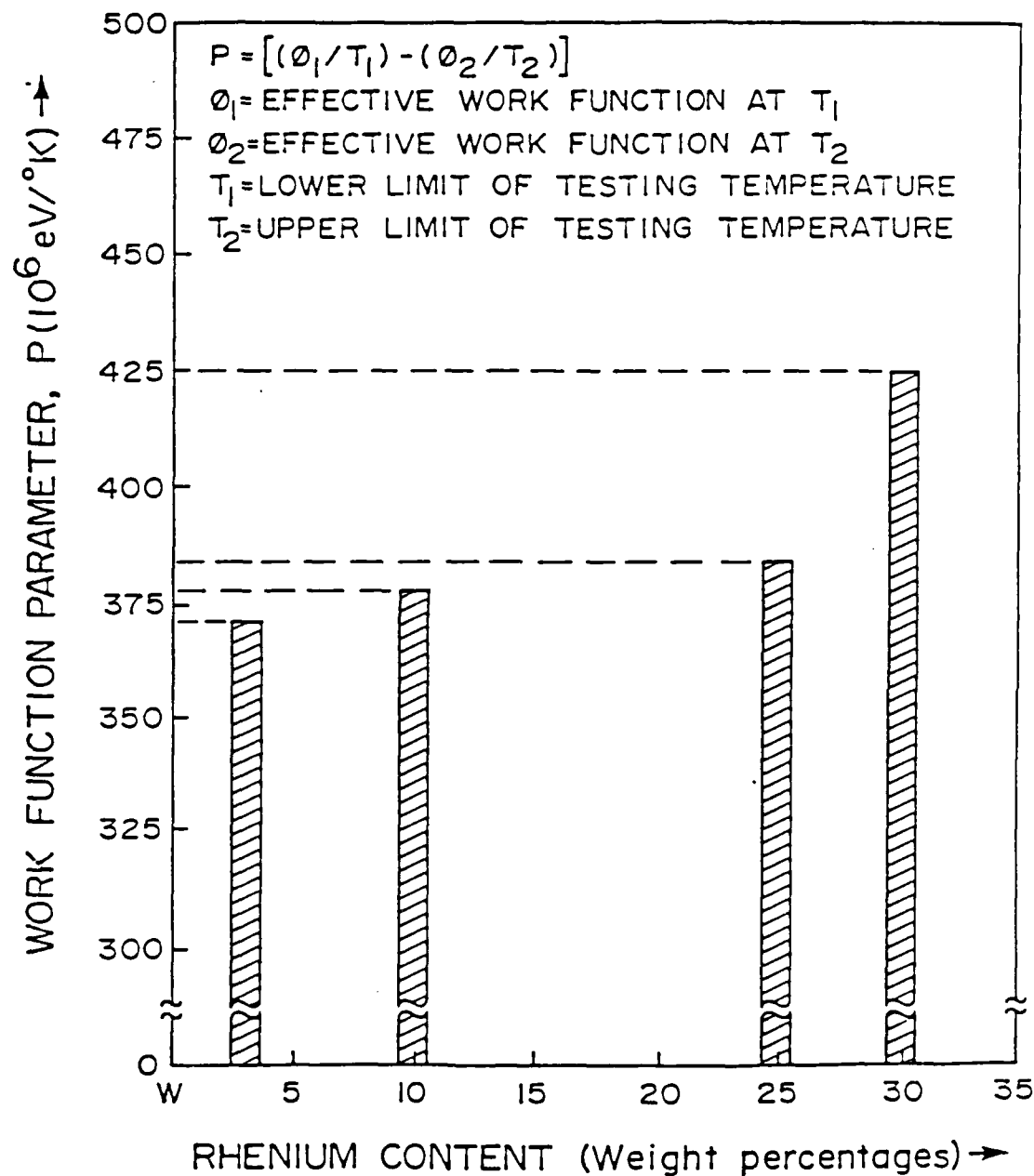


Figure 29. Variation of work function parameter, with rhenium content.

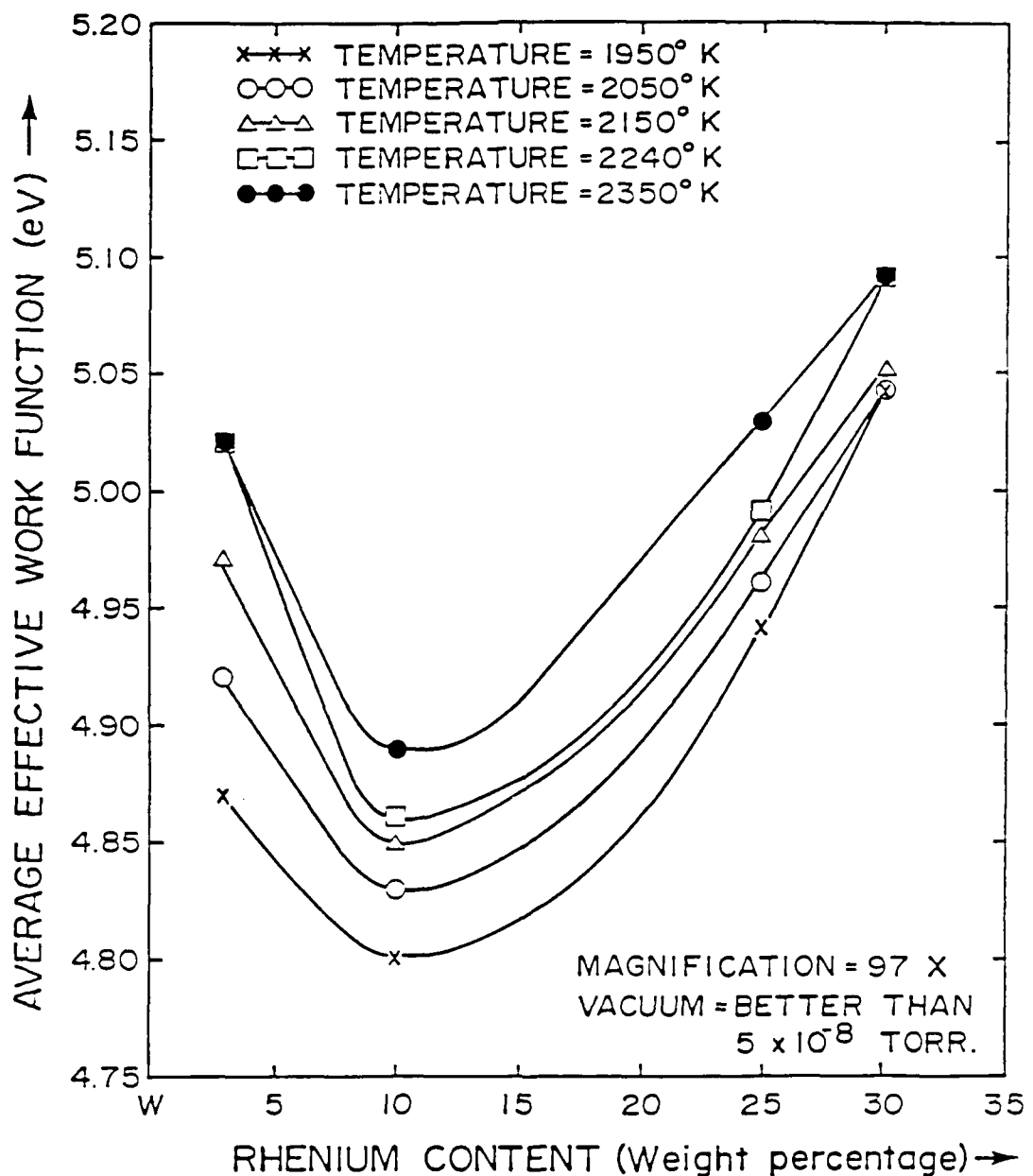
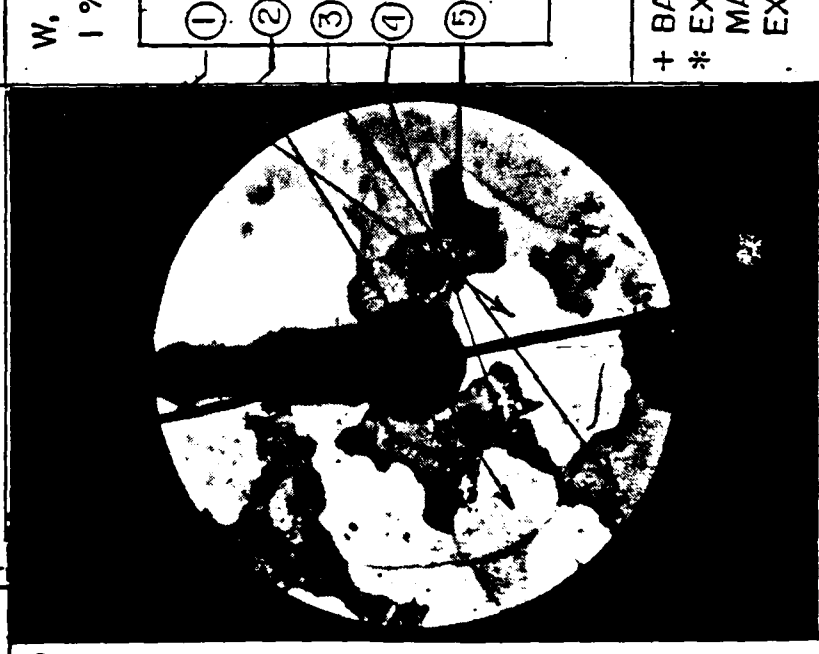


Figure 30. Variation of average effective work function with rhodium content.

### 2.6.2 Effective work functions of thoriated W,Re alloys

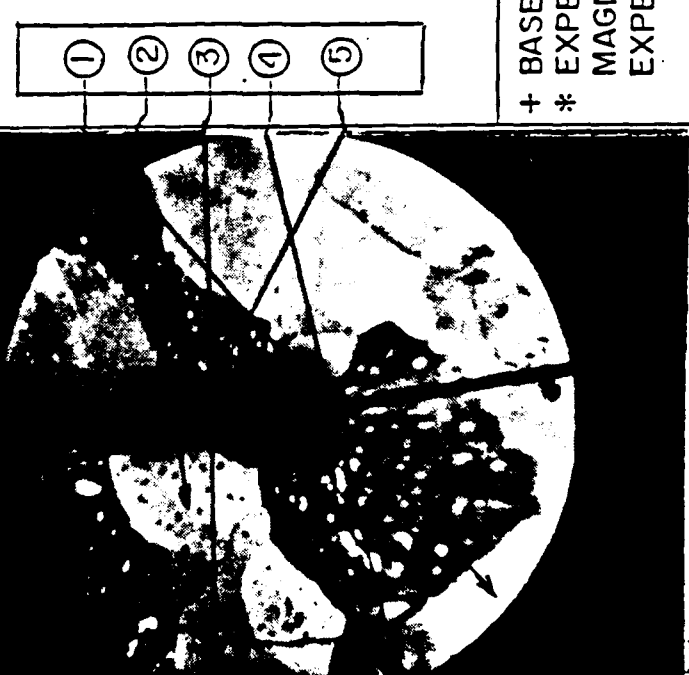
A summary of the results of the tests conducted on the four thoriated tungsten rhenium alloys, is provided in each of the Figures 31, 32, 33 and 34. The variation of the average effective work function with sample temperature and rhenium content are shown in Figure 35 and Figure 36 respectively. As in the case of W,Re, each emission micrograph has five grains numbered on it, representing increasing or decreasing intensities. Current readings were recorded from each grain at each temperature and then averaged out to give the average effective work function of that sample at that operating temperature.

The plots in Figure 35 represent the variation of average effective work function with sample temperature. As in the case of W,Re the work functions for each sample were found to increase with temperature. This would be expected from any sample because the increase in temperature dominates over the increase in current density in the Richardson-Dushman equation. When compared to corresponding plots for W,Re alloys in Figure 28, we observe that there is a marginal increase in the work function values. This is the effect of adding thoria which by itself has a bare work function of 6.3eV and together with polycrystalline rhenium which also has a higher bare work function than tungsten, generally tends to increase the average effective work function. However the variation of work function with temperature for the thoriated samples over the investigated temperature range was found to be less than that for tungsten,rhenium. This effect is probably derived from the fact that above 2100 K some of the thorium that might have been at the surface at lower temperatures, evaporates and at higher

EXPT. NO.	EMISSION MICROGRAPH (WITH GRAIN NUMBERS)	SAMPLE <sup>+</sup>	ACTUAL TEMPERATURE (°K)	EFFECTIVE WORK FUNCTION <sup>*</sup> (eV)
5		W, 0% Re, 1% ThO <sub>2</sub>	1933	4.83
			2043	4.84
			2153	4.88
			2243	4.89
			2353	4.91

+ BASED ON LESS THAN 5% OF CATHODE AREA  
 \* EXPERIMENTAL ERROR IS  $\pm 0.04$  eV  
 MAGNIFICATION = 99 X  
 EXPERIMENTAL VACUUM = BETTER THAN  $5 \times 10^{-8}$  TORR.

Figure 31. Summary of work function measurements for W, 1% ThO<sub>2</sub>.

EXPT. NO.	EMISSION MICROGRAPH (WITH GRAIN NUMBERS)	SAMPLE + W, 10% Re, 1% ThO <sub>2</sub>	ACTUAL TEMPERATURE (°K)	EFFECTIVE WORK FUNCTION * (eV)
6		1933	4.82	
	2043		4.85	
	2153		4.90	
	2243		4.91	
	2353		4.95	

+ BASED ON LESS THAN 5% OF CATHODE AREA  
 \* EXPERIMENTAL ERROR IS  $\pm 0.04$  eV  
 MAGNIFICATION = 99 X  
 EXPERIMENTAL VACUUM = BETTER THAN  $5 \times 10^{-8}$  TORR.

Figure 32. Summary of work function measurements for W, 10% Re, 1% ThO<sub>2</sub>.

EXPT. NO.	EMISSION MICROGRAPH (WITH GRAIN NUMBERS)	SAMPLE + W, 25% Re, 1% ThO <sub>2</sub>	ACTUAL TEMPERATURE (°K)	EFFECTIVE WORK FUNCTION* (eV)
7			1933	4.95
			2043	4.99
			2153	5.00
			2243	5.01
			2353	5.02

+ BASED ON LESS THAN 5% OF CATHODE AREA  
\* EXPERIMENTAL ERROR IS  $\pm 0.04$  eV  
MAGNIFICATION = 99 X  
EXPERIMENTAL VACUUM = BETTER THAN  $5 \times 10^{-8}$  TORR.

Figure 33. Summary of work function measurements for W, 25% Re, 1% ThO<sub>2</sub>.

EXPT. NO.	EMISSION MICROGRAPH (WITH GRAIN NUMBERS)	SAMPLE <sup>+</sup>	ACTUAL TEMPERATURE (°K)	EFFEFFECTIVE WORK FUNCTION <sup>‡</sup> (eV)
8.	W, 30% Re, 1 % ThO <sub>2</sub>	1933	5.06	
		2043	5.06	
		2153	5.07	
		2243	5.08	
		2353	5.09	

+ BASED ON LESS THAN 5% OF CATHODE AREA  
 \* EXPERIMENTAL ERROR IS  $\pm 0.04$  eV  
 MAGNIFICATION = 99 X  
 EXPERIMENTAL VACUUM = BETTER THAN  $5 \times 10^{-8}$  TORR.



Figure 34. Summary of work function measurements for W, 30% Re, 1% ThO<sub>2</sub>.

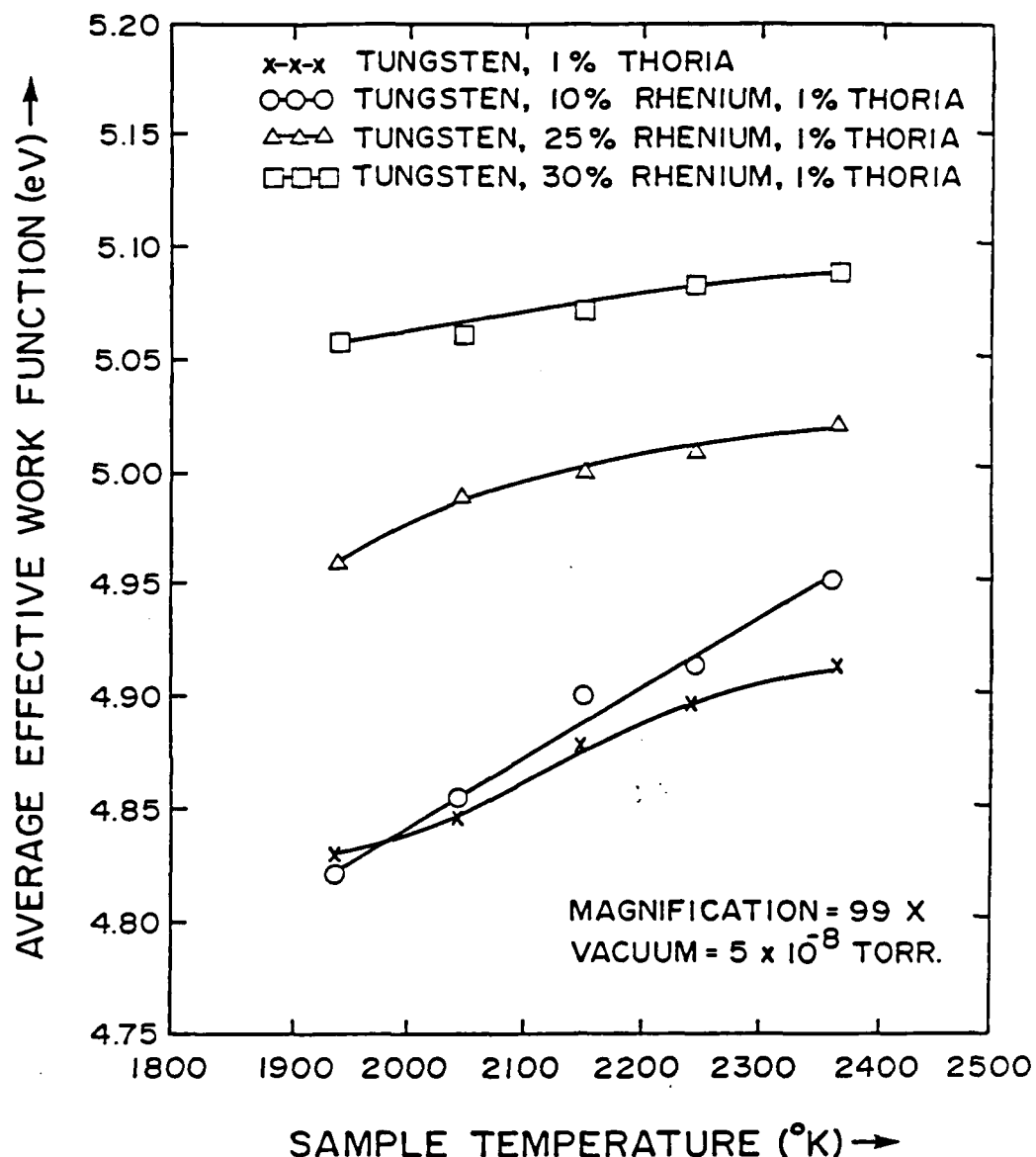


Figure 35. Variation of average effective work function with sample temperature for thoriated W,Re.

temperatures the evaporation rate is faster than the diffusion to the surface. Thus at temperatures above 2200 K the work function of the thoriated W,Re alloy approaches that of the W,Re alloy.

Figure 36 indicates the variation of average effective work function of the thoriated samples, with increase in rhenium content. The anomalous behavior that was observed for the tungsten, rhenium alloys was observed only at 1933 K for the thoriated samples. At higher temperatures there was a gradual increase in the work function with addition of rhenium. The addition of thoria generally tends to reduce the ductility of tungsten, rhenium which could have resulted in the increase in work function values for the W,10% Re, 1% ThO<sub>2</sub> sample. This, together with the anomalous behavior for the W,Re alloys in the range of 5% to 20% Re, is evidence for the support of the argument that work function may have a strong dependence on the ductility and this would certainly merit further investigation.

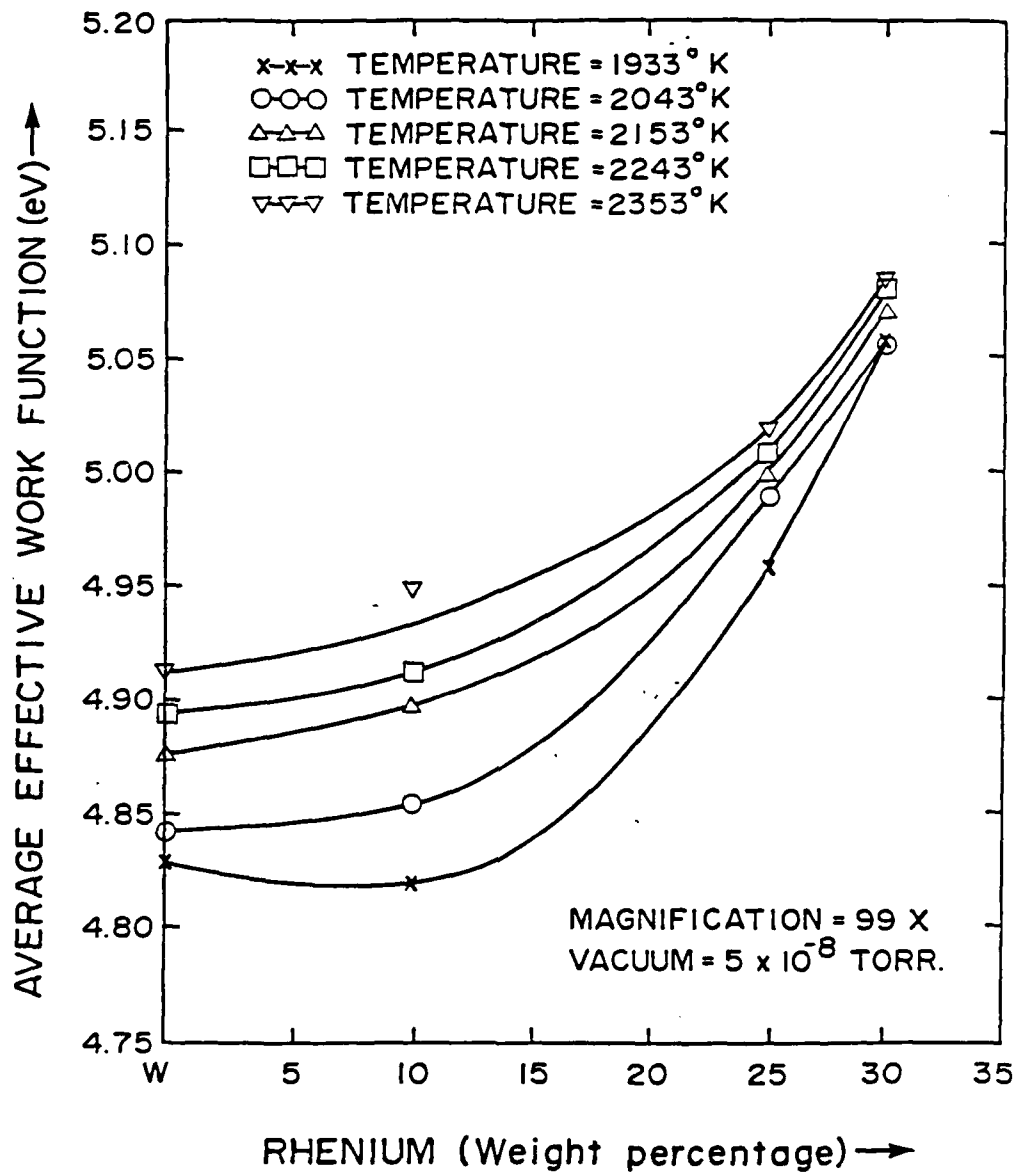


Figure 36. Variation of average effective work function with rhenium content for thoriated W,Re.

### 3. EFFECT OF TEMPERATURE ON THE EMISSIVITY OF W,Re AND THORIATED W,Re ALLOYS

Developing materials with superior thermal properties to produce higher source and sink temperatures necessitates the availability of accurate high temperature materials data. Alloying the base metal tungsten with rhenium and thoria changes the thermionic work functions of the surfaces. Since work function is a surface characteristic, its change is brought about by a physical change on the surface of the sample being tested and this would certainly affect other properties that are dependent on the nature of the surface. At elevated temperatures, spectral emissivity is one such property that deserves investigation, preferably with accurate methods. Here, we present the results of the emissivity measurements on sintered tungsten, rhenium and thoriated tungsten, rhenium alloys. A photon counting pyrometer of very high precision, built at Arizona State University and calibrated at Los Alamos National Laboratories was used for these studies.

#### 3.1 Introduction to elevated temperature emissivity measurement

Measurement of emissivity of material surfaces at high temperatures was attempted in the early 1900s. However the techniques developed were not perfected until the middle of the century when Devos [15] measured the emissivity of a straight rolled tungsten strip, by comparing the spectral radiant intensity of the wall with that of a hole in a tubular black body to which the tungsten ribbon was shaped. Emissivities were evaluated as a function of wavelength in the region  $0.23 - 2.7 \mu\text{m}$ , for temperatures ranging from 1600 K to 2800 K. Since then a number of techniques such as reflection methods, black body as part of the

specimen, etc. have been developed and improved. Gubareff [24] and his associates have compiled data on tungsten and this includes the emissivity at different temperatures and wavelengths of thermal radiation. They found that in the wavelength range of 0.2  $\mu\text{m}$  to 0.7  $\mu\text{m}$ . the emissivity decreased with temperature but observed a contradictory behavior for wavelengths greater than 1  $\mu\text{m}$ . Petrov [48] and Sadykov [56] of the U.S.S.R. were responsible for developing an experimental apparatus for determining the integral emissivity of metals and alloys at high temperatures and determining the temperature dependence of the radiating power of metals, respectively. The former used the apparatus to measure the integral emissivity of molybdenum, which was found to vary from 0.13 at 1300 K to 0.29 at 2890 K. The latter found that there was a cut-off wavelength above which the spectral emissivity increased with temperature but below which it decreased with temperature.

Branstetter and Schaal [8] studied the emittance of small cavities and came up with the fact that a cylindrical enclosure can be treated as an isothermal enclosure only if it has a length to diameter ratio of at least 10:1. Since this period, cylindrical holes with an adequate length to diameter ratio have been used to approximate isothermal enclosures. The integral hemispherical emissivity, of the IV B group metal, was determined [73] and its dependence on electronic structure was also considered. The emissivity was found to increase with temperature in each of the materials, titanium, zirconium and hafnium but only to a very small extent. The type of photon counting pyrometer with which the experiments were conducted was originally designed at Los Alamos National Laboratory by E.K. Storms and B.A. Mueller [66] in 1978.

They improved temperature measuring techniques considerably, especially at high temperatures, by constructing the photon counting pyrometer with commercially available equipment and were able to measure temperatures from 1400 K to above 2200 K within 1 K of the International temperature scale.

Measurement of high temperatures and subsequent emissivities by means of optical pyrometry involves a number of cumulative errors. Quinn [50] reviewed the methods available for the calculation of emissivity and gave guidelines for the minimization of errors due to the absence of temperature uniformity and so on. With the advent of liquid metal applications such as heat pipes, thermal energy storage capacitors, etc., it has become increasingly important to measure the emissivities of liquid metals, which are operating at high temperatures. Ratanpupech and Bautista [52] measured the normal spectral emissivities of liquid iron, liquid nickel and liquid iron, nickel alloys at a wavelength of 0.645  $\mu\text{m}$ . The emissivities were found to be fairly constant at 0.346 for iron and 0.340 for nickel over the entire temperature range. Shur et al. [62] measured the integrated hemispheric emissivity of titanium iodide in the temperature interval of 1100 to 1900 K and observed that there was a sudden change in emissivity at 1165 K when the polymorphic transformation occurs. Yashiko Ohwada [47] compared numerical results of spectral and total emissivities, among cylinders, cones, double cones, etc.

The photon counting pyrometer was most recently used [7] to obtain emissivity data at high temperatures for hafnium, iridium, molybdenum,

niobium, ruthenium, tantalum and other alloys of interest in thermionic energy conversion application.

### 3.1.1 Theory of operation of the photon counting pyrometer

The photon counting pyrometer is a device which operates on the basis of Planck's law which states that the energy emitted by a target is a function of its temperature and the wavelength of emitted radiation. On this basis one can extrapolate the temperature scale above a reference temperature, which, in this case, was the melting point of copper. Radiation flux at a known wavelength is measured by the pyrometer and converted to temperature. In this pyrometer, a photomultiplier tube measures the radiation flux directly from the source, thereby eliminating uncertainties such as using the eye to compare the flux with that from a lamp, the characteristics of which may not have been established. The greater stability of the digital mode of operation and the simplicity with which it can be calibrated has made this a very accurate pyrometer for general laboratory use.

Figure 37 shows a schematic of the photon counting pyrometer and the various elements through which radiation of a known wavelength ( $0.535 \mu\text{m}$ ) has to pass before it is recorded and printed. Figure 38 is a photograph of the actual pyrometer mounted on an adjustable tripod. Pulses produced by light striking the photomultiplier are amplified and counted with a very low dead time, permitting the measurement of counting rates up to  $10^7$  per second. The photomultiplier tube which corresponds to a particular level of excitation voltage was tested along with the discriminator amplifier, at different levels of threshold and

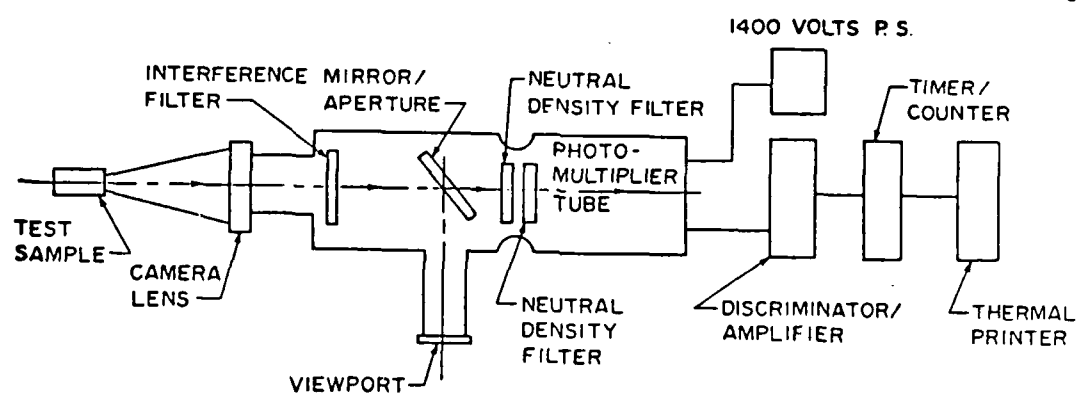


Figure 37. Schematic of the photon counting pyrometer.

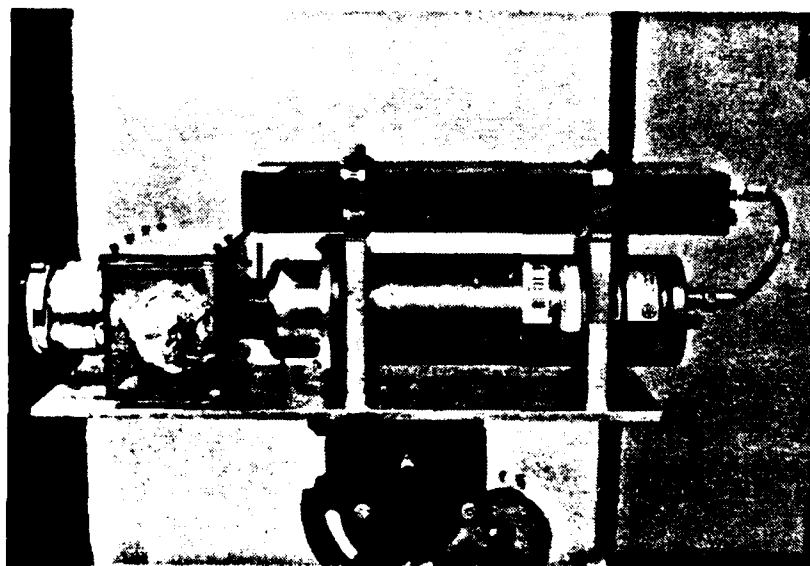


Figure 38. The photon counting pyrometer.

excitation voltages. The plateau region of the count rate-voltage curve occurred at 1400 volts and so the tube was operated at this voltage in order to obtain a linear response in the expected temperature range. The photon counter was calibrated with a black body source at a known temperature. In this case a copper furnace, operated by Dr. E. Storms at Los Alamos National Laboratories, was used for calibration. The dead time of the counting circuits and the light attenuation factors were determined for the various filters with the Equation - 10,

$$\frac{E_i}{E_{i+1}} = A_{i+1} + E_i \gamma (A_{i+1} - 1) \quad (10)$$

$i = 1, 2, 3, \dots n$

The count rate in the absence of a filter and no dead time is then given by

$$E_c = \prod_{i=1}^n A_{i+1} \left\{ \frac{E_n}{(1-\gamma E_n)} \right\} \quad (11)$$

### 3.1.2 Temperature and emissivity evaluation

Plank's spectral distribution of emissive power is given by [63]

$$e_{\lambda b}(\lambda) = \left\{ 2\pi C_1 / \lambda^5 \left( e^{C_2 / \lambda T} - 1 \right) \right\} \quad (12)$$

The ratio of the corrected number of counts at the calibration temperature  $T_0$ , to that at any other temperature  $T$ , is

$$\frac{E_0}{E} = \frac{e_{\lambda b 0}(\lambda)}{e_{\lambda b}(\lambda)} = \frac{2\pi C_1}{\lambda^5 \left( e^{C_2 / \lambda T_0} - 1 \right)} \cdot \frac{\frac{C_2 / \lambda T}{2\pi C_1}}{\left( e^{C_2 / \lambda T} - 1 \right)} \quad (13)$$

$$= e^{\left\{ \frac{C_2}{\lambda T} - \frac{C_2}{\lambda T_0} \right\}} = e^{\frac{C_2}{\lambda} \left( \frac{1}{T} - \frac{1}{T_0} \right)} \quad (14)$$

Wien's formula gives equation (15) where  $e^{C_2/\lambda T} \gg 1$ .

$$\text{or} \quad \ln(E_0/E) = \frac{C_2}{\lambda} \left[ \frac{1}{T} - \frac{1}{T_0} \right] \quad (15)$$

This is further simplified to give the unknown temperature

$$\frac{1}{T} = \frac{\lambda}{C_2} \{ \ln E_0 - \ln E \} + \frac{1}{T_0} \quad (16)$$

Substituting suitable values in Eqn. (16) produces

$$T_h = 1 / \{ 1.09 \times 10^{-3} - (\ln(E_{hc})) [3.7184 \times 10^{-5}] \} \quad (17)$$

$$\text{and} \quad T_s = 1 / \{ 1.09 \times 10^{-3} - (\ln(E_{sc})) [3.7184 \times 10^{-5}] \} \quad (18)$$

$$\text{where} \quad E_{hc} = \prod_{i=1}^n [A_{i+1} \{ E_h / (1 - \gamma \cdot E_h) \}] \quad (19)$$

$$\text{and} \quad E_{sc} = \prod_{i=1}^n [A_{i+1} \{ E_s / (1 - \gamma \cdot E_s) \}] \quad (20)$$

The directional spectral emissivity is defined as

$$\epsilon'_{\lambda}(\lambda, \theta, \phi, T_s) = \frac{e'_{\lambda}(\lambda, \theta, \phi, T_s)}{e'_{\lambda b}(\lambda, \theta, T_s)} \quad (21)$$

which is further simplified to

$$\ln [\epsilon'_{\lambda}] = \frac{C_2}{\lambda} \left[ \frac{1}{T_h} - \frac{1}{T_s} \right] \quad (22)$$

Table 9 gives all the parameters of interest that were obtained during calibration.

### 3.1.3 Primary objectives on emissivity evaluation.

To measure the emissivities in the temperature range of 1300 K to 2500 K by measuring hohlraum and surface temperatures. To determine the effect of temperature and rhenium content on the spectral emissivity of sintered tungsten and sintered, thoriaated tungsten.

## 3.2 Sample characterization and preparation.

The samples for the experiment were sintered using pure tungsten powder, pure rhenium powder and later thoria was added to these materials. Originally there were five different combinations of tungsten and rhenium, pure tungsten, W-3% Re, W-10% Re, W-25% Re and W-30% Re. Unfortunately the W-10% Re sample could not be used for experimentation as it was oxidized completely along its longitudinal axis with cracks spreading in all directions.

### 3.2.1 Electron microprobe analysis.

The as-received material was subjected to electron microprobe analysis in order to study the homogeneity of the samples which, the suppliers claimed had a porosity of less than 0.1 percent. This material was found to be more homogeneous than the ones used for thermionic emission that had a porosity of about seven percent. The results of this analysis are shown in Table 10.

Table 9. Constant parameters in evaluating emissivity.

S1. No.	Parameter	Value
1	Excitation Voltage	1400 Volts
2	Threshold	0.975 mV
3	Threshold Difference	0.300 mV
4	Dead Time	$1.1044 \times 10^{-7}$ secs.
5	Attenuation of Bell-jar A <sub>0</sub>	1.06072
6	Attenuation of N.D. Filter-1, A <sub>1</sub>	4.7780
7	Attenuation of N.D. Filter-2, A <sub>2</sub>	98.6840
8	Calibration Temperature T <sub>0</sub>	1357.95 K
9	Calibration Count Rate E <sub>0</sub>	$13.5 \times 10^3$

Table 10. Results of electron microprobe analysis (emissivity studies).

Alloy	Elements	Concentrations at different positions				
		1	2	3	4	5
W-0%Re	W	1.012	1.019	0.996	0.983	0.981
	Re	0.007	0.000	0.005	0.004	0.012
	Total	1.018	1.018	1.001	0.987	0.992
W-3%Re	W	0.955	0.950	0.945	0.965	0.962
	Re	0.042	0.049	0.038	0.034	0.052
	Total	0.996	0.998	0.982	0.999	1.014
W-10%Re	W	0.907	0.915	0.894	0.911	0.912
	Re	0.091	0.090	0.098	0.096	0.083
	Total	0.997	1.004	0.994	1.006	0.994
W-25%Re	W	0.758	0.769	0.822	0.809	0.742
	Re	0.228	0.214	0.176	0.197	0.251
	Total	0.985	0.982	0.998	1.005	0.992
W-30%Re	W	0.726	0.738	0.764	0.754	0.612
	Re	0.265	0.276	0.249	0.247	0.382
	Total	0.991	1.014	1.013	1.001	0.993

### 3.2.2 Sample fabrication and mounting details

As indicated in Figure 39, the sample for the emissivity test was a small disc, 6.35 mm diameter and 2.54 mm thick. The top and bottom surfaces were ground parallel to each other with a diamond abrasive wheel. A hohlraum corresponding to an isothermal enclosure was then drilled through the side of the disc using a copper-tungsten electrode in a Servomet Electric Discharge Machine. It has been shown [8] that deep holes drilled in an opaque material can provide emittance values near unity, so that stray radiation from other hot sources and incident on the target is absorbed rather than reflected into the pyrometer. Based on these observations, a hohlraum 0.38 mm in diameter and 3.8 mm in length was machined by electrical discharge machining. The region around the hohlraum was then polished with 240 grit carborundum wet/dry paper, to provide a flat surface, the emissivity of which was to be evaluated. The sample was then spot welded to a tantalum disc which was originally spot welded to a tantalum tube, as shown in Figure 39. The sample holder assembly was then mounted in a steel frame located inside the bell jar. Figure 40 is a photograph of the steel frame for the sample holder assembly.

### 3.3 Experimental set up for emissivity measurement

Figure 41 is a labeled schematic of the emissivity measurement system showing the various components and their relative locations. As in the thermionic emission microscope system, this system can be divided into three major categories based on their respective functions. These were the vacuum system, the electron bombardment system and the

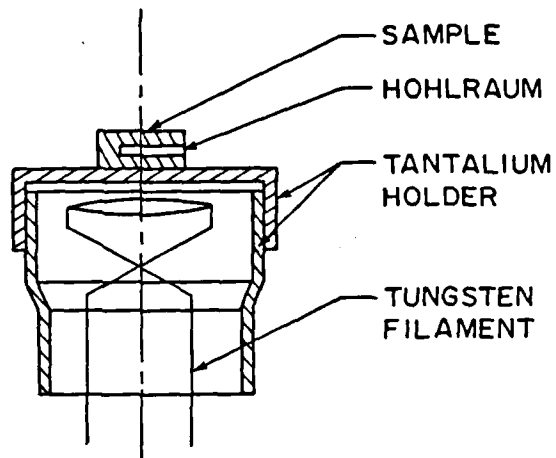


Figure 39. Cross section of the sample assembly.

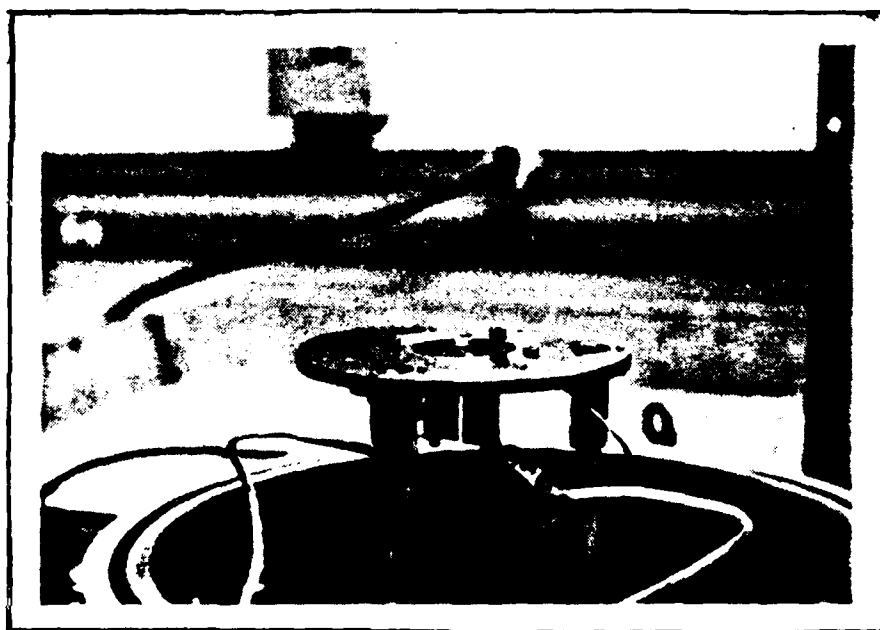


Figure 40. Steel frame to support sample holder, with filament assembly.

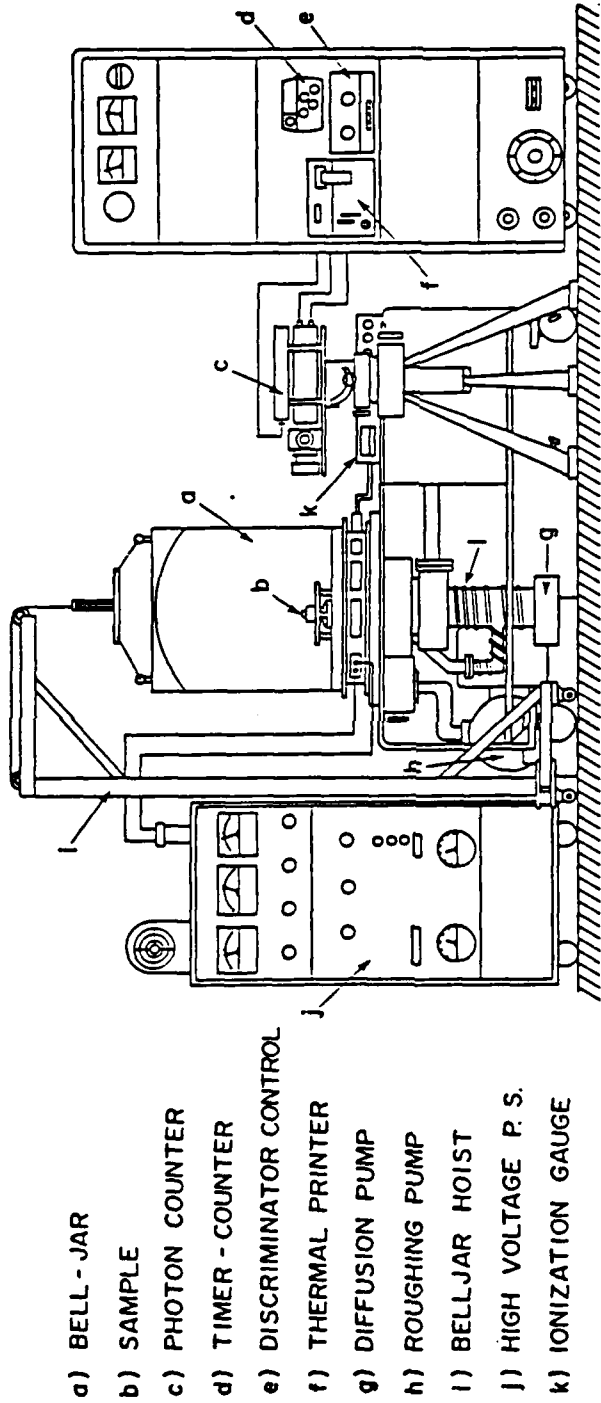


Figure 41. Schematic of the experimental set up for emissivity measurement.

temperature measurement system with the photon counter. These subsystems are described in detail in the following sections.

### 3.3.1 The vacuum and electron bombardment systems

The sample is heated to temperatures in excess of 2000 K by electron bombardment and this necessitates an evacuated chamber thereby minimizing oxidation and enhancing the efficiency of electron bombardment. A mechanical roughing pump was used to provide the rough vacuum and a diffusion pump coupled with the mechanical pump, pumped down the 60 cm. bell jar to a vacuum of better than  $5 \times 10^{-6}$  torr. An ionization gauge was used to measure pressures below  $10^{-4}$  torr while a thermocouple gauge measured higher pressures. The diffusion pump was accompanied by a liquid nitrogen baffle, and a water circulation system provided the necessary cooling.

The sample was heated by electron bombardment. An alternating current power supply was used to heat the filament. A large potential difference was applied between the sample and the heated filament to cause electrons to flow from the filament to the sample holder and heat it. The power supply that was used for activating the filament and the bombardment, is shown in Figure 42 and Figure 43 shows a glowing sample and sample holder that were being heated by striking electrons emitted by the heated filament.

### 3.3.2 Temperature measurement with the photon counter

This is the most vital part of the emissivity measurement system, as the emissivity of the surface is obtained as a function of

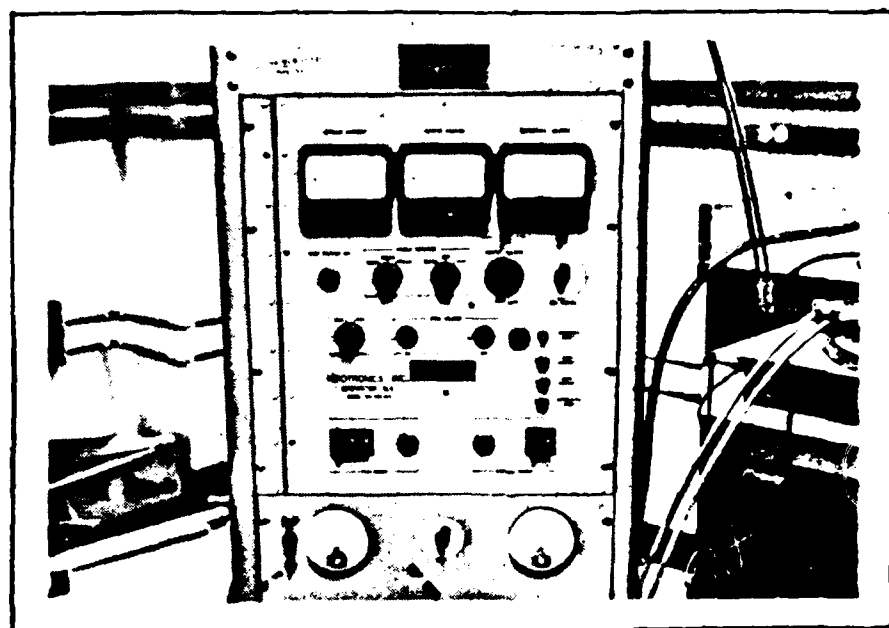


Figure 42. High voltage power supply for electron bombardment.

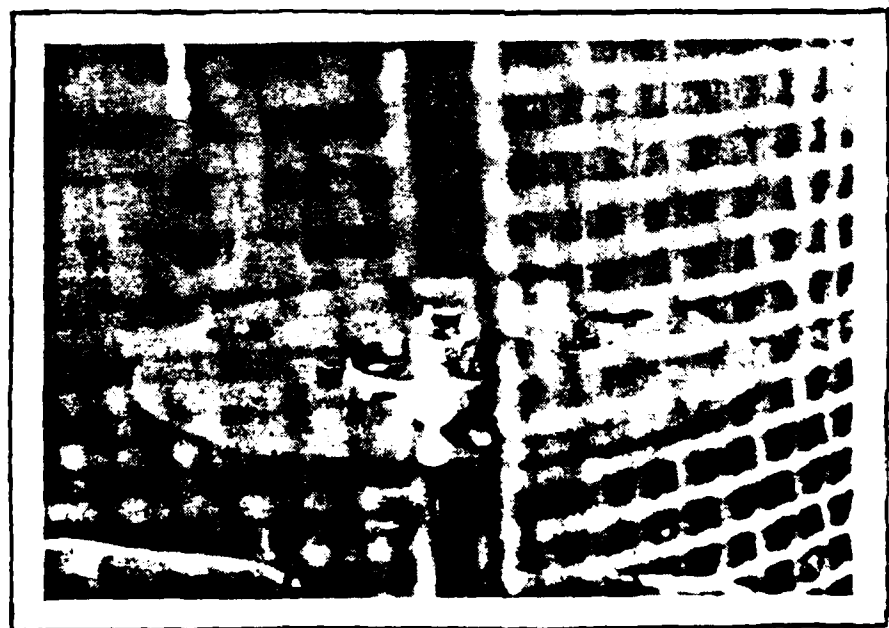


Figure 43. Sample being heated in the bell jar.

temperature. The accuracy of the values obtained depends on the accuracy of the temperatures measured.

Temperatures were measured by focusing the photon counting pyrometer (Figure 44) on the heated sample. An interference filter in the pulse counting pyrometer allows light energy of a particular wavelength ( $0.535 \mu\text{m}$ ) to be transmitted to a nickel mirror. A part of this filtered beam passes through 1) a 0.1 mm. hole in the mirror, 2) two neutral density filters, and eventually enters a photomultiplier tube. A detector in the photomultiplier tube detects and converts the energy pulses to current pulses. The discriminator-amplifier shown in Figure 45, then selects and amplifies the pulses, which are then passed on to a timer-counter eventually being displayed as a frequency of pulses. This frequency is recorded by a thermal printer and the temperatures of the hohlraum and surface, together with the emissivity, are evaluated. The details of all the components that were used in building the emissivity measurement system are provided in Appendix 3.

### 3.4 Operating procedure

The first step was to locate the sample inside the vacuum chamber and place the bell jar in position. The water supply to the diffusion pump was then initiated and the roughing pump switched on after making all the electrical connections. The diffusion pump was switched on after a roughing vacuum of  $10^{-2}$  torr was reached in order to bring the vacuum down to the  $10^{-6}$  (torr) range. The filament power supply was then activated to heat up the filament followed by the electron bombardment to attain the necessary temperature. Table 11 gives typical

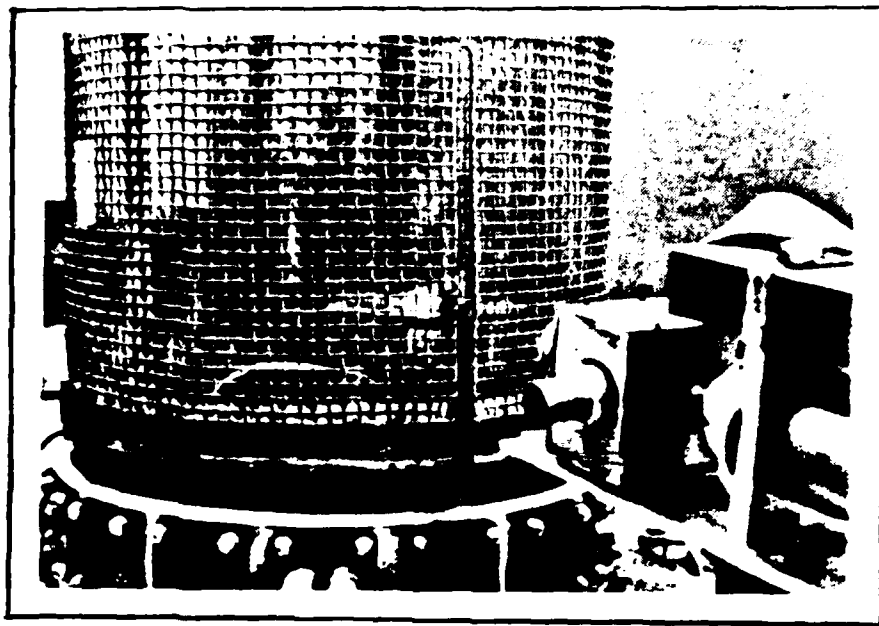


Figure 44. Temperature measurement using photon counter.



Figure 45. Printer, timer-counter and discriminator controls for the photon counter.

Table 11. Typical power supply ranges to heat the sample to various temperatures.

Test No.	Filament Current Amps AC	Filament Voltage Volts AC	Bombardment Current Millamps DC	Bombardment Voltage Kilovolts DC	Vacuum Torr	Photon Counter Scale	Approx. No. of Counts	Approx. Temperature °K
1	16.0	6.5	17.0	0.55	$4.1 \times 10^{-6}$	0	$3.8 \times 10^3$	1280°K
2	14.4	6.8	87.5	0.65	$4.0 \times 10^{-6}$	0	$24.0 \times 10^3$	1390°K
3	15.5	6.0	200.0	1.00	$2.0 \times 10^{-6}$	0	$800.0 \times 10^3$	1750°K
4	13.5	6.9	380.0	1.17	$5.0 \times 10^{-6}$	1	$2900.0 \times 10^3$	2100°K
5	10.0	4.8	220.0	3.00	$6.5 \times 10^{-6}$	2	$1100.0 \times 10^3$	2500°K

power supply ranges to heat the sample to various temperatures. Once the sample temperature had stabilized, as indicated by the pyrometer which was focused on the hohlraum, it was maintained at that temperature for one hour. At the end of this period the pyrometer was moved, to focus on the polished region around the hohlraum and the frequency of counts recorded. The hohlraum temperature was finally checked to ascertain that there was no surge in the power supply to the sample. The sample was then cooled under vacuum, its surface photographed and the entire procedure repeated at a higher temperature. All eight samples were tested in this manner at increasing temperature levels.

### 3.5 Results and discussion

The actual temperature, surface temperature and emissivity of each of the four tungsten, rhenium samples are tabulated in Table 12 and those of the four thoriated tungsten, rhenium samples are shown in Table 13. It is difficult to compare these results with those presented by earlier investigators because the conditions under which the tests were done, differ in terms of a) the wavelength of the radiation, b) the type of material (arc cast, sintered, electron beam melted etc.,), c) the surface condition for emissivity measurement and various other factors that contribute to the variation in emissivity values. However, comparisons are made wherever possible and the trends, discussed in context with the application for which it is intended.

Table 12. Temperatures of hohlräum and surface and emissivity values.

Specimen	Frequency Counts		Photon Counter Scale	Calculated Temperature °K		Normal Spectral Emissivity [ $\epsilon_\lambda'$ ]
	Hohlräum	Surface		Hohlräum	Surface	
Tungsten	3.882x10 <sup>3</sup>	2.586x10 <sup>3</sup>	0	1281	1256	0.666
	23.289x10 <sup>3</sup>	13.989x10 <sup>3</sup>	0	1101	1365	0.599
	1015.690x10 <sup>3</sup>	538.248x10 <sup>3</sup>	0	1757	1681	0.500
	8083.250x10 <sup>3</sup>	1602.072x10 <sup>3</sup>	1	2170	2027	0.416
	2136.059x10 <sup>3</sup>	1204.483x10 <sup>3</sup>	2	2722	2513	0.497
	28.849x10 <sup>3</sup>	17.159x10 <sup>3</sup>	0	1117	1379	0.521
	864.847x10 <sup>3</sup>	419.857x10 <sup>3</sup>	0	1737	1654	0.459
	2824.109x10 <sup>3</sup>	1925.449x10 <sup>3</sup>	1	2172	2062	0.516
	1050.3x10 <sup>3</sup>	482.451x10 <sup>3</sup>	2	2513	2322	0.415
	28.067x10 <sup>3</sup>	13.381x10 <sup>3</sup>	0	1115	1362	0.476
Tungsten - 3 at. % Rhenium	1085.620x10 <sup>3</sup>	518.456x10 <sup>3</sup>	0	1766	1683	0.472
	2997.55x10 <sup>3</sup>	1743.95x10 <sup>3</sup>	1	2163	2043	0.482
	750.586x10 <sup>3</sup>	297.639x10 <sup>3</sup>	2	2421	2226	0.376
	26.330x10 <sup>3</sup>	16.083x10 <sup>3</sup>	0	1110	1374	0.610
	949.055x10 <sup>3</sup>	602.975x10 <sup>3</sup>	0	1749	1694	0.609
Tungsten - 30 at. % Rhenium	1513.902x10 <sup>3</sup>	806.003x10 <sup>3</sup>	1	2017	1913	0.487
	366.093x10 <sup>3</sup>	980.99x10 <sup>3</sup>	2	2266	2116	0.432
	161.671x10 <sup>3</sup>	407.462x10 <sup>3</sup>	2	2488	2288	0.389

Table 13. Temperatures of hohlraum and surface and emissivity values for thoriated tungsten, rhenium.

Specimen	Corrected Frequency Counts ( $10^{-2}$ )		Photon Counter Scale	Calculated Temperature (K)		$\epsilon_\lambda$
	Hohlraum	Surface		Hohlraum	Surface	
Tungsten, 1% thoria	23.761	15.165	0	1413	1367	0.525
	1004.532	615.453	0	1760	1684	0.503
	2712.316	1312.075	1	2120	2005	0.483
	734.120	336.124	2	2412	2251	0.451
Tungsten, 3% rhenium, 1% thoria	26.431	11.869	0	1425	1367	0.449
	990.782	431.146	0	1750	1658	0.425
	2770.360	1169.322	1	2142	2004	0.421
	725.361	312.004	2	2390	2222	0.426
Tungsten, 10% rhenium, 1% thoria	27.120	12.006	0	1430	1365	0.410
	862.745	354.275	0	1738	1642	0.406
	2730.600	1032.441	1	2125	1973	0.377
	741.430	291.412	2	2420	2229	0.385
Tungsten, 25% rhenium, 1% thoria	**	**	**	1458	1393	0.422
	**	**	**	1771	1672	0.407
	**	**	**	2142	1769	0.378
	**	**	**	2432	2230	0.365
Tungsten, 30% rhenium, 1% thoria	**	**	**	1450	1394	0.473
	**	**	**	1761	1675	0.455
	**	**	**	2135	1992	0.406
	**	**	**	2410	2233	0.412

### 3.5.1 Variation of normal spectral emissivity with temperature and rhenium content.

Figure 46 is a plot of the variation of spectral emissivity of tungsten, rhenium at elevated temperatures. The plots show a decrease in the values of the normal spectral emissivity with increase in temperature. This behavior is caused, to some extent, by the flattening of rough projections as strain-free grains start developing on recrystallization, giving rise to a smooth surface at fairly high temperatures (2600 K). Superimposed on the plot in Figure 46(a), are the curves for the data from Gubareff [24] and Larrabee [40], where it can be seen that there is a cut-off wavelength above which the spectral emissivity increases with temperature and below which, it decreases with temperature as in the present case with radiation of wavelength 0.535  $\mu\text{m}$ . The results obtained are in good correspondence with that of Sadykov [56], who was also responsible for analytically determining the existence of the cut-off wavelength ( $\sim 0.72 \mu\text{m}$ ). The two other curves indicated in Figure 46(a) were obtained from [7], and show the emissivity data acquired from arc melted tungsten samples with different surface conditions. We could conclude that the measured data lies within the range of past test results and from the trends exhibited, the photon counting pyrometer and the associated components in the test rig could be used fairly accurately for emissivity measurement in the future.

Though tungsten, rhenium is a fairly common alloying combination, very little information is available on the emissivities of these alloys at elevated temperatures. Now that it has been established that small

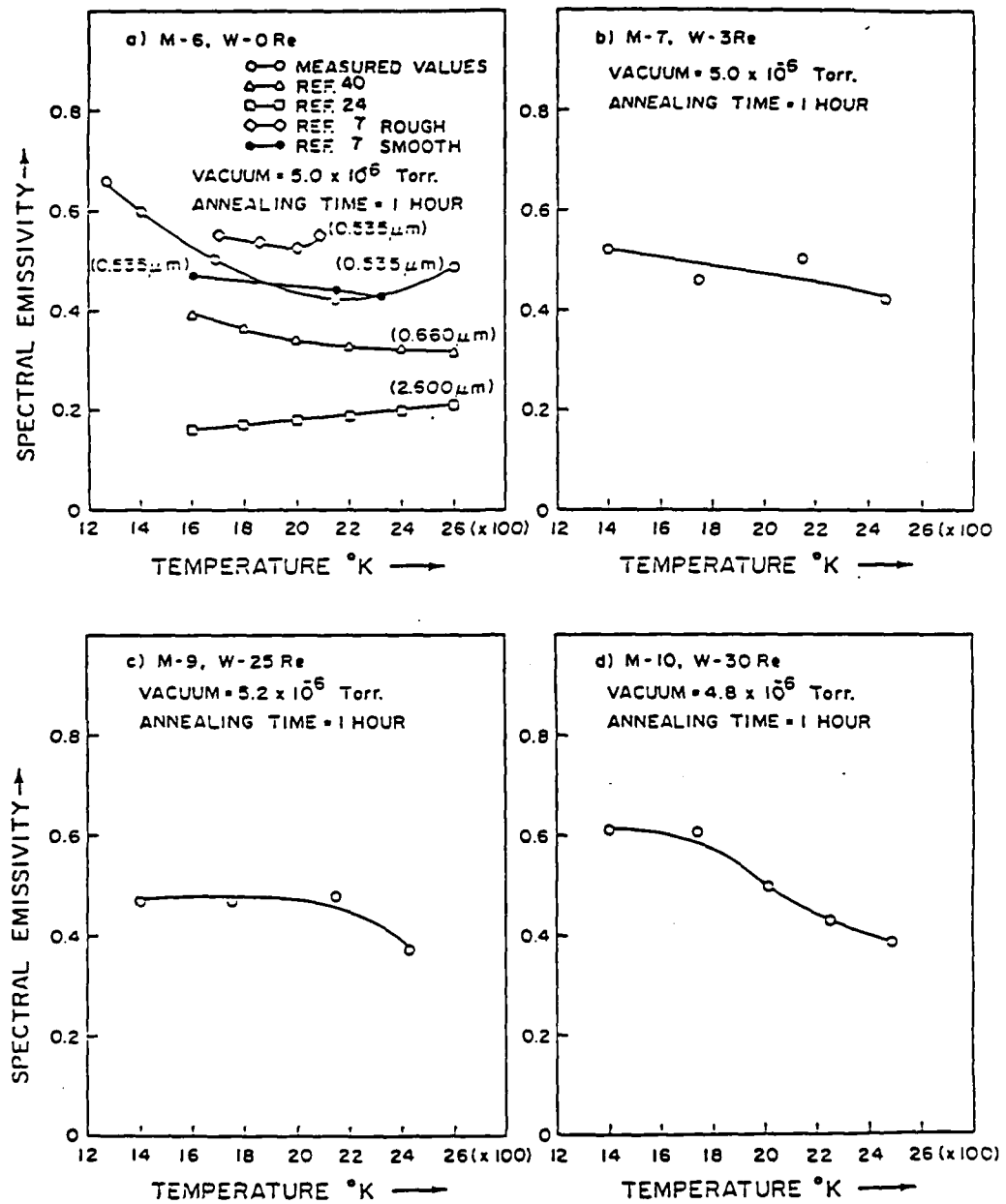


Figure 46. Variation of spectral emissivity of tungsten, rhenium at elevated temperatures.

additions of rhenium are definitely instrumental in improving some of the qualities of tungsten, such as ductility, fabricability, recrystallization temperature etc., it is important that we have a sound knowledge of some of the elevated temperature properties of this combination. All the tungsten, rhenium alloys in Figure 46 exhibited similar behavior in that the emissivity decreased with increase in temperature. The W,3% Re and W,25% Re samples showed a very small decrease whereas there was a fairly large gradient of emissivity in the W,30% Re sample. The W,30% Re sample indicated that the presence of a hard second phase material tends to make it behave in a fashion similar to that of the brittle tungsten. Microhardness values further confirmed this behavior. However, the softer and more ductile W,3% Re and W,25% Re samples had steady values of emissivity in the 1400 K to 2200 K range, which also happens to be the useful operating temperature range of emitters and collectors in thermionic energy converters. The W,25% Re sample had the lowest values of emissivity in the temperature range of interest and from TEC application point of view, this would be an ideal combination to minimize heat losses and improve the efficiency of energy conversion.

Figure 47 represents plots indicating the variation of emissivity of pure tungsten with the addition of rhenium at different operating temperatures. The behavior at each temperature (except 2150 K) seems to indicate that there is a minimum in the emissivity values at some percentage of rhenium between 3% and 25%. Due to the problem of oxidation, it was not possible to get valuable information from the W,10% Re sample. However, it is not unusual to have convolutions in

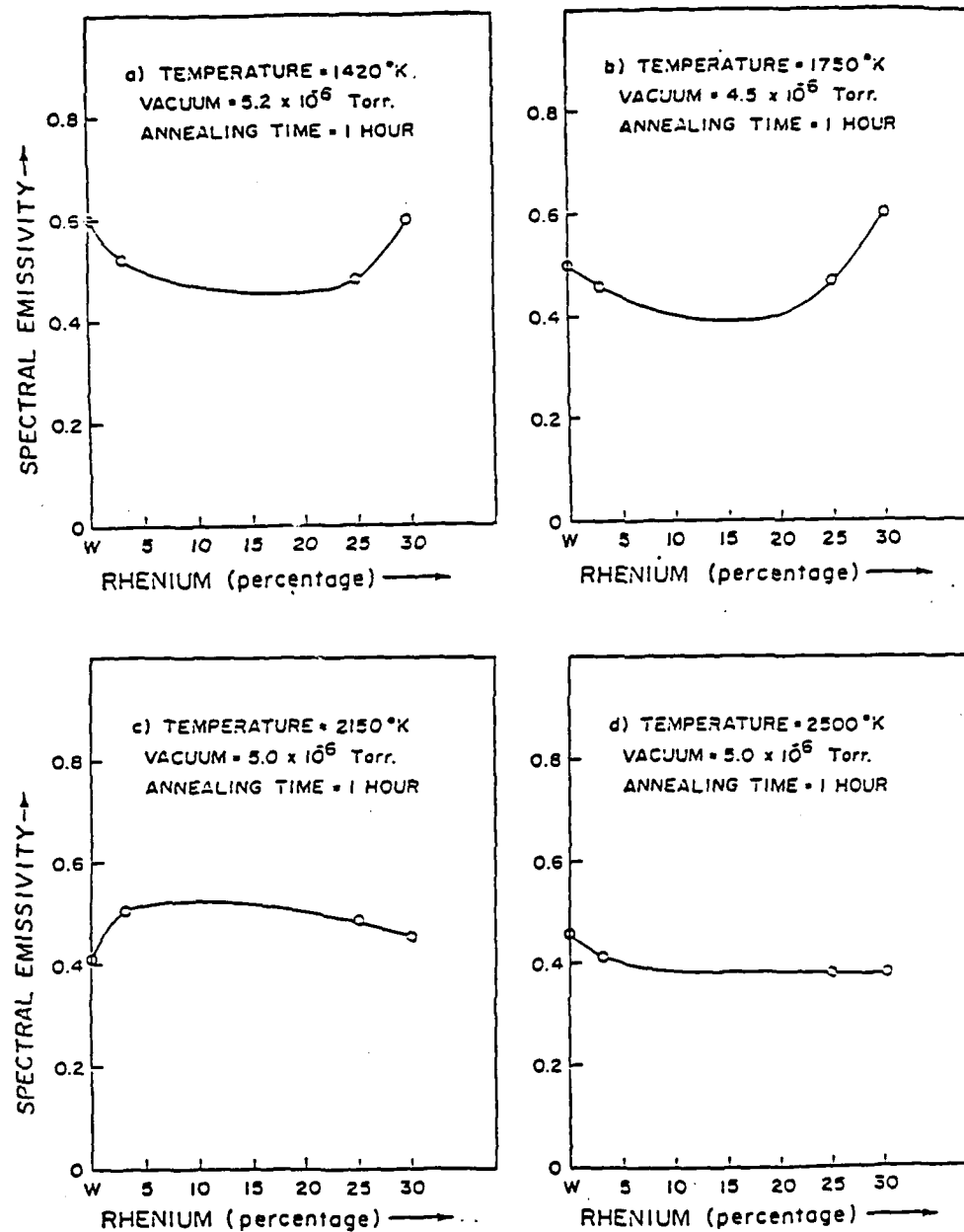


Figure 47. Variation of spectral emissivity of tungsten with the addition of rhenium.

this range, as has been shown by Klopp et al [37] for the bend transition temperature of tungsten, rhenium and the tensile strength [51] of Mo, Hf, C alloys. Thus there certainly seems to be some uncertainty in the region between 3% Re and 25% Re.

With more homogeneous material, there exists a possibility of getting uniform curves for emissivity as a function of temperature which can then be used to express emissivity of a mixture of elements, in terms of their mole fractions and individual emissivities as Ratanapuech [52] did for liquid metal alloys.

### 3.5.2 Effect of alloying sintered W,Re with thoria

Table 13, Figure 48 and Figure 49 present the effects of alloying thoria on the normal spectral emissivity of tungsten, rhenium. The measured and calculated temperatures and emissivity values in Table 13 seem to show a general trend in the decrease of spectral emissivity with the increase in operating temperature. The same trends were observed in the tungsten, rhenium alloys but the variation in the 1400 K to 2500 K range was greater than that observed in the thoriated tungsten, rhenium alloys. The decrease in emissivity with temperature is attributed to the change in surface undulations which smooth out at high temperatures. However the steady values of emissivity for each alloy in the temperature range of interest as seen in Figure 48 could be due to the fact that the grain sizes for the thoriated samples at a given temperature were smaller than their corresponding counterparts in the tungsten, rhenium alloys. This would need a more detailed investigation before it can be confirmed as there is no information available on the

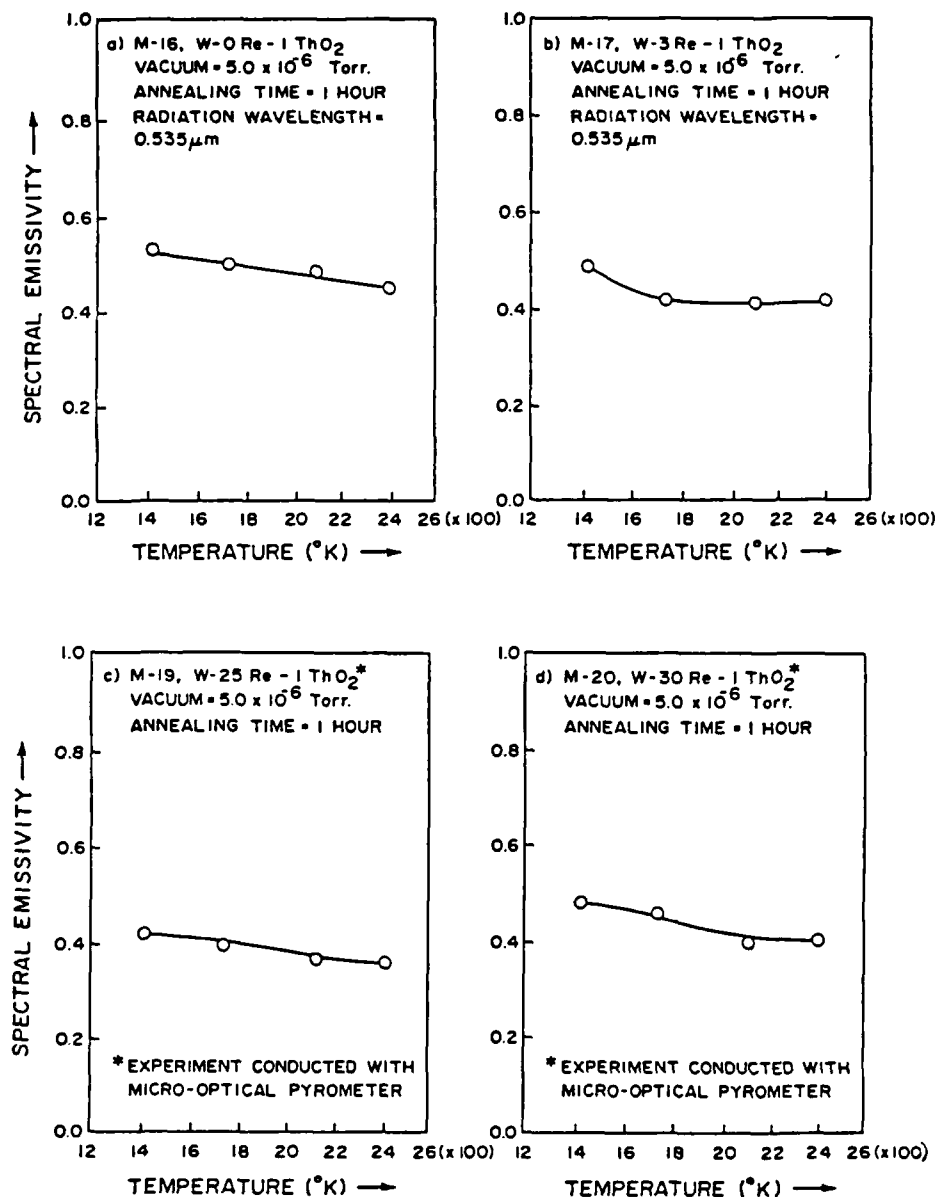


Figure 48. Variation of spectral emissivity of thoriated tungsten, rhenium at elevated temperatures.

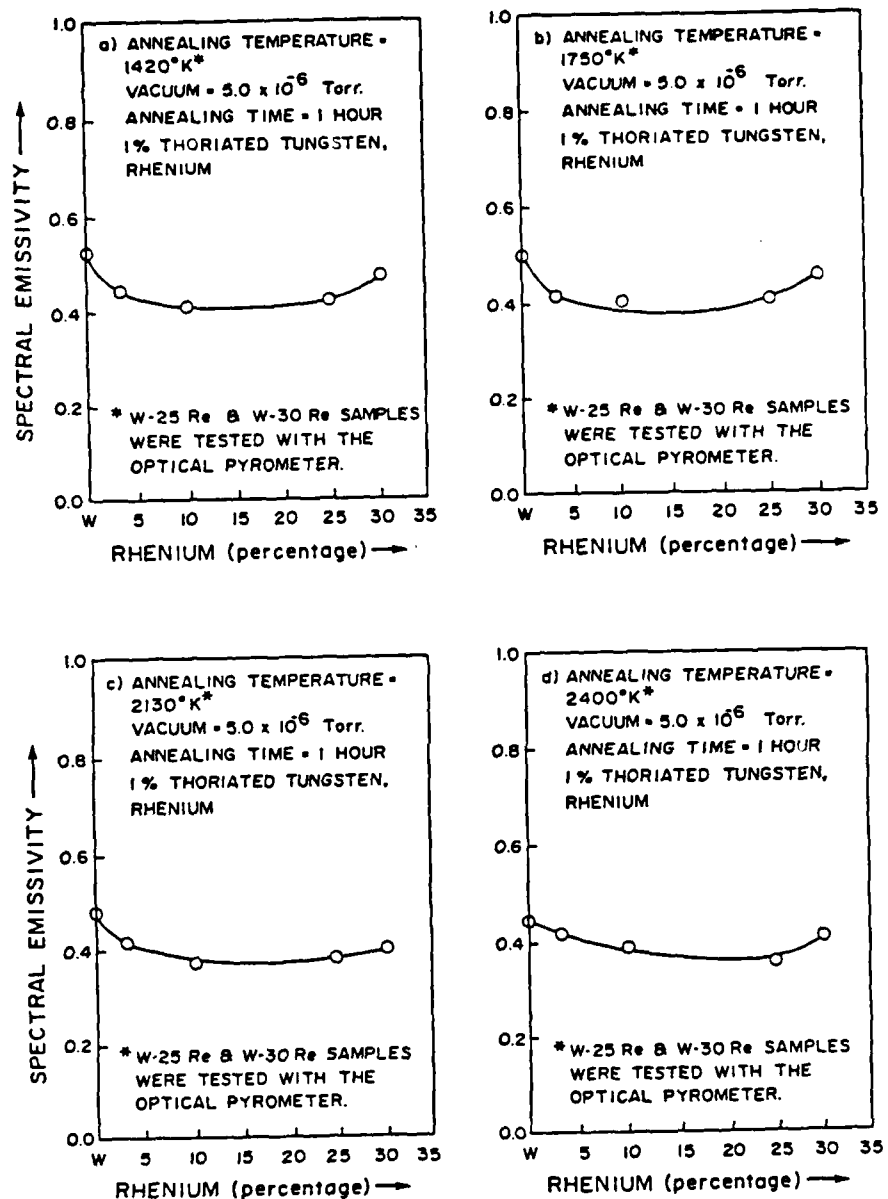


Figure 49. Variation of spectral emissivity of thoriated tungsten, with the addition of rhenium.

behavior of spectral emissivity for W,Re, ThO<sub>2</sub> alloys. Figure 49 shows the variation of the spectral emissivity of thoriated tungsten with the addition of rhenium at various temperatures. Again, there is some uncertainty as to the dip in emissivity values, in the range of 3% to 25% Re, being caused by the change in ductility of the material.

#### 4. RECRYSTALLIZATION AND GRAIN GROWTH CHARACTERISTICS OF SINTERED W,Re AND THORIATED, W,Re ALLOYS

This section reveals some of the metallurgical aspects of the tests conducted in the diffusion pumped vacuum system. The apparatus used was the same as that for the emissivity measurement system except for the fact that microhardness and metallographic tests were done on the samples, between emissivity tests.

##### 4.1 A brief introduction to elevated temperature softening

Recrystallization and grain growth are two of the numerous material characteristics that need thorough investigation in the process of developing materials that can withstand high temperatures. Refractory metals and alloys that can normally provide high source and sink temperatures for thermionic energy conversion applications, tend to be brittle and have low strength at elevated temperatures. The addition of rhenium to tungsten has been known to increase its ductility at lower temperatures by softening the base metal and this behavior is enhanced at higher temperatures. It further inhibits recrystallization of tungsten and in the process of delayed recrystallization, the final product is one of reduced grain size. Thorium and hafnium act as getters for oxygen and carbon respectively and the thoria and hafnium carbide particles thus formed segregate on grain boundaries minimizing their migration and controlling the grain growth characteristics. Thus by adding rhenium and thoria to tungsten one can obtain delayed recrystallization and controlled grain growth but the effect of various compositions on these characteristics is the basis for the research work involved in this section.

#### 4.2 Literature review

The fact that rhenium additions in small quantities soften and increase the ductility of tungsten was reported by Geach and Hughes [22] and confirmed by Jaffee et al. [34] who explained the effect as follows:

A complex oxide with appreciable surface tension is produced when rhenium is added to Group VI metals. This oxide agglomerates into round globules, instead of wetting grain boundaries and in the process, gives the alloy high intergranular strength and ductility. Interstitial solubility is lowered by rhenium additions. The contribution of valence electrons [54] from rhenium to the tungsten lattice is responsible for reduced solubility. Additions of rhenium to tungsten promote twinning during deformation [14] which is due to the fact that stacking fault energy is reduced by rhenium. Aqua and Wagner [2] confirm this observation. However, twinning only accounts for a minor fraction of the plastic deformation, usually at the onset of macroscopic strain and, its relation to the rhenium ductilizing effect is questionable. It was later suggested that increased dislocation mobility would result from rhenium lowering the lattice resistance to dislocation motion and this was found to be consistent with the well known solid solution softening in b.c.c. metals. There are two components in the flow stress, the effective stress  $\sigma_e$  and the internal stress  $\sigma_i$ . Arsenault [3] and later Christian [10] established that solid solution softening results when solute atoms produce a decrease in  $\sigma_e$  that more than offsets the increase in  $\sigma_i$  due to the presence of solute atoms. High concentrations of rhenium, unlike low concentrations, in tungsten do not produce alloy softening and this could be due to a different mechanism or due to the

fact that the increased solute contribution to  $\sigma_i$  becomes greater than the reduction of  $\sigma_e$ .

Klopp and Witzke [36] obtained the annealing response of a W, Re, Hf, C alloy by heating for one hour at temperatures ranging from 1590 K to 2810 K. Some recovery was observed to occur in the 1590 K to 1700 K range (evidenced by a slight drop in hardness) and recrystallization started at about 1740 K and was complete at about 2030 K. Arc melted tungsten ingots were annealed [45] for one hour at temperatures from 1273 K to 1873 K. Hardness checks and micrographs of these samples indicated the one-hour recrystallization temperature for this material to be between 1525 K and 1573 K. Hall et al. [26] investigated the elevated temperature properties of arc melted tungsten, rhenium alloys strengthened by a finely dispersed hafnium carbide precipitate. They found that the recrystallization temperature of W,Re increased very rapidly with increasing HfC content, reaching a maximum near 0.4 mol% HfC. They attributed this increase to the unusual stability of the HfC particles in the tungsten matrix and the possibility that these particles are very effective in pinning grain boundaries. A tungsten, nickel, iron alloy was annealed and tested [20] for microhardness at various annealing temperatures. There was a slight increase in the hardness at 1073 K and it was found that this was due to the formation of sub grains by the rearrangement of dislocations in this temperature range.

The recrystallization temperature [23] of unalloyed tungsten depends greatly on the impurity concentration, which is determined by the method of production and may vary from 1673 K for P/M tungsten to

1123 K for tungsten single crystals. It was found that when tungsten was alloyed with rhenium, the recrystallization temperature first increased with increasing rhenium content but then remained constant or decreased thereafter. Alloy softening of tungsten alloyed with rhenium was investigated by Stephens, Witzke [65]. In situ microhardness measurements were made at homologous temperatures from 0.02 to 0.2 (melting point), the range where alloy softening is normally observed in b.c.c. alloys. Results showed that alloy softening occurred at temperatures less than 0.16 (melting point) and for rhenium concentrations less than 16% Re. Alloy hardening was observed in concentrated alloys at all temperatures and in dilute alloys at homologous temperatures greater than 0.16 (melting point).

In general, tungsten, rhenium alloys with thoria and hafnium carbide have exhibited higher recrystallization temperatures. A hardness minimum exists at about 5% Re, which coincides with the highest creep strengths. The composition for good workability was found [41] to range from 18% to 32% Re.

#### 4.3 Experimental set up for vacuum annealing

All the tests for recrystallization and grain growth studies were conducted on the same experimental set up as that for the emissivity measurement tests, with minor modifications. As shown in Figure 50, the samples were annealed in a diffusion pumped vacuum system with a bell jar. The temperatures were measured with the accurate photon counting pyrometer along with its accessories such as the printer, the timer-counter and the discriminator-amplifier all of which were mounted in a

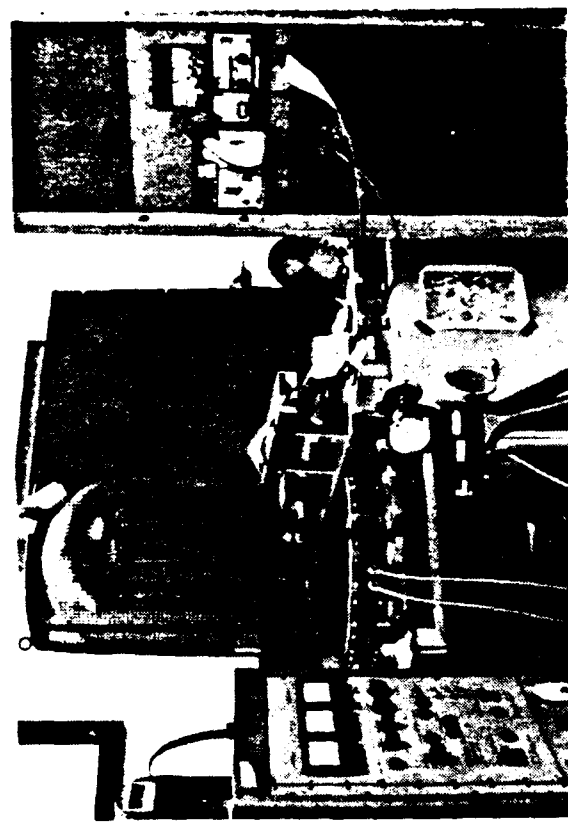


Figure 50. Experimental set up for recrystallization studies.

mobile rack. The samples were heated by electron bombardment with the necessary power from a high voltage power supply unit. In addition to these equipment, a Leitz-Wetzlar microhardness testing device and a Model PM-6 Olympus microscopic system was used for the associated metallographic studies.

#### 4.3.1 Sample preparation and associated metallography

The samples which were originally in the form of sintered rods were machined to discs of 6.35 mm. in diameter and 2.54 mm., thickness. The procedure, using the electrical discharge machine and other accessories, has already been described in the section on emissivity measurement. In addition to all the machining and polishing done for emissivity measurement, the top surface of each sample was polished with 240, 320, 400 and 600 grit carborundum wet/dry paper and then lapped with 3  $\mu\text{m}$ ., 0.1  $\mu\text{m}$ . and 0.05  $\mu\text{m}$  alumina slurries on a lapping machine. After polishing, each sample was subjected to microhardness testing in order to determine the hardness, before annealing. It was then spot welded to a tantalum holder and located in the bell jar for experimentation.

#### 4.3.2 Vacuum annealing of specimen

The cooling water circulation to the diffusion pump was started after locating the sample inside the bell jar. The diffusion pump was switched on after a roughing vacuum of  $10^{-2}$  torr was attained. With a vacuum of about  $10^{-5}$  torr, the filament was heated with alternating current. When the filament was sufficiently hot, the bombardment current and voltage were provided. The sample was maintained at ground potential. The photon counting pyrometer was then focussed on the

hohlraum in the sample and the associated circuitry, switched on. Once the sample had stabilized at a particular temperature, it was maintained at that temperature for one hour. At the end of this period, the power supplies were shut off and the sample was allowed to cool under vacuum to minimize any oxidation or contamination of the surface. Photomicrographs of the polished surface were then taken and the surface was subjected to the same sequence of polishing and lapping, as before, prior to making microhardness measurements. About twenty different microhardness readings were taken and averaged to get the final value at a given temperature. The entire process was repeated at higher temperatures.

#### 4.4 Results and discussions.

The specimen temperature, the annealing time and the subsequent microhardness values are shown in Table 14 and Table 15 for the nine different types of samples tested. Variation of microhardness with annealing temperature and rhenium content and the effect of alloying on the recrystallization temperature and grain size of tungsten are also presented in this section. In addition to this, important microstructural features of the recrystallized specimen showing thermally etched surfaces are presented for purposes of comparison. Plots obtained by previous investigators are superimposed on the current plots and the conditions under which the investigations were conducted, are indicated.

Table 14. Specimen temperature and microhardness values for tungsten, rhenium.

Specimen	Frequency Counts x 10 <sup>-3</sup>	Photon Counter Scale	Specimen Temperature °K	Anneal Duration hrs	Microhardness (Knoop) HK
Tungsten	-	-	298	-	557.50
	3.882	0	1268	-	499.111
	23.209	0	1400	-	530.00
	776.452	0	1780	-	450.44
	2810.94	1	2150	-	405.98
Tungsten, 3at.% Rhenium	1159.712	2	2600	-	392.81
	-	-	298	-	472.93
	22.591	0	1399	-	419.50
	864.847	0	1740	-	406.15
	2624.109	1	2148	-	301.07
Tungsten, 25at.% Rhenium	1050.300	2	2506	-	305.09
	-	-	298	-	669.96
	25.890	0	1408	-	510.91
	996.790	0	1755	-	456.71
	2779.530	1	2144	-	313.71
Tungsten, 30at.% Rhenium	1736.009	2	2417	-	525.59
	-	-	298	-	632.91
	25.251	0	1407	-	511.51
	903.125	0	1742	-	624.75
	1513.902	1	2020	-	525.05
	343.171	2	2254	-	493.74
	964.085	2	2483	-	363.19

Table 15. Specimen temperature and microhardness values for thoriated tungsten, rhenium.

Specimen	Frequency Counts x 10 <sup>-3</sup>	Photon Counter Scale	Specimen Temperature(K)	Anneal Duration (hrs.)	Microhardness (Knoop) HK
Tungsten 1% thoria	23.761 1004.532 2712.346 734.120	** 0 0 1 2	298 1413 1760 2120 2412	** 1 1 1 1	605.34 583.42 571.36 553.21 540.32
Tungsten 3% rhenium 1% thoria	26.431 990.782 2770.360 725.361	** 0 1 2	298 1425 1750 2142 2390	** 1 1 1 1	573.40 574.36 570.14 548.61 520.31
Tungsten 10% rhenium 1% thoria	27.120 862.745 2730.600 741.430	** 0 1 2	298 1430 1738 2125 2420	** 1 1 1 1	565.43 570.75 547.91 534.10 522.34
Tungsten 25% rhenium 1% thoria	** ** ** **	** ** ** **	298 1458 1771 2142 2432	** 1 1 1 1	690.20 634.32 640.40 622.36 568.40
Tungsten 30% rhenium 1% thoria	** ** ** **	** ** ** **	298 1450 1761 2135 2410	** 1 1 1 1	738.21 673.12 686.40 651.42 615.87

#### 4.4.1 Variation of microhardness of tungsten with elevated temperature and rhenium content.

The plots in Figure 51 indicate the annealing response of the tungsten, rhenium samples, with increase in annealing temperature. All the plots were found to have a regular trend where the hardness remains constant, over fairly large temperature ranges, except over a small interval of temperature where recrystallization occurs and there is a sudden drop in the values of Knoop hardness. Some recovery occurs in the 1250 K to 1450 K range for the tungsten sample and in the 1450 K to 1800 K range for the W,30% Re sample. A similar behavior was observed by Klopp et. al [36] for a W, Re, Hf, C alloy where the structure was highly worked even after annealing at 1590 K and recrystallization was observed to start between 1700 K and 1811 K. In this case, for the sintered W, 25% Re alloy, recrystallization was observed to start at about 1650 K and was complete at about 1900 K. It has also been reported [36] that a W, Re, Hf, C alloy recrystallized at 1970 K whereas an electron beam melted alloy of W,24% Re was fully recrystallized after 1870 K which is about the same value that was obtained in the present research activity on W, 25% Re alloy. The lower recrystallization temperature is due to greater grain boundary mobility which might have been restricted due to the presence of fine carbide particles. In the present investigation, only high temperature [1200 K to 2600 K] microhardness was of interest and so the microhardness variation at lower temperatures was not considered. The one hour recrystallization temperature for arc-cast tungsten [45] as shown in Figure 51(a) was found to be about 1500 K whereas for sintered tungsten it was about 1625

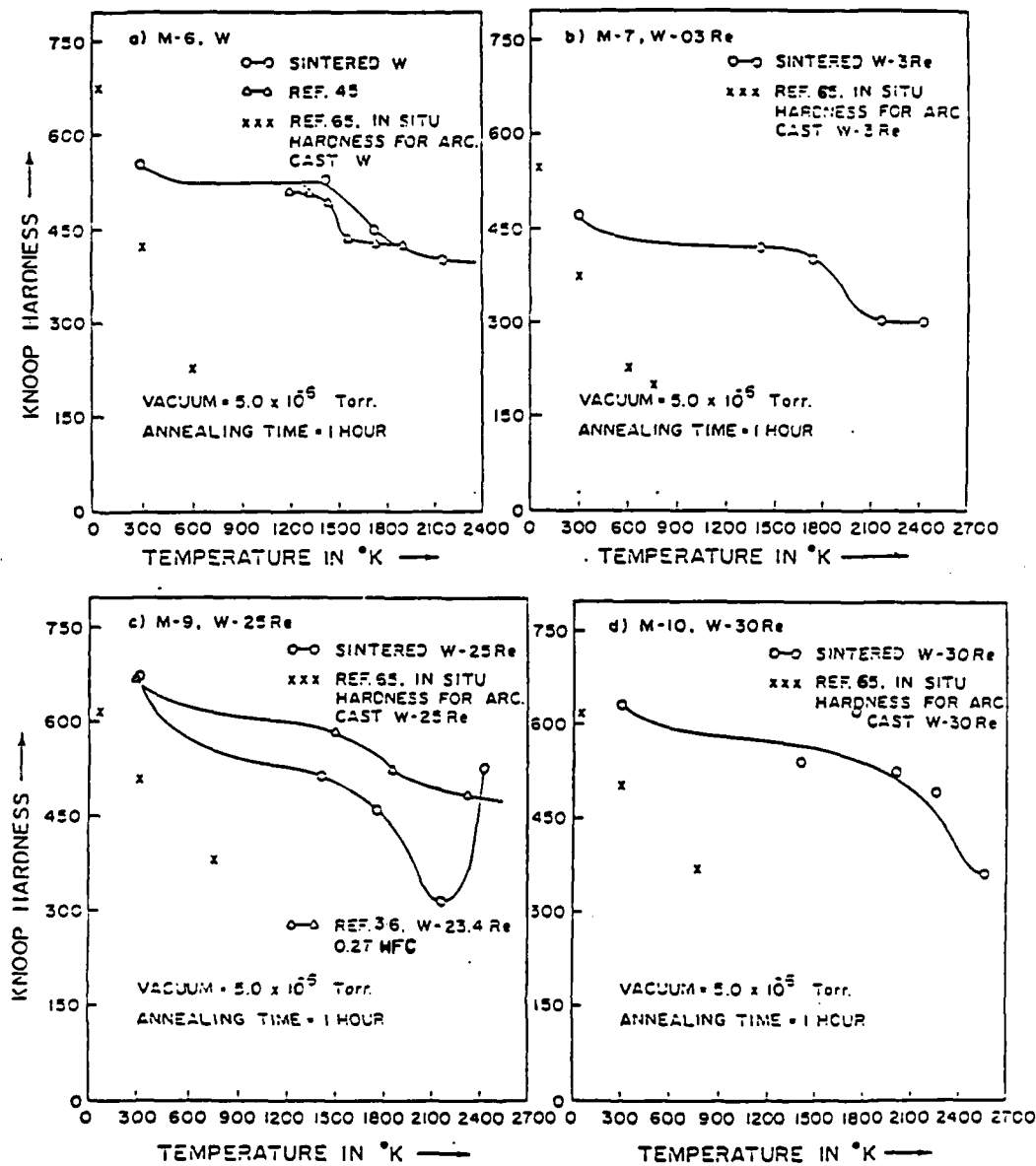


Figure 51. Effect of elevated temperatures on the microhardness of tungsten, rhenium.

K. This is probably due to the inhomogeneous nature of the sintered material, that has impurities in the grain boundaries thereby restricting its mobility. The rapid increase in the microhardness of the W,25% Re sample above 2100 K is due to the presence of the second phase in abundance at the surface of the material.

Figure 52 represents plots of microhardness vs. percent rhenium content at different annealing temperatures ranging from 1400 K to 2500 K. In each case it can be seen that the microhardness decreased for small additions of rhenium up to about 5% Re and then starts increasing gradually at first but rapidly after 27% Re which is the solubility limit. There are a number of reasons for the increased ductility of tungsten when alloyed with rhenium. Two of the primary reasons are i) the formation of deformation twins, during cold working and ii) change in the solubility of interstitial impurities. Deformation twins appear in alloys which are near the solubility limit of rhenium in the solid solution, and these alloys have the highest ductility. This mechanism, together with that of slip in the b.c.c. base metal, is responsible for the softening and increased ductility of tungsten. It is gradual at lower temperatures but abrupt at elevated temperatures, resulting in a sudden change in the hardness, above the solubility limit as in Figures 52(b) and 52(c). The addition of rhenium with seven electrons decreases the solubility of interstitial impurities. The fact that the hardness drops at 3% to 5% Re in each of the plots is proof of this decrease in interstitial impurity. Figure 52(a) also shows the dependence of hardness of cast [41] tungsten, rhenium.

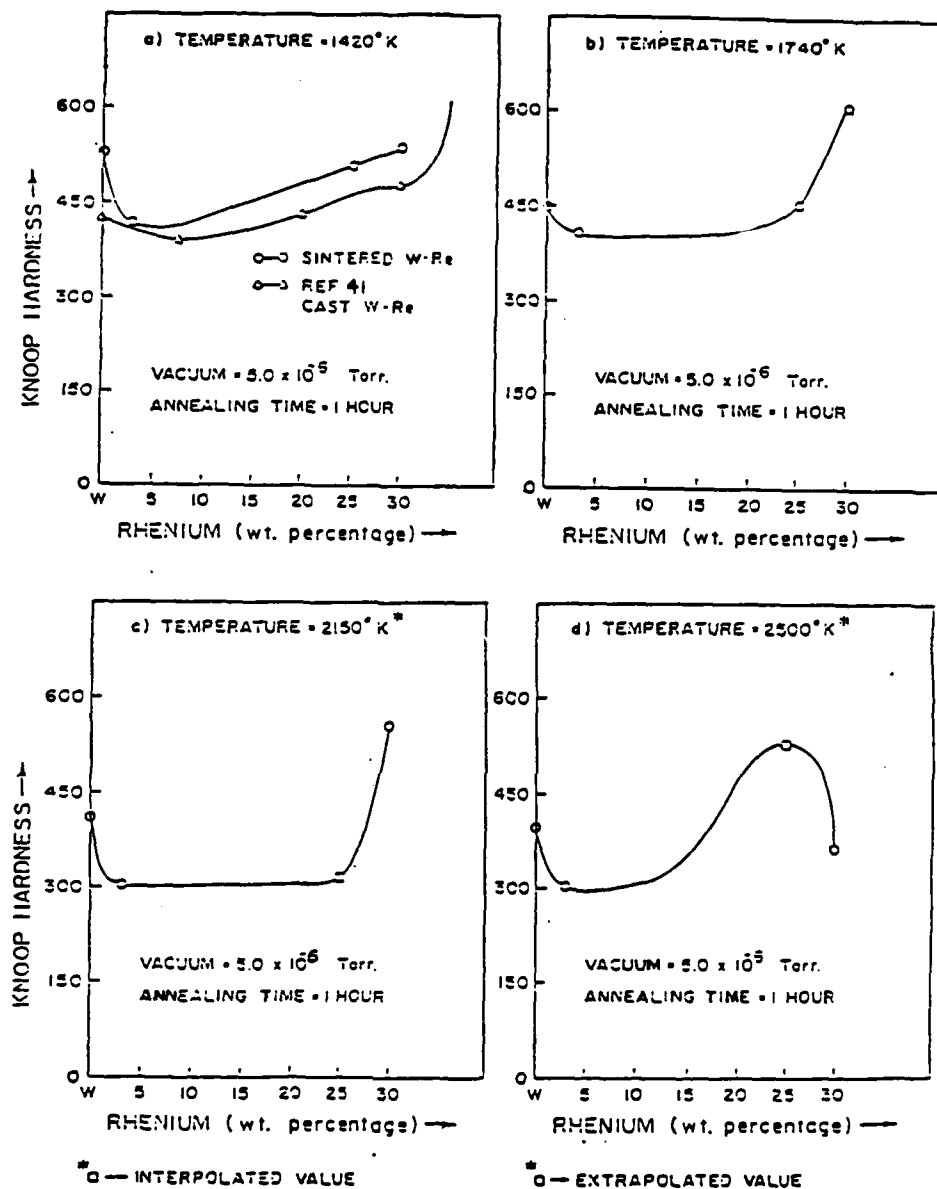


Figure 52. Variation of microhardness of tungsten with the addition of rhenium.

#### 4.4.2 Recrystallization and grain growth of sintered tungsten, rhenium.

The influences of rhenium on the recrystallization of sintered tungsten are indicated in Figures 53, 54 and 55. The microstructure of the tungsten and W, 3% Re samples did not reveal significant changes until the 2200 K range was reached. However the W, 25% Re and W, 30% Re samples showed distinct changes with increase in annealing temperature. From the microstructures, it was noticed that recrystallization occurs between 1750 K and 2150 K. At lower temperatures, the rhenium is not uniformly distributed in the material but at elevated temperatures, it diffuses into the base metal as shown in Figures 53(b) and 53(f). Grain growth is evident when the annealing temperature is increased from 2150 K to 2500 K. The mixture of small and large grains in both the samples at 2500 K reveals that secondary recrystallization has occurred and this is accelerated in the W, 30% Re sample as indicated by the microstructures in Figures 53(c) and 53(g).

Figure 54 shows the microstructures of the four different W,Re alloys after annealing at 2500 K. As indicated in these pictures, the introduction of rhenium in tungsten sharply decreases the grain size during recrystallization. A unique feature of a thermally etched microstructure was revealed in Figure 54(e) where the clearly defined grain boundaries are the current grain boundaries whereas the less sharply defined grooves are the original boundaries of grains formed prior to reaching 2500 K. One can observe how smaller grains diffuse together to form a larger grain and this could provide useful information on the mechanism of grain growth in sintered tungsten, rhenium alloys.

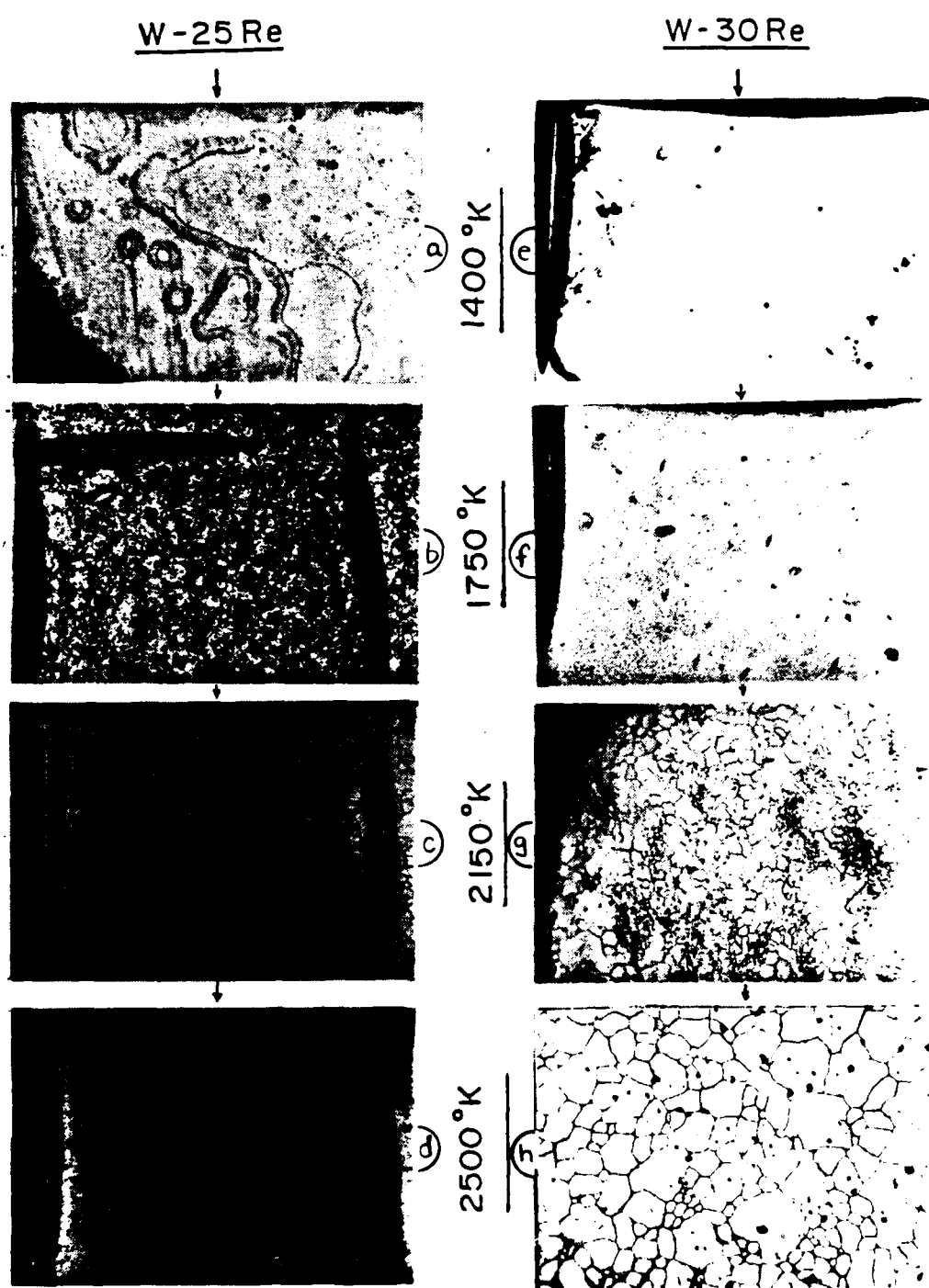


Figure 53. Microstructures of recrystallized W-25at.% Re and W-30at.% Re samples after annealing at the temperatures indicated.

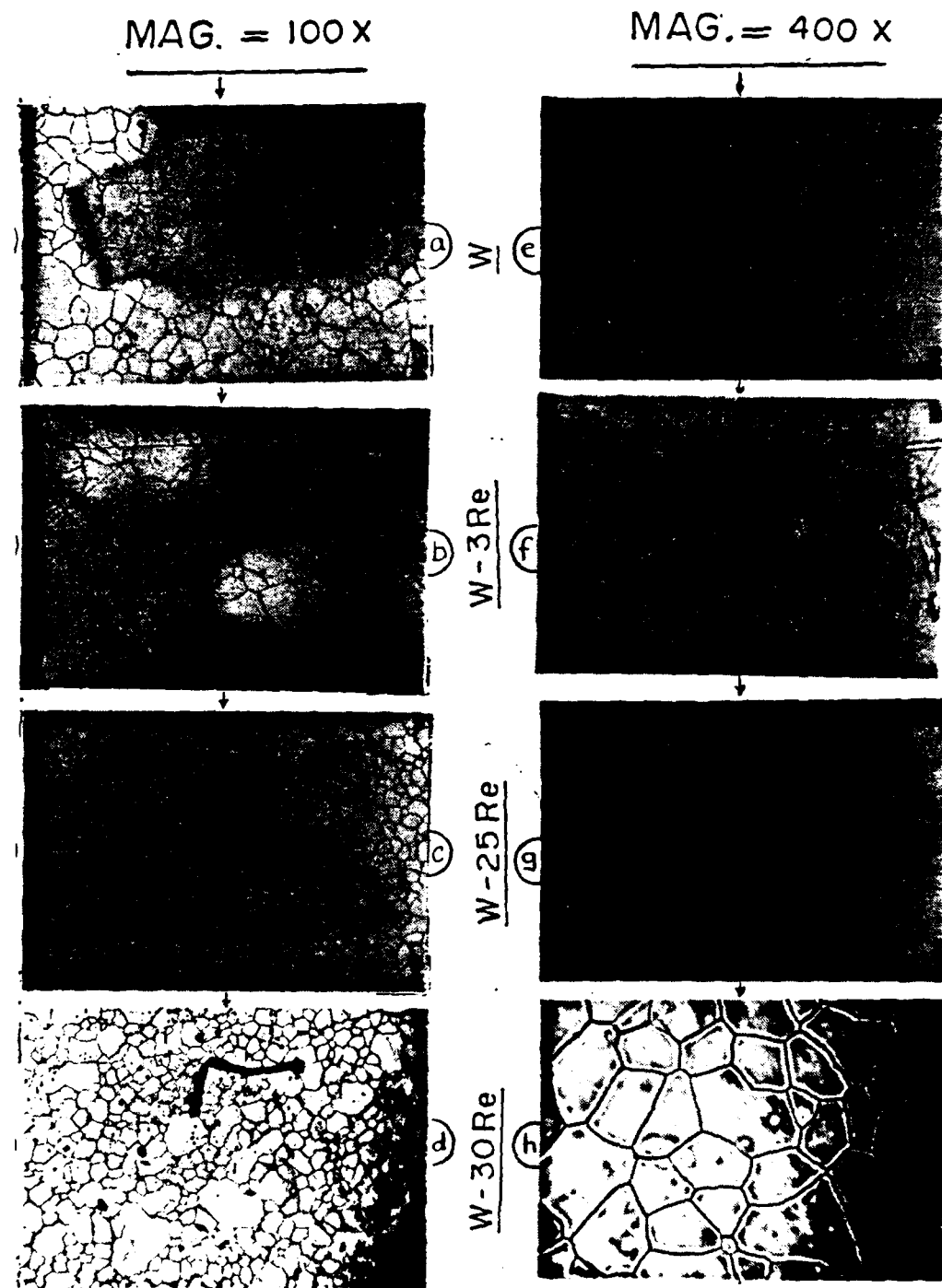


Figure 54. Microstructures of the different samples after annealing for 1 hour at 2500°K.

The recrystallization temperature as obtained from the average hardness values at softening for each of the four samples was found to increase with rhenium alloying as shown in Figure 55. An addition of 3% Re to tungsten results in an increase of recrystallization temperature from 1650 K to 1850 K. Further alloying of tungsten with rhenium had little influence on the recrystallization temperatures. Also shown are the variations of recrystallization temperature with rhenium content as obtained by Golavenenko [23] and Savitskii [58]. The results for the sintered tungsten, rhenium alloys seem to correlate well with earlier investigations. With the introduction of rhenium, the annealed grain size decreased from 62  $\mu\text{m}$ . for tungsten to 32  $\mu\text{m}$  for W,25% Re. However there was a slight increase in the grain size with further increase in rhenium content and this is believed to be the annulling effects of excess rhenium, on the influence of additions which inhibit recrystallization of sintered tungsten.

#### 4.4.3 Variation of microhardness of thoriated tungsten, with elevated temperature and rhenium content.

The results of the tests performed on the thoriated tungsten, rhenium alloys have been presented in Table 15 and Figures 56 through 60. Figure 56 represents the effect of elevated temperatures, on the microhardness of the thoriated samples. From these plots we observe that the trend is similar to that exhibited by the W,Re alloys except for the fact that in this case the average values of microhardness at all temperatures were higher than the corresponding values for W,Re. This behavior was found to be quite obvious in the W,25Re, 1ThO<sub>2</sub>, and W,30Re, 1ThO<sub>2</sub>, samples while the difference for lower percentages of

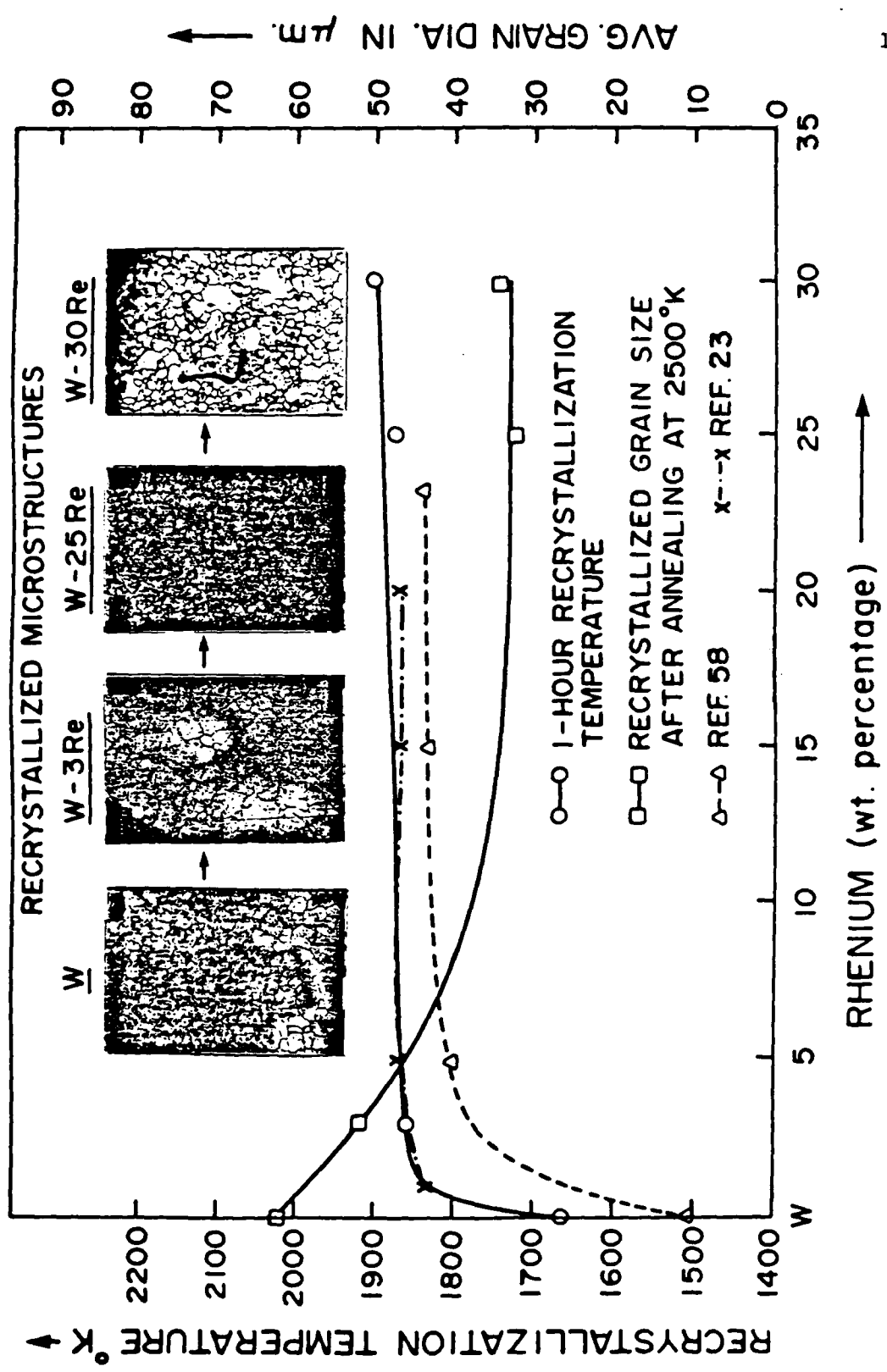


Figure 55. Recrystallization effects of alloying tungsten with rhenium.

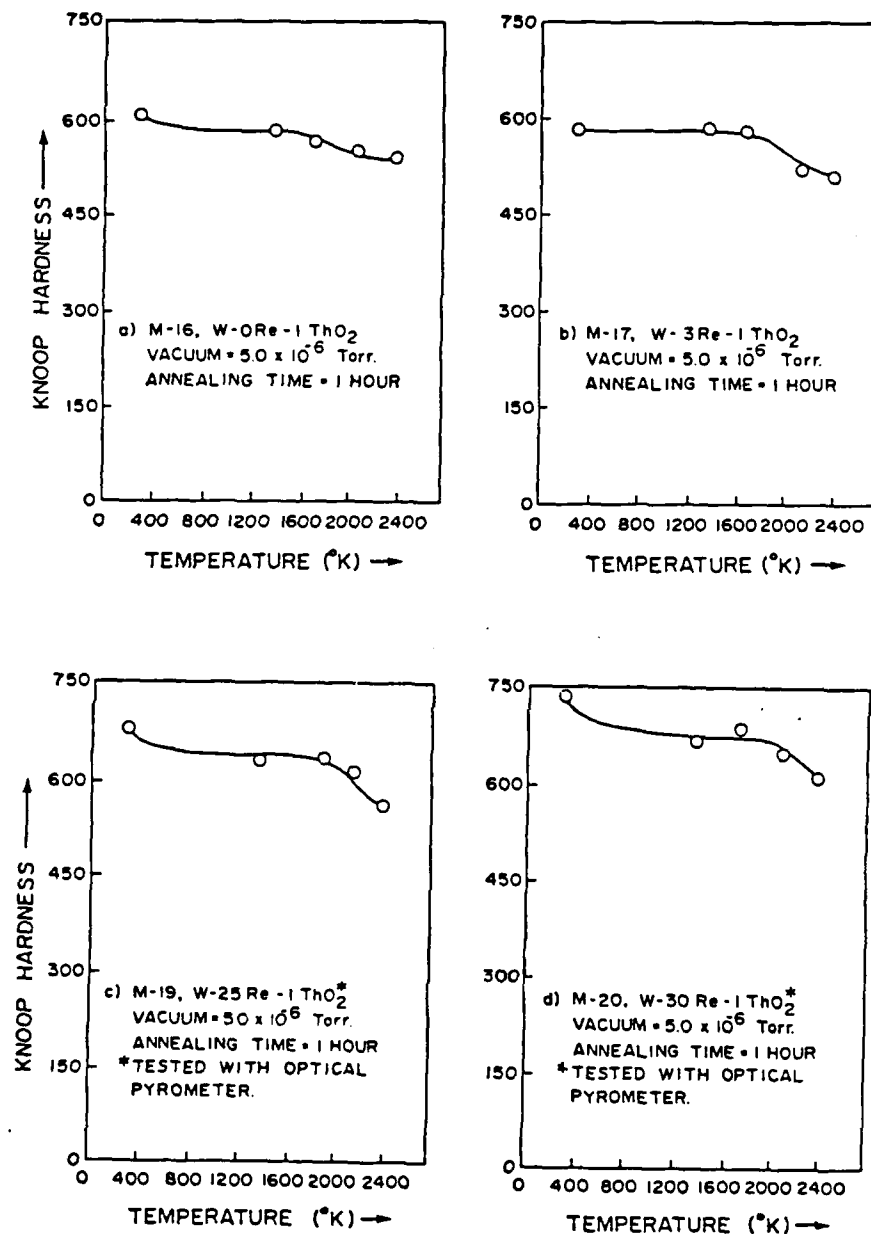


Figure 56. Effect of elevated temperatures on the microhardness of thoriated tungsten, rhenium.

rhenium was negligible. It has been reported by Sell and Stickler [60] that in the temperature range of 1500 K to 2500 K, they observed a considerable decrease in the reduction of area (of fractured tensile samples) for 2% thoriated W,Re as compared to W,Re without any thoria. Thus, thoria addition is believed to reduce ductility making the samples behave in a brittle manner similar to pure tungsten and in the process increase the microhardness. However this effect is dependent on the size of the distribution of thoria particles. As in the case of W,Re it was found that addition of rhenium to thoriated tungsten inhibits recrystallization but not to the same extent as that caused by the fine thoria particles.

Figure 57 shows the variation of the microhardness of thoriated tungsten with the addition of rhenium. In each case it was observed that the addition of rhenium causes a decrease in the hardness of 1% thoriated tungsten, up to about 5% or 7% Re and thereafter the hardness increases with increase in rhenium content. This increase is due to the loss of ductility partly due to the dispersion strengthening caused by fine thoria distribution and partly due to the introduction of the harder second phase beyond the solid solubility limit of rhenium in tungsten. The hardness minimum observed at around 5% to 10% Re content is evidence for the fact that the loss of ductility is a minimum in this region and the effect of thoria is least experienced.

#### 4.4.4 Recrystallization and grain growth of thoriated tungsten, rhenium.

The influences of rhenium and thoria on the recrystallization of sintered tungsten are indicated in Figures 58, 59 and 60. Figure 58

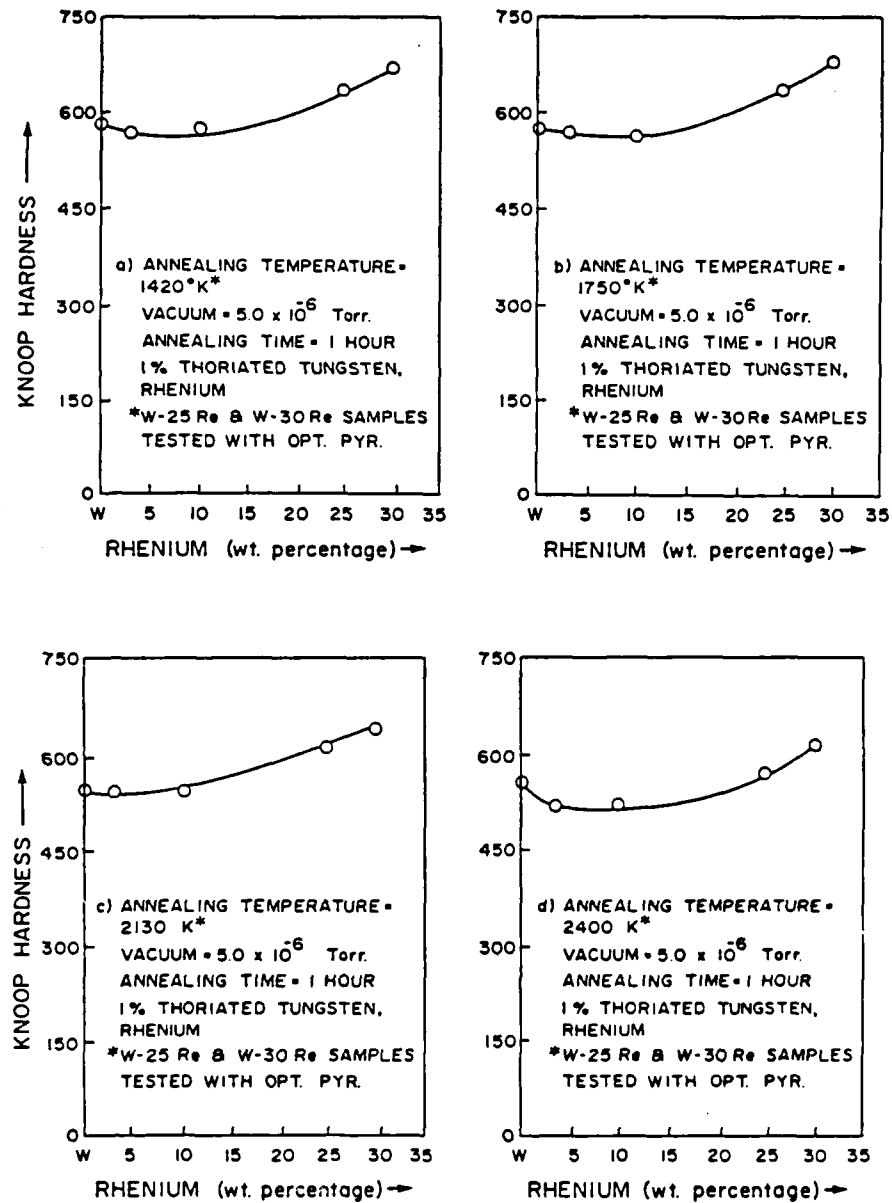


Figure 57. Variation of the microhardness of thoriated tungsten with the addition of rhenium.

gives the microstructures of the W,25Re, 1ThO<sub>2</sub>, and W,30Re, 1ThO<sub>2</sub> samples after annealing at the temperatures indicated. The major difference between these microstructures and the ones for W,Re is the presence of dark spots representing the thoria particles. It is virtually impossible to identify grains in any of the microstructures up to a temperature of 2200 K as the recrystallization in the thoriated samples is retarded as compared to that in the tungsten, rhenium alloys. Fine thoria particle dispersions strongly influence mobilities of grain boundaries and sub-boundaries and redistribution of dislocations which are strong factors that affect the formation of recrystallization nuclei and initial growth. The thoria particles segregate on grain boundaries limiting their mobility and in the process, provide smaller recrystallized grain sizes. Golavanenko [23] observed that impurities have a lesser effect on the recrystallization temperature of tungsten alloys than that of unalloyed tungsten. However it is hard to generalize this observation as the effect of dispersed particles on the recrystallization temperature depends on their quantity, dispersity and stability with respect to the parent matrix. From the microstructures presented for the four different alloys after annealing at a temperature of 2400 K in Figure 59, we can observe that the W, 1ThO<sub>2</sub> and W,3Re, 1ThO<sub>2</sub> samples did develop large and medium sized grains after recrystallization when compared to W,25Re, 1ThO<sub>2</sub> and W,30Re, 1 ThO<sub>2</sub>. If there were fine thoria particle distribution in all the samples, as claimed by the suppliers, the microstructures in Figure 58 would all be more or less identical but since this did not happen, there is reason to believe that the alloys with lower percentages of rhenium had a coarse

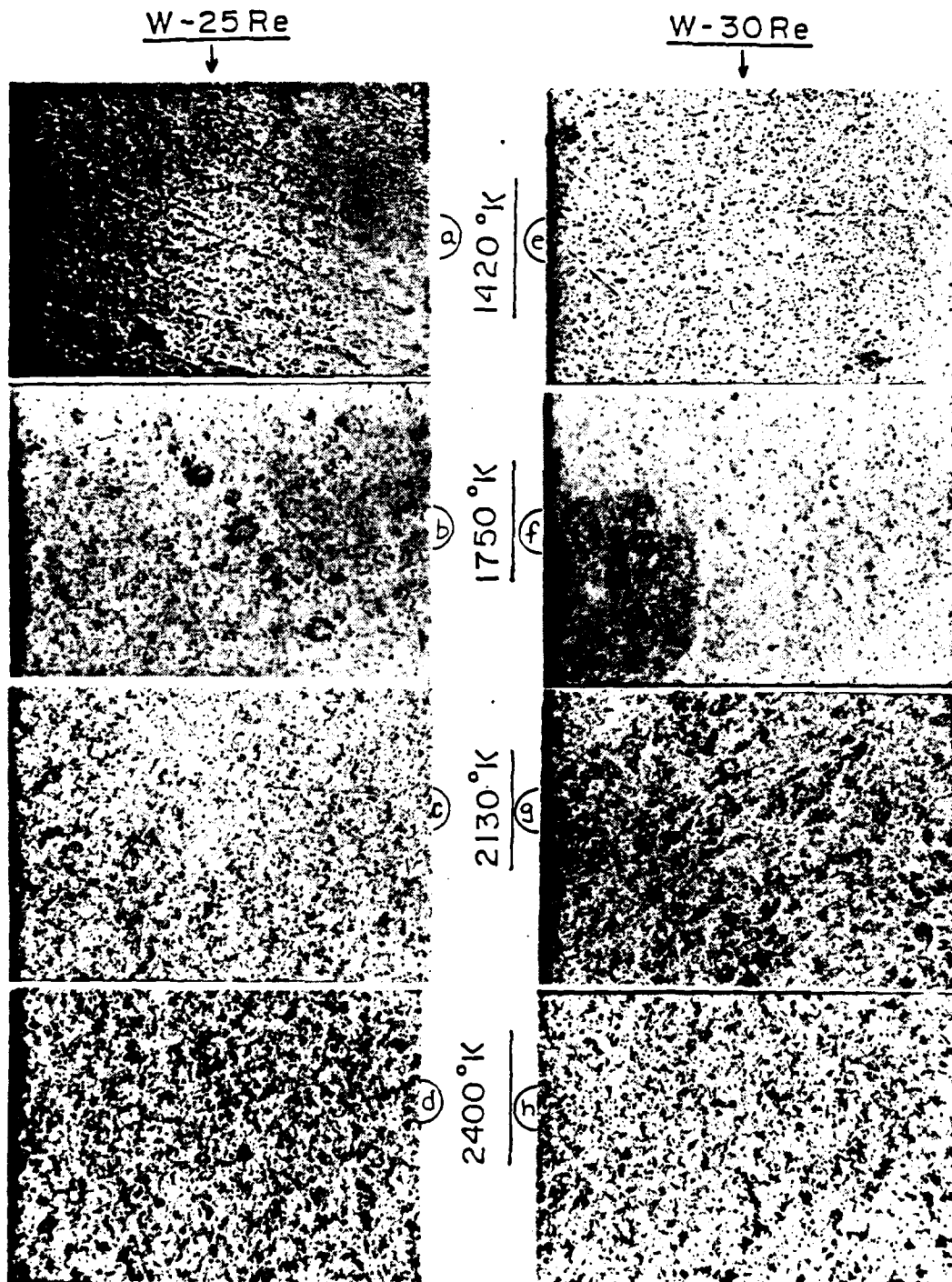


Figure 58. Microstructures of recrystallized W-25%Re, 1%ThO<sub>2</sub>, and W-30%Re, 1%ThO<sub>2</sub>, samples after annealing.

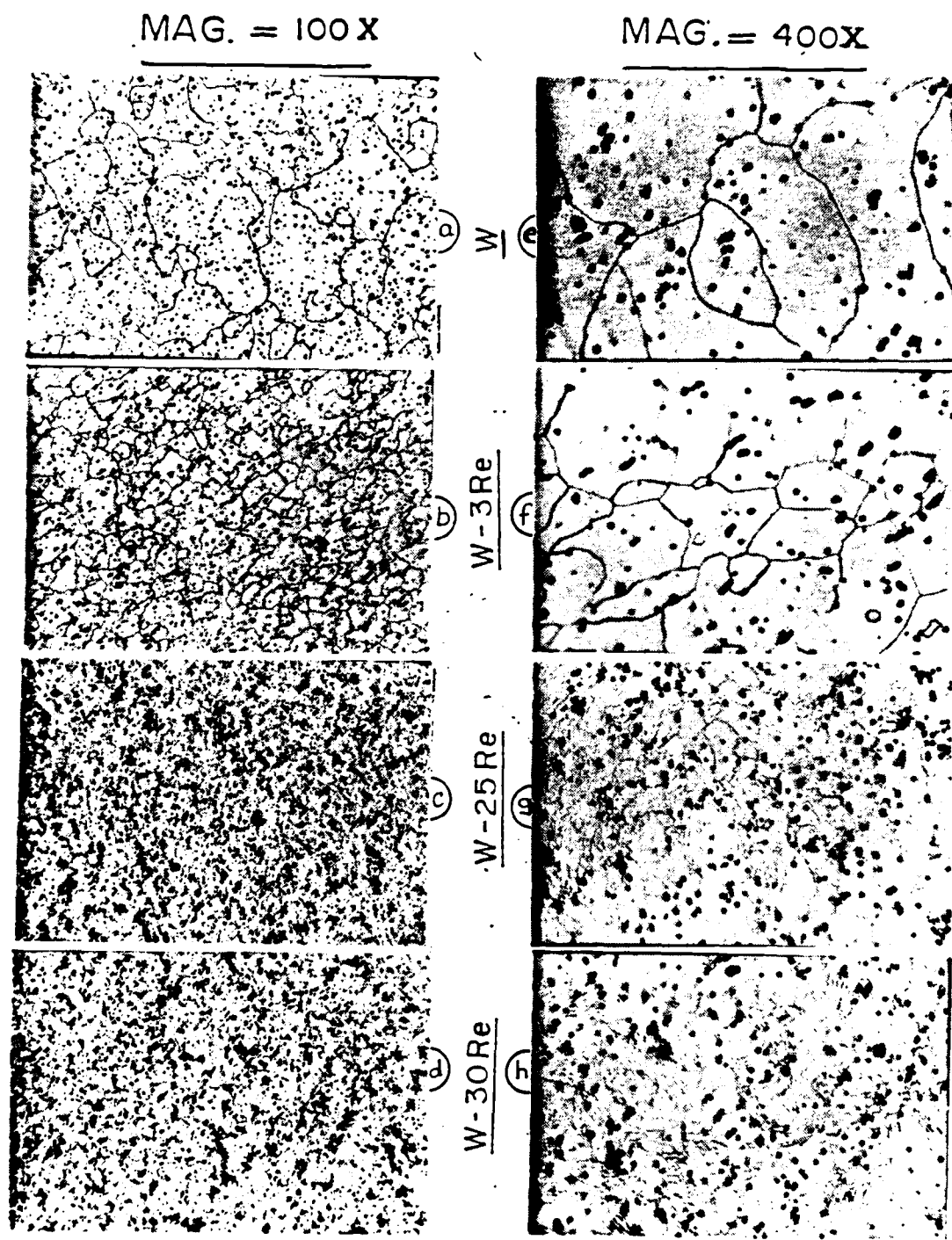


Figure 59. Microstructures of different thoriated samples after annealing for one hour at 2500 K.

thoria particle distribution whereas the alloys with 25% and 30% rhenium had a fine thoria particle distribution. From the polyhedral structure exhibited in the microstructures in Figure 59, we know that all the samples did definitely undergo recrystallization.

Figure 60 shows the variation of the one hour recrystallization temperature of one percent thoriated tungsten with the addition of rhenium up to and a little beyond the solid solubility limit of rhenium in tungsten. The addition of thoria increases the recrystallization temperature of all the alloys with the maximum increase being observed in the W,25Re, 1 ThO<sub>2</sub> alloy. This plot provides evidence for an earlier observation made, concerning the size of the thoria particle distribution. A coarse particle distribution is not very effective in dispersion strengthening and retarding recrystallization as in the W,3Re, 1ThO<sub>2</sub> alloy. In general the results of these tests agree to a certain limit with that of Golavanenko [23] who concludes that alloying of tungsten with refractory metals strengthening the solid solution (rhenium) along with dispersed hardening phases (thoria) does not increase the recrystallization temperature as compared with tungsten alloys containing only the dispersed second phase (thoria).

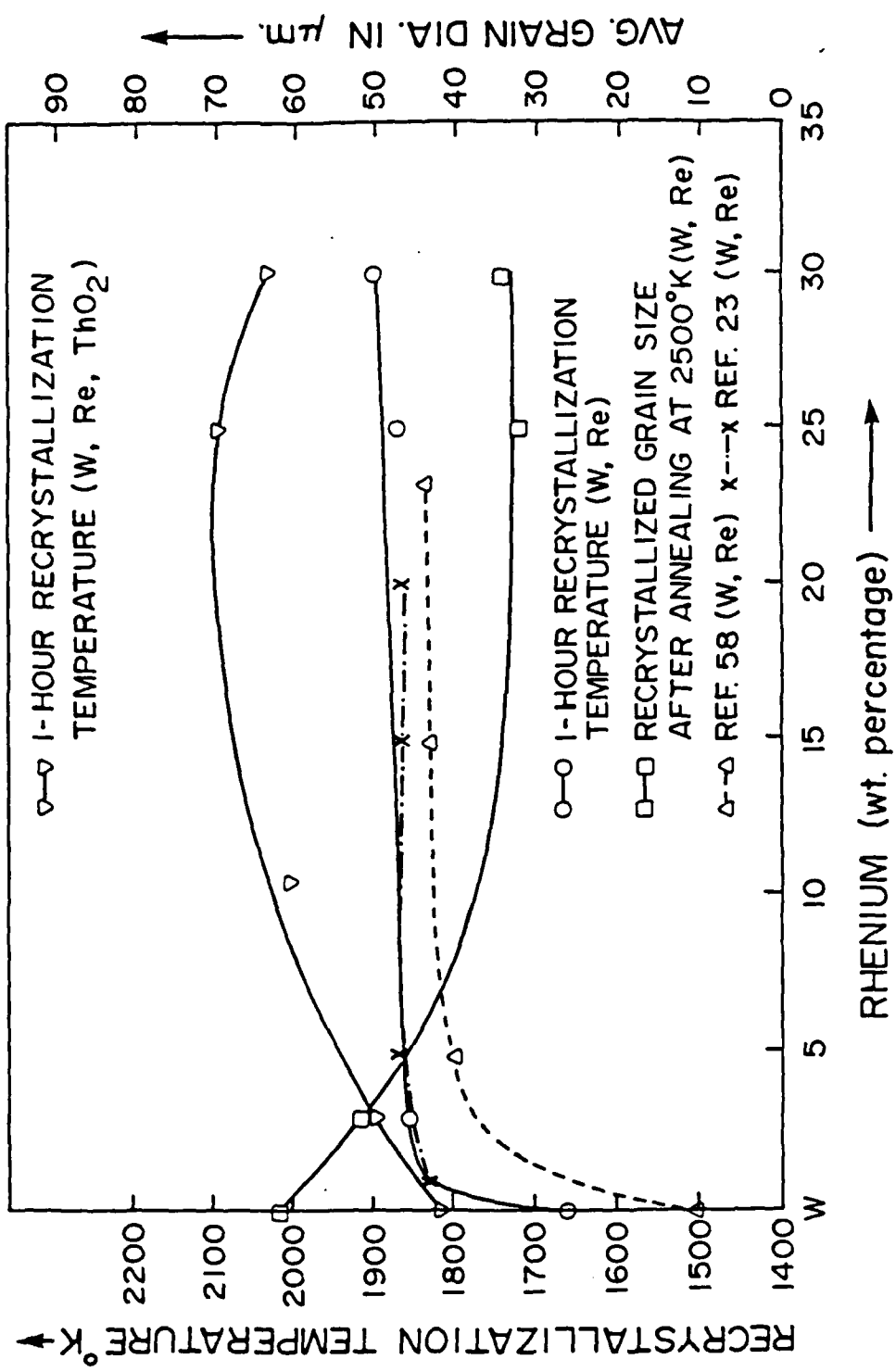


Figure 60. Recrystallization effects of alloying tungsten with rhenium and thoria.

## 5. HIGH TEMPERATURE, HIGH VACUUM MECHANICAL TESTING OF W,Re AND W,Re, ThO<sub>2</sub> ALLOYS

The thermionic emission microscope and the emissivity measurement system are very useful tools to acquire the surface characteristics of refractory metals and alloys that find application in high temperature space thermionic energy conversion. However, the bulk properties of the materials are almost as useful as the surface properties, if they are to be exposed to the low pressure/low temperature environment in outer space. A significant quantum of data is available on the bulk properties of refractory materials at high temperature but in most cases the tensile tests were conducted at room temperature and atmospheric pressure after annealing the sample to high temperatures for varying periods of time. Values obtained in this fashion do not really characterize the material at a given temperature because of a number of detrimental factors such as atmospheric contamination, irregular heating and so on. This has led a number of investigators to investigate real-time deformations and microstructural changes in refractory materials at high temperatures and moderate vacuum atmospheres.

Though tungsten, rhenium cast materials have been mechanically tested at high temperatures, a complete study of the tungsten, rhenium and tungsten, rhenium, thoria sintered materials' family has not been examined in detail. This is specially true with the post test characterization, revealing grain boundary segregation of impurities, and effects of annealing on the type of fracture, etc. This constitutes the concluding phase of the research activities for this program and the

following sections give a description of all the related activities accomplished, to date.

### 5.1 High temperature mechanical testing

Before dealing with high temperature testing, it would be appropriate to describe some of the mechanical properties that can be obtained by conventional testing under atmospheric conditions. Deformation occurs when forces are applied to a material. Energy is absorbed during deformation because a force has acted along the deformation distance. Strength is a measure of the level of stress required to make a material fail. Ductility identifies the amount of permanent strain prior to fracture, while toughness refers to the amount of energy absorbed by a material during failure. All the pertinent mechanical properties in conventional testing are shown in Table 16.

#### 5.1.1 Mechanical properties in elevated temperature tensile testing

All the properties mentioned above can also be obtained in high temperature testing but this involves some subtleties not exhibited by conventional testing methods. First of all the specimen has to be heated. This can be done by resistance heating, induction heating or electron bombardment. Resistance heating was chosen in this case because of its simplicity and the small size of the sample. The fact that the specimen is heated to the order of 2500 K makes it absolutely necessary to have the tensile system in a vacuum chamber to prevent high temperature oxidation and imminent failure of the specimen. Special ceramics that have excellent electrical and thermal resistivity have to be used and the grips holding the specimen should also be made of a high

temperature resistant material. Some means of cooling the grips have to be made available if there is excessive heat conduction from the specimen. Special vacuum chambers with provision to expand under vacuum had to be designed in addition to having a high vacuum pumping system.

#### 5.1.2 Objectives of the research on tensile testing

- a) Design a high vacuum system complete with instrumentation for temperature measurement and for heating the specimen.
- b) Fabricate the components of the system with suitable materials for the grips and the insulators.
- c) Fabricate tensile test specimen using conventional machining and electrical discharge machining with suitable fixtures.
- d) Interface the system with an Instron testing machine.
- e) Test the sample as indicated below.
  - i) Each alloy combination is to be tested at room temperature and three other higher temperatures after maintaining the samples at each temperature for a fixed period of time before deformation.
  - ii) Obtain stress-strain relationship for each specimen and the ductilities of the various material combinations.
  - iii) Take replicas of the fractured surfaces and observe fracture characteristics in SEM and utilize Auger Electron Spectroscopy for impurity segregation studies.

## 5.2 Literature survey on elevated temperature testing of refractory materials

As was stated earlier, prior to the 1960's most of the high temperature tensile data were not really the output of real-time tests but values that were the result of extrapolations from room temperature data and high temperature annealing. However there was some introductory work by Sims and Jaffee [34] in the mid fifties that involved the testing of 50 mil rhenium wires at various temperatures under a controlled atmosphere of a mixture of 5% hydrogen in helium. In general they found that the elevated temperature strength properties of rhenium were high. Elevated temperature short time tests revealed that the elongation dropped to a low value of about 1 to 3% above 500°C, whereas the stress-rupture tests showed elongations in excess of 4% at 2275 K. Barth [6] concluded that the ductile to brittle transition is of considerable importance in the case of tungsten because of the relatively high temperatures at which it occurs. It was found that the effect on the flow and fracture of annealed tungsten as the deformation temperature drops through the transition zone is that of sharply increasing the yield strength. This resulted in a corresponding reduction in ductility over a narrow temperature range.

Atkinson [5] investigated the effect of powder purity on the ductile-brittle transition temperature of tungsten. It was found that interstitial atoms tend to increase the d.b.t. temperature in tungsten. Successively lower impurity levels reflected lower transition temperatures. Klopp [51] and his associates investigated the mechanical properties of several arc melted tungsten alloys containing rhenium,

tantalum, columbium, hafnium and carbon, in the temperature ranges of 1650 K and 2470 K. They found that solid solution strengthening in tungsten alloys was most effective in W, Hf alloys and least effective in W, Re alloys. Carbon additions to different tungsten alloys produced various degrees of strengthening with the largest effect formed in W, Hf, C alloys. The strongest alloy, W, 26% C, 0.20% Hf had a tensile strength of 62.5 ksi at 2200 K. Here the tensile tests were performed in a vacuum of less than  $5 \times 10^{-5}$  torr at a constant crosshead speed of 1.5 mm/minute.

Arc melted tungsten alloys strengthened by a finely dispersed hafnium carbide precipitate have exhibited outstanding high temperature strength according to Hall [26] and others. It was found that the addition of 4% rhenium to such alloys significantly improves their low temperature ductility. The alloy that exhibited optimum properties had the composition, W, 4Re, 0.35 Hf, 0.35 C. In the swaged condition, this alloy combined a tensile strength of approximately 10 ksi at 2200 K, with a ductile-brittle transition temperature of 365 K. Sell [60] and Stickler investigated ingots of W, 5% Re, 2% ThO<sub>2</sub>, alloy sintered from blended tungsten, rhenium and thoria powders containing a coarse thoria dispersion, that would be swaged easily. Tensile tests were made in the temperature range from room temperature to 2673 K. They used light micrographs and electron micrographs of fractured surfaces to study the effect of test temperature on the mode of tensile fracture of swaged and annealed rods of W, 5% Re, 2% ThO<sub>2</sub>. In an effort to determine if particle strengthening by a HfC precipitate could be obtained in a ductile tungsten, rhenium alloy, an arc melted W, 23.4% Re, 0.27% Hf, C

alloy was tested in tension by Klopp [36] and Witzke. At 1925 K, the HfC strengthened alloy had a short time tensile strength of 62.7 ksi, more than double the strength of 28.1 ksi observed earlier for W,24 Re. However, the strength advantage decreases at higher temperatures due to HfC particle coarsening and grain boundary sliding.

Witzke [71] evaluated arc melted W,4% Re, HfC alloys containing up to about 0.8 mol. % HfC for compositional effects on mechanical properties in the as-worked condition. The data obtained showed considerable scatter, especially for the alloys containing an excess of carbon. It was found that peak strengthening occurred at or near the calculated stoichiometric HfC composition (0.3 to 0.4 mol %) but decreased rapidly with excess of either carbon or Hafnium. Uskov [67] and Borbak investigated the temperature relationship of the characteristics of fracture toughness (crack resistance) of the powder metallurgy of tungsten. The samples were heated by radiation at a rate of 1 degree/sec. Before tension, a sample was held at the specified temperature for thirty minutes. From the features of failure of tungsten at different temperatures, they concluded that there was a significant extent of the gently sloping portion on the tensile curves but this was not an indication of general plastic flow of the material. The failure of all the specimens were confirmed to be of a brittle nature, from the fractographic analysis at a test temperature of 1475 K.

Wadsworth [70] studied the effect of excess hafnium or carbon in W, 4% Re, HfC alloys at 2200 K after annealing at 2400 K. A maximum in the ultimate tensile strength was found in compositions close to those having little or no excess of either hafnium or carbon. Both excess

hafnium and excess carbon exhibited the same effect, that is the reduction in ultimate tensile strength.

### 5.3 Design and fabrication of the high temperature, high vacuum tensile stages.

Figure 61 is a photograph of the system for high temperature, high vacuum tensile testing with all the parts assembled in position in the Instron machine. A schematic of this set up is indicated in Figure 62, where the various components are labeled clearly. The entire tensile stage can be divided in two parts a) the external stage and b) the internal stage, for convenience in describing the system.

#### 5.3.1 The external stage.

Figure 63 shows a drawing of the assembly of the components of the external part of the high temperature stage together with a picture of the actual stage assembled between the crossbars in the Instron machine. It was essentially made up of the crossbars of the Instron device, the load cell, the flexible bellows coupling and the four-way cross chamber that houses the internal part of the high temperature stage. Since the test was expected to be conducted in a high vacuum atmosphere, the specimen had to be deformed in a leak tight chamber. The bellows system and the four-way cross provided a vacuum environment (better than  $10^{-7}$  torr) as well as the necessary flexibility to deform the specimen up to 28 mm. All the components in this stage were made of either mild steel or stainless steel depending on their location. Part numbers 1 through 6 shown in Figure 64 and part numbers 7 through 9, in Figure 65 were all supporting members which were designed at the Thermionic Laboratory and

Table 16. Mechanical properties in conventional mechanical testing.

Property, or characteristic	Symbol	Definition (or comments)	Common units	
			SI	English
Stress	$s$	Force/unit area ( $F/A$ )	pascal* ( $N^2/m^2$ )	psi* lb <sub>f</sub> /in. <sup>2</sup>
Strain	$e$	Fractional deformation ( $\Delta L/L$ )	—	—
Elastic modulus	$E$	Stress/elastic strain	pascal	psi
Strength		Stress at failure		
Yield	$S_y$	Resistance to initial plastic deformation	pascal	psi
Tensile	$S_t$	Maximum strength (based on original dimensions)	pascal	psi
Ductility		Plastic strain at failure		
Elongation	$\epsilon_t$	$(L_t - L_0)/L_0$	§	§
Reduction of area	R of A	$(A_0 - A_t)/A_0$	§	§
Toughness		Energy for failure by fracture	joules	ft-lb
Hardness <sup>t</sup>		Resistance to plastic indentation		Empirical units

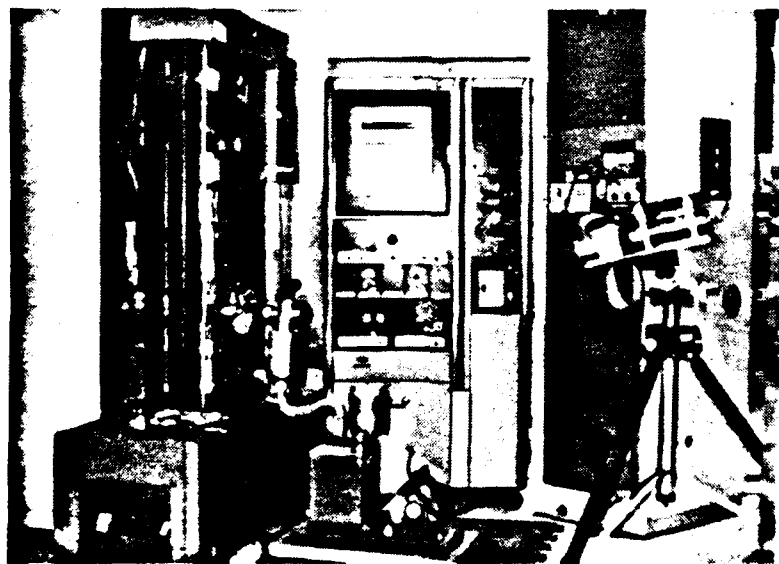


Figure 61. The high temperature, high vacuum tensile testing system.

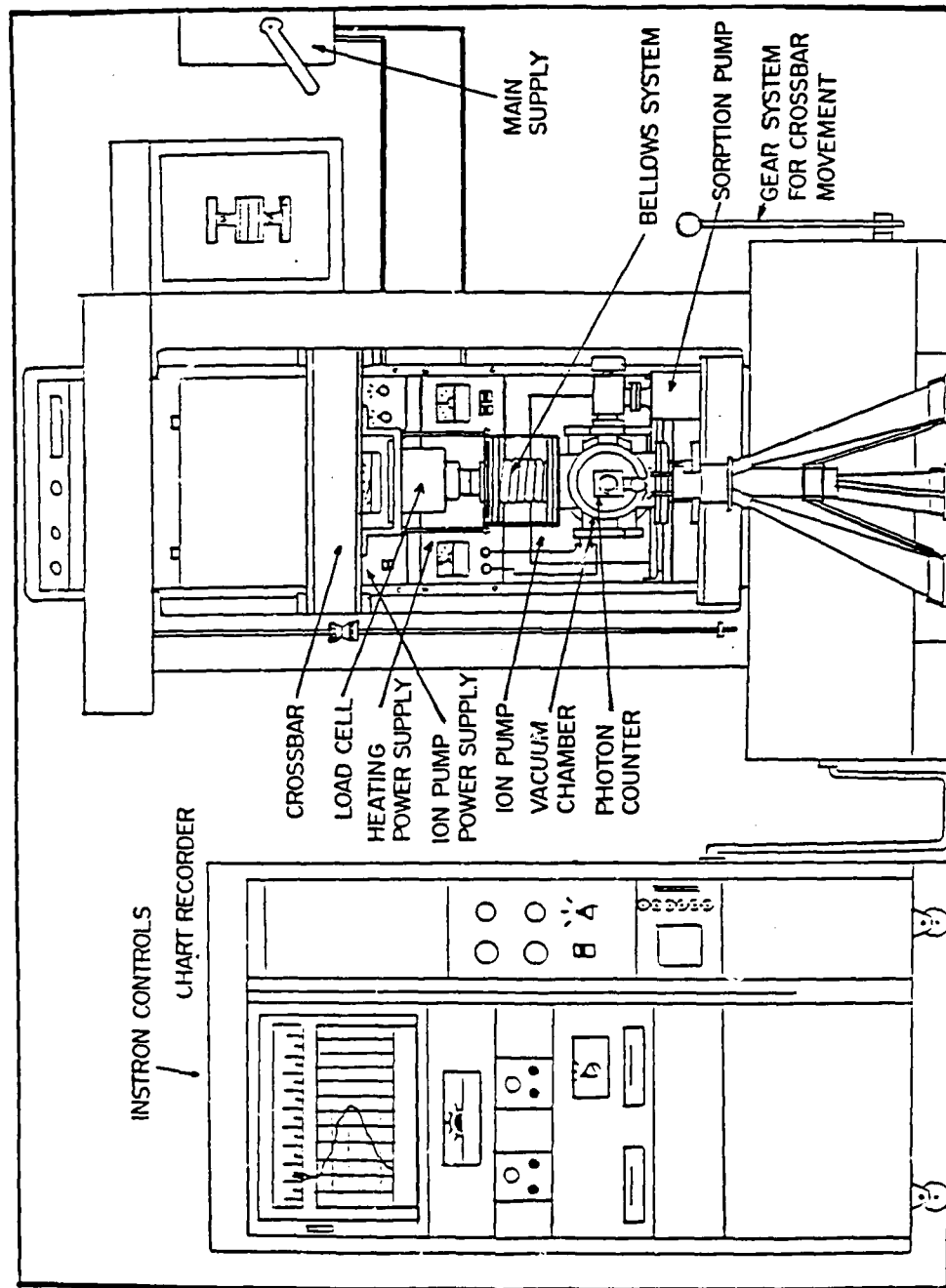


Figure 62. Experimental layout for high temperature mechanical testing.

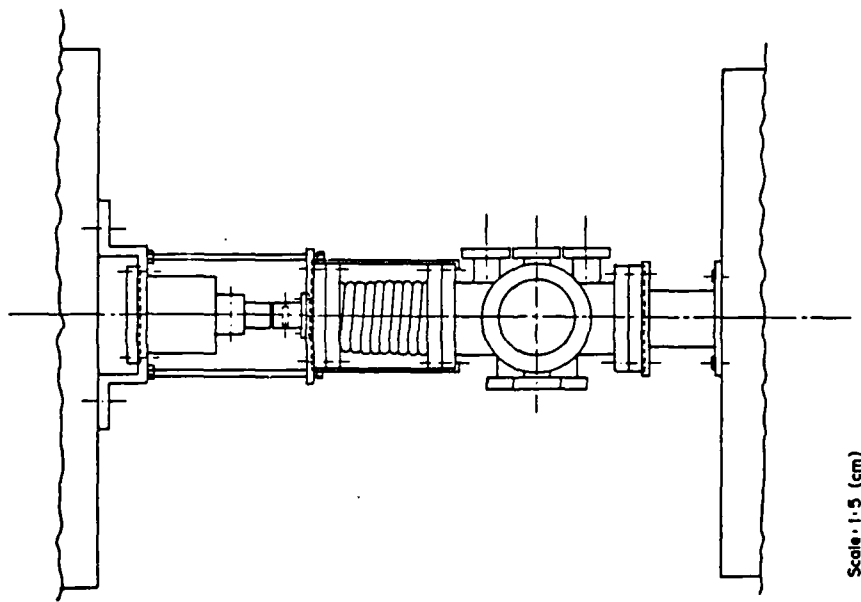
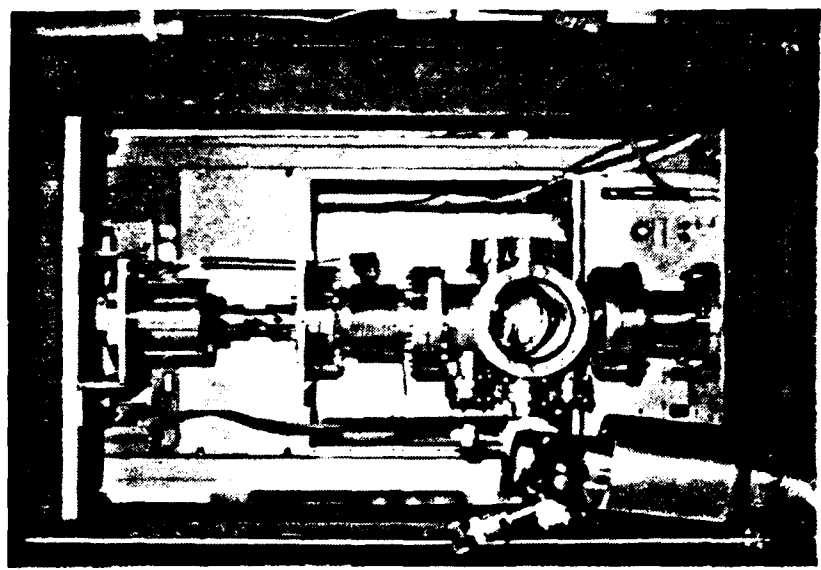


Figure 63. The external part of the high temperature stage.

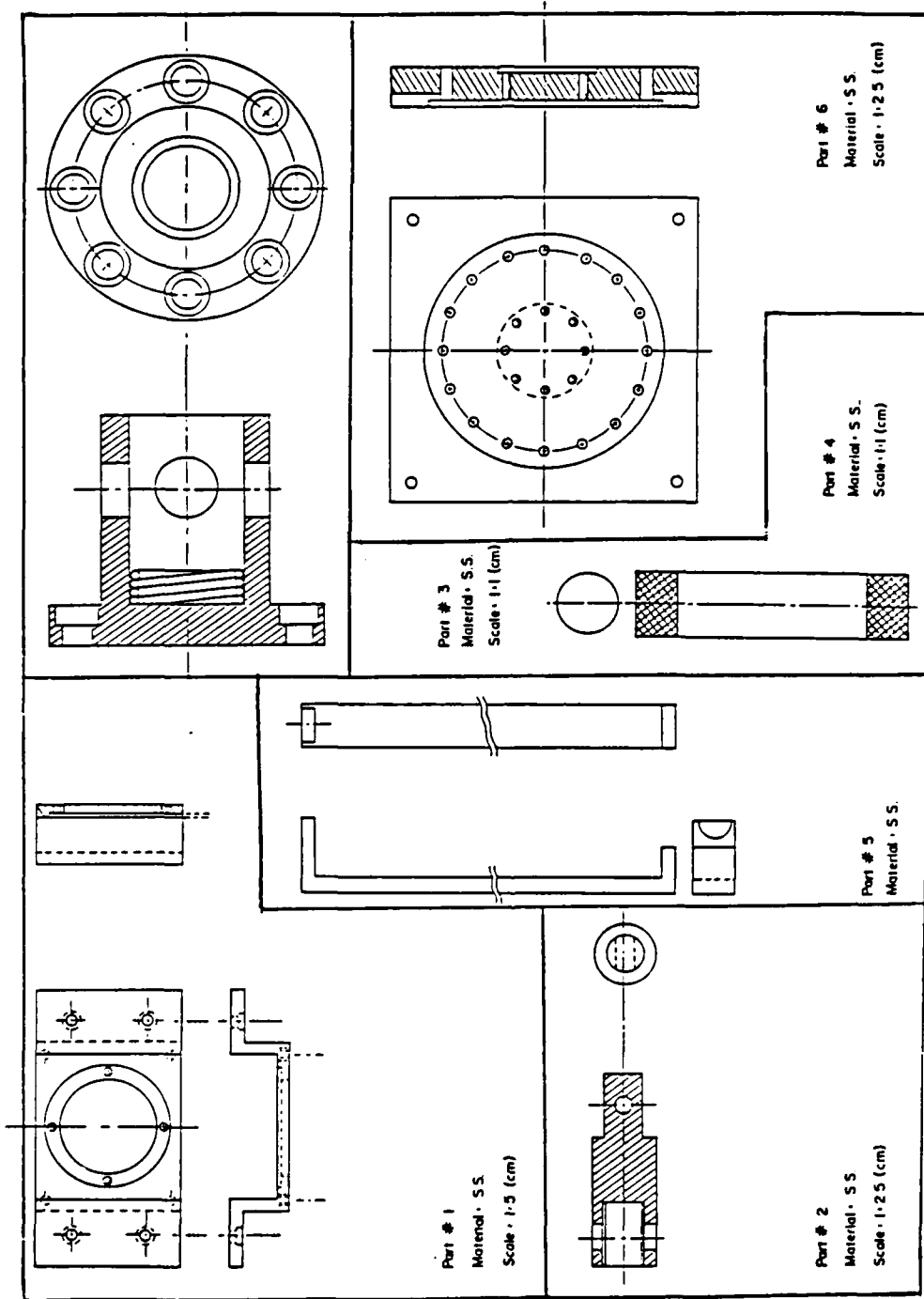


Figure 64. Parts of the external heating stage.

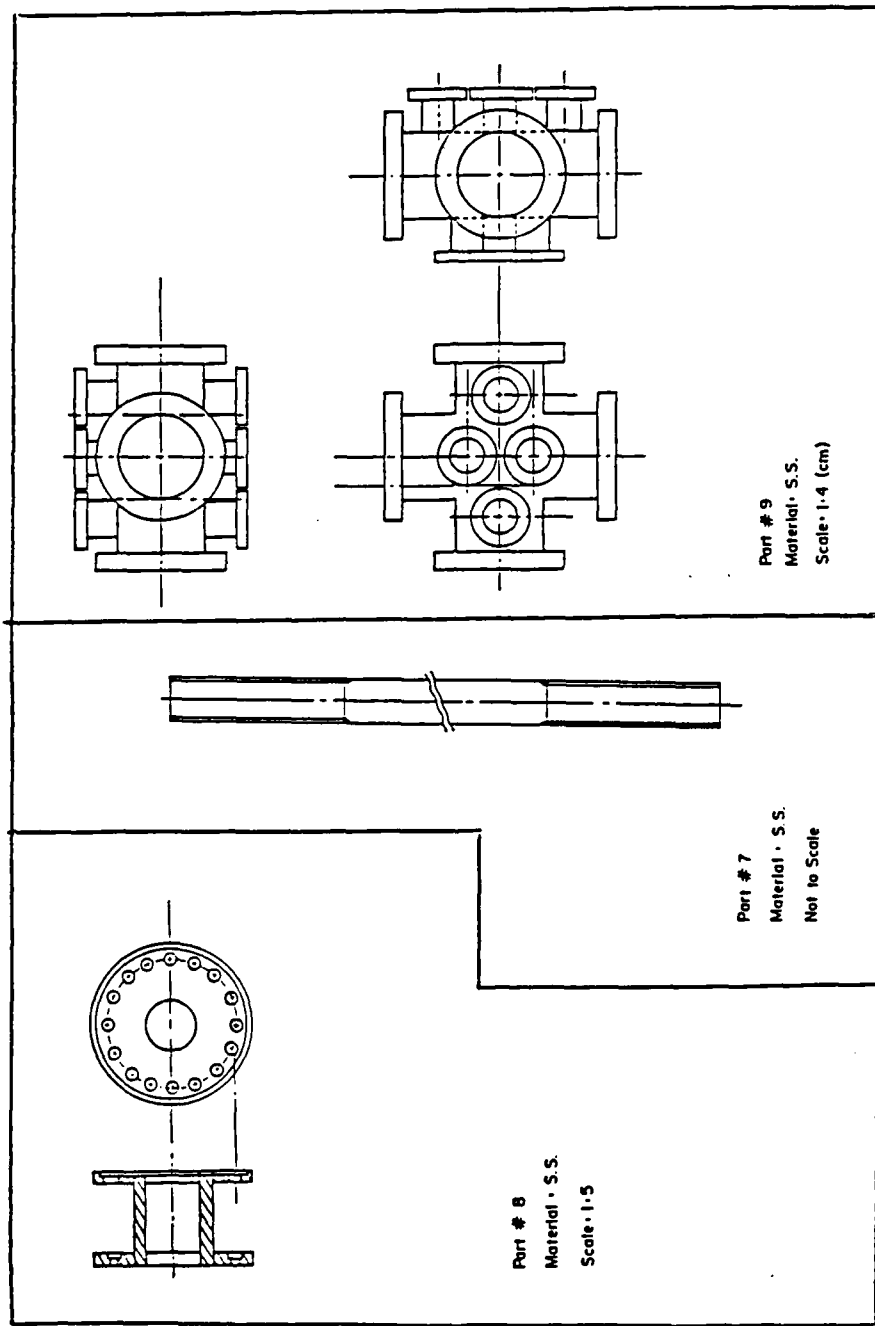


Figure 65. Other parts of the external heating stage.

were fabricated in the Mechanical Development Shop at Arizona State University. The design included suitable interfaces and tolerances between the parts. Most of the parts were drawn to scale, hence the absence of dimensions. The four-way cross chamber was designed at ASU but fabricated and leak tested at LATEC Industries, 400 Bryce Avenue, Los Alamos, New Mexico 87544. All the parts were designed with a major restriction that, while testing, under no circumstance does the cross bar exceed a movement of 25 mm. Any further movement would damage the delicate flexible coupling that was purchased from Varian Vacuum Co.

### 5.3.2 The internal stage

The internal part of the high temperature stage was the nerve centre for the entire system as this was the part where the heated specimen was held between grips, before deformation. The entire internal stage assembly was housed between two flanges in the four-way chamber (Part number 9 of the external stage). Figure 66 shows a partial cross-sectional view of the internal stage between flanges 1 and 2. The top flange was located at the top of the flexible coupling and the bottom flange was located at the base of the four-way cross chamber. The actual parts comprising this stage along with their assembly is shown in Figure 67. There were two unique features of the design of this grip assembly.

- a) Part number 15 was part of a stainless steel ball that seats into a hemispherical depression in Part number 7. This allowed accurate alignment of the grip when the specimen was about to be loaded.

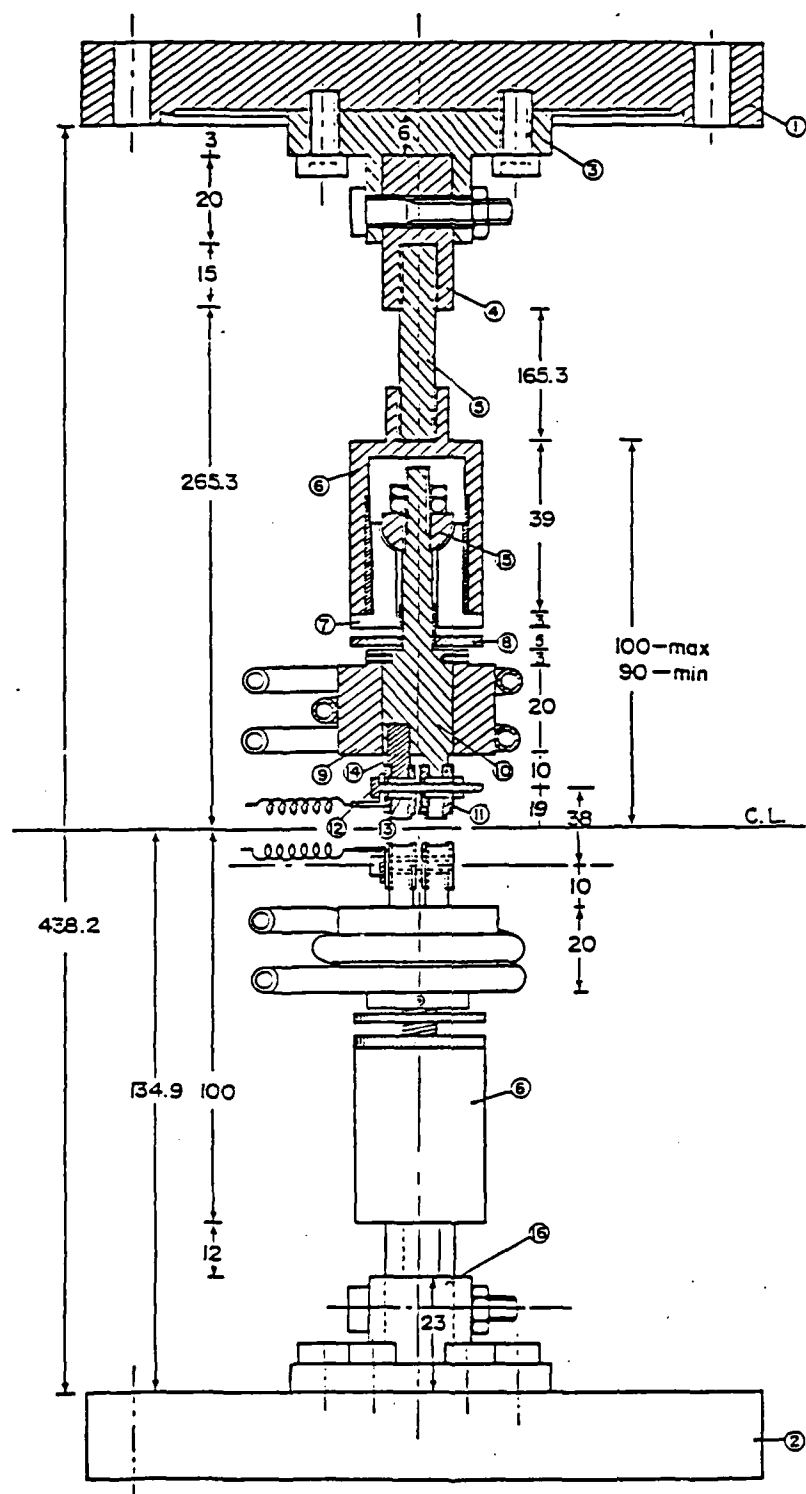


Figure 66. Partial cross sectional view of the internal stage.

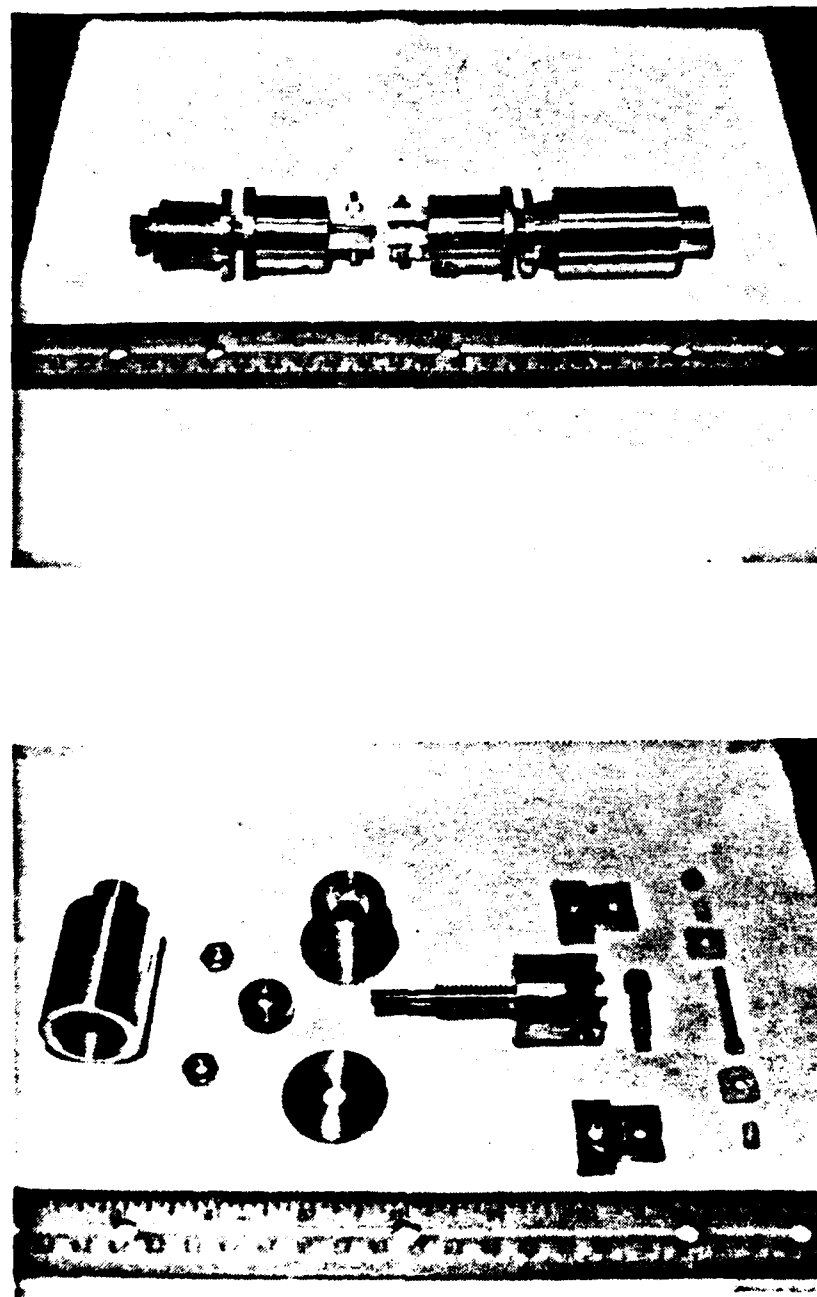


Figure 67. The various parts of the internal stage and their assembly.

b) The ring 8 was screwed onto the grip 10 and when this was tightened against the bottom of part 7, the entire grip assembly from the flange, to the pin 12, became one rigid construction and this permits compression loads to be transmitted directly to the specimen without any relative movement in between.

The grip 10 and pin 12 which were in direct contact with the specimen were made of Inconel-750X which has excellent high temperature resistance and strength. Parts 11 and 13 were special ceramic insulators made of Alumina AD-998. The properties of Inconel and the ceramics are given in Table 17.

Part 9 is an annular cylinder of copper with spiral copper tubes brazed on the external surface. Its purpose was to cool the grip if it gets too hot while heating the specimen. Because of the large thermal mass of the sink, it was anticipated that the grips would have to be cooled only if the temperature of the specimen exceeded 2500 K. All the components of the internal stage were designed with utmost caution and fabricated at the Mechanical development shop at Arizona State University.

#### 5.3.3 Fabrication and preparation of the tensile test specimen

Tungsten and its alloys, being extremely hard, are virtually impossible to be gripped between two jaws without a mechanical means of holding it. Invariably, the tungsten cuts through the grip material and slips out even before a moderate load is applied. Hence, it was necessary to design a button head sample according to ASTM [4] Standards. The final configuration of the sample, based on stress

Table 17. Important properties of Inconel 750X and ceramic AD-998.

1) Inconel 750X.
<p>Description: It is an age hardenable alloy with good corrosion and oxidation resistance. Also possesses excellent relaxation resistance.</p> <p>Major Applications: Gas turbine parts, Steam service and nuclear reactor springs, bolts, vacuum envelopes, extrusion dies, bellows forming tools.</p> <p>Nominal chemical composition: Ni+Co ~73%, Ti ~2.5%, Fe ~7%, Cr~15.5%.</p> <p>Thermal conductivity: 12 W/m°C at 20°C. 22.9 W/m°C at 815°C.</p> <p>Oxidation: Good to excellent.</p> <p>Carburization: Good to excellent.</p> <p>High temperature strength and stability: Good to Exc.</p> <p>Tensile strength: 1117-1331 MPa.</p> <p>Yield strength: 793-979 MPa.</p> <p>Elongation in 2": 30 ~ 15%.</p> <p>B.H.N.: 300 ~ 390</p>
2) Ceramic AD-998.
<p>Specific gravity: 3.96</p> <p>Rockwell hardness: 90</p> <p>Crystal size: 1 ~ 6 microns.</p> <p>Color: Ivory</p> <p>Compressive strength: 3792 MPa at 25°C. 1930 MPa at 1000°C.</p> <p>Flexural strength: 283 MPa., TYP. 25°C.</p> <p>Tensile strength: 207 MPa at 25°C. 103 MPa at 1000°C.</p> <p>Modulus of elasticity: 393 GPa.</p> <p>Shear modulus: 162 GPa.</p> <p>Poisson's ratio: 0.22</p> <p>Coeff. of linear thermal expansion: <math>3.44 \times 10^{-6}</math> /°C. at 25°C.</p> <p>Thermal conductivity: 39.7 W/m-K at 20°C. 6.3 W/m-K at 800°C.</p> <p>Specific heat: 880 J/Kg.-K at 100°C.</p>

calculations is shown in Figure 68. The specimen itself was fabricated by cutting out plates (24mm x 6mm x 0.75 mm) from the 6.4 mm. diameter rods. A special diamond embedded cutter with a thickness of 0.64 mm. was used for this purpose. Proper precautions were observed to maintain a feed rate that would not distort the machined surface. The plates were then mounted on an end milling machine and the right contours were machined using a diamond core drill operated at a speed of about 1000 rpm. In spite of the high speed and the fact that a diamond core drill was used, the machined surface was not smooth and so it had to be precision machined in the electrical discharge machine. The specimen was held in the fixture shown in Figure 69 and machined with a specially designed brass electrode assembly. The specimen was then mechanically polished with carborundum wet/dry paper and lapped to remove the bulk of the stress concentrators. It was finally electropolished in 10% aqueous solution of sodium hydroxide with an inconel cathode. Figure 70 is an electrical schematic for the electropolishing process and Figure 71 is the finished product ready to be tested in the testing stage.

#### 5.4 General instrumentation

There were three major contributors to the general instrumentation of the high temperature, high vacuum tensile testing system. These were the high vacuum system, the specimen heating system and the all important temperature measurement system.

##### 5.4.1 The ion-pump vacuum system

For the reasons mentioned earlier, it was necessary to conduct the test in an extremely clean environment. For this purpose, it was

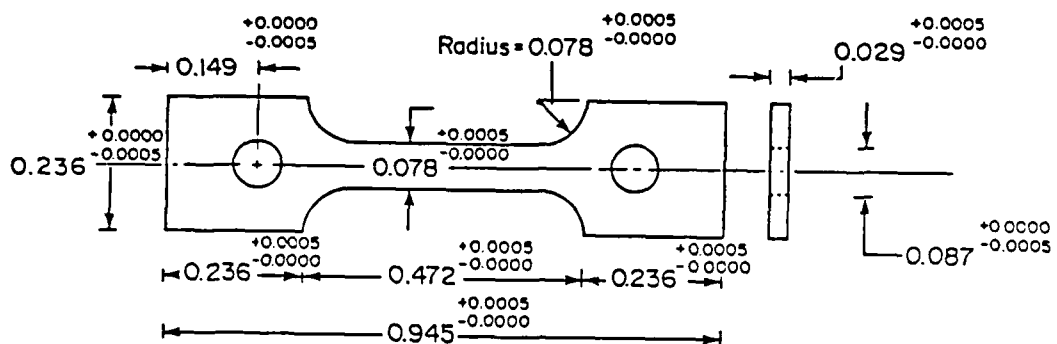


Figure 68. Configuration of tensile test specimen.

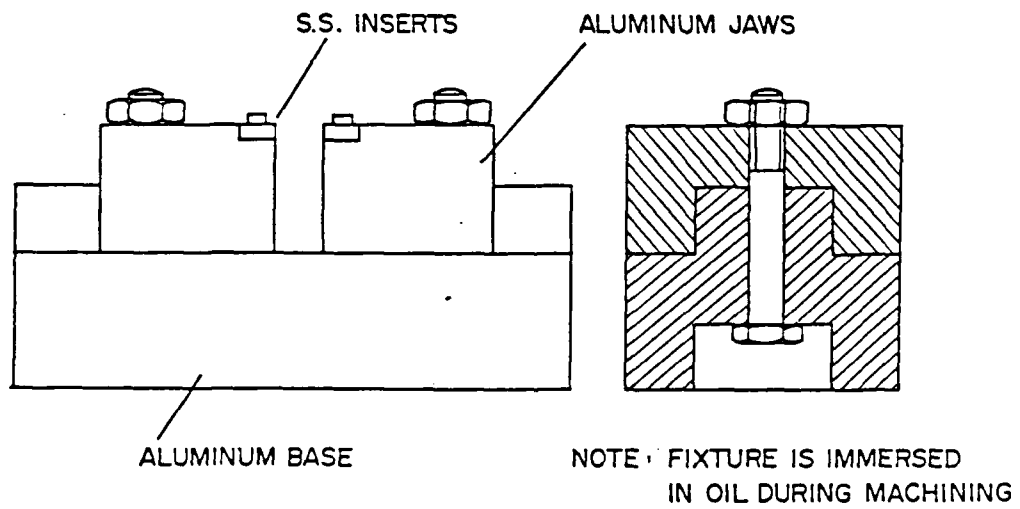


Figure 69. Fixture for holding the specimen in the EDM.

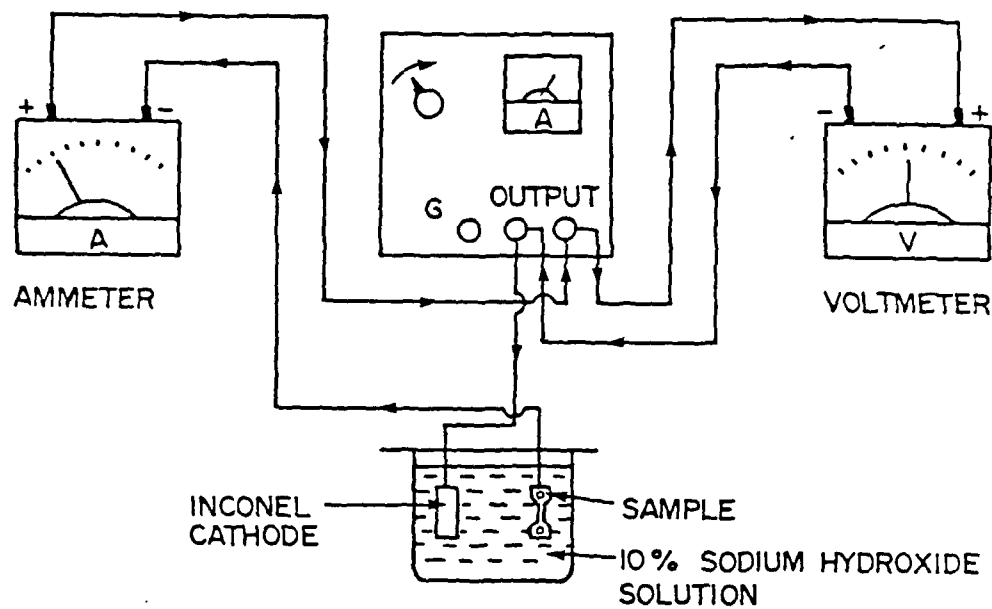


Figure 70. Electrical Schematic for electropolishing.



Figure 71. Finished product ready for testing.

decided that the heated sample would be fractured under a vacuum of better than  $10^{-7}$  torr. In order to achieve this kind of a vacuum atmosphere, the chamber had to be evacuated in two stages. The sorption pump was used for roughing purposes, to bring the vacuum down to about  $10^{-3}$  torr and then the ion-pump continued the evacuation down to the  $10^{-7}$  torr range. Every time the interior is exposed to atmospheric air, moisture seeps into small crevices thereby increasing the load on the ion-pump. To reduce this effect, nitrogen gas was purged through the entire system while switching specimens. Further, a baking system with a thermostat, was switched on when the vacuum was about  $10^{-6}$  torr. When the system was baked for seventy-two hours at 523 K, most of the adsorbed gases were eliminated thereby helping the ion pump to bring the vacuum down to the  $10^{-8}$  torr range.

#### 5.4.2 The sample heating system

The specimen was heated up using alternating current from a low voltage, high current power supply. The output from the power supply was carried to the two current feedthroughs, at the side of the four-way cross chamber, by means of copper wires as shown in Figure 62. Inside the vacuum system, copper leads carry the current, through thick tantalum sheets, the loading pin and then the specimen, and the circuit is completed back to the power supply. Tantalum was used between the copper and the inconel pin because it has a high melting point and serves as a sink to the heat generated near the pin. High quality ceramics were used to prevent any short circuits in the heating system.

#### 5.4.3 The temperature measurement system

Because of the nature of the testing and the method of heating chosen, it was impossible to get any useful thermocouple output as the potential difference in the circuit introduces spurious signals which do not mean anything as far as the temperature is concerned. Further, even if we were to use a micro-optical pyrometer, it would be impossible to drill a hohlraum in the specimen as it would act as a stress raiser. For this purpose it was decided that the pulse counting photon counter would be used to measure the surface temperature of the specimen, while it was being heated. The surface temperature would then be converted to the actual temperature with a couple of pre-calibrated plots. It was found that with this kind of measurement, the accuracy in temperature readings were  $\pm 20^{\circ}\text{C}$ .

##### 5.4.3.1 Calibration of photon counter and optical pyrometer

The calibration of the photon counter/optical pyrometer was carried out in two stages. In the first calibration test, a tungsten-rhenium disc with a sufficiently big hohlraum was spot welded to a tantalum holder and heated in the bell-jar system with a vacuum of  $2 \times 10^{-6}$  torr. The hohlraum was then viewed with the photon counter as well as the optical pyrometer at different temperatures to get the calibration plot (CC1) shown in Figure 72.

In the second calibration test, an identical series of temperature measurements were made but this time an electropolished tensile test sample with a very small hohlraum at its side, was welded to the tantalum holder instead of the disc in the first calibration test. In

AD-A173 245

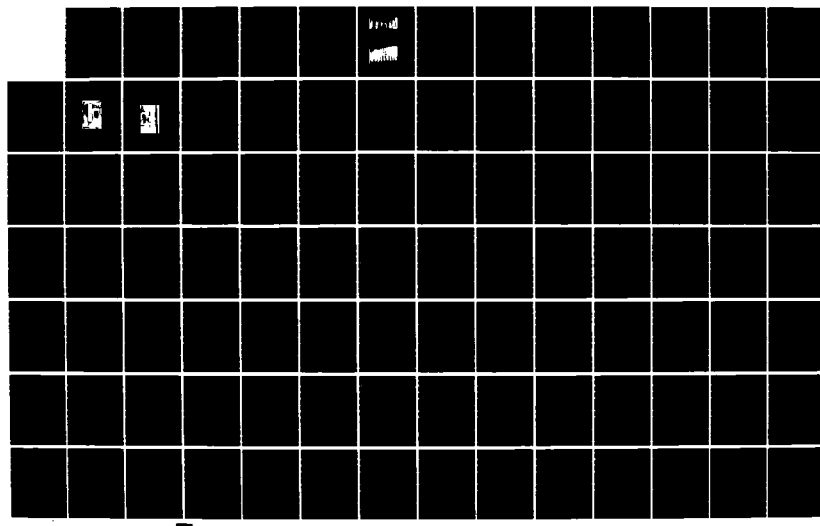
INVESTIGATION OF MATERIAL PROBLEMS FOR HIGH TEMPERATURE 4/5  
HIGH POWER SPACE. (U) ARIZONA STATE UNIV TEMPE COLL OF  
ENGINEERING AND APPLIED SCIE. D L JACOBSON ET AL.

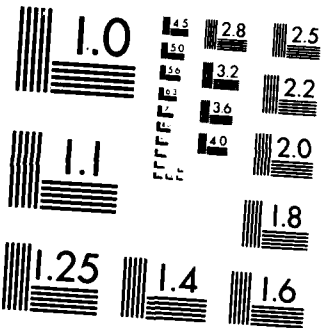
UNCLASSIFIED

JUL 86 AFOSR-TR-86-0019 AFOSR-83-0067

F/G 11/6

NL





MICROCOPY RESOLUTION TEST CHART  
NATIONAL BUREAU OF STANDARDS 1963-A

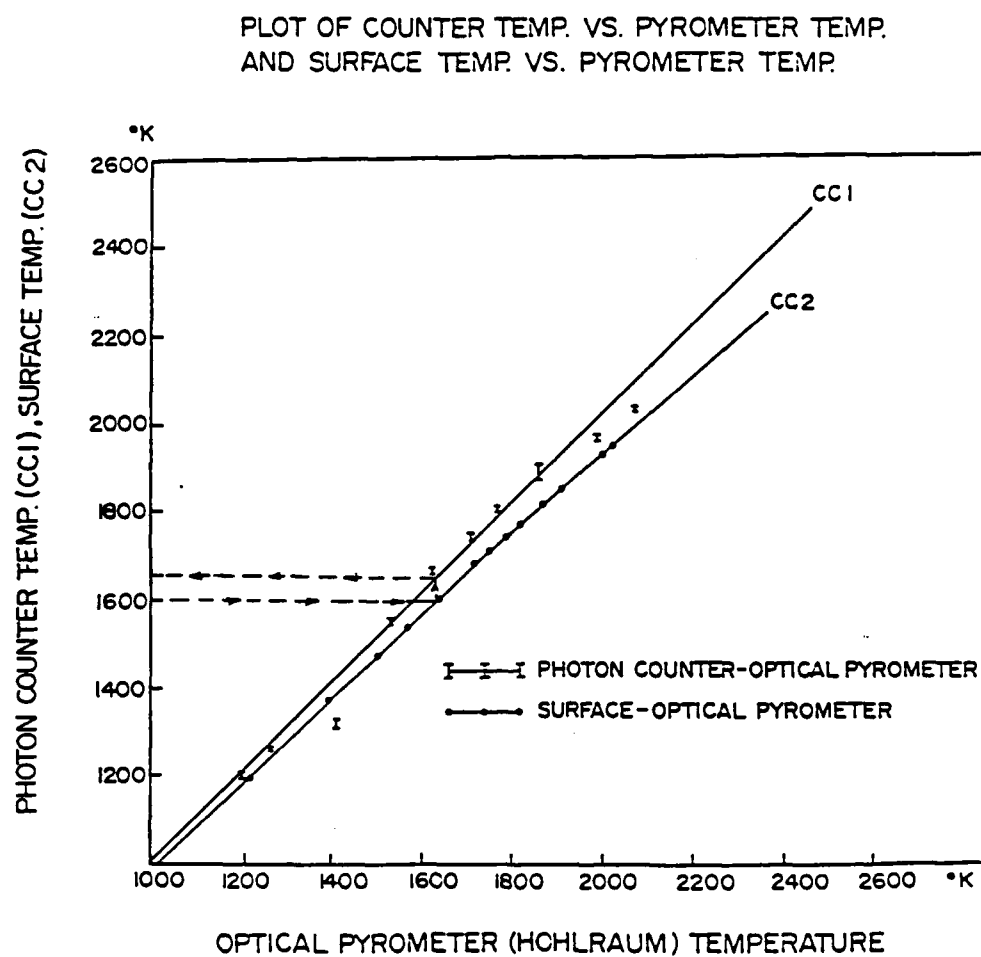


Figure 72. Calibration of photon counter/optical pyrometer

this case the hohlraum was viewed with the optical pyrometer but the adjacent surface was viewed with the photon counter to get the calibration plot (CC2). The entire calibration procedure is based on the assumption that the attenuation of the bell-jar is the same as that of the viewport in the tensile testing stage. During the actual test, the surface temperature was measured with the photon counter and the actual temperature was obtained with the calibration curves as shown in Figure 72.

### 5.5 Experimental procedure.

After the sample was electropolished, it was mounted between the inconel loading pins in the internal stage. The internal stage was then assembled in position inside the four-way cross chamber and the chamber connected to the ion-pump through an adaptor. The ion gauge, the electrical feed throughs and suitable valves for roughing were positioned on the flanges at the sides of the vacuum chamber. Flanges that were not used for any specific purpose were sealed with viewports. The entire set-up was then brought between the cross bars of the Instron tensile testing system and the load cell and flexible bellows coupling mounted in position. Electrical connections were then made through the loading pins and the sample, to provide the necessary resistance heating. The cross bar was moved such that the flexible coupling was completely compressed and adjustments were made in the internal stage to have the specimen properly gripped in position. The cross bar-stops were then located in position to limit its movement after the specimen had fractured.

The next step was to calibrate the load cell. This was done using an electronic calibration signal and the chart recorder in the Instron controls. The position of the pen was adjusted to give full scale deflection at a particular load. The movement on the chart recorder with the same calibration signal but varying multiples of the initial load setting were also checked. The sorption pump was now activated after routine electrical continuity checks. When the vacuum had attained a level of  $10^{-2}$  torr, the ion pump was switched on to bring the vacuum down to  $10^{-6}$  torr. At this stage the pumping efficiency came down due to the outgassing of adsorbed gases inside the system. At this stage, the entire system was baked at 523 K for about forty eight to seventy two hours. After baking, the vacuum was found to have improved to  $10^{-8}$  torr. The environment inside the vacuum chamber was now suitable for annealing the specimen and eventually fracturing it in tension. The electrical power is then supplied to heat up the gauge section of the specimen. When this section starts glowing, the photon counter is focussed on the lateral surface and energy counts recorded by the thermal printer. The current flow through the specimen is increased until the required temperature is attained. The specimen is then maintained at this temperature for a period of one hour before the Instron controls are activated to make the cross bar move up at a speed of 0.05 inches per minute. The chart recorder speed is adjusted using a system of gears. The load-deflection curve from the chart recorder is then filed for future analysis.

Before opening the chamber to replace the specimen, the vacuum chamber is purged with nitrogen gas until the pressure is slightly above

atmospheric pressure. The front viewport is then opened and the fractured sample stored for further analysis before inserting a new sample. The entire procedure is repeated and the sample fractured at a slightly higher temperature.

### 5.6 Results and discussion

Though the experimental set up did not pose any problems in fabrication and assembly, the fabrication of the tensile test specimen itself was a major hurdle in the process of activating the entire system. Brass and aluminum samples with known ultimate and yield strengths were first fabricated to calibrate the entire system including the resistance offered by the bellows system. However, when the tungsten samples were being fabricated, a number of problems were encountered, most of them having to do with the brittle nature of the material and improper sintering procedures. The magnitude of the complications involved can be comprehended from the fact that 150 man-hours of machining could produce just four samples from a quarter inch diameter rod with a length of 25 cms. This should have otherwise produced at least twenty samples. Figure 73 shows the various steps in the fabrication procedure from the raw material to the electropolished specimen ready to be tested. About fifty percent of the total time for machining was taken up in slicing plates from the rod, using a diamond cutting wheel. Most of the problems were encountered after this stage, as shown in Figure 74.

Figure 74 shows some of the stages at which the samples failed during fabrication. There were two reasons for this failure during

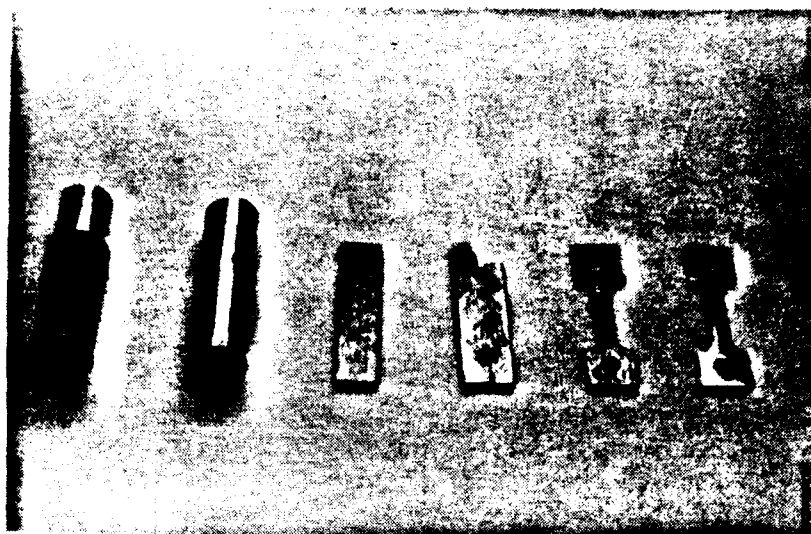


Figure 73. Various steps involved in the fabrication of the tensile test specimen.

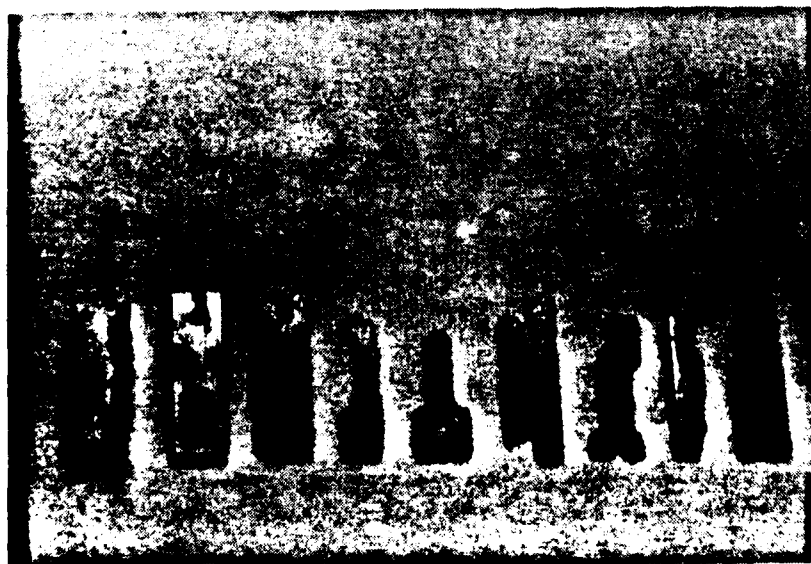


Figure 74. Stages at which the samples failed during fabrication.

fabrication. The first was that it was impossible to clamp the plates firmly in the vice because of the brittle nature of the material. Excessive stress while clamping, induced stresses inside the material and subsequent crack propagation resulting in the entire plate shattering to pieces. The second reason was that the material was not sintered in a suitable environment, at appropriate temperatures, leaving long streaks of oxidized surfaces inside the bulk of the material. The moment an end mill encountered such a surface the sample would part exposing the bluish colored oxidized surface. As seen in Figure 74, about ninety percent of the failures were due to the presence of microcracks and oxidized regions in the bulk of the material. These problems have been reported to the suppliers who are looking into the matter and suitably modifying their sintering procedures to minimize such defects in future sintered materials.

As a result of these fabrication problems, there were very few samples available for testing. Considering all the factors involved in high temperature tensile testing, it would be advisable to have at least fifty samples before any meaningful results can be derived from the tests.

Table 18 and Table 19 give high temperature tensile properties of various W,Re alloys as obtained by previous investigators. Though these do not contain all the samples of interest to us, the tables do give the trends expected of the W,Re and W,Re,ThO<sub>2</sub> alloys that were to be tested in the high temperature tensile testing system.

Table 18 is a compilation of the high temperature tensile properties of W,Re,ThO<sub>2</sub> samples manufactured by powder metallurgy

Table 18. High temperature tensile properties of W-Re-ThO<sub>2</sub> alloys [60].

Alloy	Annealing condition Hours/K.	Temperature K	0.2% offset yield stress ksi	u.t.s. ksi.	Reduction in area (%)
Pure W (P/M)	0.5/2673	1473	8.75	26.5	95
		1873	6.5	15.0	70
		2273	5.0	9.0	50
Pure W-5Re	0.5/2673	2673	4.8	4.8	18
		1473	25.1	46.1	92
		1873	18.2	27.2	80
Pure W-10Re	0.5/2673	2273	10.1	13.4	44
		2673	4.1	8.5	30
		1473	30.2	60.0	75
Pure W-5Re-2ThO <sub>2</sub>	0.5/2673	1873	22.1	30.2	45
		2273	13.2	15.1	30
		2673	9.1	10.2	35

techniques. These results were obtained by Sell et al. [60] who realized that data on pure W-5 or W-10Re alloys prepared by powder metallurgy were lacking. Tensile tests were made in the temperature range from room temperature to 2673 K. Tests above 1100 K were performed at a cross head speed of 0.05 inches per minute. It was found that when 3% Re was added to tungsten, it remarkably increases the strength up to 2173 K. Additions of 5 or 10% Re further enhances the strength but this strength enhancement is not retained at temperatures above 2273 K. The coarse 2% ThO<sub>2</sub> dispersion in the W-5Re alloy was found to have little effect on the strength of the alloy below 1773 K and only slightly improved its strength above this temperature. But they did observe a marked strengthening effect of a fine ThO<sub>2</sub> dispersion in the W-Re alloy at 1773 K. In conclusion, the general observations made in the high tempeorature tensile tests were that,

- rhenium significantly increased both the yield and ultimate stresses up to 2173 K.
- for each alloy, the yield stress, the ultimate stress and the reduction in area decreased with increase in temperature, except for the W-5Re-2ThO<sub>2</sub> alloy that exhibited a flat profile for the reduction in area.
- the high yield stress and ultimate stress values of the recovered alloy reflect the effects of substructure stabilization.
- fine ThO<sub>2</sub> dispersion could cause an increase of as much as 2000 to 4000 psi in the ultimate stress of the recrystallized alloy.

Table 19 is a summary of some previously investigated high temperature tensile properties of alloys involving W,Re,ThO<sub>2</sub>, and HfC.

Table 19. High temperature tensile properties of other solid-solution alloys of interest.

Alloy	Annealing Condition Hours/ $\text{K}$	Temperature $\text{K}$	0.2% Offset yield stress k.s.i.	u.t.s. k.s.i.	Reduction in area (%)	Reference
Pure W (arc cast)	Cold worked	1908	**	15.2	95	6, 27
	0.5/2367	2278	**	10.0	28	6, 27
W-0.75TiO <sub>2</sub>	**	1925	**	19.5	75	6, 27
	2255	**	**	9.8	25	6, 27
	2200	**	**	8.7	**	6, 38
	2600	**	**	3.2	**	6, 38
W-9.5TiO <sub>2</sub>	**	2200	**	14.0	**	6, 38
	2600	**	**	6.5	**	6, 38
W-1.77Re-0.36Ir	1.0/2255	1873	12.1	36.0	92	72
		2173	9.2	19.2	70	72
W-4.77Re-0.35Ir-0.35C	1.0/2366	1873	22.1	43.1	85	72
		2173	13.4	32.0	95	72
W-2.95Re-0.37Ir	As swaged	1922	59.6	63.7	80	51
		2200	17.6	19.6	76	51
	1.0/2258	1922	18.7	33.1	90	51
		2200	13.5	18.6	66	51
	1.0/2177	2200	12.6	19.3	68	51
	As swaged	16.11	138.0	145	145	65
W-23.4Re-0.27Ir	~1.1C	1922	56.9	62.7	84	36
		2200	15.5	16.7	87	36
	~0.8C	16.14	59.3	67.9	91	36
W-23.4Re-0.27Ir	1.0/2165	1922	32.9	34.7	95	36
		2200	17.3	17.8	95	36
	0.17/2977		46.4	48.0	13	36

This information is presented here to give the reader a feel for the trends expected in the high temperature, high vacuum tensile testing of W,Re additive alloys. It was noticed [6] that the strength of cold-worked tungsten decreases with increase in temperature. The behavior of any piece was found to depend on its prior history and structure. A large part of the problem involved in maintaining the strength of tungsten at temperatures above 1600 K was that of inhibiting or delaying recrystallization. High temperature tensile tests conducted by Hall and Sikora [27], on as-received cold worked and recrystallized tungsten, revealed that at about 1973 K the as-received material recrystallized sufficiently during testing that its strength dropped to that of the originally recrystallized tungsten. Table 27 also illustrates the strengthening of tungsten wire by ThO<sub>2</sub> additions, investigated by Knoll [38]. A 0.75 percent increase in ThO<sub>2</sub> was found to increase the elevated temperature ultimate strength from 8.7 ksi to 14.0 ksi. Yih and Wang [72] indicated that in order to maintain high ultimate strength and ductility at temperatures above 1900 K, a small quantity of hafnium has to be added to the W,Re alloy. The change in ductility of tungsten, as represented by the reduction in area, at 1900 and 2200 K is reduced considerably by the addition of rhenium and thoria. Addition of a stoichiometric quantity of carbon to the hafnium, increased the yield strength as well as the ultimate strength.

Tensile tests were performed by Raffo et al. [51], in a vacuum of less than  $5 \times 10^{-5}$  torr at a constant crosshead speed of 0.05 inch per minute. The specimens were brought to the temperature in approximately one hour and held at that temperature for the desired duration prior to

testing. They obtained data in both the as-swaged and recrystallized conditions. The most important observation made in these results was that at 2200 K the as-swaged and recrystallized tensile strengths were nearly identical indicating the effect of inhibiting recrystallization was minimal in this alloy. A W,23.4Re, 0.27Hf,C alloy was subjected to high temperature tensile testing by Klopp and Witzke [36]. They found that at 1350 K and 1650 K the swaged alloy retained its high strength. At higher temperatures however the strength decreased rapidly and at 2200 K the alloy had only a modest strength advantage over the binary W,24Re alloy. Annealing at about 2200 K reduced the tensile strength as compared to the swaged alloy.

The observations made by these earlier investigators and their results summarized in Table 18 and Table 19 should serve as an initial guideline to the tests to be conducted in the present system. Investigations can be made in areas which have not been touched upon and thereby gain useful knowledge on W,Re,ThO<sub>2</sub> alloys.

## 6. FACILITY DEVELOPMENT

As a part of the study of material problems for high temperature, high power space energy conversion systems, it was proposed that we build an electron beam floating zone refiner, that could serve the dual purpose of purifying materials and also distributing a desired impurity uniformly throughout the material. Zone melting is a general term for controlling the distribution of soluble impurities or solutes in crystalline materials. Here, a short molten zone travels slowly through a relatively long solid charge and while travelling redistributes the solutes in the charge.

Figure 75 is a schematic of the zone refining chamber built at the Thermionic Laboratory at Arizona State University. The system essentially consists of a four-way cross vacuum chamber with cooling water lines on its peripheral surface. The chamber is evacuated with a sorption pump-ion pump combination. The specimen is held in position by two linear motion feedthroughs. The electron beam source is a filament which surrounds the specimen. This electron gun can be moved up and down at several speeds with the help of the stepper motor operated ultra high vacuum linear motion drive. This unit was specially designed for high vacuum applications and supplied by Kurt J. Lesker Co. from Pennsylvania. Figures 76 and 77 provide two views of the partially completed zone refining system.

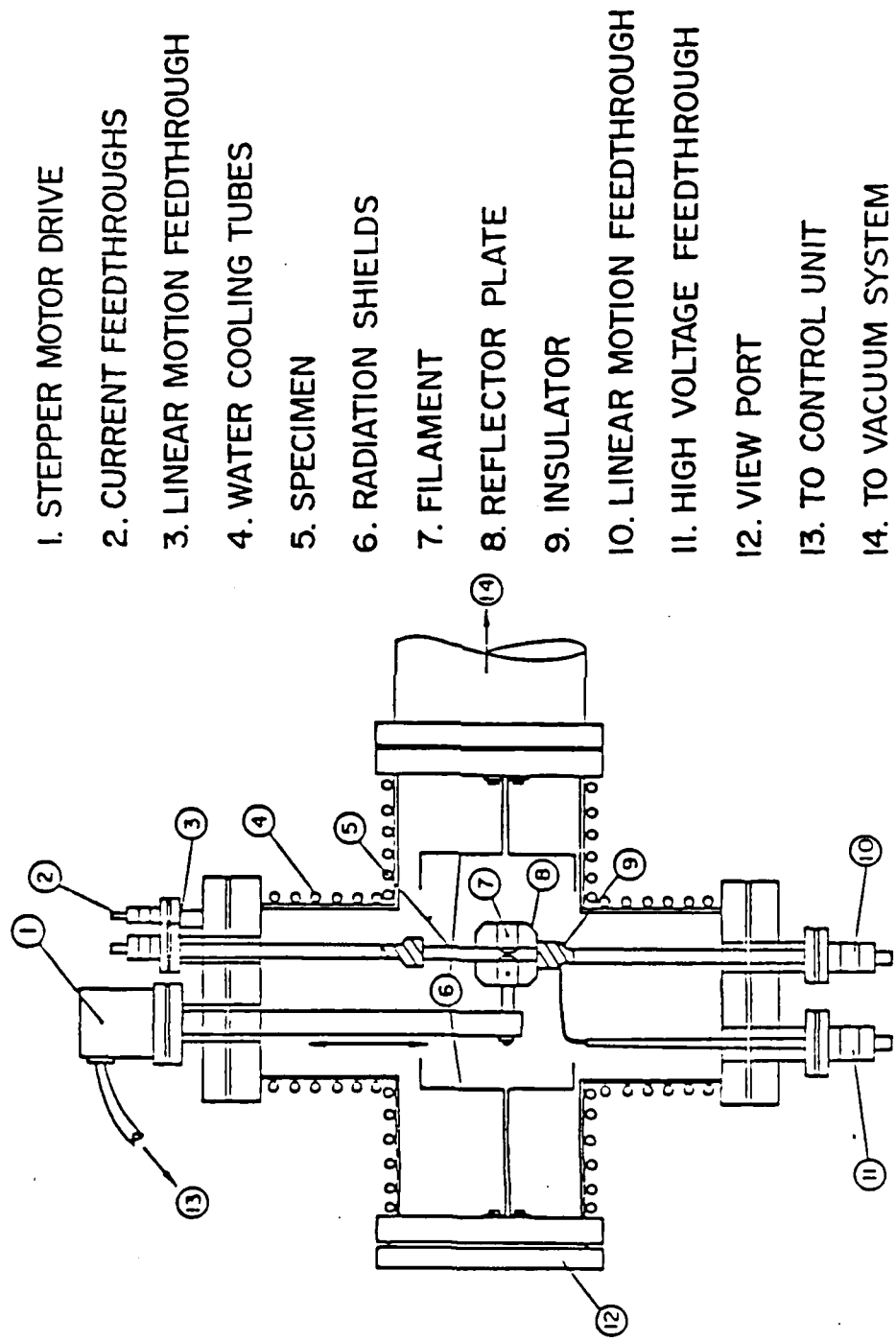


Figure 75. Schematic of the zone refining system components.

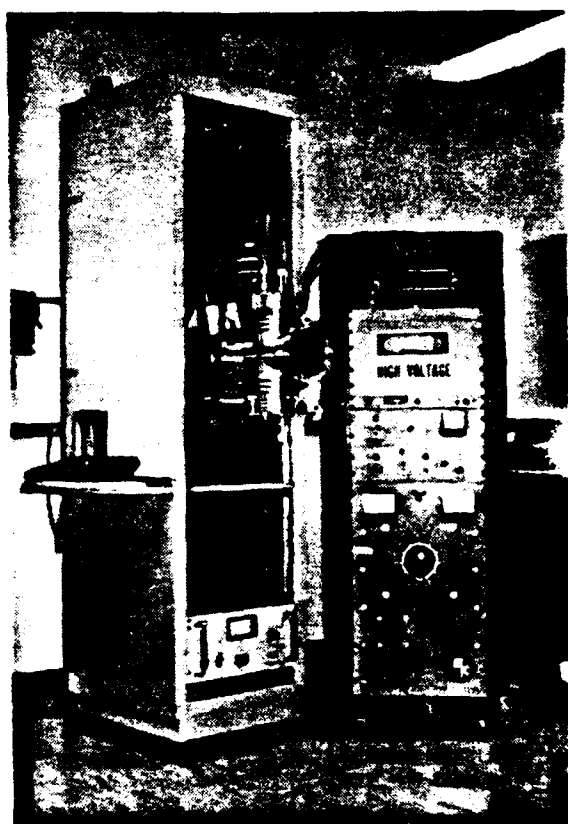


Figure 76. The zone refining system with power supply.

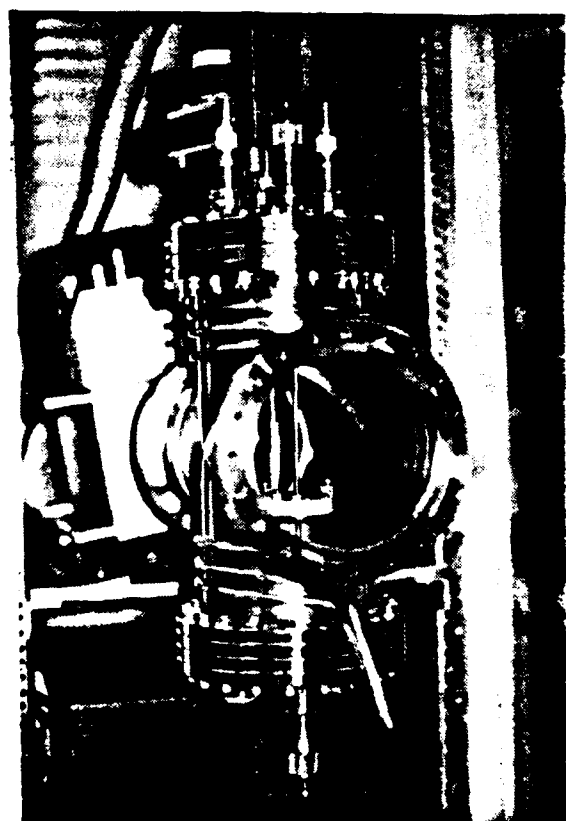


Figure 77. The zone refining chamber with the electron gun.

## 7. GENERAL CONCLUSIONS

The results from the thermionic emission microscopy of the tungsten, rhenium alloys revealed that work function is strongly dependent on temperature but is not a very strong function of rhenium content. Rhenium additions above 10% increased the work function of tungsten and delayed recrystallization considerably, thereby producing the desired small sized grain configuration. The samples tested had a porosity of 8%, as a result of which there was a lack of homogeneity in the material and this could affect both grain growth and thermionic emission. The dip in work function, as the rhenium content is increased from 3% to 25%, can be clearly understood if a detailed analysis is carried out in this range with small increments in rhenium content. A correlation between the work function and the ductility of the W,Re alloy in this range, would certainly provide some enlightening explanations for the unusual behavior observed.

Even though the experimental error in work function values was evaluated as  $\pm 0.04$  eV., there are other sources which might contribute to the error. These are, a) fluctuations in power supply, b) sample, accelerating and decelerating voltages, c) sample preparation. Precautions were observed wherever possible but there is still room for improvement in measuring the emission current more accurately.

Normal spectral emissivity data for sintered tungsten and tungsten, rhenium alloys has been obtained with a photon counting pyrometer. From the results obtained, it is observed that emissivity is not a very strong function of alloying content or temperature, but certainly depends on the surface condition for radiation of a given wavelength.

In general the emissivity of each alloy was found to decrease with temperature due to the removal of surface undulations during annealing. Suitable measures have to be taken into account for the major sources of error, which are a) dead time between pulses, and b) the size of the targeted sample. The former was corrected by using neutral density filters to reduce the number of counts, and the latter by using a camera lens and a 0.1 mm. aperture. In the present situation it is hard to say if the emissivity of the alloy is related to the emissivities of the related constituents.

As a result of the elevated temperature tests conducted on the sintered tungsten, rhenium alloys, the one hour recrystallization temperature for sintered tungsten was found to be 1625 K and that for tungsten, rhenium alloys was around 1900 K. Very little change in recrystallization temperature was observed, with increase in rhenium content. Microhardness measurements revealed the nature of the softening of tungsten, rhenium alloys at elevated temperatures. The introduction of rhenium into tungsten sharply decreases the grain size during recrystallization. This is evidenced by the fact that the recrystallized grain size decreased from 62  $\mu\text{m}$  for tungsten to 32  $\mu\text{m}$  for W-25 at.%Re. In general, the results obtained are expected to be of scientific interest and potentially useful for future research work on the elevated temperature softening of refractory metals and alloys.

The addition of 1% of thoria to each of the W,Re alloys did not change the emissivity behavior appreciably but did provide steadier and lower values of emissivity which is rather important from the point of view of application in a TEC. However the thoria did provide some

dispersion strengthening in the W,25Re and W,30Re samples and their recrystallization temperatures were increased by about 150 to 200 K. As the microstructures were not very clear it was not possible to get the recrystallized grain sizes for the alloys with 25% and 30% Re.

The addition of 1% of thoria to the samples tested for thermionic emission revealed that there was a marginal increase in the work functions when compared to the W,Re alloys. The variations with temperature and rhenium content were not as pronounced as that for the W,Re alloys, leading one to believe that ductility may have contributed to the anomalous behavior observed earlier.

## 8. RECOMMENDATIONS FOR FUTURE RESEARCH ACTIVITY

### i) Thermionic Emission:

The present research program provided some insight towards the direction of future research activity in thermionic emission and work function evaluation. W,Re and W,Re,ThO<sub>2</sub> alloys were evaluated, but there still appears to be some ambiguity in the results for rhenium contents between 5% and 15%. A detailed study of the alloys with small increments in rhenium content in this range involving correlations between ductility and work function would provide some enlightenment on the anomalous behavior that was observed in the present study.

The optimization study on the ideal W,Re,ThO<sub>2</sub>, HfC alloy would be complete only when the properties of the W,Re alloy with stoichiometric amounts of thorium and hafnium, are evaluated. This would involve using a W-25Re-1ThO<sub>2</sub>-0.3HfC alloy as the base alloy system and then testing samples with very small increments in thorium and hafnium. As far as the thermionic emission microscope is concerned, it is quite obvious that the difference in vacuum levels indicated by the ion pump and the ion gauge necessitates the use of an additional ion-pump very close to the emitter assembly. The welded bellows assembly, which has a small leak should be replaced. A baking chamber for the ion pump would certainly help bring the vacuum level to the 10<sup>-10</sup> torr range.

### ii) Emissivity measurement and recrystallization studies:

Though the general trend for the emissivity and the microhardness values of the W,Re and W,Re, ThO<sub>2</sub> samples, was to decrease with temperature, no attempts were made to check the surface composition at

each stage of the experiment. This would reveal if the results obtained are valid at the surface only or in the entire bulk of each specimen. Both Auger electron spectroscopy and scanning electron microscopy are recommended at the conclusion of each stage of annealing to get a qualitative and quantitative measure of grain boundary segregation of impurities. Further, emissivity being a surface phenomenon, would be a strong function of the surface roughness. In order to find out the effect of surface roughness, it would be interesting to have different surface roughness around the hohlraum and study the variation of spectral emissivity.

Since a diffusion pumped system was used for emissivity measurement, it becomes virtually impossible to have an environment free of contaminants, such as oil vapor etc. To avoid this problem it would be advisable to have an ion pumped vacuum chamber that would provide a clean environment for testing. The discriminator/amplifier and the timer counter have to be frequently calibrated as it was observed that their performance strayed a number of times, while testing. The performance of the photon counter should be checked for thermal radiation of wavelengths other than  $0.535 \mu\text{m}$ .

### iii) Mechanical testing and related topics:

The instrumentation for the present set up allows for heating the specimen by resistance heating. It was found that a current of the order of 60 amperes or more is necessary to heat the specimen to significant temperatures. This could prove hazardous at very high temperatures. An induction heating system should be incorporated in the

present testing chamber. This would also allow thermocouples to be mounted on the heated specimen and enable the measurement of temperatures below 1100 K. This is quite important as it would permit studies on ductile to brittle transition which cannot be done on the existing system.

The zone refiner should be able to purify and distribute restricted amounts of impurity in sintered samples. It would make the laboratory self sufficient as far as exotic alloying element combinations are concerned. The fractured surface should be observed in the scanning and transmission electron microscopes in order to get a measure of the relative amounts of brittle fracture, ductile fracture, cleavage etc. at different temperatures. A correlation between the ultimate/yield stress and the predominant type of fracture at any given temperature should prove to be an asset in the selection of a suitable alloying combination for TEC applications.

The grips used in the tensile stage should be modified to receive wires so that tensile testing on wires could be carried out at elevated temperatures. As we already have a facility to obtain cesiated work functions of wires of refractory alloys, it would certainly be interesting to determine the relationship between mechanical strength and thermionic work function.

## REFERENCES

1. S. W. Angrist: Direct Energy Conversion, 3rd ed., Allyn and Bacon, Inc., Boston, Massachusetts, 1976, pp. 249-291.
2. E. N. Aqua and C. N. J. Wagner: Trans ASM, 1966, vol. 59, pp. 367-373.
3. R. J. Arsenault: Acta Met., 1969, vol. 17, pp. 1291-1297.
4. ASTM: Designation E8-82, AASHTO No. T-68, ASTM Committee on Standards, Philadelphia, Pennsylvania, Feb. 1983, pp. 119-139.
5. R. H. Atkinsor: Conference on Govt. Sponsored Research in Tungsten, Durham, North Carolina, 1959.
6. V. D. Barth: DMIC report No. 127, Defense Metals Information Center, Columbus, Ohio, Mar. 15, 1960.
7. C. Bice: Thesis (M.S.), Arizona State University, Tempe, Arizona, May 1985.
8. J. R. Branstetter and R. D. Schall: NASA TM x-52147, NASA Technical Memorandum, Cleveland, Ohio, 1965.
9. A. A. Brown, L. J. Neelands and H. E. Farnsworth: Journal of Applied Physics, 1950, 1, vol. 21, pp. 1-4.
10. J. W. Christian: Proceedings of the Second International Conference on the Strength of Metals and Alloys, ASM, Cleveland, Ohio, 1970, pp. 29-70.
11. M. Cohen: Proceedings of the AFOSR Special Conference on Prime Power for High Energy Space Systems, Norfolk, Virginia, Feb. 1982.
12. P. Cotteril and P. R. Mould: Recrystallization and Grain Growth in Metals, 1st ed., John Wiley and Sons, New York, New York, 1976, pp. 30-115.
13. B. D. Cullity: Elements of X-ray Diffraction, 2nd ed., Addison Wesley Publishing Co. Inc., Reading, Massachusetts, 1978, pp. 421-444.
14. D. L. Davidson and R. R. Brotzen: Acta Met., 1974, vol. 18, pp. 463-470.
15. J. C. Devos: Physica, 1954, vol. 20, pp. 690-714.
16. G. E. Dieter: Mechanical Metallurgy, 2nd ed., McGraw-Hill Book co., New York, New York, 1976.

17. E. Eichen: Metallurgical Society Conference, 1965, vol. 38, pp. 177-216.
18. E. Eichen: Thermionic Emission Microscope, High Temperature, High Resolution Microscopy Symposium, Gordon and Breach, New York, New York, 1967.
19. E. Eichen and J. W. Spretnak: Trans Am. Soc. Metals, 1959 vol. 51, pp. 54-75.
20. L. B. Ekbom: NDRI report No. T-8, Materials Research Division, NDRI, Stockholm, Sweden, 1970.
21. R. L. Forgacs, B. A. Parafin and E. Eichen: The Review of Scientific Instruments, 1965, 8, vol. 36, pp. 1198-1203.
22. G. A. Geach and J. R. Hughes: Plansee Proceedings, Pergamon Press, London, England, 1956, pp. 245-350.
23. S. A. Golavanenko, A. B. Natapova, B. A. Klypin and T. M. Kasaev: Translated from Metallovedenie i Termicheskaya Obravotka Metallov, 1976, vol. 9, pp. 59-60.
24. G. G. Gubareff, J. E. Janssen and R. H. Torburg: Thermal Radiation Properties Survey, 2nd ed., Honeywell Research Center, Minneapolis, Minnesota, 1960.
25. A. G. Guy: Essentials of Material Science, 1st ed., McGraw-Hill Book Company, New York, New York, 1976.
26. R., W. Hall, P. L. Raffo, W. R. Witzke and W. D. Klopp: NASA Technical Report No. TND-5340, NASA, Cleveland, Ohio, 1969, pp. 163-172.
27. R. W. Hall and P. F. Sikora: NASA Memo No. 3-9-59E, NASA, Cleveland, Ohio, Feb. 1959.
28. R. D. Heidenreich: Journal of Applied Physics, 1955, 7, vol. 36, pp. 879-889.
29. D. L. Jacobson: Metallurgical Trans. 1972, vol. 3, pp. 1263-1268.
30. D. L. Jacobson and A. E. Campbell: IEEE Thermionic Conversion Specialist Conference, 162 Order Dept., IEEE, New York, New York, 1968.
31. D. L. Jacobson and A. E. Campbell: Metallurgical Trans., 1971, vol. 2, pp. 3063-3066.
32. D. L. Jacobson and J. Jaskie: Journal of Energy, 1981, vol. 5, pp. 186-189.

33. C. V. Jadrith: Thesis (M.S.), Arizona State University, Tempe, Arizona, Dec. 1984.
34. R. I. Jaffee, C. I. Sims and J. J. Harwood: Plansee Proceedings, Pergamon Press, London, England, 1958, pp. 380-405.
35. W. Kingery: Property Measurements at High Temperatures, 2nd ed., John Wiley and sons, New York, New York, 1959.
36. W. D. Klopp and W. R. Witzke: Journal of Less Common Metals, 1971, vol. 24, pp. 427-443.
37. W. D. Klopp, W. R. Witzke and P. L. Raffo: NASA Technical Report, No. TND-3483, NASA Lewis Research Center, Cleveland, Ohio, 1966.
38. M. Knoll: Materials and Processes of Electron Devices, 1st. ed., Springverlag, Germany, 1959.
39. V. Kuznetsov: Proceedings of the Third International Conference on Thermionics Electrical Power Generation, vol. 1, Juelich, Germany, June 1972.
40. R. D. Larrabee: Optical Society of America, Journal, 1959, vol. 49, pp. 619-625.
41. D. J. Maykuth, F. C. Holden and R. I. Jaffee: Rhenium, 1st ed., Elsevier Publications, New York, New York, 1962, pp. 114-150.
42. H. B. Michaelson: Journal of Applied Physics, 1950, 1, vol. 21, pp. 536-540.
43. J. F. Morris: Air Force Technical Report, No. ERC-R-83025, AFWAL, Tempe, Arizona, 1982.
44. J. F. Morris: Progress in Astronautics and Aeronautics, 1982, vol. 83, p. 232.
45. S. J. Noesen and J. R. Hughes: Trans. of the Metallurgical Society of AIME, 1960, vol. 218, pp. 256-261.
46. J. Nutting and S. R. Rouze: Fifth International Congress for Electron Microscopy, 1962, vol. 1, pp. CC-7-CC-9.
47. Y. Ohwada: Applied Optics 1983, vol. 22, pp. 2322-2325.
48. V. A. Petrov, V. Y. Chekhovskoi and A. E. Sheinblin: High Temperature, 1963, vol. 1, pp. 19-23.
49. O. D. Protopov, E. V. Mikheeva, B. N. Sheinberg and G. N. Shuppe: Soviet Physics - Solid State, 1966, 4, vol. 8, pp. 909-914.

50. T. J. Quinn: High Temperatures-High Pressures, 1980, vol. 12, pp. 359-372.
51. P. L. Raffo and W. D. Klopp: NASA Technical Report No. TND-3248, NASA, Cleveland, Ohio, Feb. 1966.
52. P. Ratanapupec and R. G. Bautista: High Temperature Science, 1981, vol. 14, pp. 269-285.
53. R. E. Reed-Hill: Physical Metallurgy Principles, 1st ed., Van Nostrand Co. Inc., Toronto, Canada, 1964.
54. D. A. Robins: Journal of Less Common Metals, 1959, vol. 1, pp. 396-440.
55. S. R. Rouze and W. L. Grube: Fifth International Congress for Electron Microscopy, 1962, vol. 2, pp. CC-5-CC-7.
56. B. S. Sadykov: High Temperature, 1965, vol. 3, pp. 352-356.
57. A. Sandor: Journal of Electronic Control, 1963, vol. 15, pp. 101-111.
58. E. M. Savitskii, M. A. Tylkina and K. B. Povarova: Rhenium Alloys (translated from Russian), TT 69-55081, IPST Press, Jerusalem, Israel, 1969.
59. E. M. Savitskii, T. V. Burov, L. N. Litvak, G. S. Burkhanov and N. N. Bokareva: Soviet Physics-Technical Physics, 1967, 7, vol. 11, pp. 974-976.
60. H. G. Sell and R. Stickler: Sixth Plansee Seminar, Reutte, Austria, June 1968, pp. 71-102.
61. S. Shlomo: Thesis (M.S.), Arizona State University, Tempe, Arizona, Dec. 1985.
62. B. A. Shur and V. E. Peletskii: High Temperature, 1982, vol. 19, pp. 841-850.
63. R. G. Siegel and J. R. Howell: Thermal Radiation Heat Transfer, 2nd ed., McGraw-Hill Book Co., New York, New York, 1981.
64. C. J. Smithells: Tungsten, 2nd ed., Chapman and Hall Publications, London, England, 1952.
65. J. R. Stephens and W. R. Witzke: Journal of Less Common Metals, 1971, vol. 23, pp. 325-342.
66. E. K. Storms and B. A. Mueller: Proceedings of the Tenth Materials Research Symposium on Characterization of High Temperature Vapors and Gases, NBS, Gaithersburg, Maryland, 1978, pp. 143-152.

67. F. I. Uskov and A. V. Babak: Translated from Problemy Prochnosti, 1981, vol. 1, pp. 79-82.
68. L. H. Van Vlack: Elements of Materials Science and Engineering, 4th ed., Addison-Wesley Publishing Co., Reading, Massachusetts, 1980.
69. J. D. Verhoven: Fundamentals of Physical Metallurgy, 1st ed., John Wiley and Sons, New York, New York, 1976.
70. J. Wadsworth: Metallurgical Transactions 1983, vol. 14A, p. 285.
71. W. R. Witzke: Metallurgical Transactions, 1974, vol. 5, p. 305.
72. S. W. H. Yih and C. T. Wang: Tungsten-Sources, Metallurgy, Properties and Applications, 1st ed., Plenum Press, New York, New York, 1974.
73. G. A. Zhorov: High Temperature, 1970, vol. 8, pp. 501-504.

**Appendix - 1. Details of the components of the system for thermionic emission microscopy.**

Sl. No.	Particulars	Capacity	Other Information
1.	Tungsten filament	0.020" in Dia.	Flat spiral heater, type 894 Union City filament Corporation.
2.	Filament Power Supply	0-18 VDC, 0-30 ADC	Model CR 18-30, NJE Corporation
3.	Bombardment Power Supply	0-1500 VDC, 0-1500 mADC	Model PX 6142-B, KiloVolt Corptn.
4.	Sample Voltage P.S.	0-600 VDC, 0-300 mADC	Model 407D, John Fluke Mfg. Co.
5.	Accelerating Voltage P.S.	0-300 VDC, 0-0.8 ADC	H-V. Supply 1030-20, Sorenson Incorporated
6.	Decelerating Voltage P.S.	0-300 VDC, 0-0.8 ADC	Hewlett-Packard Model 890A
7.	Electrometer	10(-1) to 10(-11) Amps	610 C, Keithly Instruments
8.	Electrometer	10(-1) to 10(-14) Amps	642, Keithly Instruments
9.	Vac-Ion Pump	10(-4) to 10(-9) Torr	Varian, 1/10 l/s, model 921-0066
10.	Ion-gauge controls	10(-4) to 10(-11) Torr	Varian, dual range ionization gauge. Model 971-1008

Appendix - 2.

Some technical data on the thermionic emission microscope.

Material of microscope main body	S.S. 304
Thickness of the wall of the chamber	(0.12")
Length of the microscope	20"
Internal diameter of main body	6.25"
Drive accuracy of x,y,z mechanism	$\pm 0.001"$ $\pm 2\%$ of F.S. in the range 3 to $10^{-11}$ amps.
Accuracy of electrometer	$\pm 4\%$ of F.S. in the range $10^{-11}$ to $10^{-14}$ amps.
Distance of collector from screen aperture	0.06"
Distance between filament and sample	0.03"
Torque for bolts on small flanges	16 ft-lbs.
Torque for bolts on large flanges	26 ft-lbs.
Experimental error for wf evaluation	$\pm 0.04$ eV
Approximate output voltage for-TEC	1 volt
Approximate current density	30 amps/cm <sup>2</sup>
X-rays emitted from the device	< 0.1 mR/hour
Noise level of electrometer	$4 \times 10^{-14}$ amps.
Best theoretical resolution	12 Å
Resolution with electrostatic lenses	400 to 1000 Å

Appendix - 3, Details of the various components of the emissivity measurement system .

Function	Sl. No.	Particulars	Capacity	Other Details
Vacuum System	1	Mechanical Roughing Pump	Up to $10^{-3}$ torr	Cenco 'HIVAC 15"
	2	Diffusion Pump	$10^{-3}$ to $10^{-7}$ torr	Central Scientific Co. Type 0162, NRC Equipment Corp.
	3	Ionization Gauge	$10^{-8}$ to $10^{-11}$ torr 60 $\mu\text{A}$ to 12 MA em.	Varian Model 971-1008 Dual range, Varian Vacuum Co.
Heating System	4	Tungsten Filament	0.020"	Flat spiral heater, Type 894 Union City Filament Corp.
	5	Filament Power Supply	0-10 V, 0-30A A.C.	Model No. 810-0.5 Hypotronics Inc.
Temperature Measurement System	6	Electron Bombardment P.S.	0-10 KV, 0-0.5A D.C.	Model No. 810-0.5 Hypotronics Inc.
	7	Photon Counting Pyrometer	Approx. 1100°K to 2900°K	Phototube Model RFI/B-213F EMI-GENCON Inc. Model 1121 Princeton Applied Research
Temperature Measurement System	8	Discriminator-Amplifier with control unit	--	Model 5300B, Hewlett-Packard
	9	Timer-Counter	> $10^6$ Counts	Model 5150A, Hewlett-Packard
	10	Thermal Printer	1 sec - 1 hr Intervals	

**SECTION 5**

**DETERMINATION OF WORK FUNCTION OF TUNGSTEN-RHENIUM  
ALLOYS USING VACUUM EMISSION VEHICLE**

## ABSTRACT

A new 3.556 mm collector assembly was designed and fabricated for a vacuum emission testing station due to the availability of the W-Re sample size. Samples of 3% and 30% rhenium were tested. Work functions of the two samples were found to be functions of heating time in the tested temperature range between 1830 K to 2127 K. Each sample was tested at five different temperatures. A plot of the effective work function versus heating time was generated at each temperature. The general pattern of these plots were an initial minimum point followed by a work function shift toward a higher stable final value. The work function of the 3% rhenium sample climbed 0.45 eV during a 6 hours testing period. The 30% rhenium sample shifted its work function earlier than the 3% rhenium one. The highest work function, approximately 5.3 eV, was found at 2011 K for the 30% rhenium sample.

## TABLE OF CONTENTS

Chapter	page
1. INTRODUCTION .....	1
2. THERMIonic EMISSION THEORY .....	4
3. DESIGN AND FABRICATION OF 3.556 MM DIAMETER COLLECTOR ASSEMBLY .....	9
4. EXPERIMENTAL APPARATUS .....	21
Introduction .....	21
Thermionic emission vehicle assembly .....	21
Temperature measurement system .....	24
Vacuum system .....	24
Electrical system .....	25
5. EXPERIMENTAL PROCEDURE .....	28
Introduction .....	28
Preparation stage .....	28
Vacuum stage .....	30
Data collecting stage .....	30
Data analyzing stage .....	32
6. EXPERIMENTAL RESULTS AND DISCUSSION .....	38
7. CONCLUSION .....	50

## LIST OF ILLUSTRATIONS

Figure	page
2.1 Schottky plot of polycrystalline materials .....	8
3.1 Presumed new collector geometry .....	11
3.2 Collector design .....	12
3.3 Collector radiator design .....	13
3.4 Guard ring design .....	14
3.5 Guard ring radiator design .....	15
3.6 Collector assembly of 3.556 mm diameter collector .....	16
4.1 Configuration of the emitter assembly .....	22
4.2 Electrical circuit of vacuum emission test station .....	26
6.1 Work function-heating time curves of W-3%Re sample at several temperatures .....	40
6.2 Work function-heating time curves of W-30%Re sample at several temperatures .....	41
6.3 Work function-heating time curves of different compositions at temperatures around 1830 K .....	42
6.4 Work function-heating time curves of different compositions at temperatures around 1900 K .....	43
6.5 Work function-heating time curves of different compositions at temperatures around 2010 K .....	44
6.6 Work function-heating time curves of different compositions at temperatures around 2065 K .....	45
6.7 Work function-heating time curves of different compositions at temperatures around 2025 K .....	46

## 1. INTRODUCTION

The interest of using thermionic energy conversion has been brought up for several reasons. First of all, power output per unit weight of a thermionic converter is relatively high compared to some other energy converters. Secondly, the thermionic converter requires less maintenance and lasts longer than other conventional converters. Finally, it can be used as a part of the nuclear generator for space applications [1].

A thermionic converter can be considered as a heat engine that uses electrons as the working media. Electrons at a hot electrode jump out to reach a cold electrode. Then, during their way back to the hot electrode through the circuit connecting two electrodes, these electrons deliver electric power to the environment.

This electron emission phenomenon was first discovered by Elster and Geitel in 1882 [2]. The same effect, which is referred as the Edison Effect, was also reported by Thomas Edison in 1883 [2]. However, it was not until Hatsopoulos categorized two types of converters in 1956 that the subject engendered much interest [2].

The amount of the electrons emitted from the hot electrode is determined by the electrode surface temperature, surface conditions, and the material of the electrode. Different materials have different emission characteristics. A proper measurement of the emission

characteristic of a material is the work function, which is defined as the energy needed to remove one electron from the material surface to infinite distance. High work function materials emit less electrons than low work function materials.

There are two kinds of work functions; bare work function and cessiated work function. Studies indicate a drastic work function change of a material by introducing foreign vapor between electrodes [3]. The most common vapor used is the cesium vapor, which lowers work functions of materials. Conventionally, the work function of the material is called bare work function, while the work function affected by the cesium vapor is called cessiated work function. An interesting fact is that the cessiated work function of a high bare work function material is lower than that of the low bare work function material. For this reason, the search for high work function materials became important to achieve low cessiated electrode work function, and thus, improve the thermionic conversion efficiency.

Materials that are suitable for thermionic applications are mostly refractory materials because higher hot electrode temperature gives higher conversion efficiency. Also, materials used for electrodes should have good mechanical properties such as high strength, stable structure, and less creep at high temperature.

The most common equipments used to measure the work

function of a material are thermionic microscopes and thermionic testing diodes. The thermionic microscope measures the work function of each individual grain, while the thermionic testing diode measures the overall work function, or usually referred to as the effective work function. By using the microscope, one can obtain the work functions of different crystalline orientations as well as observe the actual grain growth and other metallurgical changes. On the other hand, the electron current collected from the microscope is relatively small, so the accuracy of the work function measurement can be trivial.

## 2. THERMIONIC EMISSION THEORY

The electrons in a metal have both kinetic and potential energy as a function of position. According to the free electron model, the free electron gas potential energy is arbitrarily set as a reference zero [4]. Then, the total energy is equal to the kinetic energy,  $\epsilon$ , which can be represented in terms of velocity.

$$\epsilon = \frac{m(v_x^2 + v_y^2 + v_z^2)}{2} \quad (2.1)$$

where  $m$  = electron mass

$v_x, v_y, v_z$  = velocity components in  $x, y$ , and  $z$  direction.

When the kinetic energy is much higher than the Fermi energy of a metal, Fermi-Dirac distribution of state density can be substituted by Boltzmann distribution, that is

$$f(\epsilon) = \exp\left(\frac{\epsilon_f - \epsilon}{kT}\right) \quad \text{when } \epsilon \gg \epsilon_f \quad (2.2)$$

where  $f(\epsilon)$  = Fermi-Dirac distribution of state density.

$\epsilon_f$  = Fermi energy of a metal.

$k$  = Boltzmann's constant.

$T$  = absolute temperature in Kelvin.

In other words, the density of electrons in velocity space is governed by

$$f_0 dV_x dV_y dV_z = \frac{1}{4} \left(\frac{m}{\pi kT}\right)^{3/2} \exp\left(\frac{\epsilon_f - \epsilon}{kT}\right) \exp\left[\frac{-m(v_x^2 + v_y^2 + v_z^2)}{2kT}\right] dV_x dV_y dV_z \quad (2.3)$$

where  $\hbar$  = Plank's constant.

$$f_0 = \text{normalized Fermi-Dirac distribution function} = 2\left(\frac{m}{\pi kT}\right)^{3/2} f(\epsilon)$$

Let the energy required for one electron to move from the free electron gas to infinite space be the work function of a metal. That is, in order to leave the free electron gas, the electron must have a kinetic energy higher than the sum of the work function and Fermi energy. Let  $x$  direction be the normal of the electron escaping surface. Then, the  $x$ -direction velocity,  $v_x$ , of the escaping electron has to satisfy the condition of

$$v_x \geq \left[ \frac{2(\phi - \epsilon_f)}{m} \right]^{\frac{1}{2}} = v_{\min} \quad (2.4)$$

in order to penetrate the surface. The number of electrons available at velocity  $v_x$  within an infinitesimal range of  $dv_x$  is

$$n(v_x)dv_x = \frac{1}{4} \left( \frac{m}{\pi k} \right)^{\frac{3}{2}} \exp(-\frac{\epsilon_f}{kT}) \exp(-\frac{mv_x^2}{2kT}) F^2 dv_x \quad (2.5)$$

where

$$F = \int_{-\infty}^{\infty} \exp(-\frac{mv^2}{2kT}) dv_y = \left( \frac{2\pi kT}{m} \right)^{\frac{1}{2}} \quad (2.6)$$

or the corresponding integral of infinite range with respect to  $v_z$ . The emitting current density,  $J$ , can be considered as

$$J = \int_{v_{\min}}^{\infty} ev_x [1 - r(v_x)] n(v_x) dv_x \quad (2.7)$$

where  $r(v_x)$  is required by quantum-mechanical considerations of the surface conditions. It is usually assumed that  $r(v_x)$  is constant [4]. Therefore, the current density becomes

$$J_0 = \left(\frac{em^2kT}{2\pi^2\hbar^3}\right)(1-r)\exp\left(\frac{\epsilon_f}{kT}\right) \int_{V_{min}}^{\infty} v_x \exp\left(-\frac{mv^2}{2kT}\right) dv_x \quad (2.8)$$

$$= AT^2(1-r)\exp\left(\frac{-\phi}{kT}\right) \quad (2.9)$$

$$A = \frac{emk^2}{2\pi^2\hbar^3} \approx 120 \text{ Amp/cm}^2 \cdot \text{K}^2 \quad (2.10)$$

Equation (2.9) is the Richardson-Dushman relation for thermionic emission. When an electric field,  $E$ , in  $x$ -direction is used to accelerate electrons, more electrons are able to escape from the metal surface. This is called the Schottky effect. It is equivalent to think that the work function is lowered by the applied electric field. In a strong electric field, the work function is lowered by [5].

$$\Delta\psi = e\left(\frac{eE}{16\pi\epsilon_0}\right)^{\frac{1}{2}} = 3.4 \times 10^{-4} E^{\frac{1}{2}} \text{ eV for } E \text{ in V/cm} \quad (2.11)$$

Thus, equation (2.8) in strong electric field becomes

$$J = AT^2(1-r)\exp\left[\frac{-(\phi-\Delta\psi)}{kT}\right] = AT^2(1-r)\exp\left[\frac{-(\phi-3.4 \times 10^{-4} E^{\frac{1}{2}})}{kT}\right] \quad (2.12)$$

Fig. 2.1 shows a  $\ln(J)$  versus  $E^{\frac{1}{2}}$  Schottky plot defining the emission property of a polycrystalline material. At low  $E$ , in case one, the slope is determined by the absolute average patch field,  $E_p$ .  $E_p$  is the electrostatic field resulting from the inequality in the work functions of adjacent grains. The region of case two is a transition toward the strong-field emission of case three region. The extrapolation of the case three region obtains the zero field current density. Reform equation (2.9),

$$\phi = -kT\ln\left[\frac{J_0}{AT^2(1-r)}\right] \quad (2.13)$$

By substituting the zero field current density into equation

(2.13), the work function of the metal can be calculated.

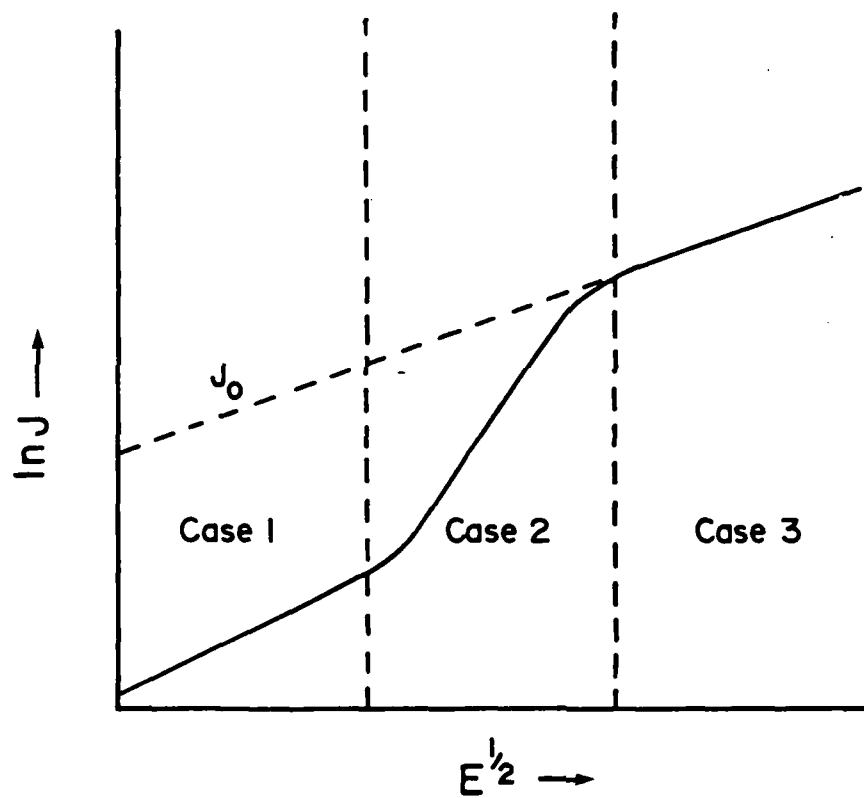


Fig.2.1 Schottky plot of polycrystalline materials

### 3. DESIGN AND FABRICATION OF 3.556 mm DIAMETER COLLECTOR ASSEMBLY

Electrons emitted from the sample are collected by the collector. A guard ring around the collector prevents the collection of electrons from outside the testing area. Both the collector and the guard ring are kept at the same positive voltage relative to the grounded sample. The collected current and the applied voltage can be used in the Richardson-Dushman equation to calculate the effective work function of the sample surface.

This mechanism produces the overall effective work function, an average over a relatively large test area. Moreover, the work function testing of certain crystalline orientations can be performed precisely and directly if a large single crystal sample is available. However, a large collector area results in considerable heat that has to be dissipated by the collector. The radiator must sufficiently dissipate the heat in order to eliminate any electron back emission current.

This system had a collector of 16 mm diameter, which means the sample diameter had to be larger than 16 mm. Due to the availability of the sample size, a smaller collector was needed. The requirements for the present collector were:

1. 3.556 mm diameter collecting surface.
2. Minimized collector and guard ring surface temperature.
3. Minimized collector-guard ring gap.

#### 4. Rigidity of the collector assembly structure.

A presumed model, as shown in Fig. 3.1, was established based on the structure of the diode station. Modifications had been made before a final design was completed. The final design is shown in Fig. 3.2-6. The following assumptions had been made in calculating the required radiator collecting surface area:

1. One dimensional steady-state thermal conduction.
2. Molybdenum collector surface work function  $\phi_c = 4.5$  eV
3. Maximum operating collector current density  $J = 0.25$  Amp/cm<sup>2</sup>
4. Emitter surface temperature  $T_e = 2800$  K
5. Emitter surface emissivity  $\epsilon_e = 0.3$
6. Collector surface temperature  $T_c = 700$  K
7. Collector surface emissivity  $\epsilon_c = 0.25$
8. Collector radiator surface emissivity  $\epsilon_r = 0.6$
9. Chamber wall temperature  $T_{enc} = 303$  K
10. Chamber wall emissivity  $\epsilon_{enc} = 0.2$
11. Maximum bias voltage  $V_{bias} = 10000$  V

The collector heat input includes two parts; the heat from emitter radiation and the heat from electron potential drop upon reaching the collector surface. The total heat input,  $Q_{Tot}$ , must equal to the heat output of the collector radiator. In order to simplify the calculation of the radiation heat, assume the spacing of electrodes is

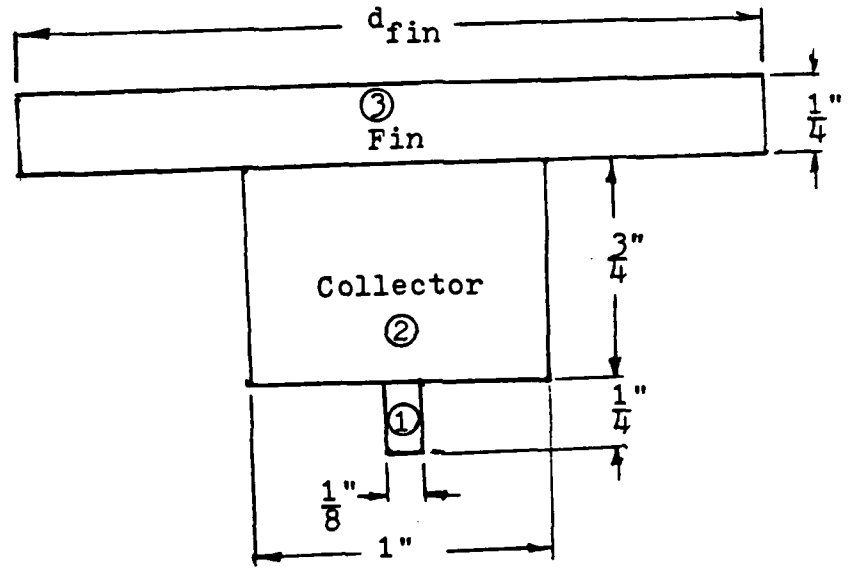
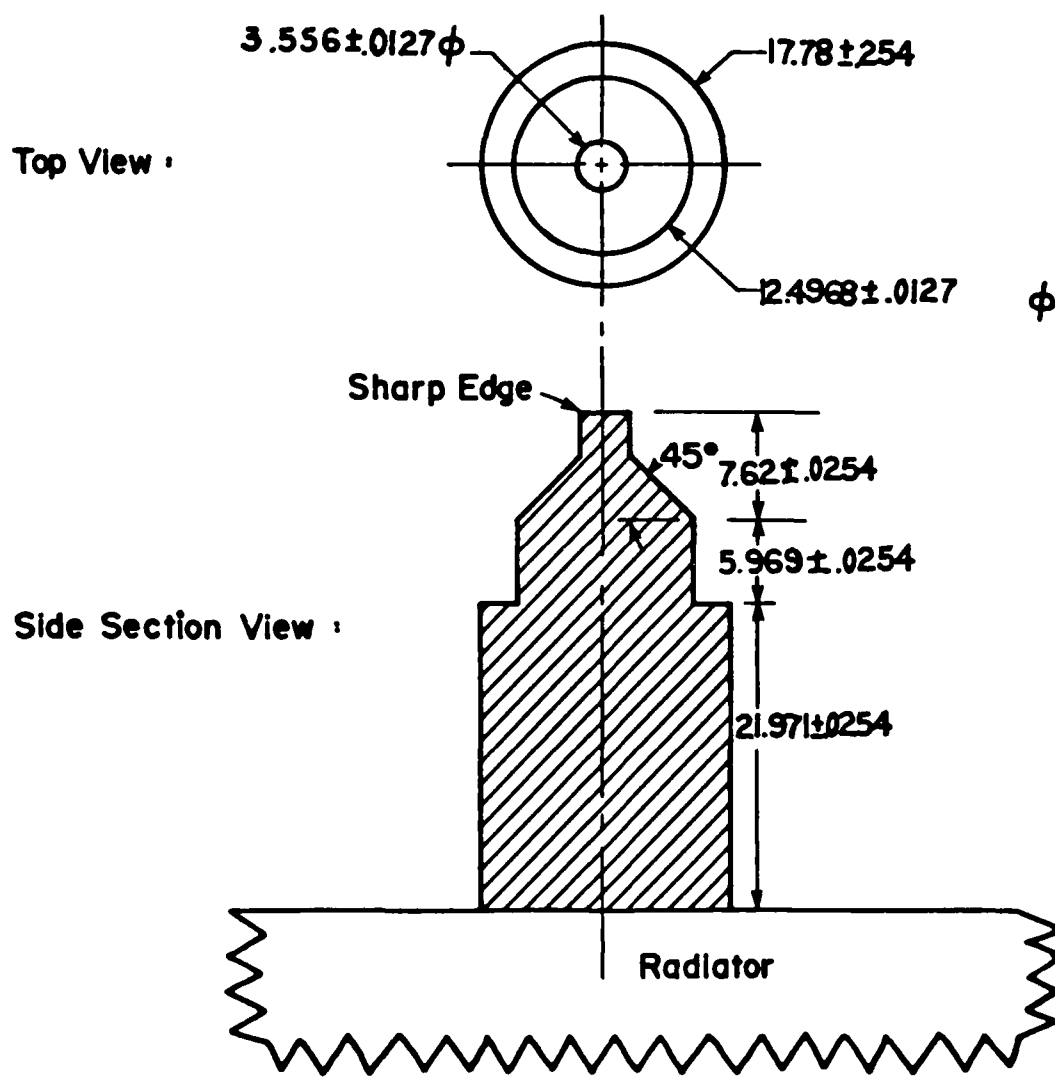


Fig. 3.1 Presumed new collector geometry.

**Part Name : Collector**

**Unit : CM**

**Material : Molybdenum**

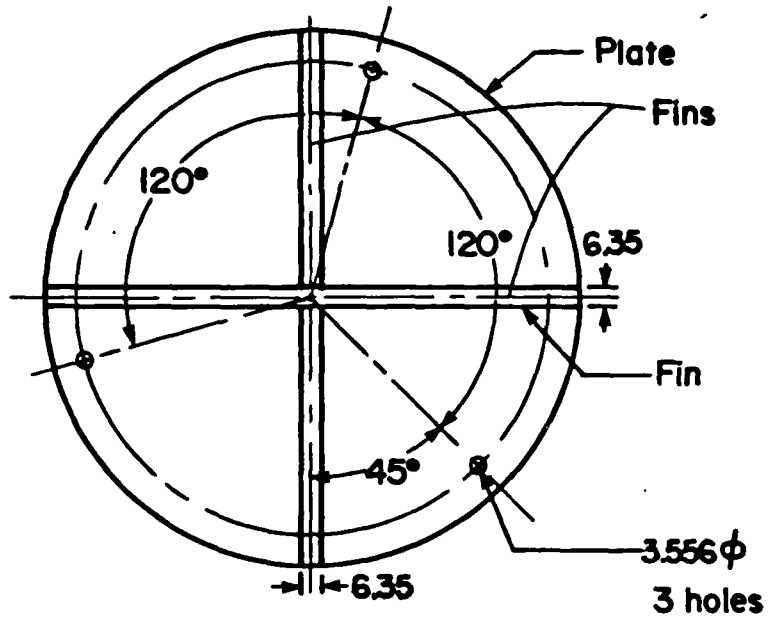


**Fig. 3.2 Collector design.**

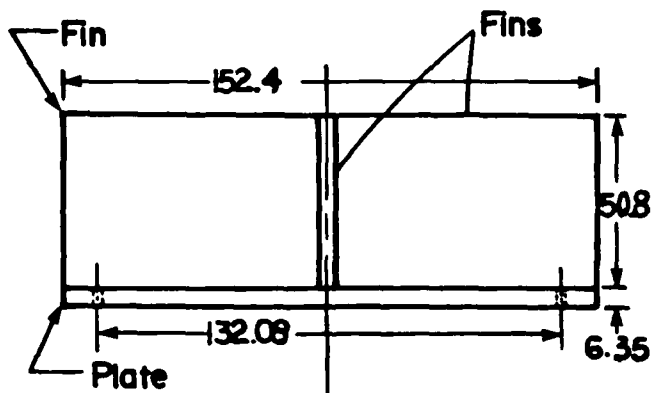
**Part Name : Collector Radiator**

**Unit : CM**

**Top View :**



**Side View :**



**Material : Copper**

**Fig. 3.3 Collector radiator design.**

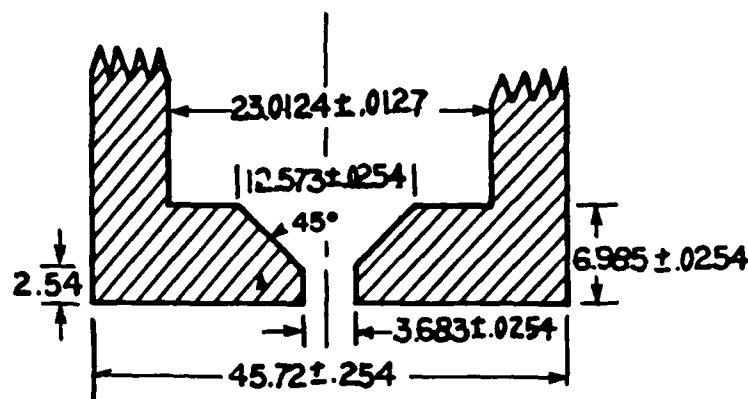
Part Name : Collector Guard Ring

14

Unit : CM

Material : Molybdenum

Side Section View :



Bottom View :

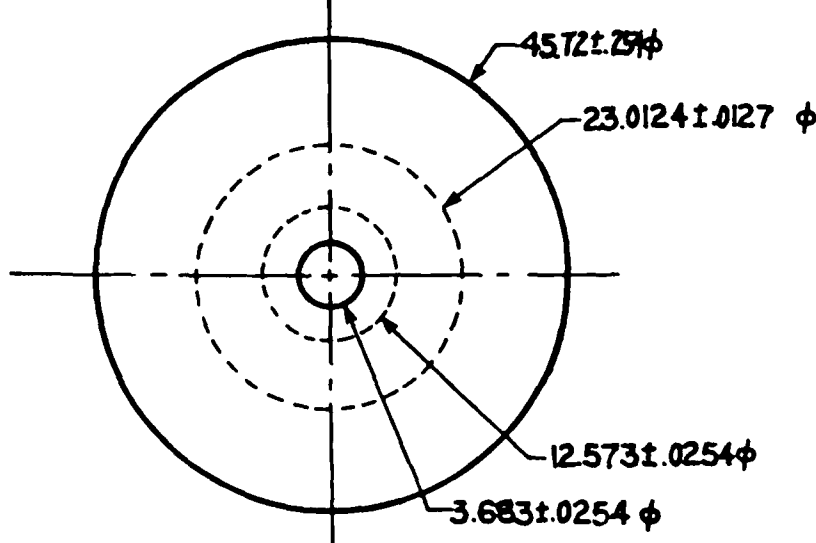


Fig. 3.4 Guard ring design.

Part Name : Guard Ring Radiator

Material : Copper

Unit : CM

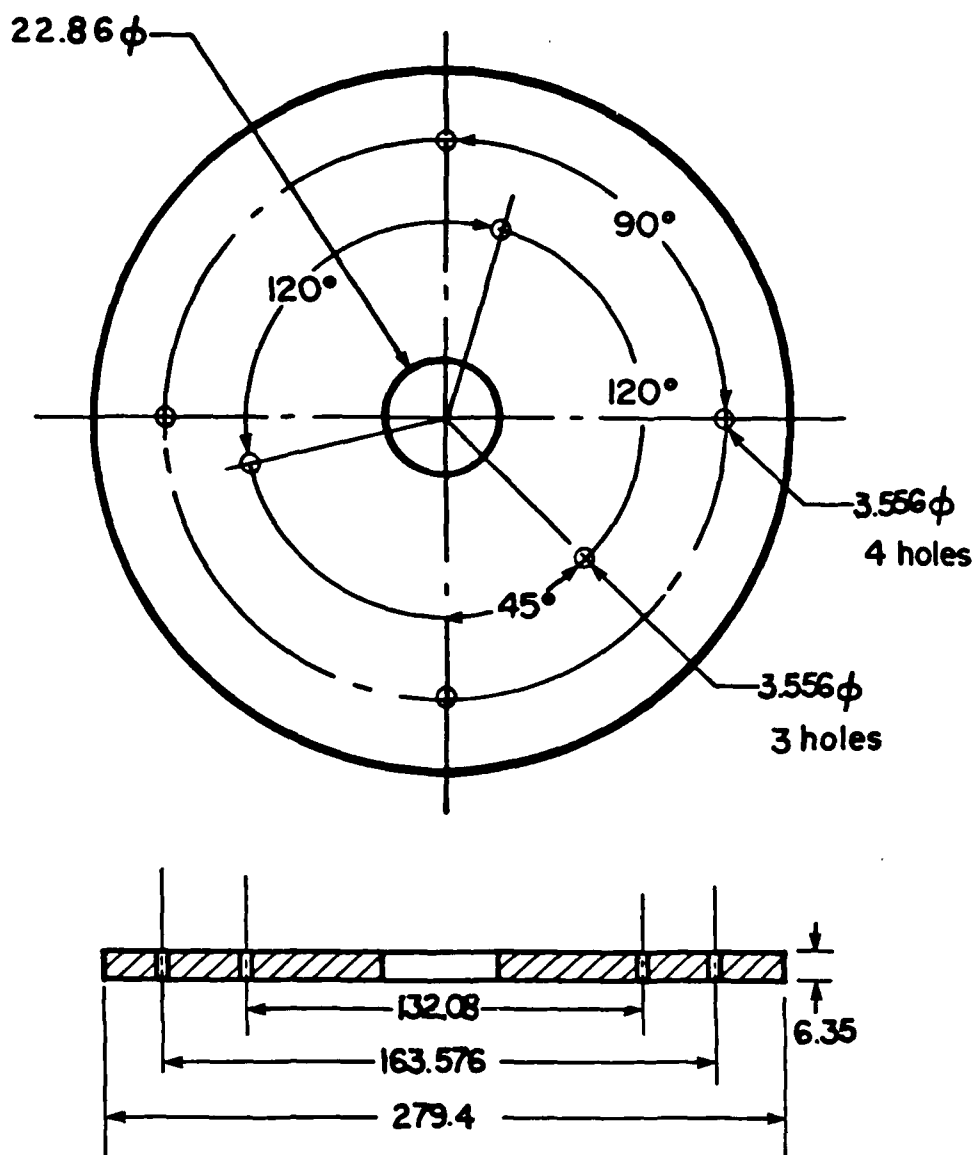


Fig. 3.5 Guard ring radiator design.

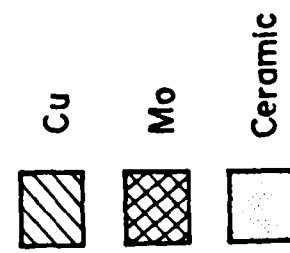
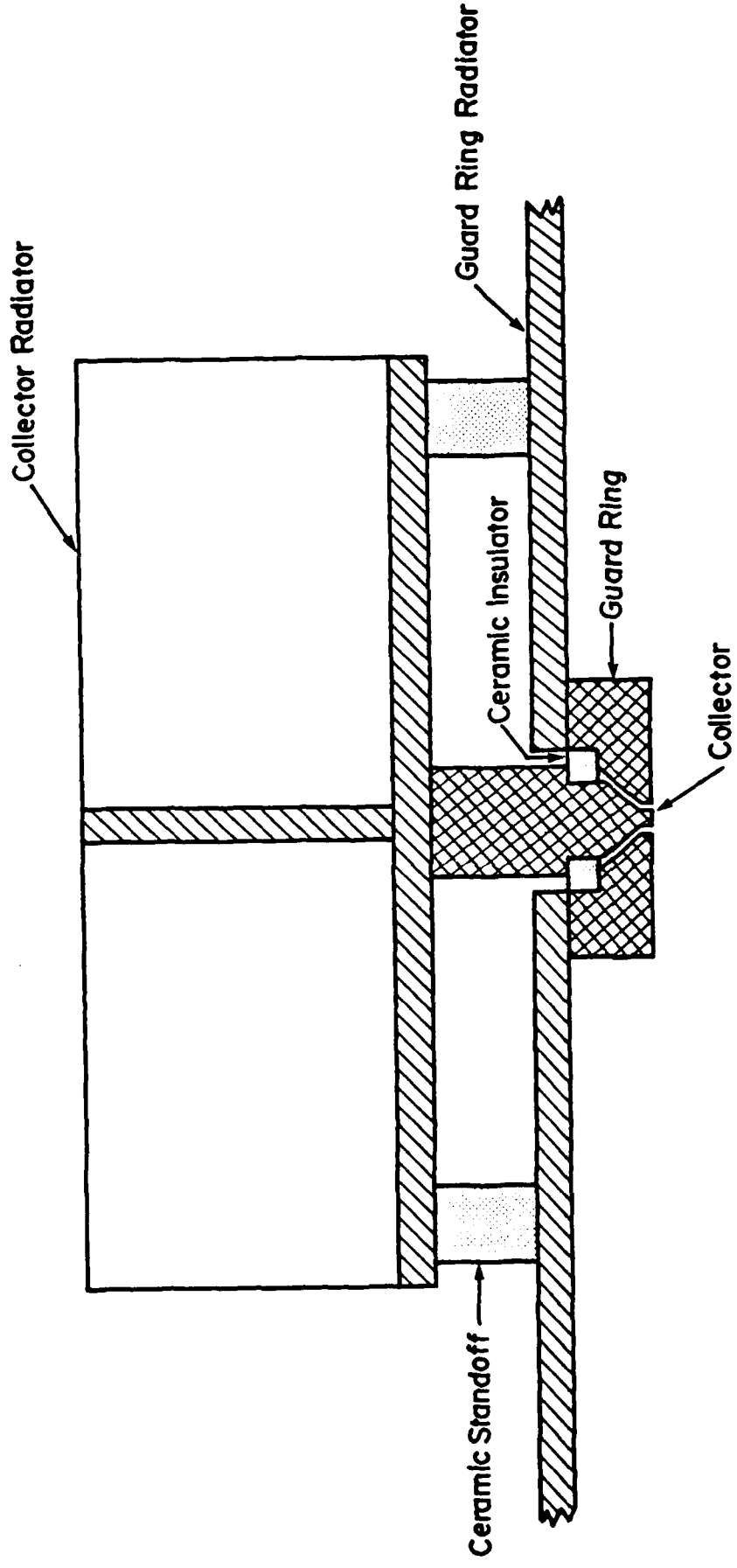


Fig. 3.6 Collector Assembly of 3.556 mm diameter collector.

sufficiently close to zero. According to the calculation of Robert Siegel and John R. Howell [6], the effective emissivity of this system is

$$\epsilon_{\text{eff}} = \left( \frac{1}{\epsilon_e} + \frac{1}{\epsilon_c} - 1 \right)^{-1} \quad (3.1)$$

Therefore, the radiation heat received by the collector surface is

$$Q_{\text{rad}} = \epsilon_{\text{eff}} \sigma (T_e^* - T_c^*) A_c = 5.4434 \text{ W} \quad (3.2)$$

where  $\sigma$  = Stefan-Boltzmann constant =  $5.6697E-8 \text{ W/m K}^4$

$A_c$  = collecting area =  $9.9315E-6 \text{ m}^2$

This assumption leads to an overestimated value in actual radiation heat input of the collector.

When an electron arrives to the collector surface, the potential of the electron drops to the Fermi level of the collector material. Thus, a small amount of heat, equals to the work function of the collector material, must be released at the same time. However, a more important source of heat release comes from the electron kinetic energy resulting from the electron-accelerating bias voltage. The kinetic energy of each electron is equal to the biasing voltage multiplied by the electric charge of one electron. When the electron hits the collector surface, most of the kinetic energy is transformed into thermal energy. Therefore, the equation of electron heating at the collector surface is

$$Q_{\text{el}} = (\phi_c + V_{\text{bias}}) J A_c = 24.9408 \text{ W} \quad (3.3)$$

The total heat input at the collector surface becomes

$$Q_{\text{tot}} = Q_{\text{rad}} + Q_{\text{el}} = 30.3842 \text{ W} \quad (3.4)$$

$Q_{\text{Tot}}$  must be conducted to the radiator and radiated toward the chamber wall which is constant temperature of 303 K. Assume that the temperature at collector-radiator is constant. Also assume that the thermal resistance of the collector-radiator contact surface is negligible. Let  $R$  be the total thermal resistance of the collector. According to M. K. Ozisik [7], the total thermal resistance of a composite slab is equal to the sum of the thermal resistance of each slab.

$$R_{\text{Tot}} = \sum_i \frac{L_i}{A_i K_i} \quad (3.5)$$

where  $L_i$  = length of the  $i$ th slab.

$A_i$  = cross-section area of the  $i$ th slab.

$K_i$  = thermal conductivity of the  $i$ th slab.

The conductivity of molybdenum was found to be 125 W/m.K [8]. Modify equation (3.5) to get the total thermal resistance of the collector.

$$\begin{aligned} R_{\text{Tot}} &= \frac{4}{Km\pi} \left[ \frac{3.175 \times 10^{-3}}{(3.556 \times 10^{-3})^2} + \int_0^{4.445 \times 10^{-3}} \frac{dh}{(3.556 \times 10^{-3} + 2h)^2} \right. \\ &\quad \left. + \frac{5.969 \times 10^{-3}}{(1.2497 \times 10^{-2})^2} + \frac{2.1971 \times 10^{-2}}{(1.778 \times 10^{-2})^2} \right] \\ &= \frac{4}{125\pi} [251 + 100.43 + 38.22 + 69.5] = 4.677 \text{ m}\cdot\text{K/W} \end{aligned} \quad (3.6)$$

$$Q_{\text{Tot}} = \frac{T_c - T_r}{R_{\text{Tot}}} \quad (3.7)$$

Substitute appropriate values of  $Q_{\text{Tot}}$ ,  $T_c$ , and  $R_{\text{Tot}}$ , then the radiator temperature is calculated to be 558 kelvin. Assume equation (3.1) and equation (3.2) are suitable for the

radiation between the radiator and the chamber wall. Then, the radiator surface needed to dissipate  $Q_{Tot}$  is  $0.0343 \text{ m}^2$ .

The guard ring design, as shown in Fig. 3.4 and Fig. 3.5, has a minimum cross-section area of  $6.45 \text{ cm}^2$ , which may conduct heat to the  $609 \text{ cm}^2$  guard ring radiator. Although some of the guard ring radiator surface is blocked by the collector radiator, the guard ring should still be cool enough while testing a 19 mm diameter sample. In other words, the new collector assembly has the ability of testing any sample size from 3.556 mm to 19 mm in diameter.

The collector assembly is illustrated in Fig. 3.6. The gap between the collector tip and the guard ring is  $0.0635 \pm 0.01905 \text{ mm}$ . When fabricating the new collector assembly, a minimized collector-guard ring gap was an important objective. Therefore, the alignment of parts was done as precisely as possible. The most important and the most difficult work was making the ceramic insulator. The insulator must fit perfectly in both the guard ring cup and the collector tip at the same time. An inaccurate insulator may allow the undesired freeplay which may lead to collector-guard ring short. Sixteen unfired insulators of slightly different dimensions were made in the Mechanical Development Shop of Arizona State University. The material used was LAVA stone, grade A. The insulator size after firing depends strongly on the maximum firing temperature. Unfired insulators of various dimensions were fired separately to obtain a tight-fit insulator for both the

collector and the guard ring.

The radiators were blackened to increase the emissivity of bright copper surfaces. Ebonol C special from Enthone Inc. was used to form black cupric oxide coating on the surfaces. The cleaning and etching solution contained 10 Vol.% hydrochloric acid and 5.7 wt.% ferric chloride. After three minutes of the etching treatment, radiators were rinsed with running water. The blackening solution, 11 wt.% ebonol C special, was heated to approximately 100°C. Then, radiators were dipped into the solution for 5 to 10 minutes for fully blackened surface. Radiators were again rinsed with running water, and a heat gun was used for drying up.

In conclusion, the Vacuum Emission Test Vehicle performs accurate work function testing. However, the collector size limited the testing of the sample larger than 16 mm diameter. The new collector-guard ring assembly accommodate a variety of sample sizes from 3.556 mm diameter and up without being overheated. The collector tip surface temperature can be maintained below 700 K while the sample temperature reaches 2800 K. The guard ring temperature depends mostly on the testing sample size. The rigid structure and the precise fabrication control the collector-guard ring gap down to  $0.0635+0.01905$  mm.

#### 4. EXPERIMENTAL APPARATUS

##### 4.1 Introduction

A thermionic emission test station was used to determine the average effective work function characteristic of Tungsten-Rhenium alloy samples. This test station consists of four systems; the thermionic emission vehicle assembly, the temperature measurement system, the vacuum system, and the electrical system. A high vacuum chamber holds the operating thermionic emission vehicle assembly in the  $10^{-7}$  -  $10^{-9}$  torr vacuum range.

##### 4.2 Thermionic Emission Vehicle Assembly

The thermionic emission vehicle assembly is the most important system of the test station because it generates the emission current that determines the effective work function of a material. As shown in Fig. 4.1, a tungsten filament serves as the electron source of the electron bombardment heating of the sample. The spacing between the filament and the sample (or the sample holder) was set to be approximately 0.5 mm at room temperature. This gap compensates the thermal expansion of the filament to provide the optimized spacing. Samples were machined to be approximately 9.6 mm diameter and 2.6 mm thick. Hohlraums (temperature measuring hole) paralleled to the emitting surface were drilled by an electrical discharge machine to the dimension of 0.70 mm diameter and 7.00 mm deep. The 10:1

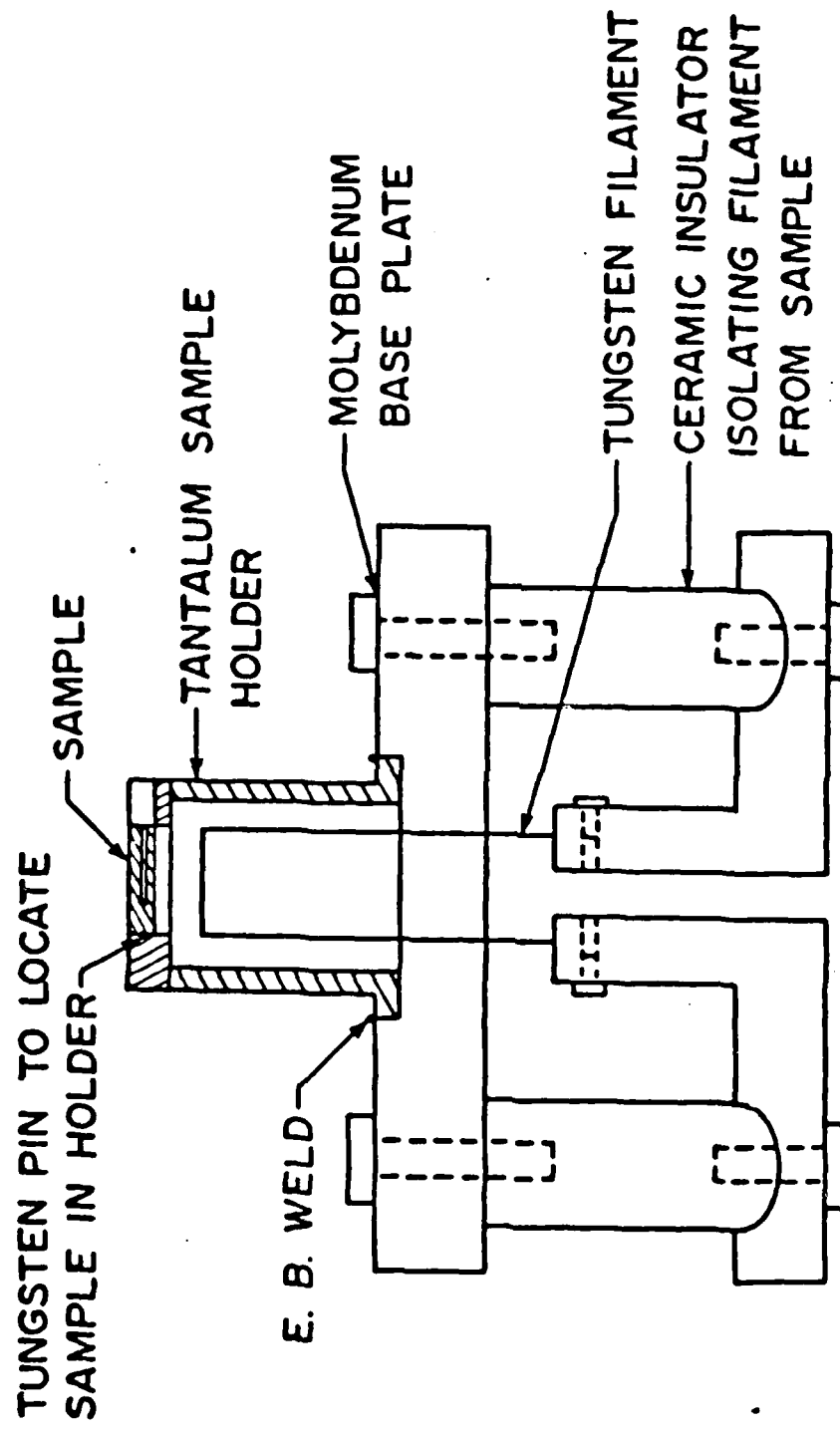


Fig. 4.1 Configuration of the emitter assembly.

ratio of the hole depth and the hole diameter satisfies the condition for an isothermal enclosure. Therefore, the temperature observed through the hohlraum is a good approximation of the bulk temperature.

The collector assembly includes a collector, a guard ring, and their radiators. The guard ring prevents the collector from collecting electrons outside the collector surface area. The collector surface area at room temperature is 9.9 mm<sup>2</sup>. Both the collector and the guard ring are kept at the same positive voltage relative to the grounded sample. The collector and the guard ring are made of molybdenum while their radiators are made of copper. The surfaces of the radiators were blackened for better thermal radiation.

A negatively charged electron repeller is located between the sample assembly and the collector assembly. The repeller isolate the collector radiator from collecting electrical noise. This noise was verified to be secondary electrons knocked out by bombardment electrons. These electrons could be collected by the highly positively charged collector radiator. An electron seal covering the back side of the sample mount also helps to depress the noise. At lower operating temperature, 1800-1900 Kelvin, the noise level was observed to be of the same order of the signal level if the electron repeller and the electron seal had not been used.

#### 4.3 Temperature Measurement System

The temperature measurement system consists of a pyrometer and a temperature guage from Pyrometer Instrument Company. A 4.5 VDC power is supplied to the system by three 1.5 V batteries connected in series. By comparing the color of the hohlraum and the filament inside the pyrometer, an accuracy of  $\pm 12$  Kelvin can be achieved. Two red filters of different transmittance are located between the filament and the eye-piece. These filters can be selected to depress the brightness of both the filament and the hohlraum. Three other grey filters located between the object lens and the filament are controlled by a scale range selection knob. Three temperature ranges on the temperature guage correspond to the filters.

According to equation (2.8), the accuracy of temperature readings affects the accuracy of the calculated work function proportionally. Therefore, the temperature measurement system, together with the view port on the vacuum chamber, were calibrated by a NBS ribbon filament lamp. The result of the calibration is

$$T = 60.1 + 1.2487 T_m \quad (4.1)$$

where  $T$  = actual temperature in Kelvin.

$T_m$  = temperature indicated on the guage.

#### 4.4 Vacuum System

Two sorption pumps containing highly porous material

are able to carry the vacuum chamber pressure to below 30 millitorr. A thermocouple vacuum gauge located between the sorption pumps and the vacuum chamber monitors the roughing stage pressure. A metallic valve isolates these pumps and the vacuum gauge from the chamber when a lower pressure is achieved by operating an ion pump. A high negative potential, -5000 VDC, is applied to five 40 l/s capacity pump elements at the lower portion of the vacuum chamber for trapping air molecules. The chamber base pressure can either be read directly from the ion pump control unit or be converted from the ion pump current. An ionization gauge is used to monitor the pressure close to the thermionic emission vehicle assembly.

#### 4.5 Electrical System

A schematic of the electrical system of the vacuum thermionic emission test station is shown in Fig. 4.2. As mentioned in section 4.4, the ion pump control unit provides -5000 VDC to cathodes of ion pump elements. The collector of the ionization gauge is grounded, while the grid can have up to 600 VDC when degassing the gauge. The filament of the ionization gauge is supplied by up to 12 VAC. The lead voltage of the electron bombardment filament, 0-30 VAC, is floating on 0 to -5000 VDC bombardment voltage. The collector and the guard ring are connected to two high voltage power supply separately for 0-5000 VDC bias relative

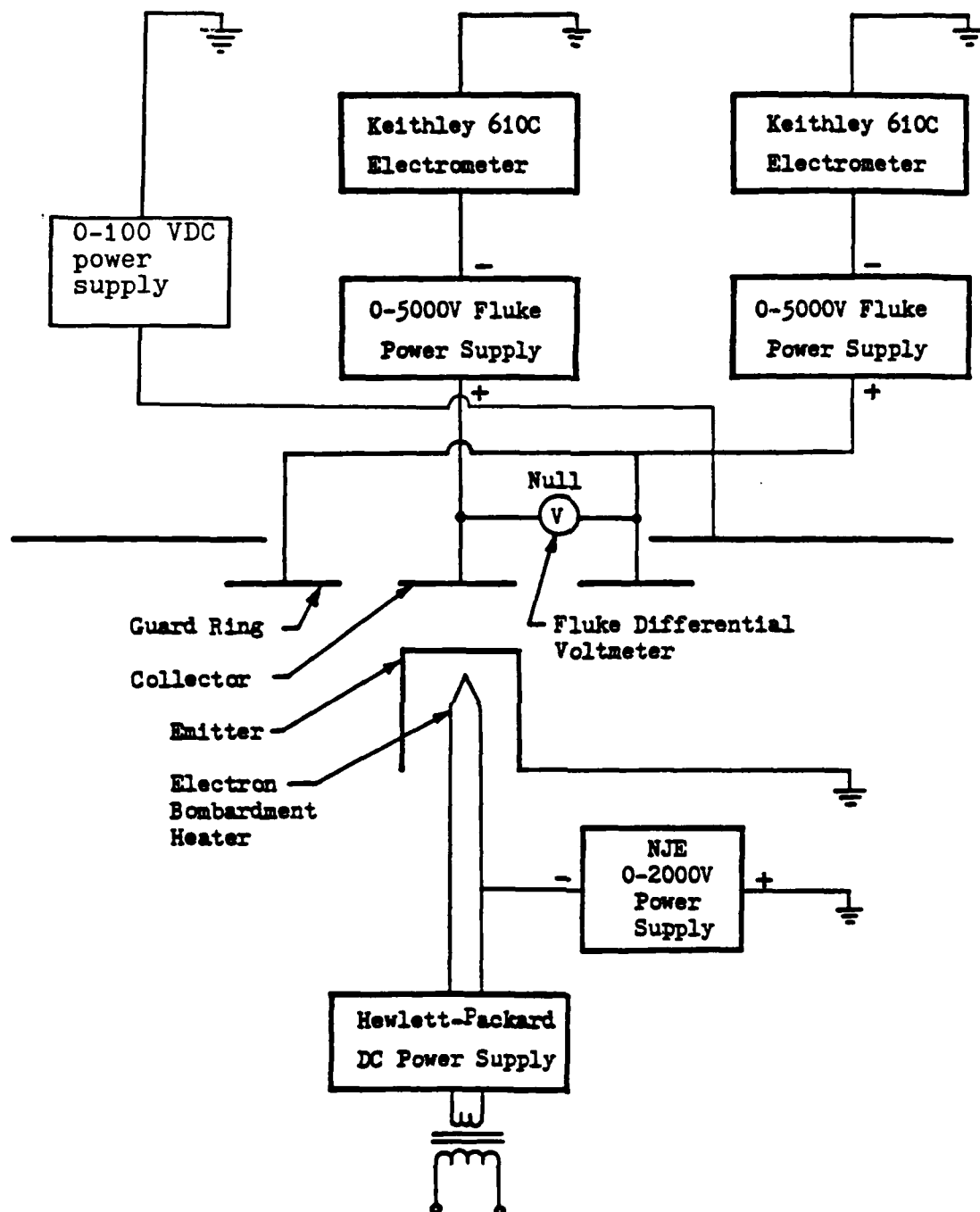


Fig. 4.2 Electrical circuit of Vacuum Emission Test Station.

to the grounded sample. The electron repeller is connected to a 0 to -100 VDC power supply. A DC differential voltmeter monitors the potential difference between the collector and the guard ring. An electrometer measures the collector current for work function determination.

## 5. EXPERIMENTAL PROCEDURE

### 5.1 Introduction

The experimental procedure of work function determination, using the thermionic emission test station, included four stages: the preparation stage, the vacuum stage, the data collecting stage, and the analysis stage. Each stage affected the achievement of the following stage, so that the precise work of each stage was very important. In the preparation stage, the sample was assembled and the circuit inside the vacuum chamber was connected. The vacuum stage consisted of the use of adsorption pumps, and the ion pump. Various electrical equipment were used to obtain the necessary sample temperature, collector voltage, and collector current data. Finally, the data was analyzed by a computer program to generate the work function versus time function curves of different temperatures and compositions of W-Re alloy samples.

### 5.2 Preparation Stage

The sample was fixed in the hole of the sample mount by inserting a tungsten bar through the side of the sample mount. The emitting surface should be parallel to the sample mount surface. The electron bombardment filament was assembled to have 0.5 mm spacing toward the sample. Then, the sample assembly was fastened on the supporting structure. The hohlraum on the sample should be lined up with the

presumed viewport direction for the later sample temperature measured by the optical pyrometer. The vertical position of the sample was determined by the relation between three supporting rods and the base plate. These rods were threaded for fastening the sample mount and adjusting the position of the sample mount. The emitting surface of the sample was set to be 1.0 mm lower than the collecting surface. This could be achieved by raising the sample mount by adjusting the nuts on the supporting rods until the sample and the collector barely touched each other. Then, each nut was turned 450 degree counter clockwise to lower the sample because the rod has 32 threads per inch.

The sample should be grounded properly so that the electric potential would keep at zero and thus, eliminate the noise superimposed on the output data. Also, conductions from the collector and the guard ring to the feedthroughs on the vacuum chamber should be maximized for the same reason.

The final step of this stage was to close the vacuum chamber. Twenty C-clamps were equally placed around the rim of the chamber. Each clamp was tightened to deform the copper O-ring to achieve ultrahigh vacuum sealing. A torque wrench provided equal torque to every clamp. Beginning with a lower torque (3-4 kg-m), a particular sequence was followed. Upon finishing all C-clamps, a small increase (0.1-0.3 kg-m) in torque was set for further tightening until the maximum torque was reached. The copper O-ring was

reusable unless a maximum torque of 7 kg-m had been applied. Starting from approximately 4 kg-m, the maximum torque was increased by 0.3 kg-m for each reuse of the O-ring.

### 5.3 Vacuum Stage

The vacuum stage started with the use of two adsorption pumps to pump the system down to about  $10^{-2}$  torr pressure. The first adsorption pump worked from 1 atm down to about  $10^{-1}$  torr before it was isolated by the valve. Then, the second pump started, and brought the system down to the cross-over pressure,  $10^{-2}$  torr, that the ion pump was turned on. The ion pump could pump the system down to the order of  $10^{-9}$  torr. The pumping rate was first rather fast until about  $10^{-7}$  torr. As the pumping rate slowed down, a bake-out case heated up the whole chamber to 150-250 °C to accelerate the molecule trapping rate of ion pump elements. After the bake-out procedure, the vacuum chamber pressure reached the order of  $10^{-9}$  torr (bottom pressure). At this time, the pressure at the middle height was in the order of  $10^{-8}$  torr, which could be checked by the ionization gauge.

### 5.4 Data Collecting Stage

Three different data were needed for the determination of the effective work function of the sample: the sample temperature, the bias potential applied to the collector and the guard ring, and the collector current. An optical pyrometer, two high voltage power supplies, one DC

differential meter, and two electrometers were used at this stage.

The sample temperature was monitored by the pyrometer through the hohlraum close to the emitting surface of the sample. Thus, the temperature measured by the pyrometer could be a good approach for emitting surface temperature.

The positive bias potential was assumed to be the same as the voltage measured by the voltmeter. Since the current in this circuit was less than 10<sup>-5</sup> ampere, the potential drop caused by circuitry resistance was negligible, so that the voltage measured from the voltmeter was considered to be the voltage at the collector and the guard ring surfaces. The DC differential meter measured the supplied potential difference between the two power supplies. This difference was eliminated by the fine adjustment knob of the power supplies. This prevented the collector-to-guard ring leakage current, and made the electric field perpendicular to both the sample and the collecting surface.

The collector current was measured by the electrometer connecting the collector power supply and the ground. As the applied positive bias increased, the collector current increased correspondingly. As the collector current changed, the potential difference between the collector and the guard ring changed. Therefore, a minor adjustment was made to zero the potential difference. At all times, the electron bombardment current was controlled to

keep the sample surface temperature constant. The data measurement was taken a few minutes after every change of the electron bombardment to allow the system to retain a steady state condition.

The sample-collector spacing and the applied bias potential determined the electric field that drew current from the sample. For each applied bias, a corresponding collector current was taken as a data point. Usually, in this system, the bias applied to the collector and the guard ring was below 1000 VDC before the linear region of the Schottky plot can be well defined. In this work, each set of data contained 8 bias voltages starting from 300 VDC with 100 VDC increment each, and their corresponding collector currents.

Since work functions of W-Re samples are functions of time, data collecting must be conducted frequently to monitor the work function changes. Most work function changes occurred within the first three hours of heating. Therefore, data sets were taken approximately every 4-7 minutes during the three hours. Then, as the work function became steadier, data sets were collected once every 10-30 minutes within the remaining three hours of testing. An overnight (at least 12 hours) cooling before heating up to another temperature was necessary.

#### 5.5 Data Analyzing Stage

An interactive BASIC program, "PLOT1.BAS", was written for cutting short the time-consuming work function evaluation. This program has been successfully used on IBM personal computers and its compatibles. The program inquires the sample temperature, the time of heating, and the collector current measured for the calculation of effective work function. Data files are opened for data and work function storage. At the end of the data, a plot of work functions versus heating time is shown on the screen. The plot can also be printed on paper by using any printer interfacing to the computer.

The program is listed as follows:

```
10 DIM DX(50),DY(50),XFLT(50),YFLT(50)
20 NREG=6
30 PRINT " 1. DATA ENTRY    2. PLOT CURVE ---SELECT NO."
40 INPUT C
50 IF C=1 GOTO 80
60 INPUT "INPUT FILE NAME.....";F$
70 GOTO 510
80 INPUT "INPUT THE SAMPLE NAME.....";F$
90 OPEN F$ FOR OUTPUT AS #1
100 INPUT "INPUT SAMPLE TEMPERATURE";T
110 PRINT #1,F$,"",T
120 INPUT "INPUT CURRENT SCALE.....";S
130 OPEN "DATA1ST" FOR OUTPUT AS #2
140 PRINT #2, "SAMPLE TEMPERATURE= ",T
150 INPUT "INPUT TIME IN MINUTES.....";TIME
160 INPUT "INPUT CURRENT X "S
170 IF TIME=0 THEN PRINT #1,TIME, TIME
180 IF TIME=0 GOTO 510
190 E=0
200 K=E+1
210 E=200+E*100
220 INPUT I
230 IF I<0 THEN E=E-2
240 IF I<0 THEN GOTO 200
250 IF I=0 GOTO 460
260 PRINT #2,E,I*S
270 DX(E)=SQR(E)
280 DY(E)=LOG(I*S)
290 IF E<6 GOTO 450
300 SDX=0
310 SDY=0
320 SDXY=0
330 SDXSQ=0
340 FOR J=E+1-NREG TO E
350 SDX=SDX+DX(J)
360 SDY=SDY+DY(J)
370 SDXY=SDXY+DX(J)*DY(J)
380 SDXSQ=SDXSQ+DX(J)^2
390 NEXT J
400 B=(NREG*SDXY-SDX*SDY)/(NREG*SDXSQ-SDX^2)
410 A=(SDY-B*SDX)/NREG
420 LR=A+B*DX(E)
430 WKFN=8.59903E-5*T*LOG(T^2*.1021725*120/EXP(A))
440 PRINT "WORK FUNCTION= " WKFN
450 IF E<8 GOTO 200
460 PRINT #2, "WORK FUNCTION= ",WKFN
470 PRINT #2, "TIME= ", TIME
480 PRINT #2, " "
490 PRINT #1, TIME, WKFN
500 GOTO 150
510 X=30
520 Y=180
530 SCREEN 2,0
540 LINE(X,Y-155)-(X,Y)
550 LINE-(X+525,Y)
```

```

560 LINE-(X+520,Y-2)
570 LINE-(X+523,Y)
580 LINE (X+523,Y+1)-(X+525,Y+1)
590 LINE-(X+520,Y+3)
600 LINE-(X+525,Y+1)
610 LINE-(X-2,Y+1)
620 LINE-(X-2,Y-155)
630 LINE-(X-7,Y-152)
640 LINE-(X-2,Y-154)
650 LINE-(X,Y-154)
660 LINE-(X+5,Y-152)
670 LINE-(X,Y-155)
680 NX=6
690 NY=8
700 XS=INT(500/NX)
710 YS=INT(150/NY)
720 FOR I=1 TO NX
730 LINE (X+I*XS,Y)-(X+I*XS,Y-2)
740 NEXT I
750 FOR I=1 TO NY
760 LINE (X,Y-I*YS)-(X+3,Y-I*YS)
770 NEXT I
780 CLOSE #2
790 CLOSE #1
800 OPEN F# FOR INPUT AS #3
810 YSCALE=YS*NY/0.8
820 YMIN=4.6
830 XSCALE=XS*NX/360
840 XADJ=30
850 YADJ=180
860 INPUT #3,M#,T
870 N=0
880 N=N+1
890 INPUT #3,DX(N),DY(N)
900 IF DX(N)=0 GOTO 950
910 XFLT=XADJ+XSCALE*DX(N)
920 YFLT=YADJ-YSCALE*(DY(N)-YMIN)
930 CIRCLE (XFLT,YFLT),5
940 GOTO 880
950 PRINT
970 PRINT
980 PRINT " eV ",M#,"TEMPERATURE= "T" K"
990 PRINT
1000 PRINT "5.4"
1010 FOR I=1 TO 2
1020 FOR J=1 TO 8
1030 PRINT
1040 NEXT J
1050 IF I=1 THEN PRINT "5.0"
1060 IF I=2 THEN PRINT "4.6"
1070 NEXT I
1080 PRINT "      0          60          120          180          240          300
360 MINUTES"
2000 STOP

```

To run the program, one must first load PLOT1.BAS into BASIC-A compiler. Then, hit function key 2 to start running the program. PLOT1 will ask if one wants to enter data or plot work function versus heating time data. If "plotting data" is answered, PLOT1 will ask for the "file name" to be plotted. Once the "file name" is answered, the program will plot the data on the screen. If one responds "data entry", a series of questions, including the "sample name", "sample temperature", and the "current scale", will be asked on screen. After all the questions are answered, a DO-LOOP will start operating by asking for the "heating time". A response of the heating time will promote the starting of the collector current entry. Eight collector current data will be inputted into the program, but only the last six will be used for linear regression. Any error in current data entry can be erased by a subsequent input of "-1". When there are less than eight data available, an input of "0" continues the program. PLOT1 will combine all the informations, such as collecting area, sample temperature, and Richardson's constant, together to calculate the effective work function. The calculated work function will be shown on the screen, as well as stored, corresponding to the heating time, in a data file of the sample name. Another data file, DATALST, will contain all the input and output information as a raw data sheet. After the data storage, the DO-LOOP will ask for the "heating time" and do the same procedure until a "zero" is inputted to terminate it. Then, all calculated wor

functions versus heating time will be plotted on the screen as the last step of PLOT1. A copy of the plot can be printed on paper.

## 6. EXPERIMENTAL RESULTS

Two samples, W-3%Re and W-30%Re, had been tested. Each sample was tested at five different temperatures over the range of 1833 K to 2127 K. Effective work functions of both samples showed time dependency as well as temperature dependency. Each sample was tested at constant temperature for 4 to 6 hours unless a circuit shortage between the collector and the guard ring occurred. The vacuum was kept at the order of  $10^{-8}$  torr most of the time. Data sets were measured every 4 to 10 minutes during the first 3 hours. Then, experiments were stopped, depending on the stability of the measurement. Data sets were entered into PLOT1 to calculate effective work functions corresponding to the heating time.

Fig. 6.1 and Fig. 6.2 illustrate the combination of five time-dependent work function curves of W-3%Re and W-30%Re samples. Most initial work function drops of the 3% Re sample were observed while those of the 30% Re sample were not obvious. Each curve contains a valley followed by a plateau. Generally, the plateau region of the 30% Re sample began earlier than that of the 3% Re sample. The highest stable work function found was W-30%Re sample at 2011 K.

All curves of the 3% Re sample, except the 1833 K one, have approximately 0.45 eV work function difference between the maximum and the minimum. At 1833 K, the work function shifted only 0.16 eV. The work function of the valley region

decreased with increasing sample temperature. When the sample temperature was lower than 1898 K, the final stable work function value increased with the temperature. At a temperature higher than 2012 K, the final stable work function decreased with the increasing temperature.

The W-30%Re sample shows different time dependent characteristics besides earlier shift in work function toward the plateau region. At all temperatures of this sample, the changes in work function were less than those of the 3% Re sample. However, the shift of the 30% Re sample at 2011 K was clearly larger than the four other corresponding temperatures. Also, at 2011 K, the sample showed the earliest work function shift of all, approximately 60 minutes after heating began.

Fig. 6.3 through Fig. 6.7 show comparisons of two samples at five tested temperatures. At plateau regions, the differences in work functions were no more than 0.04 eV. But, at valley regions, 30% Re sample always had higher work function than 3% Re sample.

Alloying elements were known to have strong effect on work functions of metals. Work function could be changed if the lattice constant is changed by adding foreign atoms to the pure metal [9]. Work function could also vary if phase transformation is involved. The atomic radii of tungsten and rhenium are 1.37 and 1.38 angstroms respectively [10]. In the case of W-3%Re sample, solid solution of 3% rhenium

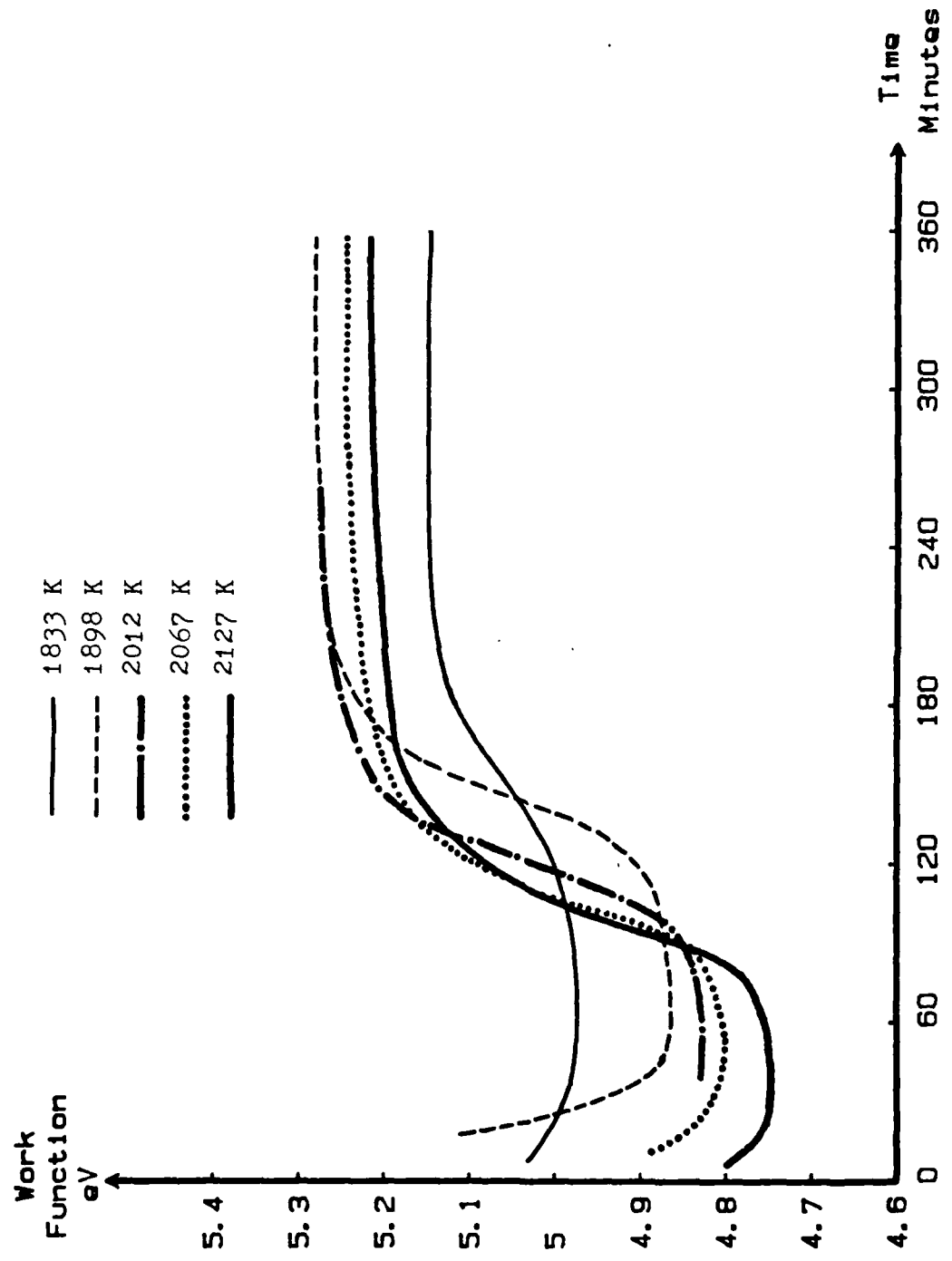


Fig.6.1 Work function-heating time curves of W-3%Re sample at several temperatures.

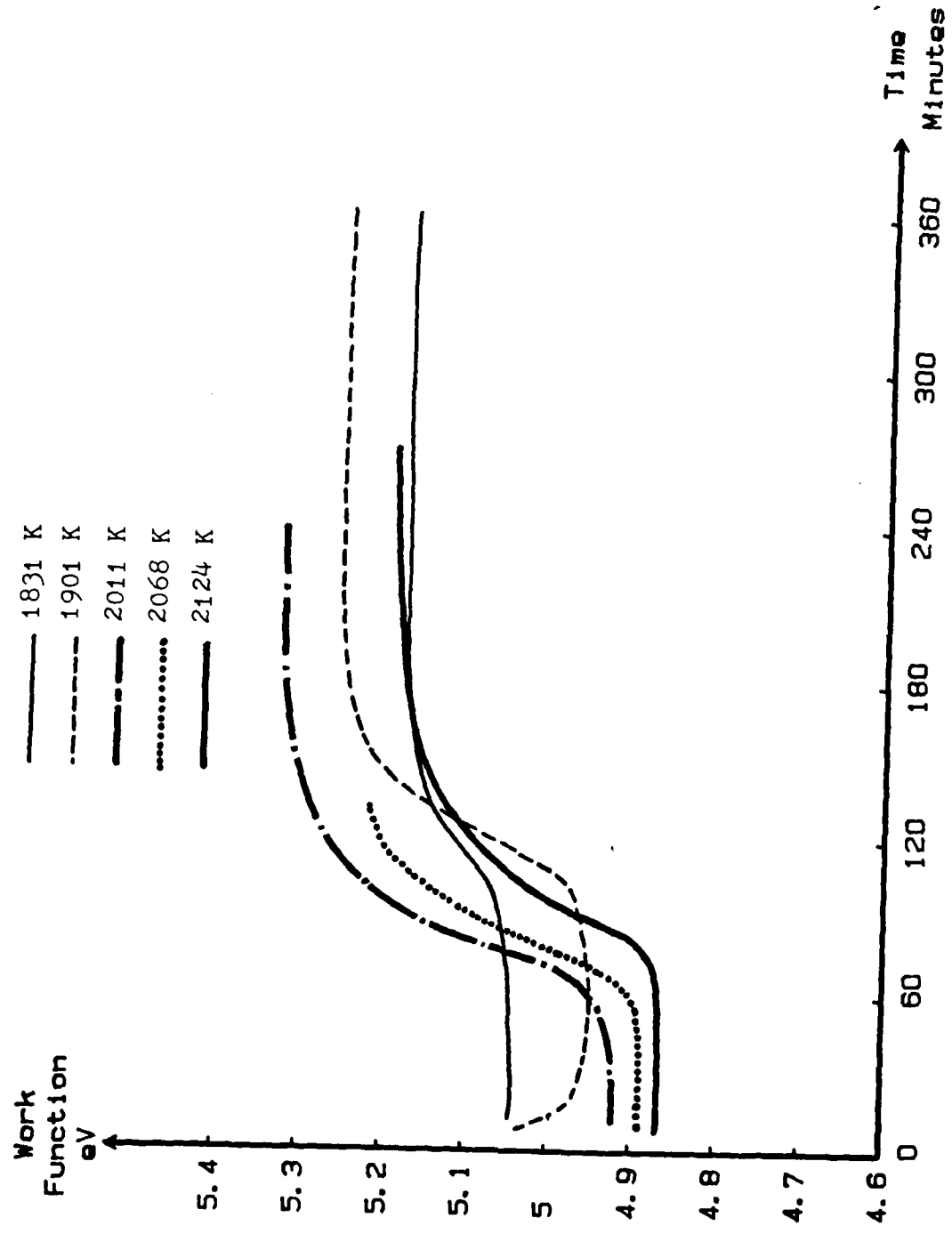


Fig. 6.2 Work function-heating time curves of W-30%Re sample at several temperatures.

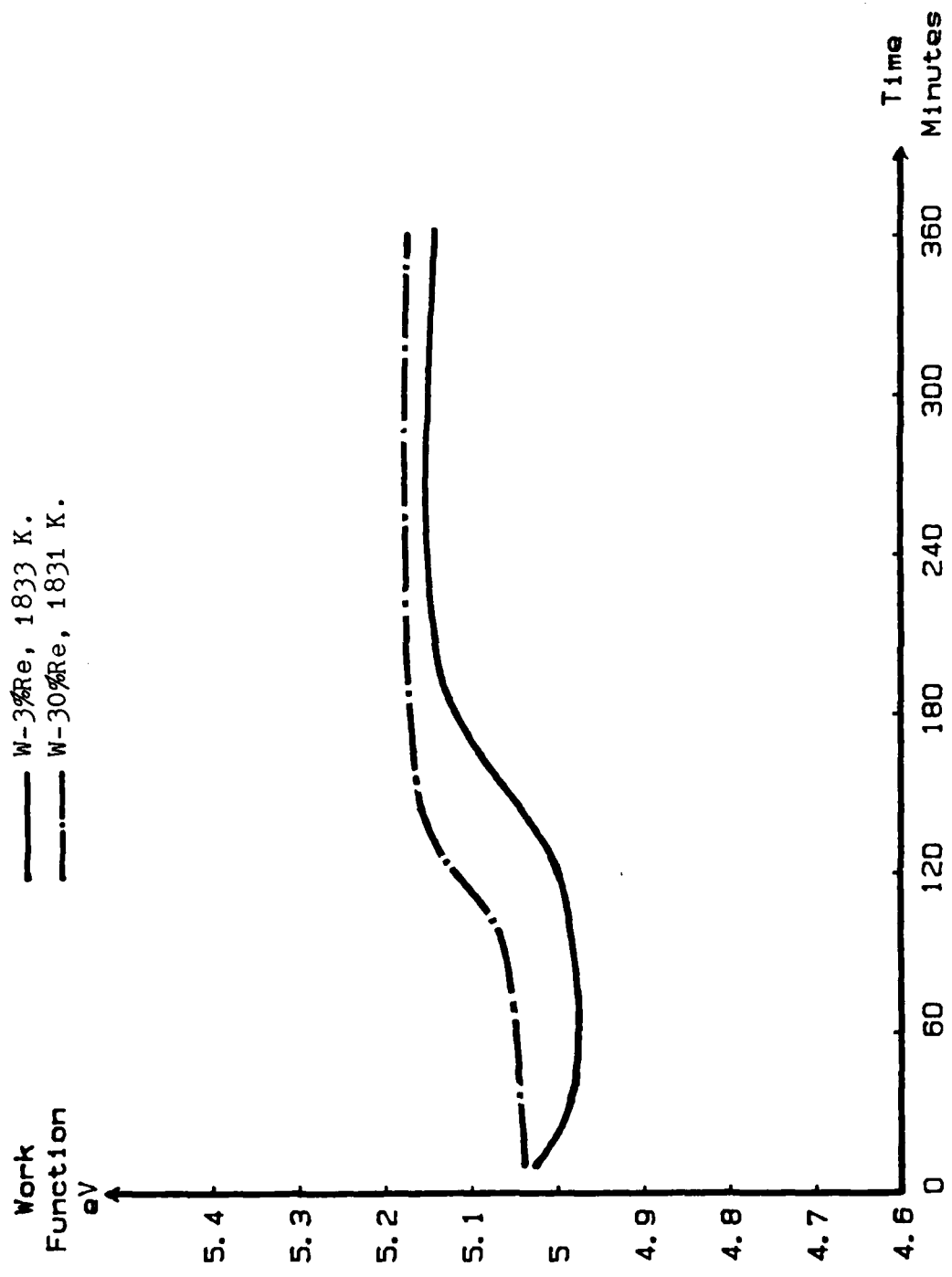


Fig. 6.3 Work function-heating time curves of different compositions at temperatures around 1830 K.

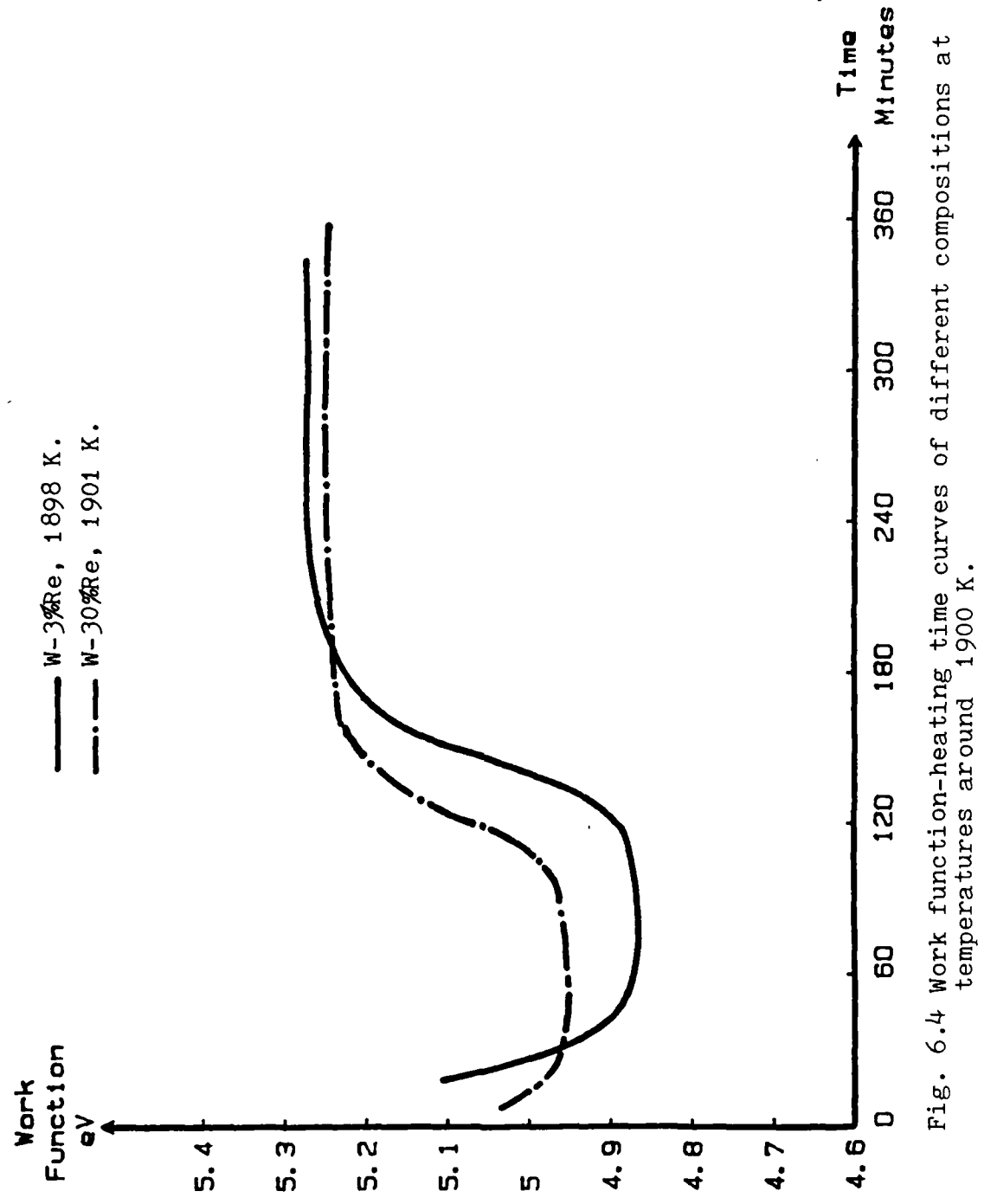


Fig. 6.4 Work function-heating time curves of different compositions at temperatures around 1900 K.

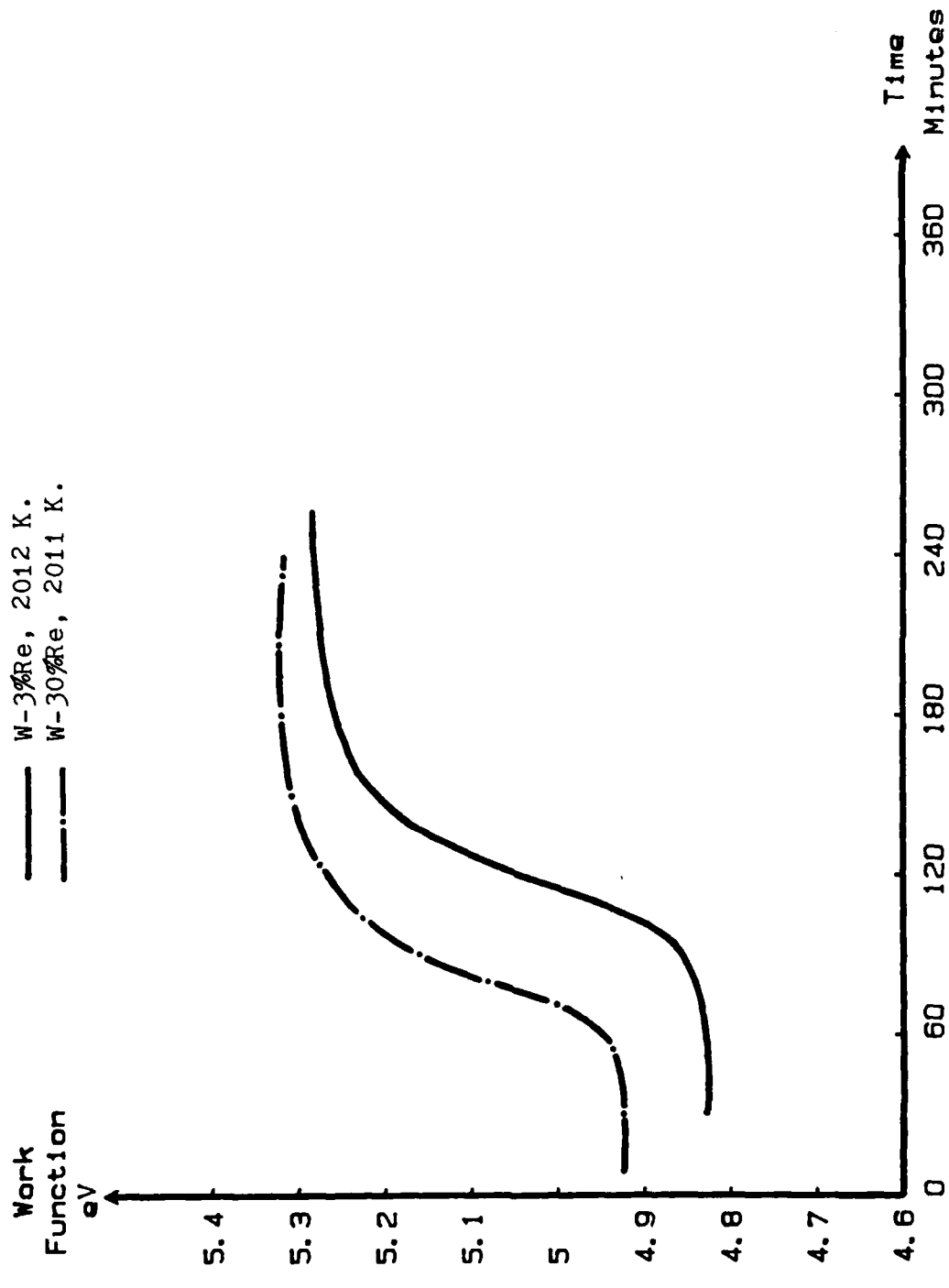


Fig. 6.5 Work function-heating time curves of different compositions at temperatures around 2010 K.

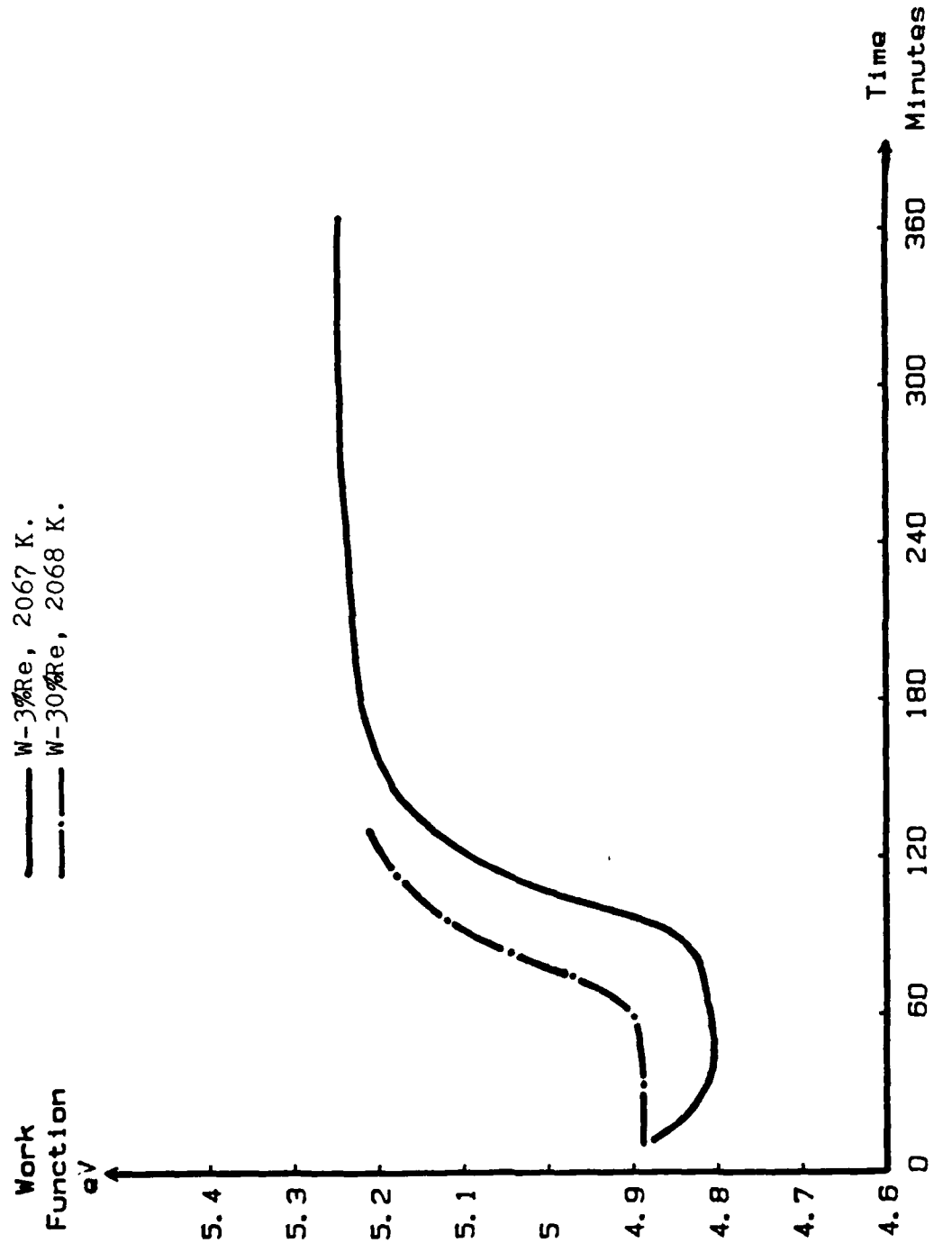


Fig. 6.6 Work function-heating time curves of different compositions at temperatures around 2065 K.

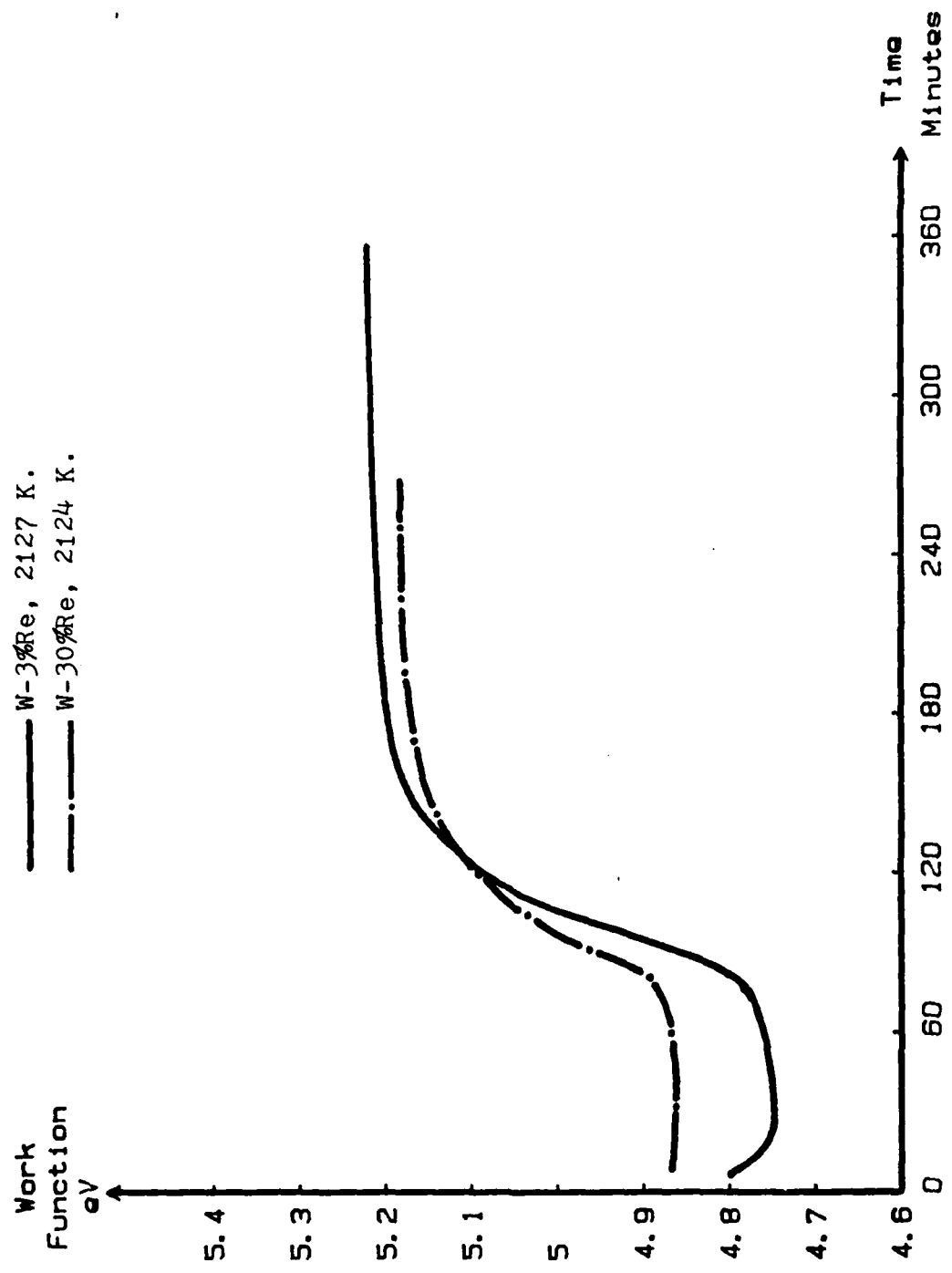


Fig. 6.7 Work function-heating time curves of different compositions at temperatures around 2125 K.

can not expand the lattice constant appreciably, so the work function was not affected by volume effect. The sample of 30% rhenium had a phase transformation at a temperature of approximately 2000 K. At a temperature below 2000 K, W-30%Re has a mixture of  $\alpha$  phase and  $\sigma$  phase. At a temperature above 2000 K, it has only one phase. However, due to the presence of high rhenium content, volume effect is appreciable. At high temperature, the evaporation rate difference of tungsten and rhenium atoms on the emitting surface can result in a depletion layer, which provides higher work function. This is a possible factor of the time dependent work function of the W-30%Re sample.

Time dependent work function was observed by B. Ch. Dyubua et al. [11] in their W-Ta and W-Mo system investigation. Work functions of W-Re samples were extremely sensitive to the heating time and the temperature. The heating of samples at 2000 K for 50 hours did not affect the work functions. A further heating at 2300 K for 15 hours of W-3%Mo sample produced at 0.6 eV climb in work function. Samples of higher molybdenum content were generally subjected to smaller work function climbs. A subsequent annealing at 1300~1700 K partially restored the initial properties. The behavior of this work function climb was explained by the desorption of atoms adsorbed on the surface. The test result of the present W-Re samples showed similar work function behavior. For the 3% rhenium

sample, 0.45 eV climbs were observed after heating for more than 4 hours at 1900-2100 K. For the 30% rhenium sample, climbs were obviously smaller. At lower temperature, heating time did not seriously affect work functions of both samples. A subsequent cooling at room temperature for 12 hours was applied along with heatings to recover the property. Therefore, the desorption effect is also possibly feasible for the W-Re system.

The oxygen partial pressure on the emitting surface was found, by T. L. Matskevich [12], to have strong effect on the work function. Two zirconium carbide samples were out gassed for 40 hours at 2500-2600 K and then tested at 1530 K with the presence of the oxygen partial pressure in the order of  $10^{-6}$  torr. As shown in Fig. 6.B, the work function started with an initial value followed by a minimum, and finally reached a stable maximum value within 4 hours. The difference between the minimum and the maximum values was about 0.7 eV. This curve is very similar to the curves of W-Re samples observed. Furthermore, according to Matskevich investigation, the minimum and the maximum work functions also depended on the sample temperature. At higher temperature, both the minimum and the maximum values tended toward the initial work function value. The W-Re samples showed the same behavior. The difference between the minimum and the maximum work function decreased as the temperature increased. T. L. Matskevich [12] adopted the explanation of G. K. Hall and C. H. Mee [13] of having

negatively penetrated oxygen ions for the appearance of the minimum point. Then, T. L. Matskevich [12] suggested that the maximum value of the work function was due to the coverage of the emitting surface with oxygen adatoms. These two explanations may be appropriate for the case of W-Re alloys.

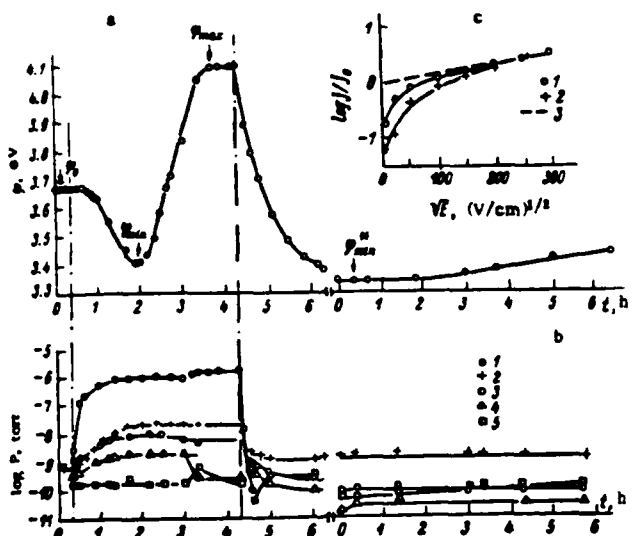


Fig. 6.8 a: Work function of zirconium carbide as a function of the time at 1550 K. b: Partial pressures of the gases as a function of the time. 1) O<sub>2</sub>; 2) CO + H<sub>2</sub>; 3) CO<sub>2</sub>; 4) H<sub>2</sub>O; 5) H<sub>2</sub>. c: Schottky curves measured at 1550 K. 1) The cathode work function is  $\Phi_0$ ; 2)  $\Phi_{\min}$ ; 3) theoretical Schottky line.

## 7. CONCLUSION

A 3.556 mm diameter collector assembly was designed and built to be used in the vacuum emission test station due to the size of available samples. An electron repeller and an electron seal were applied to the system to reduce the noise from electron bombardment heating.

Two W-Re alloy samples, 3% Re and 30% Re, were tested in the temperature range of 1830 K to 2130 K under the pressure of  $10^{-9}$  to  $10^{-7}$  torr. Initial experiment identified work functions of the two samples were functions of heating time. Therefore, the investigation goal became the effect of the composition, the temperature, and the heating time effect on W-Re alloys. Work functions of these samples were plotted versus heating time at different temperatures. Comparisons of the samples at approximately same temperature were made to understand the composition effect on the work function.

The general pattern of these work function-heating time curves was a initial minimum value followed by a climb toward a maximum value. This maximum work function was considered as a stable value of the material at the temperature. Except at about 1830 K, the 3% Re sample showed 0.45 eV climbs in work function, which was appreciably higher than the maximum 0.4 eV climb of the 30% Re sample at 2011 K. The highest work function was found to be 5.3 eV of the 30% Re sample at 2011 K. It was found by comparing

curves of different compositions, the Re content did not vary stable values considerably at each temperature. However, the minimum values of the 3% Re sample were always lower.

Volume effect is not thought to be a main factor of the work function climbs because the lattice parameters of tungsten and rhenium are close. But, the rhenium depletion and/or the oxygen adsorption could be a possible explanation of work function climbs. Further investigation of W-Re alloy work function is important in understanding the mechanism of the climb in terms of heating time and composition.

## REFERENCES

1. Lee B. Holcomb, "NASA's Thermionic Technology Program", 13th Intersociety Energy Conversion Engineering Conference, Vol.3, 1978, pp.1909-16.
2. Stanley W. Angrist, Direct Energy Conversion, 3rd ed., Allyn and Bacon, 1976, pp.249-50.
3. G. N. Hatsopoulos and E. P. Gyftopoulos, Thermionic Energy Conversion, Vol.1, MIT Press, 1973.
4. J. S. Blakemore, Solid State Physics, W. B. Saunders Co., 1974, pp.170-95.
5. G. N. Hatsopoulos and E. P. Gyftopoulos, Thermionic Energy Conversion, Vol.2, MIT Press, 1979, pp.266-9.
6. Robert Siegel and John R. Howell, Thermal Radiation Heat Transfer, McGraw-Hill, 1972, pp.238-42.
7. M. K. Ozisik, Basic Heat Transfer, McGraw-Hill, 1977.
8. Thermophysical Properties of Matter, TPRC Data Series, Vol.1, 1970, p.122.
9. B. Ch. Dyubua, A. I. Pekarev, B. N. Popov, and M. A. Tylkina, Radiotekhn. i elektron., Vol.7, 1962, p.1566.
10. R. A. Flinn and F. K. Trojan, Engineering Materials and Their Applications, Houghton Mifflin Co., 1981, p.303.
11. B. Ch. Dyubua and O. K. Kultashev, "Work Function of Solid Solutions of Tungsten with Molybdenum and Tantalum", Soviet Physics-Solid State, Vol.8, No.4, 1966, pp.882-5.
12. T. L. Matskevich, "Work Function of Zirconium Carbide-Oxygen", Soviet Physics Tech. Physics, Vol.23, No.8, 1978, pp.972-5.
13. G. K. Hall and C. H. Mee, Surface Science, Vol.28, 1971, p.598.

**SECTION 6**

**HIGH TEMPERATURE, HIGH VACUUM MECHANICAL TESTING  
OF TUNGSTEN-30 PERCENT RHENIUM ALLOY**

## TABLE OF CONTENTS

CHAPTER	PAGE
1. INTRODUCTION.....	1
2. EXPERIMENTAL PROCEDURE.....	6
mechanical testing.....	6
scanning electron and optical microscopy.....	9
transmission electron microscopy.....	9
3. EXPERIMENTAL RESULTS.....	11
4. SUMMARY.....	13
5. ATTACHMENT.....	38
6. APPENDIX.....	39

## LIST OF ILLUSTRATION

FIGURE	PAGE
1. Tensile strength vs test temperature.....	14
2. Normalized Young's modulus vs test temperature.....	15
3. Plot of elongation vs test temperature.....	16
4. Optical micrograph of W-30% Re at 1600°C.....	17
5. Optical micrograph of W-30% Re at 1800°C.....	18
6. Optical micrograph of W-30% Re at 2000°C.....	19
7. Optical micrograph of W-30% Re at 2200°C.....	20
8. SEM fractograph of W-30% Re at 1600°C.....	22
9. SEM fractograph of W-30% Re at 1800°C.....	24
10. SEM fractograph of W-30% Re at 2000°C.....	26
11. SEM fractograph of W-30% Re at 2200°C.....	28
12. SEM fractograph of arc-melted,pure W at 2100°C. ....	30
13. SEM fractograph of P/M,pure W at 2200°C .....	32
14. TEM micrograph shows segregation of Re from W matrix..	34
15. TEM micrograph shows $\sigma$ phase.....	35
16. Plot of yield strength vs grain size $^{-1/2}$ .....	36

## ABSTRACT

The mechanical properties of tungsten-30 percent rhenium were investigated by using Instron tensile testing equipment with a high temperature, ultrahigh vacuum system. The relationship between the normalized Young's modulus, ultimate tensile strength, yield strength, elongation (ductility) and the test temperature was examined. The experimental results showed that higher test temperatures resulted in lower ultimate strength, lower yield strength, lower normalized Young's modulus and higher elongation. Analytical techniques such as scanning electron microscopy (SEM) and transmission electron microscopy (TEM) were used to study the solid solution strengthening effect and microstructure changes of tungsten-30 percent rhenium at the various testing temperatures.

## 1. INTRODUCTION

### 1.1 Some Factors Affecting The Properties Tungsten and its Alloys

As tungsten and its alloys are often used in high temperature environments, their stress-rupture, creep and fatigue behaviors at elevated temperatures are of major concern. On the other hand, most tungsten hardware must also function at low temperatures; therefore, the low temperature ductility must be considered. Comparison of the mechanical properties of tungsten without referring to the purity, fabrication history, and other conditions is sometimes misleading. Furthermore, different fabrication processes such as extrusion, swaging or rolling yield different properties in the final products. As a rule, lower working temperatures and higher amounts of work result in higher strength. Grain size and impurity content are other factors that affect the properties of the material.

### 1.2 The Present Explanation for the Solid Solution Strengthening Mechanism of Tungsten-Rhenium Alloys

Solid solution addition can increase the strength by a variety of mechanisms such as: (a) the segregation of solutes to stacking faults (Suzuki interaction), (b) elastic interaction of solute atoms with moving dislocations to increase the Peierls-Nabarro stress or the friction stress,

c) solute interaction with vacancies and dislocation jogs and  
(d) the segregation of solutes to grain boundaries so as to influence grain boundary sliding or migration. Davison and Brotzen [1] have proposed that the addition of rhenium to tungsten promotes twining during deformation, because the stacking fault energy is reduced by rhenium. However, twining only accounts for a minor fraction of the plastic deformation, usually at the onset of macroscopic strain, with slip contributing to the remainder. The exact effect of twining is not well understood.

Stephfen and Witkze [2] have suggested that rhenium would decrease the lattice resistance (Peierls-Nabarro stress) to dislocation motion which would result in increased dislocation mobility. This is consistent with the well known solid solution softening in bcc metals and is attributed to the same cause. There are two components in the flow stress: a thermal component,  $\sigma^*$ , called effective stress and an a-thermal component,  $\sigma_i$ , called internal stress. The latter increases with solute additions, dominating above the temperature of 0.2 Tm (where Tm is the absolute temperature of the melting point of the metal) but does not vary significantly with temperature. It is generally accepted [3] that the Peierls-Nabarro stress is responsible for the large temperature dependence of  $\sigma^*$  in bcc metals at low temperature. The natural extension of this is, therefore, that the alloy softening effect is caused by solute reduction in the Peierls

barriers due to the alloy electronic configuration.

### 1.3 The Dispersion Strengthening Mechanism of Thoriated Tungsten-Rhenium Alloys

The strengthening effect of solid solution generally becomes negligible at a temperature above  $0.5 T_m$ , in which case dispersion-strengthening alloys are superior. Theories of dispersion strengthening have been reviewed by Ansell [4]. In general, the dispersed second phase should meet the following conditions:

- (1) The particle size of the second phases should be of submicron range with an interparticle spacing of less than 0.5 microns [5].
- (2) The second phase should be chemically stable and resistant to agglomeration during processing and at the service temperature.

The more common methods are conventional pressing and sintering, isostatic pressing followed by extrusion, or hot pressing; the last method, as recommended by Sell et al. [6], has less tendency for the second phase to become agglomerated and yields end products of better quality. In the lamp industry, thoriated tungsten wire has been well known for its fabricability, strengthening effect and high electron emissivity. H. G. Sell claimed that thoriated tungsten alloys demonstrate their highest tensile and creep strength at temperatures above 2,000 degrees Celsius.

Dispersed second phase particles act in two distinct ways

to retard the motion of dislocations. The particles may be cut by the dislocation; or the particles resist cutting, and the dislocations are forced to bypass them. When particles are small and/or soft, dislocations can cut and deform the particles. There are four mechanisms that produce this type of strengthening effect:

- (1) The strain field resulting from the mismatch between a particle and the matrix would be a source of strengthening.
- (2) "Chemical hardening" occurs when a dislocation shears through a particle; since this process increases the surface area of the particle, work must be done to shear the particle.
- (3) The difference between the elastic moduli of the matrix and the particle is a source of strengthening.
- (4) The Peierls stress between the particle and the matrix can strengthen the material.

As cutting the particles becomes more difficult, the dislocations instead find a way to move around the particles (Orowan mechanism).

The proposition of strengthening tungsten additively by using rhenium in solid solution and thoriated as a dispersed second phase has been pursued by D. J. Maykuth et al. [7] and by G. W. King et al. [8]. This class of materials appears to be potentially attractive because of the improvement in low temperature ductility which has been observed for tungsten-

rhenium alloys [9]. G. W. King has produced evidence that solid solution strnngthening and dispersed second phase strengthening are additive effects in tungsten-30 percent rhenium-one percent thorium dioxide. In regard to strengthening by a dispersed second phase at elevated temperatures, the most important factors are the particle size and the interspacing of the thoria dispersoids. Generally speaking, tungsten-rhenium alloy has a lower ductile-brittle transition temperature, higher recrystallization temperature, better fabricability and higher tensile strength at elevated temperatures.

## 2. EXPERIMENTAL PROCEDURE

### 2.1 Mechanical Testing

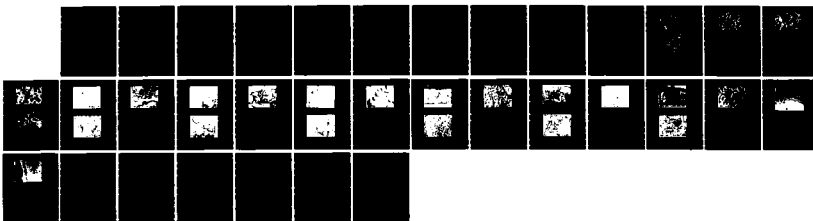
The mechanical testing of the specimens was accomplished on an Instron tensile testing machine with a 10-pound to 1,000-pound variable range tensile load cell. The specimens described in [10] were first mechanically polished to a smooth, shining finish in order to ensure the same surface conditions for all of the specimens. The specimens were installed in the test chamber and connected via a 150-amp electrical feedthrough to a Nobatron DCR 20-250A high current power supply which provided the necessary electrical resistance heating of the specimen. After installation of the test specimens, the viewing port was cleaned to prevent any extraneous attenuation of the optical pyrometer readings. The system was then checked for electrical malfunctions, sealed and rough pumped to 10 millitorr using a Welch Scientific Company Model 1402 Duo Seal mechanical vacuum pump. A 150-liter per second ion pump reduced the pressure further to  $2.0 \times 10^{-7}$  torr. After baking the ion pump and test chamber for eight hours at 250 degrees Celsius, a vacuum of  $4.0 \times 10^{-9}$  torr was obtained. At this point, an initial current of 50 amps was applied to the specimens to allow degassing of the specimens and alignment of the EMI-Gencom RFI/B-013F optical pyrometer.

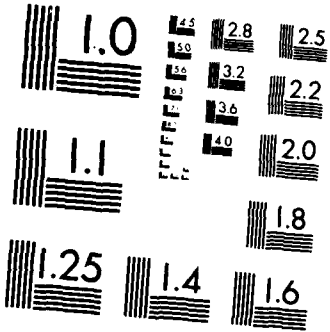
This optical pyrometer had been calibrated using a

National Bureau of Standards ribbon filament lamp with a Hewlett-Packard 6260A direct current power supply and an Omega 881C digital multimeter. The maximum uncertainties of the temperature values of the ribbon filament lamp were estimated to be: plus or minus 2.5 degrees Celsius at 800 degrees Celsius, plus or minus 1.5 degrees Celsius at 1,100 degrees Celsius and plus or minus 3.0 degrees Celsius at 2,300 degrees Celsius (see Attachment 1). Compensation for the attenuation of the pyrometer by the viewing port was made by placing the viewing port between the pyrometer and the ribbon filament lamp during calibration (see Appendix 1).

Once the pressure had stabilized, the current through the specimens was increased until the pyrometer reading, which is actually a photon count, corresponded to the desired temperature. Experiments were done in the 1,400-degree Celsius to 2,200-degree Celsius range. The currents varied from 60 amps at the low temperatures to 130 amps at the high temperatures. Voltages varied from 3.0 volts to 6.0 volts. The increased temperatures resulted in a final vacuum of approximately  $5.0 \times 10^{-7}$  torr during the experiments. The photon count was displayed on a Hewlett-Packard 5312A HP-IB interface with a hard copy printout of time and temperature being produced every 10 seconds by a Hewlett-Packard 5150A thermal printer. A Princeton Applied Research 1121 amplifier/discriminator and control unit provided the required signal conditioning between the pyrometer and the interface.

AD-A173 245 INVESTIGATION OF MATERIAL PROBLEMS FOR HIGH TEMPERATURE 5/5  
HIGH POWER SPACE. (U) ARIZONA STATE UNIV TEMPE COLL OF  
ENGINEERING AND APPLIED SCIE. D L JACOBSON ET AL.  
UNCLASSIFIED JUL 86 AFOSR-TR-86-0819 AFOSR-83-0067 F/G 11/6 NL





MICROCOPY RESOLUTION TEST CHART  
NATIONAL BUREAU OF STANDARDS 1963-A

When the temperature had stabilized, the Instron chart was calibrated, and the chart speed was adjusted to one inch per minute. The load cell range was adjusted to the anticipated forces. The 20-pound range was used at the higher temperatures, and the 50-pound range was used at intermediate temperatures. It was necessary to use the 100-pound range at 1,400 degree Celsius. All experiments were conducted at a cross head speed of 0.02 inches per minute. The strain rate was  $7.0 \times 10^{-4}$  per second.

During the experiments, variations in the cross sectional area of the specimens due to necking caused changes in the electrical resistance of the specimens. This resulted in temperature variations which were controlled manually by adjusting the voltage of the electrical resistance heating power supply with reference to the photon count. Any anomalies on the load-displacement chart were marked with the cross head position and the time. In all cases the anomalies could be traced to temperature deviations from the nominal value. The load-displacement chart required a correction for the effect of the flexible coupling that allowed the vertical motion of the cross head to be transmitted to the specimens in the vacuum chamber. The coupling acted as a linear spring, and the force shown on the chart was a superposition of the force on the test specimen plus the force on the coupling. After the specimen fractured, the cross head was returned to its initial position and then

extended back through the experimental range of motion. The resulting curve revealed the effect of the coupling alone. This curve was subtracted graphically from the specimen-coupling load-displacement curve to yield the actual specimen load-displacement curve. The fractured specimens were maintained under vacuum until they had cooled to room temperature. At this point, the test chamber was filled with a nitrogen atmosphere to prevent condensation. Finally, the test chamber was opened to the atmosphere, and the specimens were removed for further study.

## 2.2 Scanning Electron (SEM) and Optical Microscopy

The fractured specimens were examined by SEM as well as low power optical microscope. All of the fractured specimens were mounted on the special holder for the JEOL 840X scanning electron microscope which operates at 15 Kv. The distance between the electron gun and specimen was approximately 39 mm. The specimen current was in the  $10^{-9}$  amp range, and the vacuum condition was approximately  $10^{-6}$  torr. The fracture surfaces were examined from both the top view and the side view. Then the characteristics of the fracture surfaces were recorded by using secondary electron images.

## 2.3 Transmission Electron Microscopy (TEM)

To prepare a sample for TEM, a 3.0-mm diameter disk was cut from the 1800 degree Celsius fracture sample. The disk

was mechanically polished to a thickness of 100 microns and then dimpled. Finally, the sample was ion milled until it was penetrated. The thickness near the area of penetration is estimated to be 1,000 angstroms. A Philip-400T TEM was used to examine the microstructure of the thin film specimen.

### 3. EXPERIMENTAL RESULTS

#### 3.1 Mechanical Testing

All of the mechanical properties versus the test temperatures are shown in Figures 1 through 3. All of the results are well in agreement with the published data from H. G. Sell [6] for similar materials. The ultimate strength at 1,600 degrees Celsius is 19 ksi decreasing to 3.9 ksi at 2,200 degrees Celsius. The elongation at 1,600 degrees Celsius is 26 percent, increasing with temperature to 38 percent at 2,200 degrees Celsius.

#### 3.2 SEM and optical Microscopy

The side views of the fractured specimens are shown on Figures 4 through 7. Figure 5(a) shows the micrograph at 310x near the fracture tip. Figure 5(b) shows the micrograph a short distance from the fracture tip. There is significant difference in the metallographic picture. Grain boundary separation and elongation along the tensile axis can be seen near the fracture tip.

The electron micrographs of tungsten-30 percent rhenium show that the fracture mode is grain boundary sliding as shown on figures 8 through 11. Figures 8(a) through 8(c) shows the SEM fractographs of the 1,600-degree Celsius sample at magnifications of 250X, 2,500X and 10,500X. Figures 9 through 11 show the same phenomenon at various temperatures.

The fractographic examination reveals three important aspects:

- (1) The fracture mechanism of tungsten-30 percent rhenium is the result of grain boundary sliding.
- (2) There are variations in grain size between samples tested at different temperatures. Higher test temperatures resulted in larger grain sizes.
- (3) The porosity of the fracture is due to the powder metallurgy sintering process that was used in the processing of the tungsten-rhenium alloy.

Figures 12(a) and 12(b) are the micrographs of arc-melted, pure tungsten which was fractured at a test temperature of 2,100 degrees Celsius. The fracture mode is intergranular with plastic deformation. Figures 13(a) and 13(b) are the fractographs of powder metallurgy (P/M), pure tungsten which was fractured at a test temperature of 2,200 degrees Celsius. The fracture mode is intergranular with much more plastic deformation than the arc-melted, pure, tungsten specimen.

### 3.3 Transmission Electron Microscopy

Figures 14 and 15 show the micrograph of tungsten-30 percent rhenium at magnification 220,000x. Figure 14 shows the segregation of rhenium from the tungsten matrix. Figure 15 shows the  $\sigma$  phase (tetragonal structure).

#### 4. SUMMARY:

##### 4.1 According to Hall-Petch equation:

$$\sigma_y = \sigma_0 + kd^{-1/2}$$

$\sigma_y$  : observed yield strength

$\sigma_0$  : is equal to the yield stress of single crystal

d : average grain diameter

k : is a measure of the stress for propagation of  
yielding through a polycrystal

From the optical micrographs, the average grain diameter can be estimated, the  $\sigma_y$  vs  $d^{-1/2}$  is presented at Fig.16. The experimental results is in agreement with the theoretical prediction in the range of 1600°C through 2200°C for W-30% Re alloys

4.2 The fracture mechanism of the W-30% Re is grain boundaries sliding. However, the pure tungsten is intergranular with certain amount of plastic deformation.

4.3 Optical micrographs show the separation of grain boundary of W-30% Re near the fractured tips, it is also consistent with the observation of the SEM fractographs.

4.4 The segregation and σ phase of W-30% Re shown on Fig.14 and Fig. 15 is the result of quick cooling rate. However, the mechanism of microstructure affecting the mechanical properties is still unclear. It is required to study the microstructure extensively.

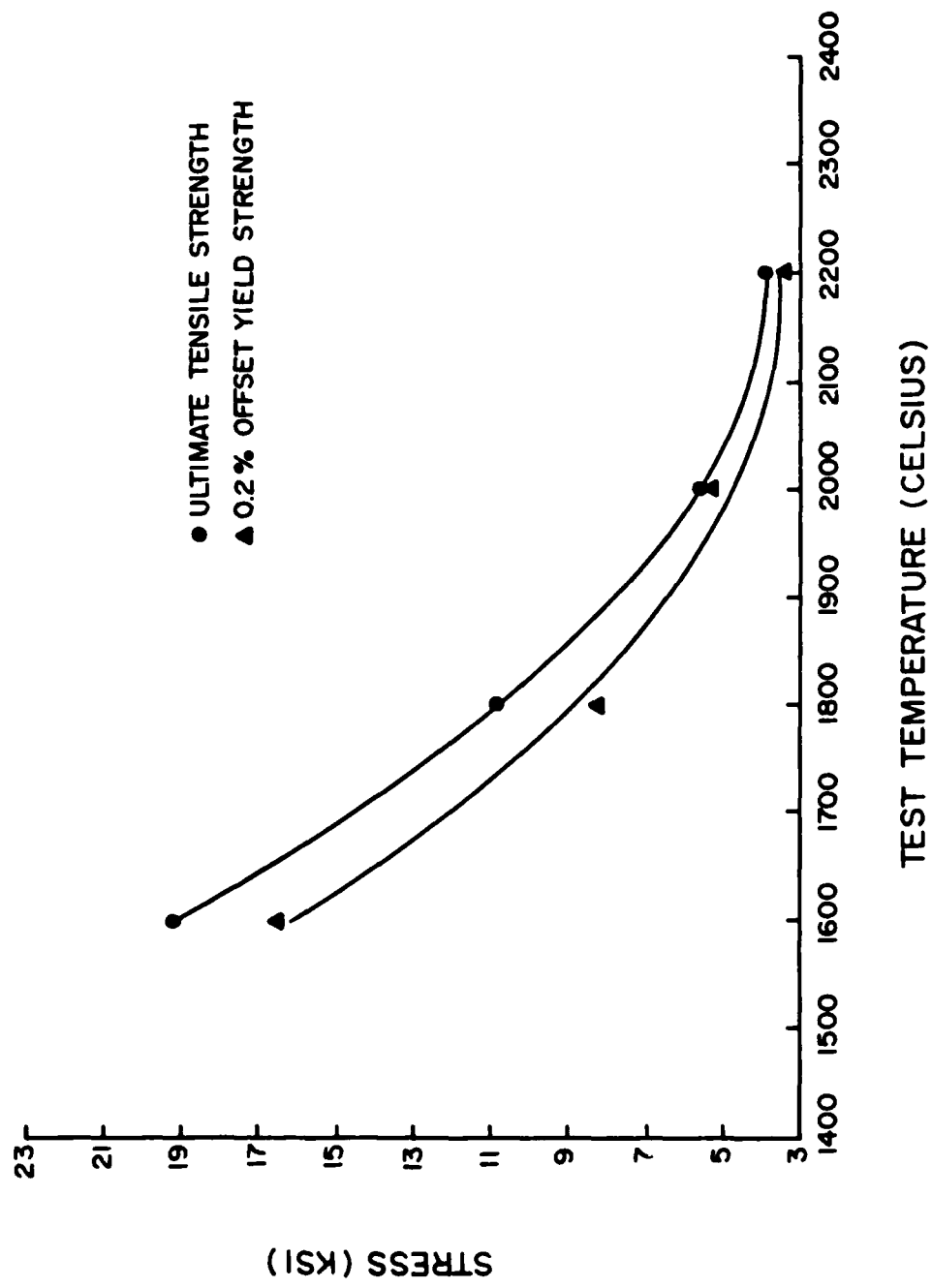


Fig. 1. Tensile strength vs test temperature.

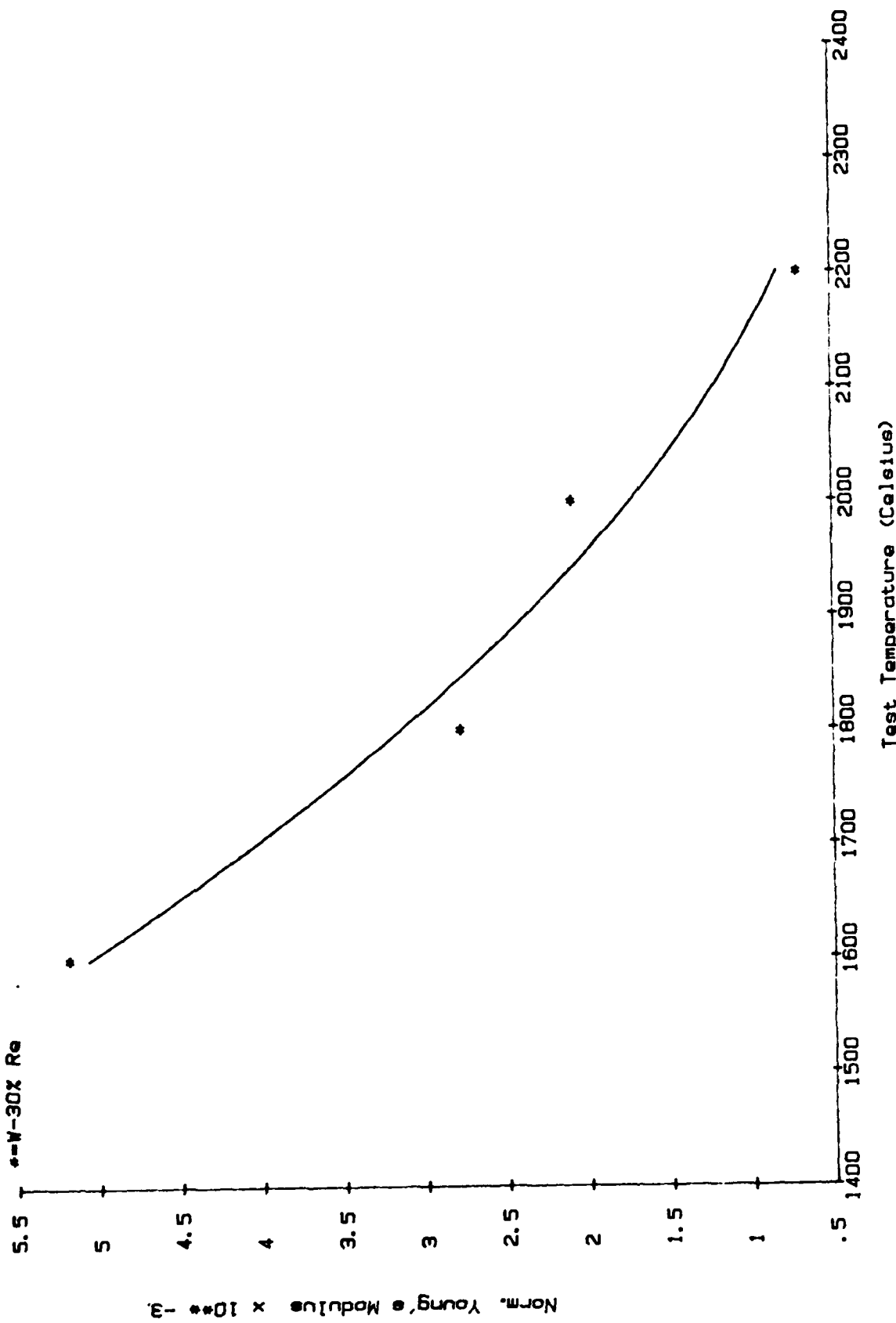


Fig. 2 Normalized Young's modulus vs test temperature

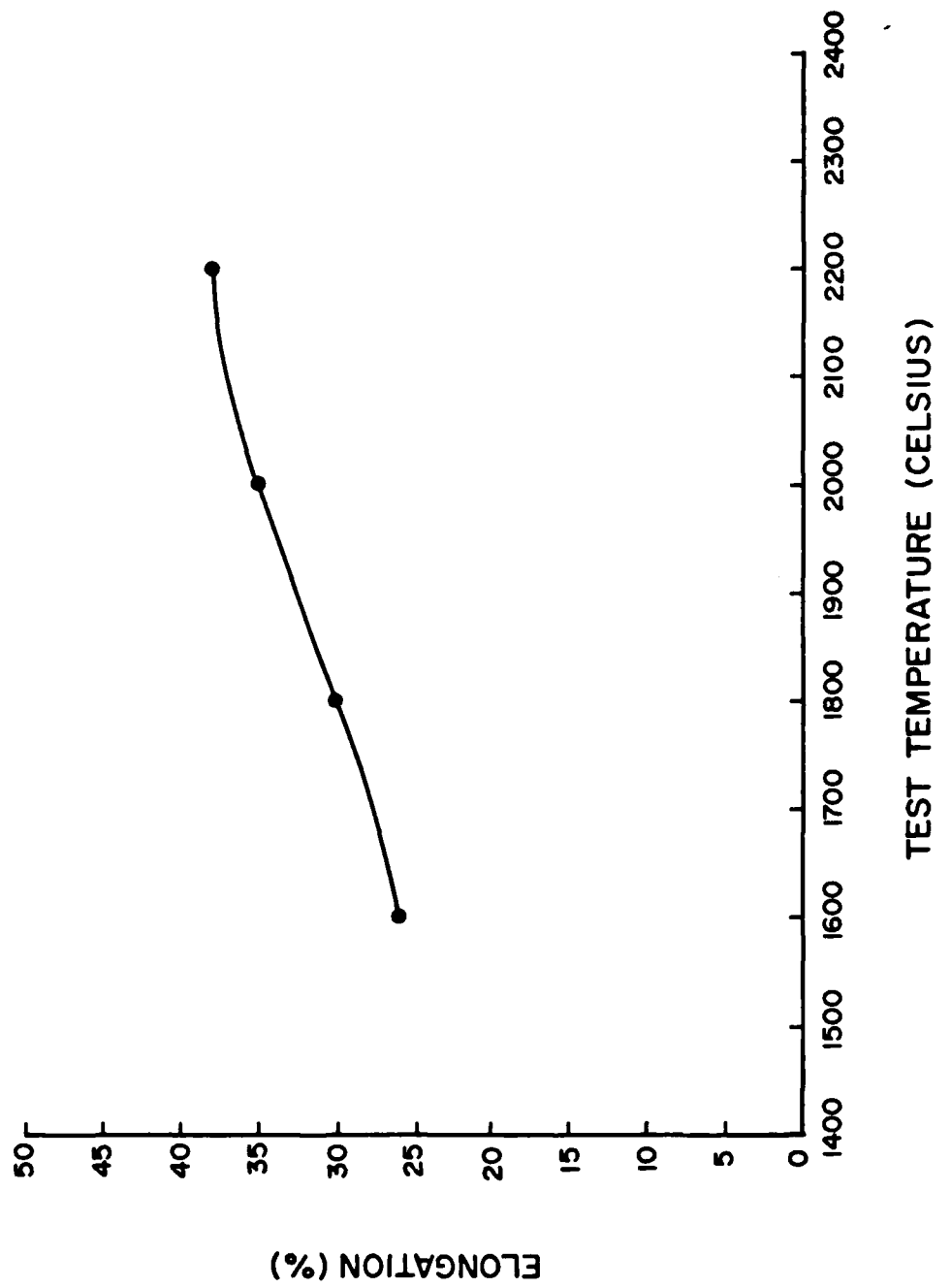


Fig. 3. Plot of elongation vs test temperature.



(a)

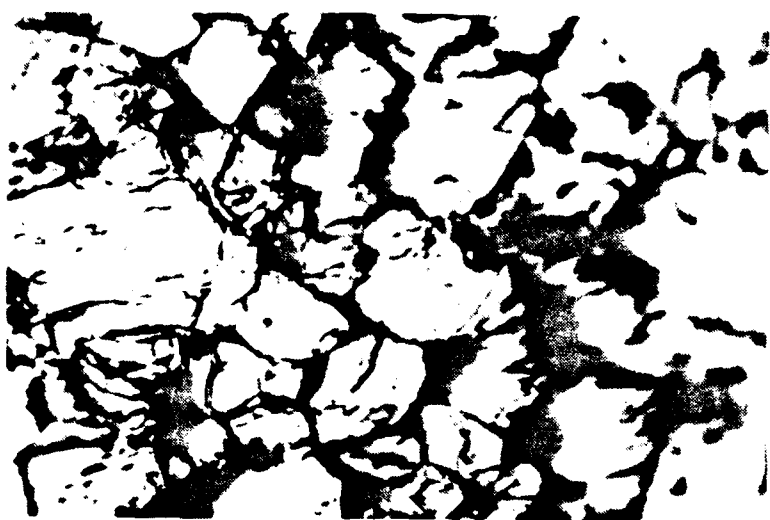


(b)

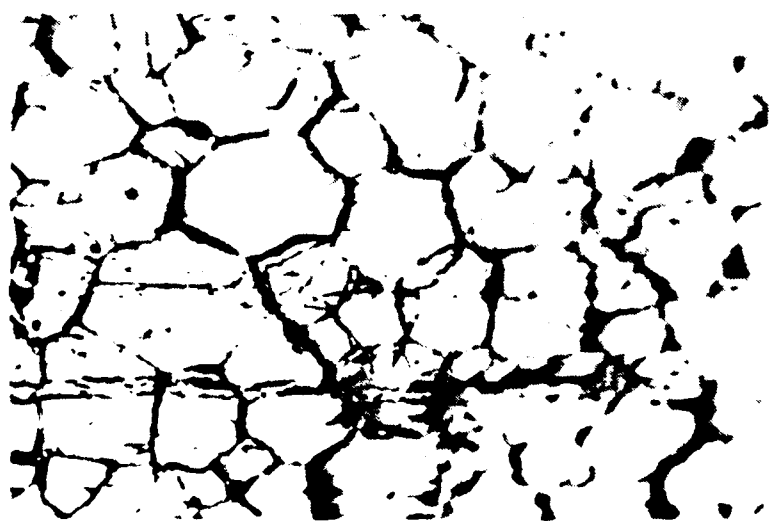
Fig.4. Optical micrograph of W-30% Re at 1600°C  
and magnification 310X.

(a) near fractured tip

(b) away from fractured tip a little bit



(a)

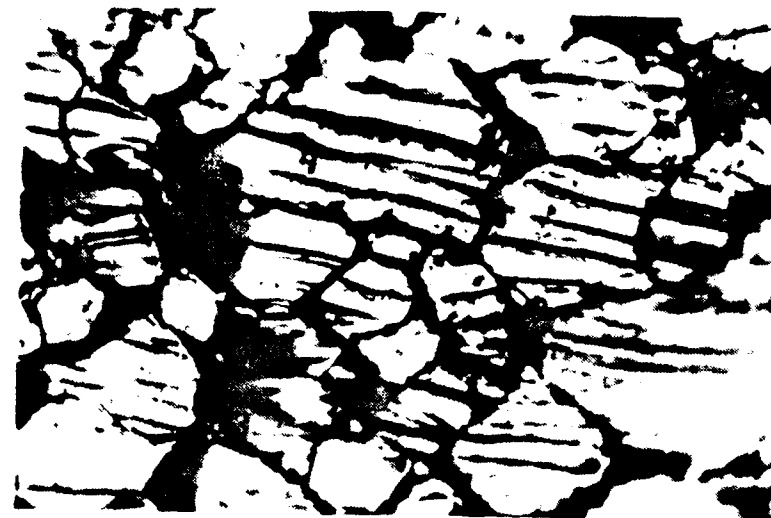


(b)

Fig.5. Optical micrograph of W-30% Re at 1800°C  
and magnification 310X.

(a) near fractured tip

(b) away from fractured tip a little bit



(a)



(b)

Fig.6. Optical micrograph of W-30% Re at 2000°C  
and magnification 310X.

(a) near fractured tip

(b) away from fractured tip a little bit



(a)

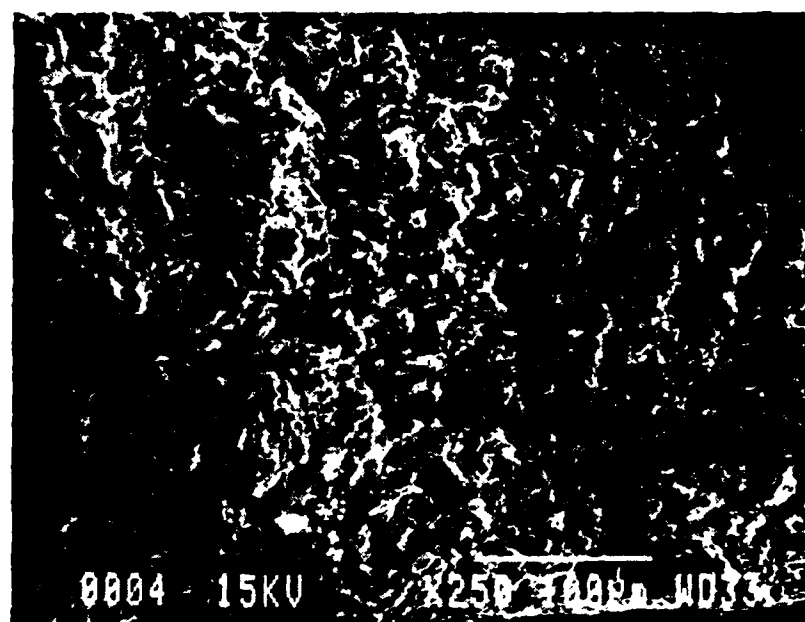


(b)

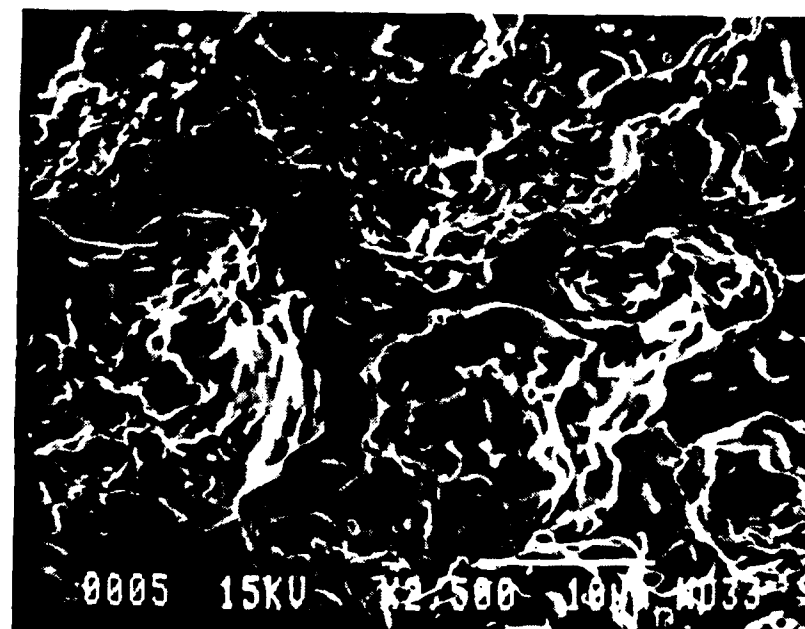
**Fig.7. Optical micrograph of W-30% Re at 2200°C  
and magnification 310X.**

**(a) near fractured tip**

**(b) away from fractured tip a little bit**



(a)



(b)



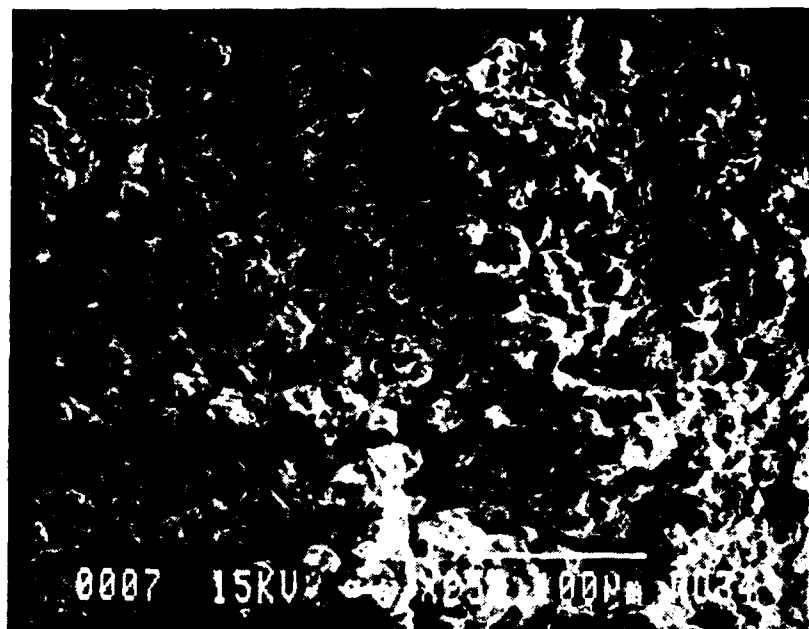
(c)

Fig.8 SEM fractograph of W-30% Re at 1600°C.

(a) magnification 250X

(b) magnification 2,500X

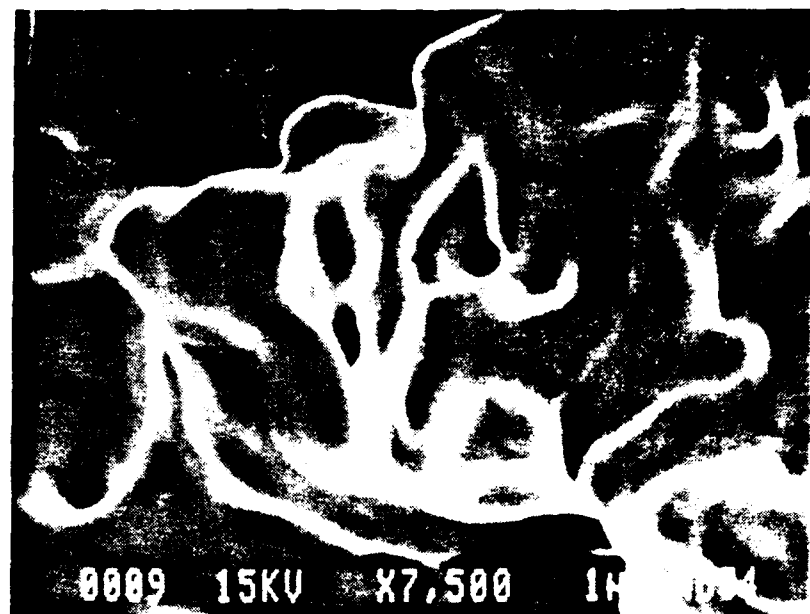
(c) magnification 10,000X



(a)



(b)



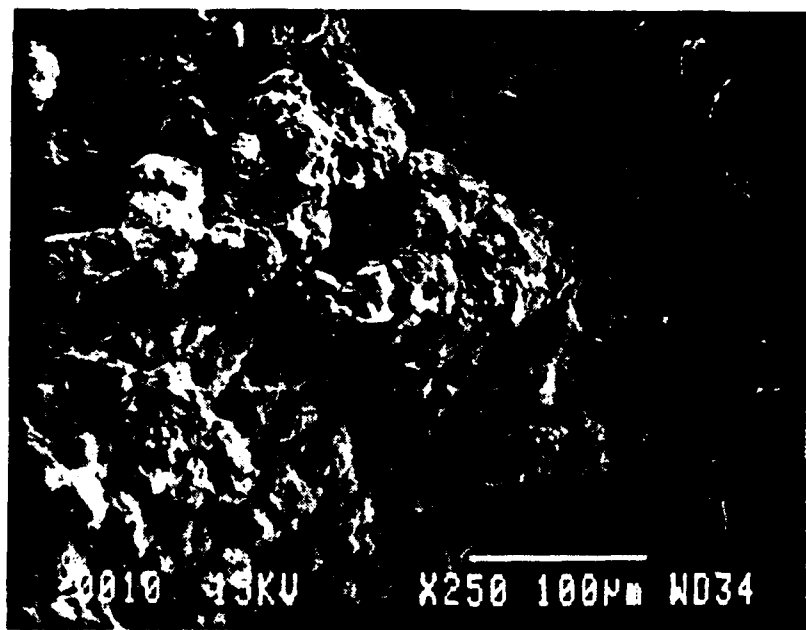
(c)

Fig.9 SEM fractograph of W-30% Re at 1800°C.

(a) magnification 250X

(b) magnification 2,500X

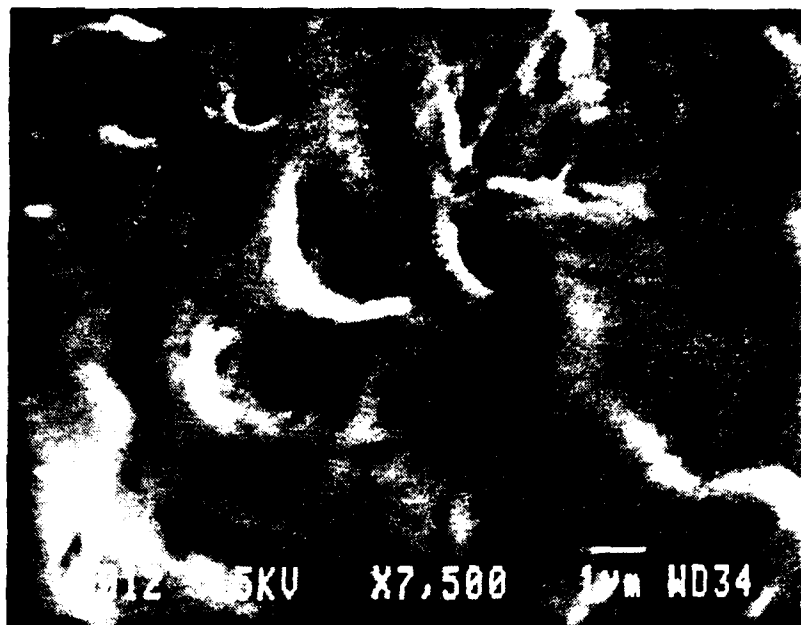
(c) magnification 7,500X



(a)



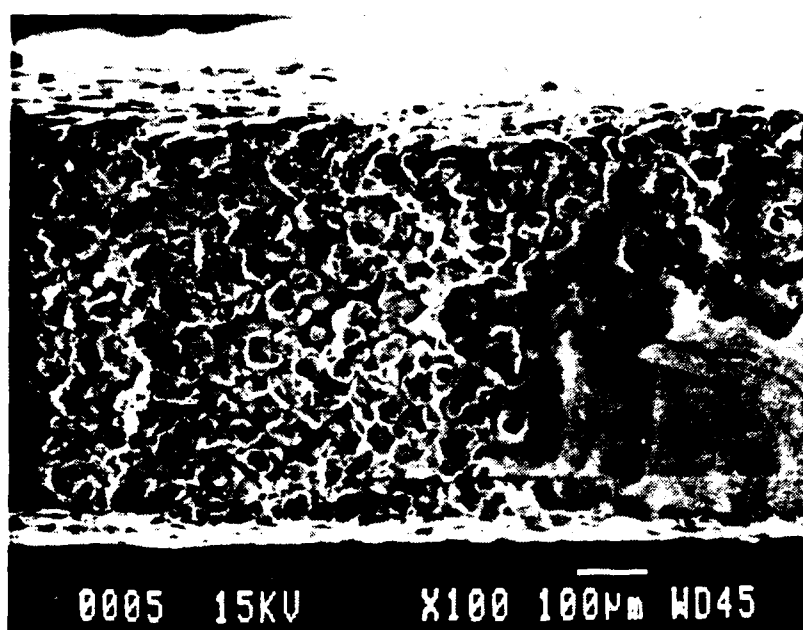
(b)



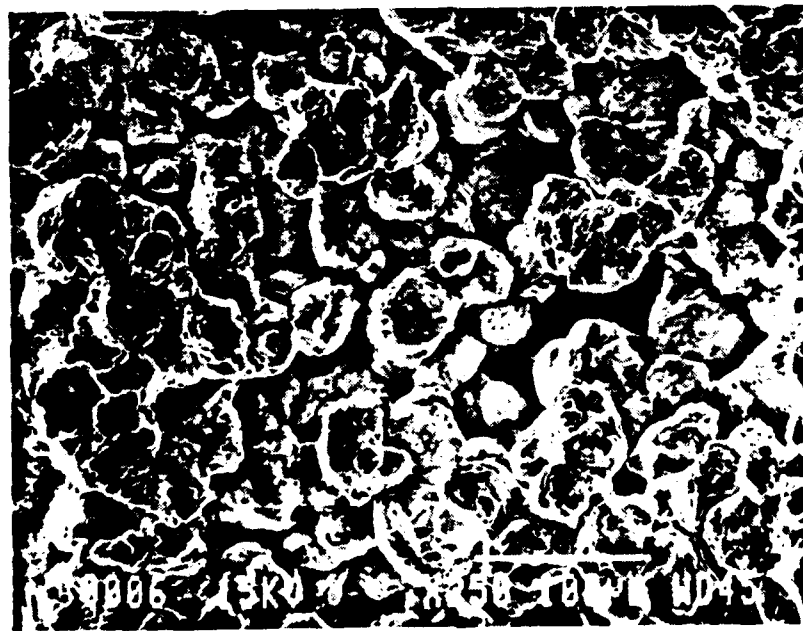
(c)

Fig.10 SEM fractograph of W-30% Re at 2000°C.

- (a) magnification 250X
- (b) magnification 2,500X
- (c) magnification 7,500X



(a)



(b)



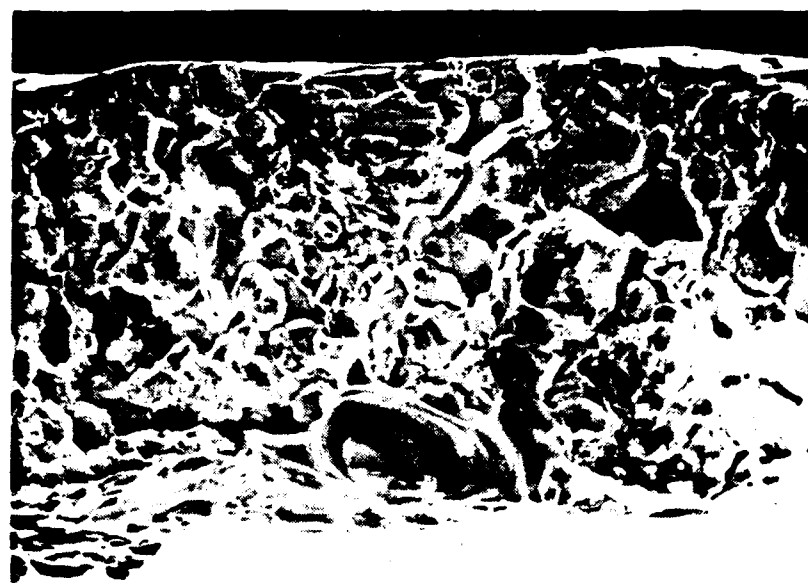
(c)

Fig.11 SEM fractograph of W-30% Re at 2200°C.

(a) magnification 250X

(b) magnification 2,500X

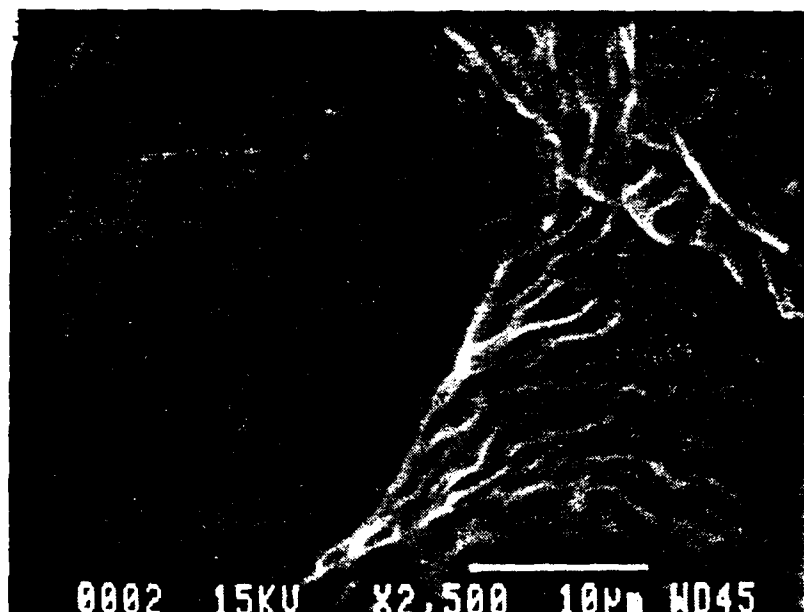
(c) magnification 7,500X



(a)



(b)



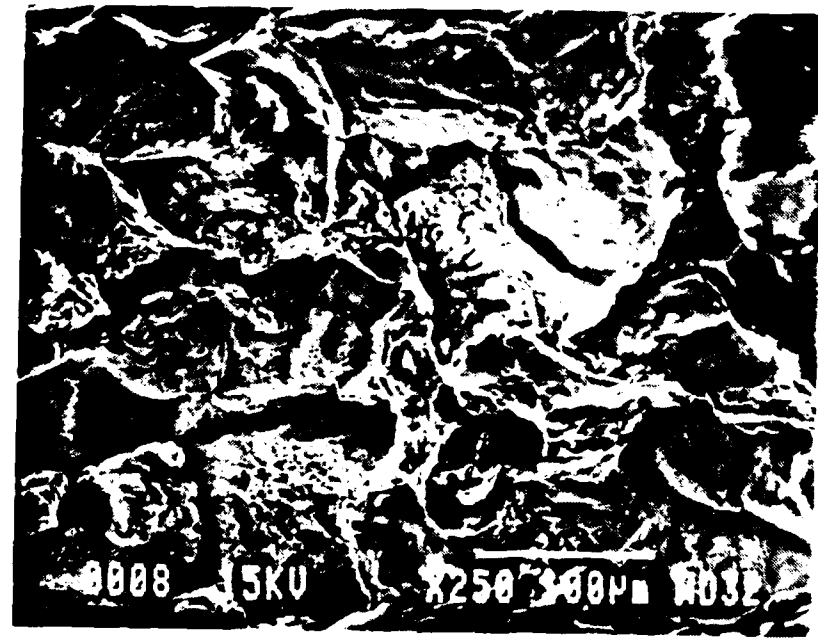
(c)

Fig. 12 SEM fractograph of arc-melted, pure W at 2100°C.

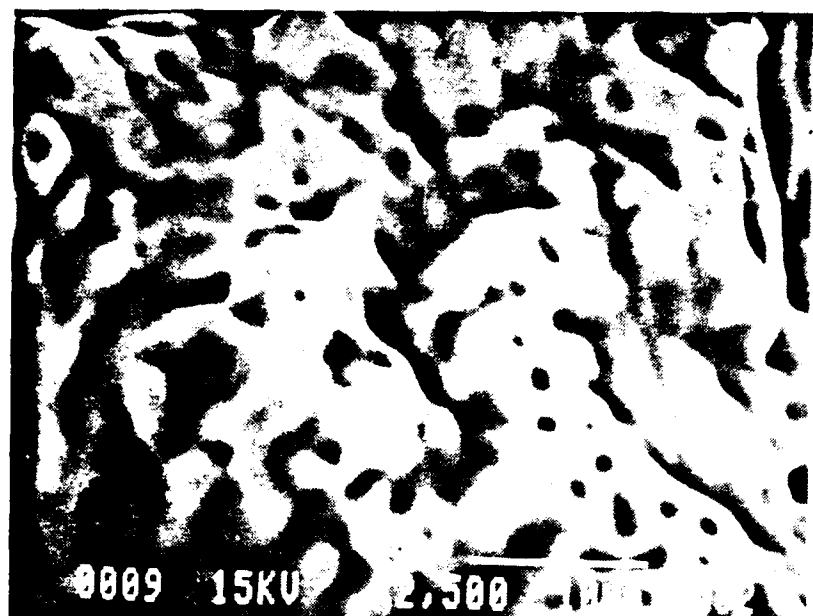
- (a) magnification 100X
- (b) magnification 250X
- (c) magnification 2,500X



(a)



(b)



(c)

Fig.13 SEM fractograph of P/M, pure W at 2200°C.

- (a) magnification 100X
- (b) magnification 250X
- (c) magnification 2,500X



Fig.14 TEM micrograph shows segregation of Re  
from W matrix at magnification 220,000X.

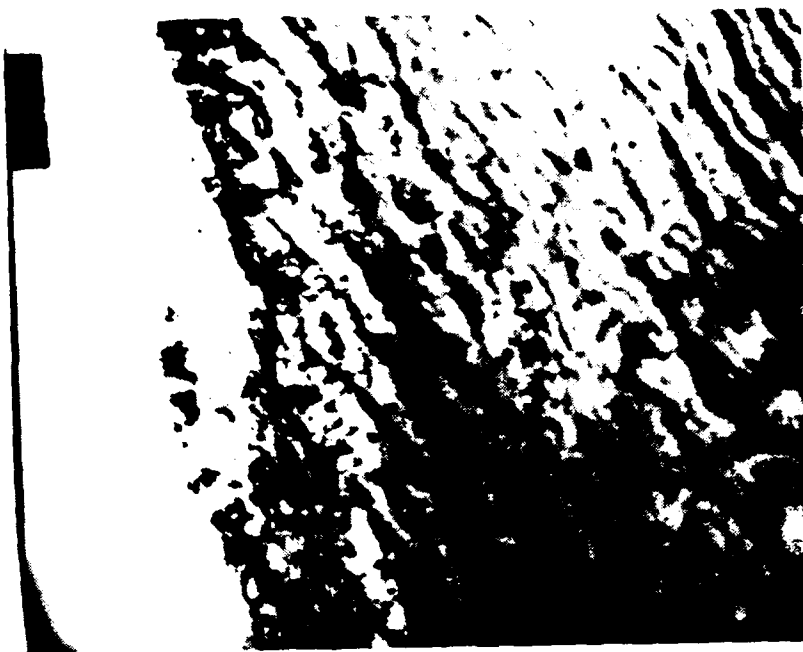


Fig.15 TEM micrograph shows  $\sigma$  phase at magnification  
220,000X.

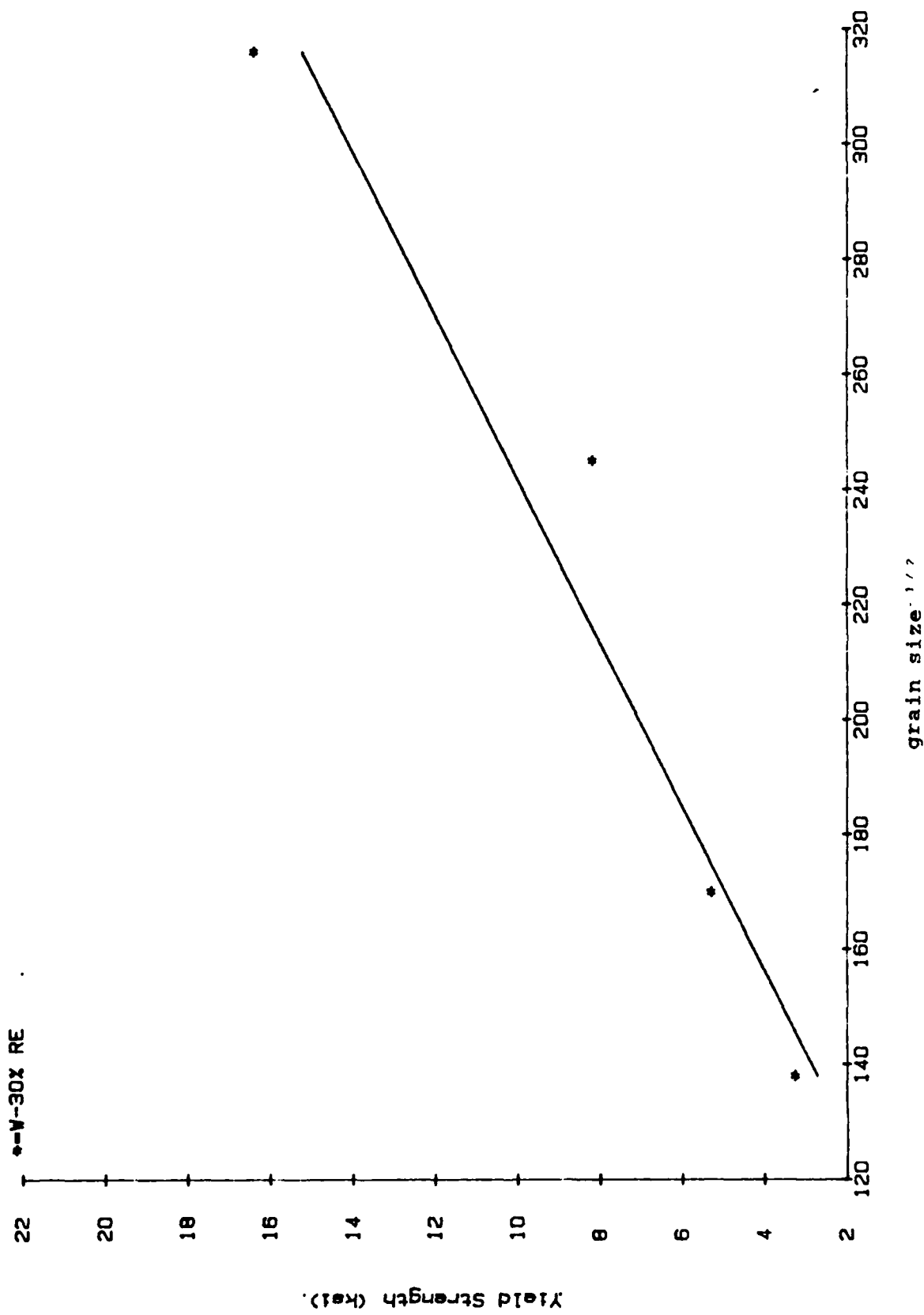


Fig.16 Plot of yield strength vs grain size 117

**ATTACHMENTS**

U.S. DEPARTMENT OF COMMERCE  
NATIONAL BUREAU OF STANDARDS  
WASHINGTON, D.C. 20234

NATIONAL BUREAU OF STANDARDS

REPORT OF CALIBRATION  
RIBBON FILAMENT LAMP

Submitted by

Arizona State University  
Tempe, Arizona 85281

Brightness Temperature (at 0.655 micron) versus Lamp Current

Degrees C (IPTS-68)	Amperes (abs.)	Degrees C (IPTS-68)	Amperes (abs.)
800	10.33	1600	21.66
900	11.14	1700	23.71
1000	12.12	1800	25.86
1100	13.29	1900	28.10
1200	14.65	2000	30.42
1300	16.19	2100	32.83
1400	17.88	2200	35.33
1500	19.71	2300	37.92

The maximum uncertainties of the temperature values reported are estimated to be  $\pm 2.5$  degrees at 800 °C,  $\pm 1.5$  degrees at 1100 °C, and  $\pm 3$  degrees at 2300 °C. The values in the above table and the uncertainties apply at the conclusion of the calibration. The typical change when the lamp is operated at the higher temperatures is a decrease of about one degree per ten hours at all temperatures.

These values apply when the lamp is operated base down and the portion of the filament at the notch made vertical. The center contact should be at a positive potential and the room temperature at 25 °C. The sighting should be made on the center of the filament across from the notch, with the arrow, etched on the back of the envelope, appearing at the notch. The calibration was performed using the NBS photoelectric pyrometer described in the paper, "The NBS Photoelectric Pyrometer and Its Use in Realizing the International Practical Temperature Scale Above 1063 °C," R. D. Lee, Metrologia 2, 150 (1966). The magnitudes of the effects when altering these conditions are discussed in NBS Monograph 41, Theory and Methods of Optical Pyrometry (1962). The text of the International Practical Temperature Scale of 1968 may be found in the April 1969 issue of Metrologia (Vol. 5).

Sightings were made such that the angle subtended at the lamp filament by the entrance pupil of the pyrometer was 0.14 radian.

For the Director  
Institute for Basic Standards

*Albert T. Hatterbury Jr.*

Henry J. Kostkowski  
Chief, Optical Radiation Section  
Heat Division

P.O. No.: 505625  
Test No.: 211745  
Date: March 6, 1975

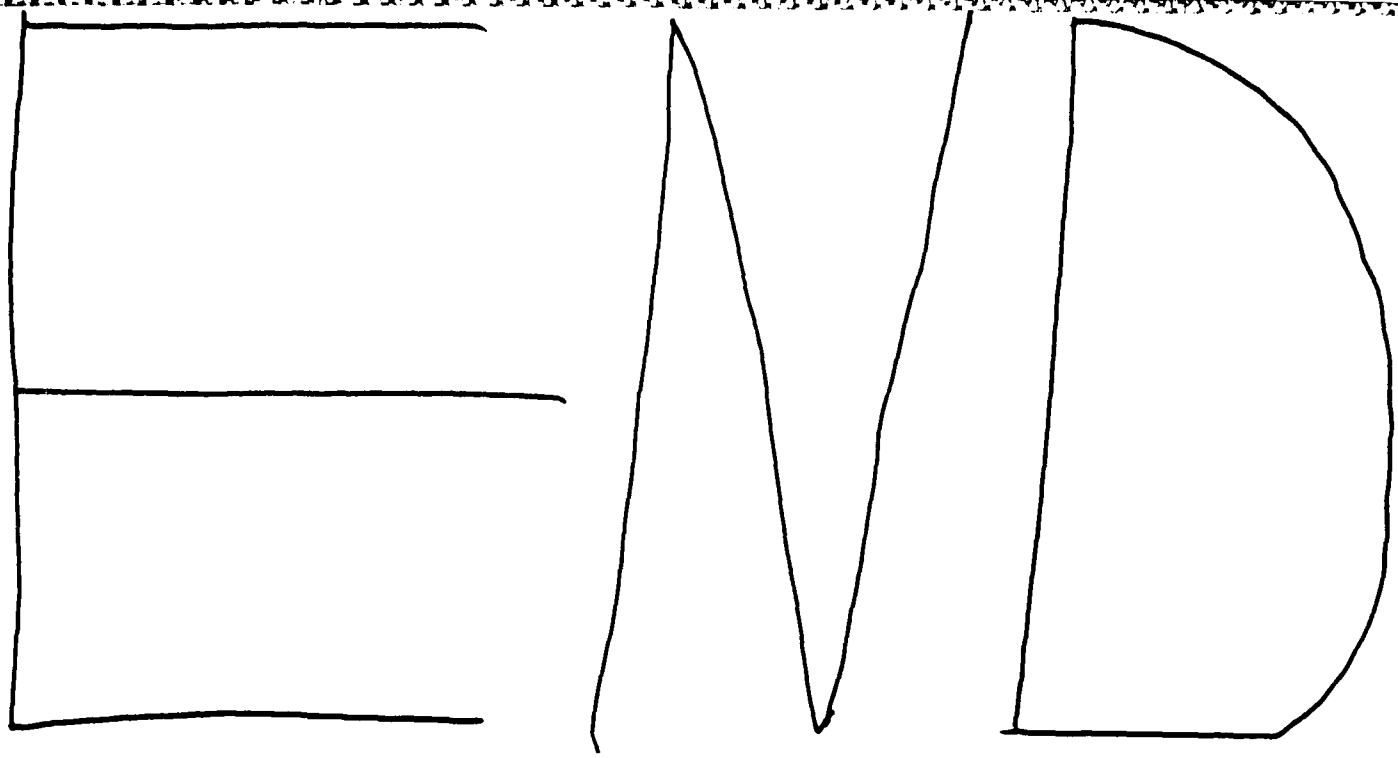
### OPTICAL PYROMETER CALIBRATION

PYROMETER SCALE	TEMPERATURE (CELSIUS)	PHOTON COUNT
II	2,200	737
II	2,100	592
II	2,000	390
I	2,000	4,035
I	1,900	3,221
I	1,800	2,196
I	1,700	1,266
I	1,600	657
0	1,600	2,354
0	1,500	1,194
0	1,400	462
0	1,300	172.40
0	1,200	58.350
0	1,100	19.349
0	1,000	8.120
0	900	5.652
0	800	5.560

APPENDIX 1

## REFERENCE LIST

1. Davidson,P. L., and Brotzen, F. R., (1970), *Acta Met.* **18**, 463-470.
2. Stephens,J.R., and Witzke, W.R.(1971), *J. Less- Common metals*, **23** ,325-342.
3. Christian,J.W. (1970), *Proc. 2nd. Intern. Conf. Strength of metals and alloys*, ASM, Cleverland, Ohio , **1**, 29-37.
4. Ansel, G.S.(1970), Physical Metallurgy (2nd. ed.) (R. W.Cahn,ed) pp.1083-1128, North-Holland , Amsterdam.
5. Guard,R.W. (1962), Strengthening mechanism in solid, Seminar of ASM, Oct.13 and 14, 1960, pp.253-278, Reinhold, Publ., New York.
6. Sell, H.G. Morcom, W. R. and King,G.W, (1966), Rept. AFML- TR-65-047, part ii ,Westing house Lamp Division, Bloomfield, New Jersey.
7. Maykuth, D.J., H.R. Ogden and R.I. Jaffee : In Refractory metals and alloys iv. Res. Dev. Vol.1 , R. I. Jaffee et al,Eds Gordon and Breach, New York 1969.
8. King,G. W., W.R. Morcom and H.G. Sell: In Refractory metals and alloys. iv RES. Dev. vol.1, R. I. Jaffee et al eds Gordon and Breach , New York 1969.
9. Jaffee , R.I., C. T. Sims and J. J. Harwood: in Plansee Proceedings 1958, F. Benesovsky, ed p.380.
10. Ramalingam, M. L., Investigation of Sintered Tungsten, Rhenium Additive Alloys for High Temperature Space Application,Doctoral Dissertation,Arizona State University,1986.



12 - 86

